# Growth Mechanisms of Carbon Nano-fibers, -tubes, and Graphene on Metal Oxide Nano-particles and -wires

by

Akira Kudo

B.Eng., Materials Science and Engineering, Tohoku University (2009)

Submitted to the Department of Materials Science and Engineering
in partial fulfillment of the requirements for the degree of

Doctor of Philosophy

at the

MASSACHUSETTS INSTITUTE OF TECHNOLOGY

June 2016

© Massachusetts Institute of Technology 2016. All rights reserved.

Author . . . . . . . . . . . . . . . . . . . . . . . . . . . . . . . . . . . . . . . . . . . . . . . . . . . . . . . . . . . . .
Department of Materials Science and Engineering
April 26, 2016

Certified by . . . . . . . . . . . . . . . . . . . . . . . . . . . . . . . . . . . . . . . . . . . . . . . . . . . . . . . . . . .
Brian L. Wardle
Professor of Aeronautics and Astronautics
Thesis Supervisor

Certified by . . . . . . . . . . . . . . . . . . . . . . . . . . . . . . . . . . . . . . . . . . . . . . . . . . . . . . . . . . .
Michael S. Strano
Carbon P. Dubbs Professor of Chemical Engineering
Thesis Co-advisor

Certified by . . . . . . . . . . . . . . . . . . . . . . . . . . . . . . . . . . . . . . . . . . . . . . . . . . . . . . . . . . .
Yang Shao-Horn
W.M. Keck Professor of Energy
Professor of Mechanical Engineering
Professor of Materials Science and Engineering
Thesis Reader

Accepted by . . . . . . . . . . . . . . . . . . . . . . . . . . . . . . . . . . . . . . . . . . . . . . . . . . . . . . . . . . .
Donald R. Sadoway
John F. Elliott Professor of Materials Chemistry
Chairman, Department Graduate Committee

# Growth Mechanisms of Carbon Nano-fibers, -tubes, and Graphene on Metal Oxide Nano-particles and -wires

by

Akira Kudo

Submitted to the Department of Materials Science and Engineering
on April 26, 2016, in partial fulfillment of the
requirements for the degree of
Doctor of Philosophy

## Abstract

Carbon nanostructures (CNS) such as carbon nano-fibers (CNFs), -tubes (CNTs), and graphene are of interest for a diverse set of applications. Currently, these CNS are synthesized primarily by chemical vapor deposition (CVD) techniques, using metal catalysts. However, after CNS synthesis, those metals are oftentimes detrimental to the intended application, and extra steps for their removal, if available, have to be taken. As an alternative to metallic catalysts, metal oxide catalysts are investigated in order to better understand metal-free CVD processes for CNS synthesis. This thesis furthers the mechanistic understanding of metal oxide mediated CNS growth, especially metal oxide nanoparticles (MONPs) for CNTs, thereby addressing yield and expanding the range of known catalysts and atmospheric CVD conditions for CNS growth. CNT and CNF growth from zirconia nanoparticles (NPs) are first studied, and a technique is developed to grow CNTs and CNFs from metal NP (MNP) and MONP catalysts under identical CVD conditions. The morphologies of the catalyst-CNT and -CNF interface for zirconia NPs are found to be different than for iron or chromium NPs *via* high resolution transmission electron microscopy (HRTEM) including elemental and phase analyses, and evidence of surface-bound base growth mechanisms are observed for the zirconia NPs. Titania NP growth conditions are investigated parametrically to achieve homogeneous and relatively (vs. zirconia) high growth yield, where clusters of CNTs and CNFs separated by only tens of nanometers are observed. Catalytic activity of titania NPs are estimated to be an order of magnitude lower than iron NPs, and a lift-off mechanism for titania NP catalysts is described, indicating that several layers of graphene will cause lift-off, consistent with HRTEM observations of 4-5 layer graphite within the CNFs. Potential catalytic CNS activity of chromia, vanadia, ceria, lithia and alumina NPs are explored, establishing for the first time CNT growth from chromia and vanadia precursor-derived NPs, although the phases of those NPs are not determined during growth. The insights acquired from MONP-mediated CNS growth are applied to demonstrate continuous, high-yield, few-layer graphene formation on titania nanowires.

Thesis Supervisor: Brian L. Wardle
Title: Professor of Aeronautics and Astronautics

Thesis Co-advisor: Michael S. Strano
Title: Carbon P. Dubbs Professor of Chemical Engineering

# Acknowledgements

First of all, I thank Professor Brian L. Wardle for his mentorship throughout my Ph.D. course. Professor Wardle's technical comments, scholarly presentation in publication, and passion to produce scientific results with impact always drove me to the higher standard of a researcher. I also thank for his generosity that allowed me to explore my interests that are tangential to my thesis topic and to learn as mush as possible from well-organized MIT courses even after passing the qualifying exam.

My thesis co-advisor, Professor Michael S. Strano, has also been a great advisor in shaping ideas into high-profile journal publications. I appreciate his insights very much that were indispensable to complete my thesis work. I would also like to thank my thesis committee members, Professor Silvia Gradecǎk and Professor Yang Shao-Horn.

I am grateful to the member of NECST lab, Nano-Engineered Composite aerospace Structure laboratory. In particular, Dr. Stephen A. Steiner III has always inspired me with his scientific insights, hands-on creativity, and honest attitude toward science. John Cane was always helpful when I have problems and questions with electronics. I always had a good time with Dr. Namiko Yamamoto, Richard Li, Dr. Sunny Wicks, Itai Stein, Doug Jacobs, Jeonyoon Lee, Hanna Vincent, Dale Lidston, Emily Thomson, and all other NECST lab members (excuse me running out of space) for having fun at riverside deck parties, group social, meaningful discussion, etc.

I thank my collaborators for their support too: Dr. Stephan Hofmann in University of Cambridge, Dr. Bernhard C. Bayer in University of Vienna, Dr. Piran R. Kidambi in MIT MechE, Professor Jing Kong and Dr. Sung Mi Jung in MIT EECS. Professor David Bell and Adam Graham at Harvard University Center of Nano Systems always offered me help and suggestions with electron microscopy techniques. Professor Taeghwan Hyeon in Seoul

National University kindly offered samples to this thesis work.

I also thank very much friends I made through the activities of Japanese Association of MIT (JAM) who played sports, traveled, and planned cultural parties together.

Finally, I thank my grandparents, elder brother and his family, and especially mother and farther for their understanding on my studying abroad for 6 years of time with their love and warmth that have always supported me.

# Contents

# List of Figures

# List of Tables

# Abbreviations and Symbols

| | |
|---|---|
| $A$ | Interfacial area between the titania NP catalyst and the multilayer graphene, Å$^2$ |
| $C_{44}$ | Shear modulus, kg·m$^{-1}$·s$^{-2}$ |
| $E$ | Bending strain energy, eV |
| $E_b$ | Strain energy stored per carbon atom in a graphene layer, eV |
| $E_{indiv(n,\alpha)}$ | Strain energy for the individual layer model as function of $n$ and $\alpha$, eV |
| $E_{plate(n,\alpha)}$ | Strain energy for the plate model as function of $n$ and $\alpha$, eV |
| $E_{res}$ | Residual strain energy in the reduced strained volume of multilayer graphene after lift-off, eV |
| $L$ | Length of the titania NP corner along z axis in Figure 5.9, nm |
| $N$ | Number of carbon atoms in the volume that stores strain energy |
| $R$ | Radius of curvature, Å |
| $V$ | Volume of the bent multilayer graphene that stores strain energy, Å$^3$ |
| $\Gamma$ | Adhesion energy of mutilayer graphene on the titania NP catalyst, eV·Å$^{-2}$ |
| $\Pi$ | Porosity, % |
| $\alpha$ | Angle of the MONP catalyst corner, ° |
| $\beta$ | Angle defining the volume of bent graphene around MONP corner, ° |

| | |
|---|---|
| $\gamma_1$ | Interfacial energy between graphitic layer and MONP catalyst, eV·Å$^{-2}$ |
| $\gamma_2$ | Surface energy of the multilayer graphene, eV·Å$^{-2}$ |
| $\gamma_3$ | Surface energy of the titania NP catalyst, eV·Å$^{-2}$ |
| $\kappa_{(n)}$ | Bending stiffness of multilayer graphene as function of $n$, eV |
| $d$ | Distance between the titania NP catalyst surface and the multilayer graphene, Å |
| $d_{hkl}$ | Lattice distance for a set of Miller indices (h, k, l), Å |
| $k$ | Boltzmann constant, eV·K |
| $n$ | Number of graphitic layers |
| $r$ | Radius of a CNF, Å |
| $t$ | Nominal thickness of multilayer graphene before bending, Å |
| $t_{eff(n)}$ | Effective thickness of the multi-layer graphene as function of $n$, Å |
| ● | MONPs firmly corroborated in this work |
| ○ | MONPs firmly corroborated already before this work |
| ▲ | MONPs adequately supported in this work |
| ⋆ | MONPs investigated for the first time in this work |
| △ | MONPs adequately supported before this work |
| $A_i$ | Area of $i$th wall of a multi-wall CNT, Å$^2$ |
| $d_{002}$ | Inter-layer distance of graphene layers in graphite, Å |
| $l$ | Length of a CNF, Å |
| $M$ | Number of walls in a CNT |

| | |
|---|---|
| $N_{CNF}$ | Number of carbon atoms in a CNF |
| $N_{CNT}$ | Number of carbon atoms in a CNT |
| $a_0$ | Area per carbon atom in a graphene layer, Å$^2$ |
| A-CNTs | Aligned CNTs |
| CNF | Carbon nanofiber |
| CNS | Carbon nanostructure |
| CVD | Chemical vapor deposition |
| EDX | Energy dispersive X-ray spectrometry |
| FFT | Fast Fourier transform |
| HRTEM | High-resolution transmission electron microscopy |
| $Al(NO_3)_3 \cdot 9H_2O$ | Aluminum nitrate nonahydrate |
| MNP | Metal nanoparticle |
| MONP | Metal-oxide nanoparticle |
| NP | Nanoparticle |
| NWAG | Nanowire aerogel |
| APF | Accessory photoreactor furnace |
| RF | Resorcinol-formaldehyde |
| SEM | Scanning electron microscopy |
| SiN | Silicon nitride |
| SOFC | Solid-state oxide fuel cell |
| TEM | Transmission electron microscopy |

| | |
|---|---|
| TG-DTA | thermogravimetry-differential thermal analysis |
| UV | Ultraviolet |
| XPS | X-ray photoelectron spectroscopy |
| YSZ | Yttria-stabilized zirconia |
| BrLPF | Blu-ray Laser Photoreactor Furnace |
| CNT | Carbon nanotube |
| CoMoCAT | Cobalt-molybdenum catalyst |
| $CrO_2Cl_2$ | Chromium (VI) oxychloride |
| DSSC | Dye-sensitized solar cell |
| E-TEM | Environmental TEM |
| FqPF | Full-quartz photoreactor furnace |
| HiPCO | High pressure carbon oxide |
| IPA | Isopropyl alcohol |
| $LiNO_3$ | Lithium nitrate |
| **R** | Mean graphite domain size |
| $TiOSO_4 \cdot xH_2O$ | Titanium (IV) oxysulfare hydrate |
| $v_0$ | Volume per a carbon atom in graphite, $Å^3$ |
| $VOSO_4 \cdot xH_2O$ | Vanadium (IV) oxysulfate hydrate |
| XRD | X-ray diffraction |
| $ZrOCl_2 \cdot 8H_2O$ | Zirconium (IV) oxychloride octahydrate |

# Chapter 1

# Introduction

Metal oxide nanoparticles (NPs) as catalysts for chemical vapor deposition (CVD) will extend the potential applications of carbon nanostructures (CNS) that were not compatible with conventional metal catalysts. Multiple combinations of CVD parameters, namely substrate materials, carbon feedstock, and metal oxide species are tested, and resulting CNS growth is characterized by *ex situ* scanning electron microscopy (SEM), transmission electron microscopy (TEM), Raman spectroscopy, and X-ray photoelectron spectroscopy (XPS). Acquired insights on surface-bound growth mechanisms with metal oxide catalysts will lead to metal-free CVD processing. In this chapter, approaches to synthesize CNS are introduced from the earliest to the state-of-the-art, including CVD, the most important method employed in CNS research today. The implications of replacing the current leading metal catalysts with novel metal oxide catalysts is discussed, and the challenges associated with metal oxide catalyst research are then presented. Finally, this chapter concludes with a brief outline of the work carried out in this dissertation.

## 1.1 Motivation

Low-dimensional CNS consisting of $sp^2$ networks of carbon atoms were the focus of many recent studies. See Figure 1.1 for an illustration of common 0D, 1D, and 2D nanocarbon materials. The primary driver for of research on these materials, especially the 1D carbon nanotubes (CNTs) and 2D graphene, is the structure-dependent tunability of their

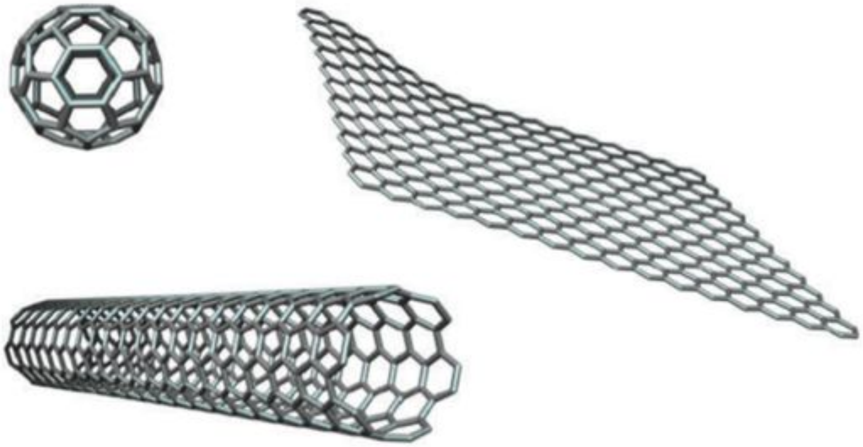

Figure 1.1: Structures of representative 0D, 1D, and 2D nanocarbon materials reproduced from Guldi and Sgobba:[11] fullerene (upper left), carbon nanotube (bottom), and graphene (upper right).

physical properties, which makes nanocarbons the leading candidate materials for applications in the field of electronics, energy devices, biomedical technologies, and structural components.[1,2] Since the highlight of CNTs by Iijima in 1991,[3] the investigation and development of scalable synthesis techniques of CNTs with low defect density was one of the primary research focuses. These early works first yielded the arc discharge method, closely followed by the laser ablation method, and finally the CVD method[4,5] that is the current benchmark CNT synthesis technique in research. Using the high growth yield of CVD, commercial-scale CNT production processes were developed, such as the High Pressure Carbon Oxide (HiPCO) method[6,7] and Cobalt-Molybdenum CATalyst (CoMoCAT) method.[8] Since the first report of the unusually large electron/hole mobility of monolayer graphene at room temperature in a study published in 2004 by Novoselov et al.,[9] many studies over the last several years have attempted to develop graphene synthesis techniques that rival those of CNTs that could enable its widespread commercial application. To manufacture single crystal graphene flakes with large areas, CVD has again emerged as the most efficient synthesis technique.[10]

CVD synthesis techniques of CNTs and graphene usually employ metals as catalyst NPs or catalytic substrates in order to decompose the hydrocarbon feedstock into the underlying carbon atoms and catalyze crowth of the CNSs. However, residue of those metal catalysts, which can be found in the resulting CNS as impurities, has in part limited the wide-spread usage of CNSs for many prospective applications. Research into the development of cleaning techniques that could eliminate these metallic residues has been explored, but a metal-free synthesis route is likely best achieved by the development of metal-free CNS growth *via* CVD. the only surefire to overcome contamination by trace metals is the invention of metal-free CVD approaches.

Since the late 2000's, several research groups have reported potential metal oxide NPs that could function as catalysts to grow CNTs *via* CVD. However, these reports were shortly followed by challenges that hindered the widespread adoption of these metal-free CVD processes. First of all, the growth yields of non-metallic catalysts are much lower than those of leading metal catalysts, such as Fe, under similar growth conditions. This not only made the efficient characterization of the CNTs grown by non-metal species very difficult, but also made the identification of CNTs genuinely grown by the metal oxide species, as opposed to those grown *via* random metal contaminants, extremely challenging to substantiate. In addition, the growth mechanisms that govern the behavior of metal catalysts may not be representative of the underlying physics and chemistry of CNT growth *via* unconventional non-metal catalysts. Without knowledge of the growth mechanisms that govern the performance of unconventional catalysts, there is no clear path of study that promises to improve the growth yield *via* this class of catalysts. Since solving these problems related to CNT growth is also closely related to the study of direct graphene synthesis on non-metallic substrates, especially a group of metal oxides usually described as high-k materials, this emerging research field requires additional work.

## 1.2 Thesis Outline

The aim of this thesis is to investigate metal oxides as catalysts for CVD that can facilitate growth of CNSs.

In Chapter 2, a brief review of CNS growth *via* CVD is provided. Technical features of standard CVD are introduced, followed by a discussion of challenges with respect to compatibility with popular applications of CNTs and graphene. Next, metal oxide NPs as alternative catalysts are presented, including a discussion of both their potential to accelerate graphitic nanostructure applications, and their shortcomings which hinder wide-spread implementation of this new category of catalyst. In this chapter, the primary challenge underlying the identification of the origin of the grown nanocarbons is also discussed. This is primarily due to the low growth yield that is easily overshadowed by random metal contamination in the experimental environment, and the difficulty associated with determining both the oxide NP surface and bulk chemistry during the growth process. At the end of this chapter, the criteria to help evaluate growth by metal-oxide species is outlined.

In Chapter 3, the goals and methodology used throughout this work are articulated. Two important issues with metal-oxide NP (MONP) catalysts, increasing growth yield and elucidating growth mechanisms, are introduced as the object of this dissertation.

In Chapter 4, *ex-situ* characterization of carbon nanofibril growth, both CNTs and CNFs, from zirconia NP catalysts is presented. Using a high-resolution transmission electron microscope (HRTEM), the difference between the growth morphologies resulting from zirconia and metal NPs grown under identical CVD conditions is presented. Zirconia is found to facilitate surface-bound growth mechanisms of CNTs and CNFs, in good agreement with its physicochemical properties (around 2× higher melting point and lower diffusivity of carbon atoms compared to popular metals used as CNT growth catalysts in CVD). The relationship between the appearance of NPs, namely shape and size, and their effect on growth mechanisms is discussed. Zirconia NPs were also applied to carbon xerogel and aerogel substrates to demonstrate enhanced growth yield in the presence of high surface-area carbon as a demonstration of the insight acquired from the HRTEM characterization.

In Chapter 5, quantitative analyses on the chemical kinetics and lift-off process of CNT growth on MONP catalysts are outlined. With titania NPs as model catalysts, a parametric study on CVD conditions was implemented to show that a higher growth yield of turbostratic CNTs and CNFs was achieved for titania NP catalysts than their zirconia counterparts. Chemical kinetics from decomposition of hydrocarbons on the catalyst surface to graphitization of amorphous carbon are discussed to estimate the catalytic activity of titania NPs relative to iron NPs. A phenomenological thermodynamic model is built to explain the lift-off step of the graphitic carbon formed on a corner of the titania NP catalyst.

In Chapter 6, multiple MONP species are investigated to study aspects that were not fully explored in previous studies. Chromia and vanadia NPs are prepared and tested to see the effects of MONP reduction into metals, as well as the chemical resistance against carbide formation. Using ceria, lithia, and alumina NPs, the effect of surface electronic structure on catalytic activity is also explored. These results of growth mechanisms across multiple metal oxide species enables the development of a more systematic understanding on the set of criteria, with emphasis on chemistry, that a MONP must meet in order to be an effective catalyst for carbon nanostructure synthesis.

In Chapter 7, the knowledge acquired so far is extended to the growth of graphitic nanostructures (mainly few-layer nanographene) on metal oxide nanowires. The motivation of using nanowires as substrates, and its advantages when compared to the graphene growth using flat substrates, are outlined. The resulting morphologies of carbon deposition on titania nanowire aerogel (NWAG) at different durations of CVD reactions helps demonstrate the catalytic effect of the titania nanowire surface to the graphitization of amorphous carbon. This effect is also validated quantitatively through peak intensity analysis from Raman spectra.

In Chapter 8, the challenges and preliminary results of photocatalysis-assisted CVD growth of CNTs are presented. While a part of the initial motivation of this MONP catalyst work, there were multiple hurdles to install proper equipment and implement this new vector of CVD synthesis. The resulting purpose-built reactor furnace prepared for photocatalysis-assisted CVD (laser furnace) is introduced in detail, as well as how the entire system was modified since the idea was conceived by Steiner[12]. Preliminary results with titania NP catalysts and nanowire substrates are introduced, followed by recommendations for future work.

Chapter 9, the final chapter, summarizes the important contributions of this thesis. Recommendations for future work for MONP catalysts and titania NWAG are presented, especially toward the practical installation of metal oxide-mediated CNS growth. Remarks on synergistic effect of photocatalysis with CVD grwoth of CNS are also provided.

# Chapter 2

# Background

The development and refinement of an effective synthesis route *via* CVD is a milestone that must be achieved to enable the scalability, and ultimate commercialization, of low dimensional materials, especially carbon nanomaterials. In this chapter, the CVD synthesis of CNSs is explained in more detail, and its advantages over leading alternative synthesis route and current limitations are discussed. Also, the challenges of using metals as one of the most important CVD parameters, *i.e*. catalysts, are outlined, and how metal oxides can potentially solve those problems is presented. The criteria to establish a metal oxide species as a new catalyst for CNS synthesis is detailed. Finally, this chapter concludes with a discussion of the similarities and differences of the growth mechanisms that govern the behavior of metal and metal oxide catalysts.

## 2.1 CVD Synthesis of CNSs by Metal Catalysts

CVD has a number of key advantages when compared to its predecessors, which mainly include the arc discharge and laser ablation that dominated CNS synthesis before the advent of CVD. Unlike the two earlier techniques, which require complicated setups that included a high voltage arc or a high power laser and a collector equipped with a quencher, the CVD setup is much simpler and more facile, where a compact, tabletop conventional tube furnace connected to gas tanks through mass-flow controllers is sufficient to produce CNTs including aligned CNTs (A-CNTs). See Figure 2.1 for an illustration of representative setups of the arc discharge, laser ablation, and CVD techniques. Also, the CVD technique has the added advantage of a low reaction temperature, where a CNT growth temperature as low as 500°C was recently achieved with a proper combination of carbon feedstock and MNP catalysts,[13,14] whereas a CNT growth temperatures of 1000°C to even few thousands °C were necessary to produce CNTs by the arc discharge and laser ablation techniques. More importantly, CVD dominates the two previous techniques in terms of growth yield. CNTs grown by CVD can be manufactured in the form of a ”forest”, an array of vertically aligned CNTs that is typically a few microns to millimeters tall.[15,16] These advantages can enable facile mass production of CNTs, and allows scientists to study properties and performance of large-scale devices comprised of CNTs. CVD is also a popular production method for graphene[17]. CVD enables growth of large single crystalline domains of graphene that are particularly suitable for quantification of the growth mechanisms, and to exploit graphene's extraordinary properties, especially for application in electronic devices. Depending on the purpose and growth, CVD variants that can tune a wide variety of the growth conditions were developed, such as atmospheric pressure CVD[18,19], vacuum CVD (or equivalently, low pressure CVD)[19–21], and plasma enhanced CVD.[22,23] When growing CNTs *via* CVD, a substrate material, typically a silicon wafer with thin oxide layer, onto which a few nanometers-thick metal layer is deposited, is employed. CVD processing of CNS begins by flushing the air inside of the quartz tube using an inert gas flow, an inert career gas (Ar is typical) and a reducer, *i.e.* hydrogen flow, and the temperature starts to be elevated. En route to the reaction temperature, the native oxide layer on the metal surface is removed by the reductive gas. The metal film dewets and splits into nanoparticle catalysts as the temperature inside the furnace is elevated. At the reaction temperature, the carbon feedstock starts to flow, and CNT growth takes place at the metal nanoparticle (MNP) catalyst sites on the substrate surface. Gas flow is stopped after a desired length of time, and the furnace starts to cool down. When growing graphene *via* CVD, a piece of metal sheet is used instead of a silicon wafer topped with a metal layer, and the rest of setup and CVD parameters can be shared with CVD for CNTs.

CVD, however, is not without shortcomings when used for graphitic nanostructure synthesis. CVD is an empirical process that is known to be difficult to control and character-

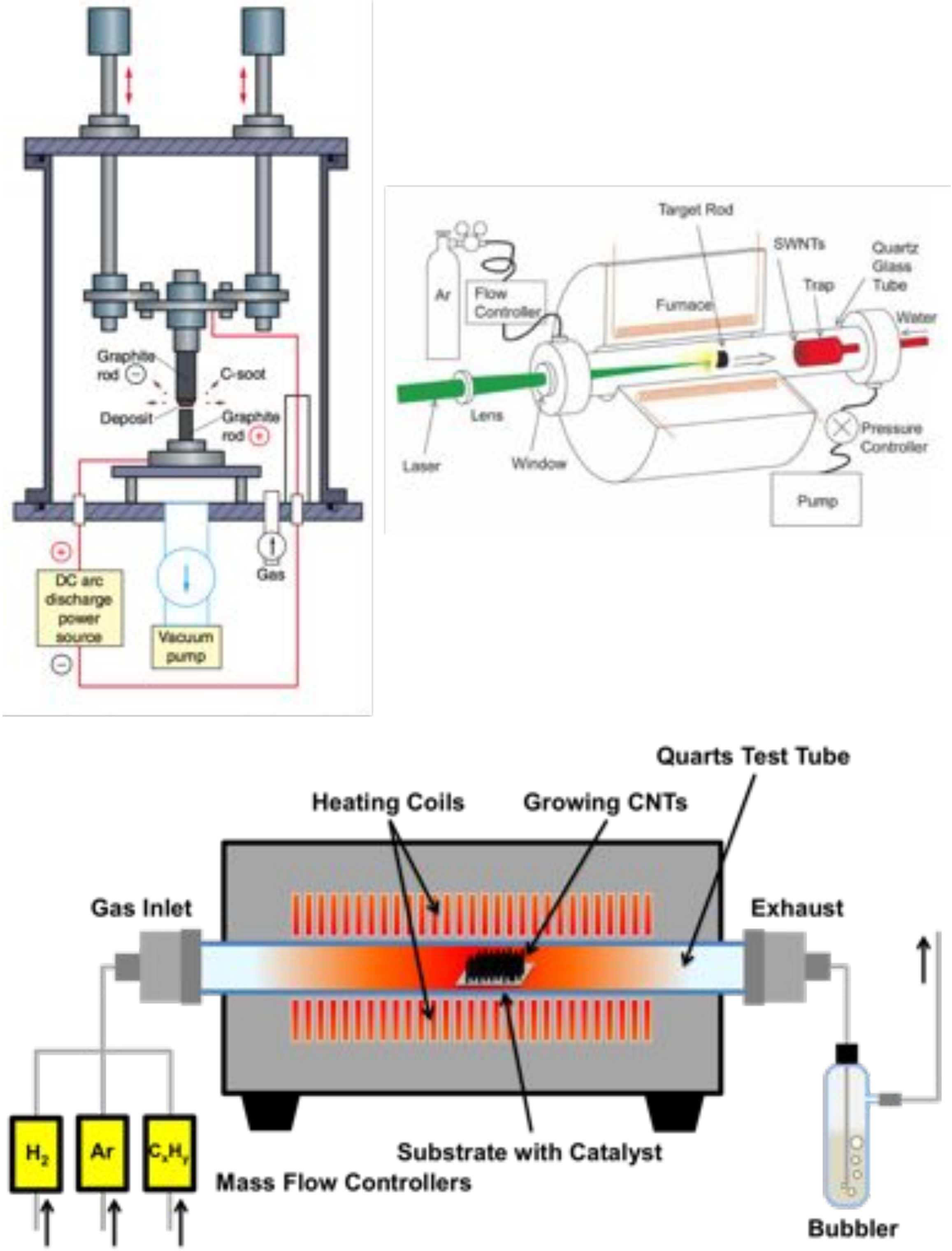

Figure 2.1: Schematic illustrations of typical apparatus for carbon nanostructure synthesis, reproduced from Ando et al.[4] Arc discharge method (upper left), laser ablation method (right), and CVD method (bottom).

ize, and the resulting nanostructures are highly sensitive to subtle changes in parameters such as carbon feedstock, catalyst species, reaction temperatures, substrate material, gas flow ratio, etc. Moreover, several inconspicuous parameters may be critical as well: residual water inside the quarts tube, the position of the sample inside the quartz tube, and even hydrocarbon and other contamination accumulated inside the exhaust tube after multiple runs. Therefore, the discovery of the key parameters define today's state-of-the-art CVD processes was not straighforward. For example, one of the most important parameters, usage of metallic nanoparticles as catalysts for CNT growth, was actually a fortunate discovery rather than a result of a systematic parametric study.[24] Even after the metallic nanoparticles were established as effective carbon nanofibril growth catalysts, decades passed before every piece of knowledge and experience could be consolidated into a reliable CNT growth technique *via* CVD around 2000. Today we know that nanoparticles of metals, such as iron,[25] nickel,[26] cobalt,[27] and other metallic species[28] and their alloys[29,30] supported on an inert and stable substrate can convert low-mass carbon feedstock into hollow, one-dimensional graphitic nanostructure such as CNTs. Popular carbon feedstock species reported so far include methane,[31] ethylene,[32] acetylene,[33] alcohol vapor,[34] and benzene.[35] Graphene growth also uses sheets of nickel[36] and copper[37] as a catalytic substrate. The selection of materials (*e.g.* carbon feedstock, other gas species, substrate, catalyst etc.), combined with operational parameters (*e.g.* temperature, reaction time length, flow rate of every gas species, etc.) has resulted in the synthesis of CNSs with different morphologies (*e.g.* length and diameter of CNTs, number of layers of graphenes, crystallinity of the CNS, etc., *e.g.* see Figure 2.2).[38] While usage of metals as catalysts was a breakthrough in the development of CVD techniques for CNS synthesis, this catalyst chemistry placed a limitation on the application of these products. Metals used in the growth process usually reside in the produced CNSs, and those metal residues could be potentially problematic for a variety of applications. In particular, characterization results can become very confusing, due to the contribution from metallic residues that are difficult to decouple from the signal originating from the synthesized CNS. For example, while electrochemical and electronic properties of CNS are key to many device applications, these could potentially be altered by even a trace amount of metal residue.[39–41] Unless metallic

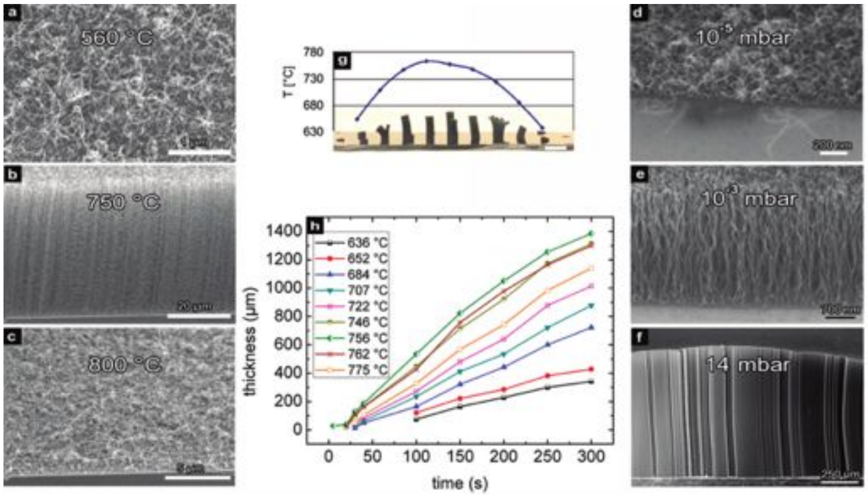

Figure 2.2: An example of a CNT growth study *via* CVD for a range of parameters, reproduced from Wirth et al.[38] In this work the effect of reaction temperature and carbon feedstock partial pressure on resulting morphologies of CNTs are investigated. Fixed parameters are substrate material (alumina), catalyst species (iron), carbon feedstock (acetylene), and reaction time (5 minutes). (a)-(c) SEM images of CNTs grown at different temperatures at atmospheric pressure. (d)-(f) SEM images of CNTs grown at different partial pressures of acetylene at $\sim 700°$C. (g) The temperature profile across the entire sample substrate. The scale bar is 2 mm. (h) Lengths of vertically aligned CNTs as function of reaction time at different temperatures measured by in-situ optical imaging. The resulting morphologies of CNTs differ from sparse and entangled filaments to dense and well-aligned arrays.

residues can be reduced to a negligible order of magnitude, the measured performance of such devices will not be reliable. Another concern is that metal residues usually takes the form of nanoparticles, which are highly reactive and could be modified by small chemical and physical stimulation. At high temperature environments or in an acidic/alkaline solution, which commonly occurs in the prospective applications, metal residue is easily redistributed *via* coagulation, diffusion, vaporization, dissolution, and other physical/chemical processes to cause unwanted phenomena that are difficult to track. For instance, residual metals were reported to exhibit significant bio-toxicities, and therefore hinder biomedical applications such as imaging and cancer treatment.[42] It should also be noted that the combination of CVD parameters, perhaps alternatively called the ”recipe”, using metals as catalysts may not be compatible, or at least not an ideal match, with the device packaging that would be utilized in industrial applications. To stabilize MNP catalysts, CVD growth of CNTs are currently coupled with silicon wafer substrates, which are not necessarily a desirable substrate for all prospective applications. One of the most desired applications of graphene is electronics, which requires the transfer of graphene monolayers synthesized on a metal substrate to another sheet of dielectrics, especially 'high-k' materials.[43] In general, CNTs produced for electronic applications need to avoid metal residues, since the metal contaminants may migrate into other semiconductor components and diminish their functionality by randomly altering the doping profiles. For these reasons, additional post-growth steps have to be taken between the synthesis of CNS and their practical application, such as transportation,[44] purification,[45] etc. While all these processes were designed to ensure that the CNSs and their properties remain intact, post-processing could in reality damage those CNSs and deteriorate their performances. In summary, metal-free synthesis of CNS is key to fully realize their potential, and there is an increasing demand for technical advancement in this area.

## 2.2 Metal Oxide Nanoparticles: Unconventional Catalysts

Since the late 2000's, non-metallic nanoparticles have garnered much attention as nanoparticle catalysts for graphitic nanostructure growth *via* CVD. Starting with semiconductor nanoparticles such as Ge, SiC, and Si,[46] materials of interest as catalyst for CNT growth were extended to include metal oxides such as alumina,[47,48] silica,[48–51] zirconia,[52] titania,[48,53,54] erbia,[48] and tantala.[55] Even diamond[56] and alkali metal salt nanoparticles[57] are reported to facilitate CNT growth. A recent publication introduces an unintentional growth of CNS from yttria-stabilized zirconia (YSZ) during solid-state oxide fuel cell (SOFC) testing.[58] Nanoscale graphene platelets and related nanostructures are also synthesized on metal oxide nanoparticles such as magnesia[59,60], gallium oxide[59] and hafnia,[61] as well as polycrystalline graphene films on alumina[62] and silica.[63] Establishment of metal-free growth of graphitic nanostructure has a significant benefit as mentioned in the previous section, and therefore has become a major driving force for this research field. Catalyst nanoparticles that are stable and inert at multiple potential environments are of particular interest, particularly metal oxides.

While the field was expanded by this unconventional, newly emerged group of catalysts and their potential, researchers also encountered a number of challenges. First of all, claiming catalytic activity of a new metal oxide species, especially when concerned with CNT growth, is not straightforward. After a few reports were published, researchers noticed that the growth yield from those metal oxide nanoparticles were quite low compared to popular MNP catalysts. This means that even a trace amount of random metals as contamination could lead to the growth of a misleading amount of CNTs that could be confused by growth from the metal oxide if due diligence is not exercised. Such contamination can be introduced by touching substrates with metallic tweezers, incomplete washing of glassware, and mishandling of samples that could lead to their contact with/exposure to human skin, floor tiles, tap water drops and so on. Therefore if only SEM micrographs and energy dispersive X-ray spectrometry (EDX) data are provided in a report, the evidence of the growth efficacy of a new metal oxide species may not be sufficient to support any claims of catalytic activity for CNT synthesis. Also, to conclusively prove that metal oxides are responsible for the observed (potential) CNT growth, their bulk chemistry during growth, and possibly surface chemistry too, has to be confirmed. Since most CVD recipes include high temperatures and hydrogen to avoid excessive deposition of amorphous carbon,[64] reduction of MONPs into MNPs as the reactor temperature is being elevated is a real possibility, and the observed CNT growth may originate from nanoparticles that were reduced to their underlying metal species. Alternatively, there is also a chance that metal oxides are carbothermally reduced to the corresponding carbide phase as hydrocarbon molecules are decomposed.[65] In-situ investigation of growth mechanisms using environmental HRTEM, the utility of which was proven with a MNP catalyst systems,[66–70] could be the best solution to observe oxidation state of the examined material. However, due to the low growth yield even with atmospheric pressure CVD, catalytic activity of metal oxide nanoparticles is not likely to be observed *via* in-situ HRTEM observation, where only CVD with a lower pressure of carbon feedstock can be executed to avoid damage to the vacuum system and environment that HRTEM requires. An alternative in-situ technique is in-situ XPS. Although not an imaging technique, XPS separately captures emitted electrons from different electronic states of an element, *e.g.* zirconium atoms, including different valence states of zirconium cations ($Zr^{3+}$ and $Zr^{4+}$), will be independently observed in metallic zirconium, zirconium carbide, and zirconia using this technique. The utility of *in-situ* XPS was previously demonstrated in studies that explored CVD growth of CNTs *via* zirconia and tantala nanoparticles.[52,55]

Therefore, to conclusively identify a metal oxide species as an active catalyst, the majority of the following criteria have to be fulfilled:

(1) An *ex-situ* HRTEM micrograph showing that a nanoparticle is attached to a CNT and/or CNF

(2) Lattice fringes and a corresponding diffraction pattern or fast Fourier transform (FFT) pattern of the nanoparticle acquired with the ex-situ HRTEM characterization

(3) EDX spectrum from the area around the nanoparticle acquired with the *ex-situ* HRTEM characterization (<100 nm in diameter, EDX equipped with a TEM is necessary)

(4) *In-situ* HRTEM or *In-situ* XPS during CVD

(5) Compelling proof, *via* both references and analysis, to ensure that the examined metal oxide was neither reduced to the underlying metal nor involved in the formation of a carbide

A complete dataset of (1) – (3) is necessary. If multiple of such dataset are available, that could be regarded as a strong validation even with ex-situ characterization only. (4) is the most desired, although very often time-consuming. (5) is always necessary and available with phase diagrams, thermodynamic data handbooks, and the Ellingham diagram. An example of a compelling HRTEM image (would be item (2) in the above discussion) from previous literature is shown in Figure 2.3. Another problem is that a fundamentally different picture of CNT growth *via* metal oxide catalysts has to be established. For CNT growth *via* popular MNP catalysts, it is currently known that the 1D graphitic structures form *via* the following multi-step reaction:[71,72] 1) adsorption of hydrocarbon feedstock molecules on the MNP catalyst surface, 2) decomposition of hydrocarbon feedstock molecules into carbon atoms on their surface, 3) diffusion of carbon atoms into the bulk of the MNPs until the miscibility limit is attained, and surface diffusion of carbon atoms leads to the construction of an sp$^2$ network, and 4) precipitation of oversaturated carbon as graphitic nanostructures, here a CNT. Scenarios where growth occurs when the catalyst nanoparticle detaches

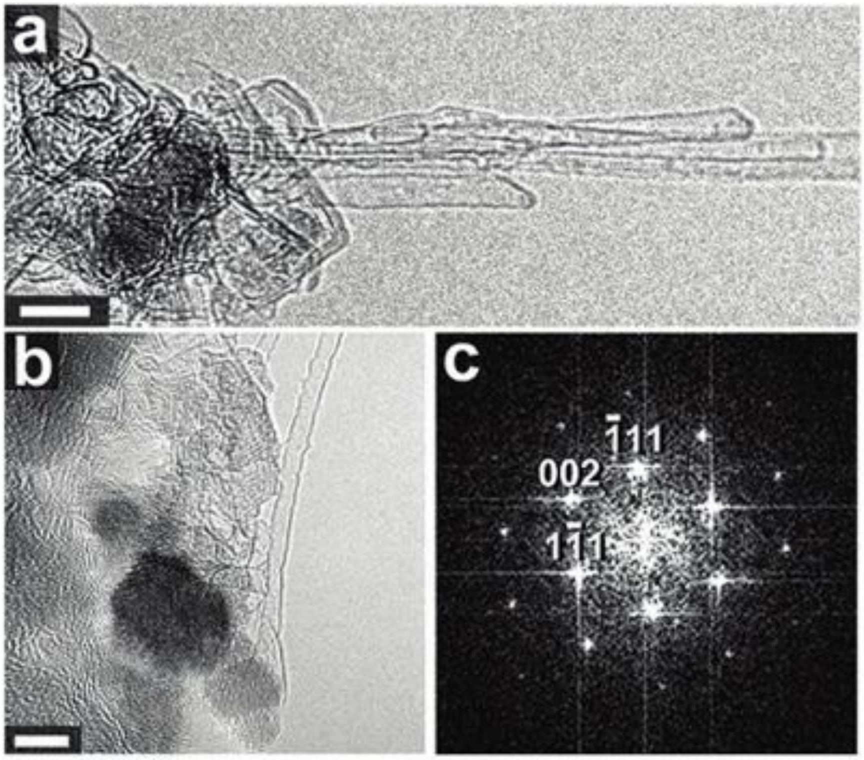

Figure 2.3: An example of compelling HRTEM micrograph demonstrating CNT growth *via* diamond nanoparticles, reproduced fromTakagi et al.[56] (a) and (b) show CNTs attached to nanoparticles at a lattice-fringe resolved magnification. (c) An FFT pattern taken form the nanoparticle imaged in (b) which corresponds to diamond.

from the substrate, so called tip-growth, or when the catalyst nanoparticle is attached to a substrate while growing a CNT, so called base-growth or equivalently root-growth, are both possible. This ”solvation-precipitation” process, illustrated in Figure 2.4, is unlikely to apply to MONPs, especially due to their considerably higher melting point and lower miscibility with carbon atoms than the MNP catalysts. Graphene synthesis encountered a similar issue. A nickel foil employs basically the same solvation-precipitation process for graphene synthesis so that graphene can be synthesized on both sides on the sheet.[73] A copper foil, even though not predicted by phase diagrams to employ the solvation-precipitation process, serves as a catalyst with temperatures as high as 1000°C for CVD synthesis of graphene, which approaches the melting point of copper (1085°C) and hence indicates solvation of carbon atoms as interstitials.[74] For these reasons, it is necessary to figure out new mechanisms that govern growth of both CNTs and graphene on metal oxides. For CNT growth,

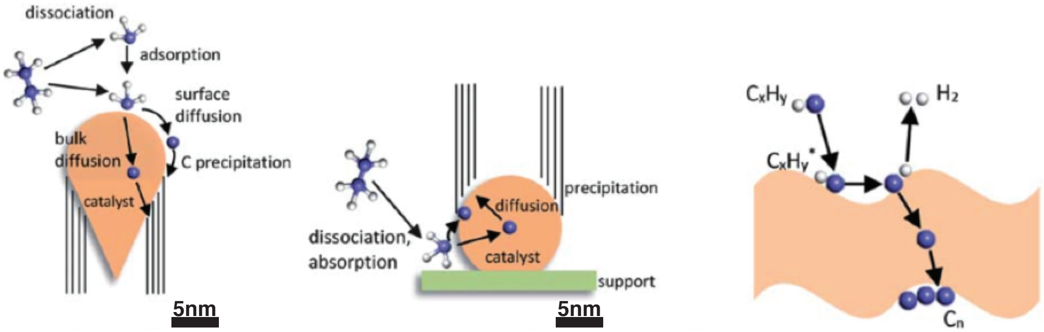

**(a) Tip-growh** **(b) Base-growh** **(c) Graphene growth**

Figure 2.4: Schematic illustrations for CNT growth *via* CVD using MNP catalysts, reproduced from Robertson.[72] (a) Solvation-precipitation process for tip-growth (catalysts detaches from the substrate) and (b) base-growth (catalysts stay on the substrate). (c) Elementary reactions on metal catalyst surface.

while an in-depth discussion on the topic is not currently available, a rough sketch of what the growth process could look like was proposed previously in a review article on MONG catalysts, and is shown in Figure 2.5.[75] As Figure 2.5 demonstrates, a corner of the metal oxide nanoparticle could intuitively play an important role in the growth mechanics, since the observation of a higher density of surface defects is expected to enhance adsorption, decomposition, and perhaps catalytic activity toward graphitization. For graphene synthesis, copper is the most popular catalytic substrate, especially when a highly crystalline, large single domain of graphene is desired. When synthesized on metal oxides, graphenes tends to split into smaller domains, which again indicates the presence of different mechanisms than the ones postulated for graphene synthesis by metallic copper substrates. However, graphene production on both metal and metal oxide catalytic sheets seem to be influenced similarly by surface defects, *e.g.* steps and kinks, which help facilitate the nucleation of the graphene sheets.[60,76] According to these investigations, structural sensitivity (alternatively written as ‘structure sensitivity’, in a variety of previous literature and textbooks) will be an essential part of the mechanisms that govern both CNT and graphene synthesis metal oxide-mediated CVD.

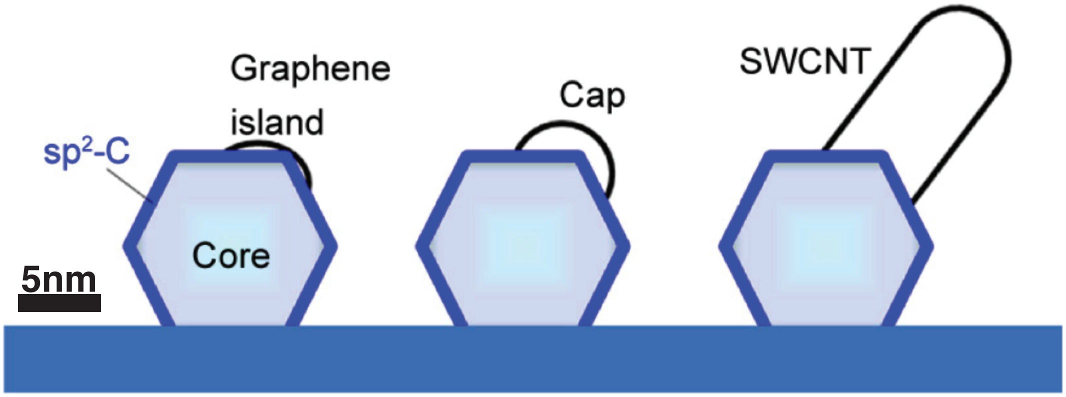

Figure 2.5: Schematic illustrations for CNT growth *via* CVD using metal oxide nanoparticle catalysts, reproduced from the review article by Homma et al.[75]

## 2.3 Conclusions

CVD for CNS synthesis was discussed in detail, and the key advantages and limitations of this technique were identified. Although indispensable for CVD synthesis of a wide variety of nanostructures, metallic contaminants that result from metal catalysts constrain the application of their resulting CNSs. Metal oxide catalysts, on the other hand, offer a potential route for CVD production of pristine CNSs with minimal unwanted metallic species. This thesis will investigate metal oxide catalysts that will further the state of the art in metal-free CNS synthesis. In the next chapter, the goals of this dissertation are detailed, and the general methodology followed to meet these objectives is discussed.

# Chapter 3

# Objectives and Approach

This chapter presents the goals of this thesis, and how they are approached. The goals of this thesis include improving growth yield and elucidating growth mechanisms for MONPs, which could help expand commercialization and utilization of CNSs. This work is carried out using atmospheric CVD, which is the most versatile and commonly utilized type of CVD for CNS synthesis. Many conventional techniques for studying growth, *e.g.*, *in-situ* TEM, are not available for MONPs due to the very low growth yield. While a standard *ex-situ* HRTEM is most frequently used for characterization in this dissertation, aberration-corrected TEM (or Cs-corrected TEM) is also used which can take HRTEM images at higher magnification with lower damage potentially induced in the samples.

## 3.1 Objectives of Current Work

The primary objectives of this dissertation are to improve the efficiency and scalability of processes utilizing these unconventional catalysts, and to elucidate the physics that govern the synthesis of CNSs *via* MONP catalysts.

Two aspects of MONP catalyst growth are explored: growth yield, and the mechanisms underpinning the growth process. To date, growth yields reported by studies that fulfill the criteria outlined in Chapter 2 are far too low to apply to practical applications. It should be noted, however, that the combination of CVD parameters for optimized growth yield (catalyst species, substrate material, gas species and flow rates, CVD temperature and time length, etc) *via* MONP catalysts was not investigated as extensively as the CVD growth conditions for metal NP catalysts. Finding CVD recipes using MONPs that approach the growth morphology produced by metal catalysts could attract interest from a variety of disciplines, just as the first report of reproducible, high-yield growth of carbon nanofibrils *via* CVD encouraged researchers to pursue CNTs. By exploring the mechanisms that lead to CNS growth *via* MONPs, which could be very different from the process we observe and/or expect from metal NP catalysts, the hurdle that currently prevents yields of MONP catalyzed growth from being comparable to metal NP growths may be identified. This could enable the development of tuned recipes that allow MONP catalysts to grow metal-free CNSs for a wide variety of high value applications.

## 3.2 Thesis Approach

In this section, the methods and general approach that serve as the foundation of this dissertation are discussed.

### 3.2.1 Growth Yield Investigation

As mentioned above, while there is a vast parameter space that was previously unexplored for MONP catalyst studies, there is a firm starting point based on past work with zirconia MONPs. The first step is to investigate carbonaceous materials as the substrate. Recent work presented that zirconia NPs are not only active catalysts for CNT growth, but also for graphitization, with carbon aerogel as the substrate material.[52] Those results allude to a solid-state carbon source being partially responsible for enhanced CNT growth yield from zirconia NP catalysts. Carbonaceous materials are often incompatible with metal NPs since they interact during CVD to deteriorate the inherent properties of the substrate material (*e.g.* growing CNTs on carbon fibers with metal NPs damages the fibers),[77] which makes the capability of MONPs to form CNSs without side reactions worth exploring further.

The relatively large number of studies dealing with silica and titania NP-mediated CNT growth indicates that homogeneous CNT growth with high yield is more likely to originate from silica and/or titania NP than zirconia NP catalysts. Herein titania NP is selected for a parametric study with a ‘standard’ substrate for metal NP growth of CNS. Several CVD parameters are attempted to quantify their effect on the resulting growth yields, and they include:

- Basic hydrocarbon as feedstock: methane, ethylene, and acetylene
- Single-crystal silicon wafer with a thermally grown silica layer, that includes a thin layer of sputtered alumina on top
- CVD Temperature

### 3.2.2 Growth Mechanisms Investigation

Unless high growth yield is achieved, and the entire piece of silicon wafer substrate ($\sim$ 10 mm $\times$ 10 mm) is homogeneously covered by CNTs, it is necessary to find and image individual NPs that successfully facilitate the growth of CNTs. Since CNT growth occurs with NP catalysts which are usually no larger than $\sim$ 10 nm in diameter, this type of investigation necessitates the usage of HRTEM to understand the growth mechanisms. Moreover, HRTEM is also capable of carefully excluding metal contamination, with its localized EDX and lattice fringe analysis among others. Abberation-corrected TEM is more suitable for the investigation of CNSs because of its sub-nanometer spatial resolution at only 80 kV of acceleration voltage, which is less damaging to the grown CNS.

It should be noted that research on the growth mechanisms at play in MONP catalysts is currently very limited. As a result of the parametric study detailed above, the yield of titania NP catalysts could be utilized to compare MONP catalytic activity to that of Fe catalysts. The lift-off step, which occurs at the beginning of CNT and CNF growth, is also modeled based on HRTEM observations and considers thermodynamic interactions between strain and adhesion energies.

It is also within the scope of this dissertation to search for new MONP catalysts and to explore their efficacy at facilitating the growth of CNTs, and other CNS, *via* CVD. Zirconia and titania are both oxides of group IV elements, therefore the physicochemical properties that arise from their metal cations are similar. Those properties include electronic structure of their surface, which governs the catalytic process, and resistance against reduction/carbothermal reduction, and are therefore of high interest. MONPs of other group elements are selected to compare their behavior under the same CVD conditions, which ensures that growth mechanisms proposed for MONPs are developed with a systematic understanding as a function of the chemistry of the metal cation. The various elements that comprised this study, and the approach utilized for their investigation, are as follows:

- Chromia and vanadia NPs to show the trend of resistivity against reduction and relate it to the growth mechanisms by investigating the morphologies by Cs-corrected TEM.
- Ceria, lithium oxide, and alumina NPs for observing effects on CNS morphologies from different outermost electronic orbitals of metal cations.

Finally, the insights acquired from investigating MONPs for CNT and CNF growth are applied to understand CNS growth on titania NWAG. The three-dimensionally entangled titania nanowires that compose NWAG are found to offer high growth yield of CNSs for quantitative analysis of morphologies by Raman spectroscopy. Abberation-corrected TEM is used to observe the transition of amorphous carbon patches to continuous few-layer graphitic domains.

### 3.2.3 Limitations of the Current Work

Since the yield of CNT and CNF growth *via* MONP catalysts is very low, the studies pursued in this thesis encountered the following limitations:

**Growth Yield:**

- Quantitative techniques are difficult to apply with CNT and CNF growth, *e.g.* thermogravimetry-differential thermal analysis (TG-DTA) to evaluate converted amount of carbon feedstock.
- Comparison of growth yield of CNT and CNF is fundamentally based on the visual information acquired from non-quantitative SEM and HRTEM imaging (although estimates are made).

**Growth Mechanisms:**

- Possible formation of thin film ($\lesssim$ 1 nm in thickness) of non-oxide phases on the MONPs, such as carbide, metal, and carbonate, are difficult to identify and quantify.
- Formation of non-stoichiometric oxide in catalytically active MONPs during CVD also could not be characterized.

Based on findings and observations from this work, suggestions to overcome these limitations are provided in Chapter 9.

# Chapter 4

# CNT and CNF Growth from Zirconia NP Catalyst

In this chapter, the mechanisms and morphologies of CNT and CNF growth from zirconia NP catalysts are discussed in comparison to those grown from MNP catalysts. Although the growth mechanisms for zirconia NPs were not known, they were assumed to be very different from the ones employed by popular MNPs, and were shown to be highly surface-bound *via* extensive *ex-situ* TEM imaging. Futhermore, applying the insight obtained from the identified mechanisms, enhanced growth yield from zirconia NP catalysts was demonstrated using carbon xerogels and aerogels as the growth substrates. As described previously, although *in-situ* TEM and XPS are among the best methods for investigation, such were not possible due to insufficient growth yield with zirconia NP catalysts. In reality, even for growth with conventional MNP catalysts, the difficulty associated with transferring the very sparsely grown CNTs also hindered *ex-situ* TEM characterization. This problem was approached by designing a TEM grid capable of *in situ* CNT growth *via* CVD, which in turn required a dedicated effort to decouple growth catalyzed by metal contaminations from those genuinely facilitated by zirconia NPs.

## 4.1 Introduction

Zirconia was identified as a MONP catalyst for CNT growth *via* CVD, using *in-situ* XPS, at the early stages of non-MNP catalyst research in 2009.[52] Differences in the morphologies of CNSs grown from MONP catalysts (*e.g.*, zirconia) and conventional oxide-supported MNP catalysts (Fe and Cr) are investigated using HRTEM and localized EDX analysis. In this chapter CNSs (CNTs and CNFs of varying morphologies) directly synthesized on TEM grids are discussed, on which MONP and oxide-supported MNP catalysts were deposited on two different regions of the same TEM grid. By characterizing the CNS growth originating from these two types of NP catalysts on the same grid, potential differences that may arise due to process parameter variations are eliminated, enabling direct comparison of the growth yielded by these two systems. It was discovered that zirconia NP-grown and MNP-grown CNSs clearly exhibit different morphological features as well as the features in the environments surrounding the catalyst particle, providing experimental support that growth with zirconia NPs proceeds *via* a surface-bound mechanism. Growth was performed on both lacy carbon-coated Cu TEM grids and metal-free silicon nitride (SiN) grids with and without pyrolytic carbon, and comparable results were obtained with both types of TEM grids. This verified that the observed growth does not result from interactions with Cu, and helped validate the localized analysis approach as a rigorous means for characterizing NP catalysts and mechanisms. On the basis of these observations, we propose a growth model that correlates zirconia NP size, shape, and the observed intermediary CNS features, and use this information to demonstrate a practical method for enhancing the yield of CNTs and CNFs resulting from CVD growth employing zirconia NPs.

## 4.2 Experimental

Preparation of two types of zirconia NP precursor solutions and samples for CVD on lacy-carbon coated Cu TEM grids are explained in detail, in addition to the techniques utilized to introduce MNPs on the same TEM grids. Next, we focus on how to determine the phase of catalyst that grows CNTs and CNFs. The chemical procedure of zirconia precursor-doped carbon gel samples from resorcinol-formaldehyde (RF) polymer synthesis is provided.

### 4.2.1 Synthesis and Deposition of Zirconia NP Catalysts onto TEM Grids

Zirconia NPs are prepared *via* two different synthesis approaches, and are deposited onto lacy carbon-coated Cu TEM grids (Pacific Grid Tech, product number Cu-400LC. 3.05 mm OD Cu grid with 30 nm thick lacy carbon film). The lacy carbon film is amorphous and has random holes with mean diameter of 42 $\mu$m. In the first approach, saturated dispersions of zirconium (IV) oxychloride octahydrate ($ZrOCl_2 \cdot 8H_2O$, Sigma-Aldirch, product number 31670 > 99.5%) in isopropyl alcohol (IPA, VWR CAS No 67-63-0, > 99.5%) are prepared, and its diluted supernatant (1 g of the supernatant in 11.45 g of IPA) is drop-cast onto the TEM grids to create polydisperse zirconia NPs on the TEM grid. In the second approach, monodispersed 4 nm-diameter zirconia NPs supplied from Prof. Taewang Hyeon's group at Seoul National University were used.[78] Solutions of the zirconia NPs are prepared by dispersing 10 mg of NPs in 15.72 g (20 mL) of IPA followed by ultrasonication for 5 min. Prepared solution is then drop-cast onto the TEM grid. In order to evaluate whether metal adatoms, which might already be present in the TEM grid, may affect growth from the spatially separated zirconia NPs on lacy carbon, the same growth process is used on SiN TEM grids (Tedpella, product number 21569-10). Both pristine SiN grids and pyrolytic carbon-coated SiN grids are tested, in order to assure SiN TEM grids are clean enough and to replicate carbon-based substrate on SiN TEM grids. Pyrolytic carbon-coated SiN grids are prepared in fused quartz process tubes (25 mm OD $\times$ 22 mm ID $\times$ 76.2 cm length) placed inside a Lindberg/Blue M MiniMite 1-inch diameter electric clamshell tube furnace. Process tubes are baked in air at 800°C for one hour prior to the process. First, a pristine SiN grid is placed in the process tube, and the tube was flushed with 750 sccm of argon at room temperature for 2 minutes to remove residual air from the tube. Next, a flow of 400 sccm of hydrogen and 100 sccm of argon was introduced and the temperature was ramped to 850°C. Once at temperature, a flow of 200 sccm of ethylene was added, and the flow rate of hydrogen is reduced to 300 sccm. After 15 min, the hydrogen and ethylene were turned off and the system was cooled to room temperature.

### 4.2.2 Deposition of MNP Catalysts onto TEM Grids

Previous work by our group on zirconia-mediated growth showed that contacting substrates with metallic tools, such as stainless steel tweezers, deposits catalytically-active MNPs locally at the site of contact. For this reason, in previous work the use of metallic tools was rigorously avoided (*e.g.*, by only using plastic tweezers, insertion rods, and storage containers, etc.) to avoid unintended introduction of metals onto catalyst substrates. In this study, the previous discovery was leveraged to controllably introduce MNPs (of Fe and Cr) onto the desired part of the TEM grid as shown in Figure 4.1 using stainless steel tweezers.

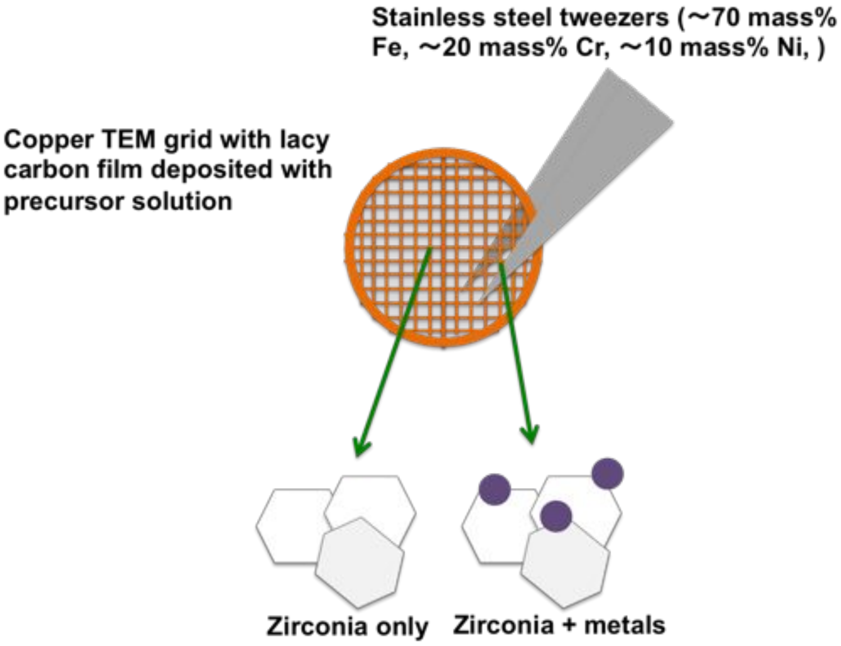

Figure 4.1: Schematic illustration of controlled metal introduction for TEM grid direct growth sample.

Here in contrast, the use of those metal tools enabled spatially resolved observation of the growth behavior of both zirconia-supported MNPs and isolated unreduced zirconia NPs on different parts of the grid *pari passu*, *i.e.*, experiencing the same growth conditions, by *ex-situ* HRTEM.

### 4.2.3 Direct CVD Growth of CNTs and CNFs on TEM Grids

CVD and annealing processes are performed in the same setup as used to prepare pyrolytic carbon-coated SiN TEM grids. Argon, hydrogen, and ethylene (Airgas, UHP grade, 99.999%) are used for CVD. Sample grids are first placed on a piece of silicon wafer, and inserted into the process tube about 4 cm beyond the zone center toward the exhaust end of the tube. Prior to CVD, samples are thermally treated at 800°C under a flow of 200 sccm of argon for 60 min, and then cooled down to room temperature. CVD processing was also the same as preparation of pyrolytic carbon-coated SiN TEM grids, except that the flow rate for ethylene is 100 sccm and for hydrogen remains 400 sccm during reaction. Resulting CNSs were then characterized by HRTEM and point-localized EDX (JEOL 2010F).

### 4.2.4 Elemental Analysis and Phase Assignment by EDX and FFT

FFT patterns of HRTEM images are generated by Gatan Digital Micrograph. By analyzing angles between diffractions and lattice distances measured by ImageJ that correspond to each Miller index, we determine if the NPs attached to the grown CNT or CNF are zirconia, and if so, the phase of the zirconia NP. EDX is also acquired in the area centered on the NP in order to testify the species and the phase. A short script is coded in the language ‘C’ to calculate the angles between diffractions based on lattice parameters obtained from the literature (Zr,[79] cubic zirconia,[80] tetragonal zirconia,[81] monoclinic zirconia,[82] zirconium carbide,[83] $\alpha$ and $\gamma$ Fe,[84,85] Cr,[86] Cu,[87] copper (I) oxide,[88] copper (II) oxide[89]), and the calculated angles are compared to the angles measured in the FFT patterns. The crystallographic data used in phase assignment is available in Appendix. Cu and its oxides are fully investigated in order to distinguish zirconia NPs from Cu and/or copper oxide NPs.

### 4.2.5 Preparation of Carbon Gel-Supported Zirconia

RF gel precursors are prepared according to the method of Mulik et al.[90] and the method of Pekala et al.,[91] which give comparable results. Briefly, according to the method of Mulik et al., 0.337 g of resorcinol (Sigma-Aldrich, product number W358908, > 98%) and

0.447 mL of formaldehyde (Sigma-Aldrich, product number 252549, 37 wt % in water, contains 10-15% of methanol as stabilizer) are added to 11.5 mL of acetonitrile (Sigma-Aldrich, product number 271004, 99.8%) to which a solution of 0.03 mL of concentrated aqueous HCl (Sigma-Aldrich product number 320331, 12.1 N) in 0.636 mL of acetonitrile is added. The mixture is poured into 29 mm × 10 mm poly-(tetrafluoroethylene) molds and allowed to gel overnight in a sealed container with a 1 cm layer of acetonitrile in the bottom to produce an acetonitrile-rich atmosphere. Finally, the pore liquid in the gels is exchanged with pure acetonitrile in preparation for supercritical drying or evaporative drying. Alternatively, according to the method of Pekala et al., 1.98 g of resorcinol, 2.93 g of formaldehyde solution, and 9.65 g of catalyst solution (0.202 g of sodium carbonate dissolved in 100 g of deionized water) are added to 94.24 g deionized water and stirred overnight. Next, the solution is transferred into sealed polypropylene vials which are then placed in an oven at 80°C for $2-3$ days. The resulting RF gels are cut out of the molds with metal-free tools and the pore liquid of the gels is exchanged with pure acetone in preparation for supercritical drying or evaporative drying. RF gels are either supercritically dried from $CO_2$ to yield an RF aerogel[12] or alternatively evaporatively dried in a sealed container to produce an RF xerogel. Zirconia NP precursor solutions are then drop-cast onto the RF xerogels and aerogels and evaporatively dried. Finally, the zirconia-deposited xerogels and aerogels are pyrolyzed at 800°C for 10.5 h under a flow of 200 sccm Ar to convert them into four different sample combinations of zirconia NPs on carbon substrates: zirconyl-derived polydisperse NPs on xerogel, monodisperse NPs on xerogel, zirconyl-derived polydisperse NPs on aerogel, and monodisperse NPs on aerogel.

## 4.3 Results

Two different types of growth observed with zirconia NP catalysts in this work are explained in detail and contrasted with that from MNPs. The synthesized CNSs from zirconia NP catalysts are characterized to be turbostratic carbon based on HRTEM imaging and Raman spectroscopy.

### 4.3.1 Growths Observed in This Work

CNSs were grown directly on TEM grids and observed with HRTEM. Characterization of NP catalysts and morphologies of CNSs were mainly done with lacy carbon-coated Cu TEM grids, and local characterization of catalyst NPs found that Cu does not interact with the growth process. Growths were also performed on metal-free SiN TEM grids, which yielded comparable results, further verifying the observed results were not due to contributions from Cu and validating the local characterization approach on lacy carbon-coated Cu grids as a means for excluding interactions from Cu (see Appendix.A) After CVD, elongated CNSs extending from catalyst NPs were consistently observed. Typically, over the majority of the grid, CNSs attached to zirconia NPs are observed. On the part of the grid where MNPs were deposited, CNSs extending from MNPs supported by zirconia NP agglomerations are observed. In these experiments, the metal-on-zirconia aggregates represent conventional oxide-supported metal catalysts and serve as a control for comparing nanostructure morphology against metal-free oxide NPs on other parts of the grid. Analysis of CNSs attached to metal-free oxide NPs were made using NPs located away from the metal-NP-deposited region of the grid and were verified to be metal-free using lattice fringe analysis and EDX. We observe three types of CNS morphologies on our TEM grids, one of which is associated with growth from MNPs and two of which are associated with growth from zirconia NPs.

### 4.3.2 Growth from Zirconia: Type 1 and Type 2 Growth

Growth from zirconia NPs presents two different morphologies. In some cases, turbostratic CNTs are observed extending from zirconia NPs that are two to three times larger in diameter than the CNT (see example in Figure 4.2a). We refer to this morphology as Type 1 growth. Unlike oxide-supported MNPs, no encapsulating graphitic cage is observed around zirconia NPs exhibiting Type 1 growth. Instead, CNTs are found attached to exposed corners of the zirconia NPs as seen in Figure 4.2b. Closer inspection of the interface between the CNT and zirconia NPs (Figure 4.2c) reveals a rolled-up graphitic appendage approximately the same diameter as the CNT. This appendage does not encapsulate the zirconia

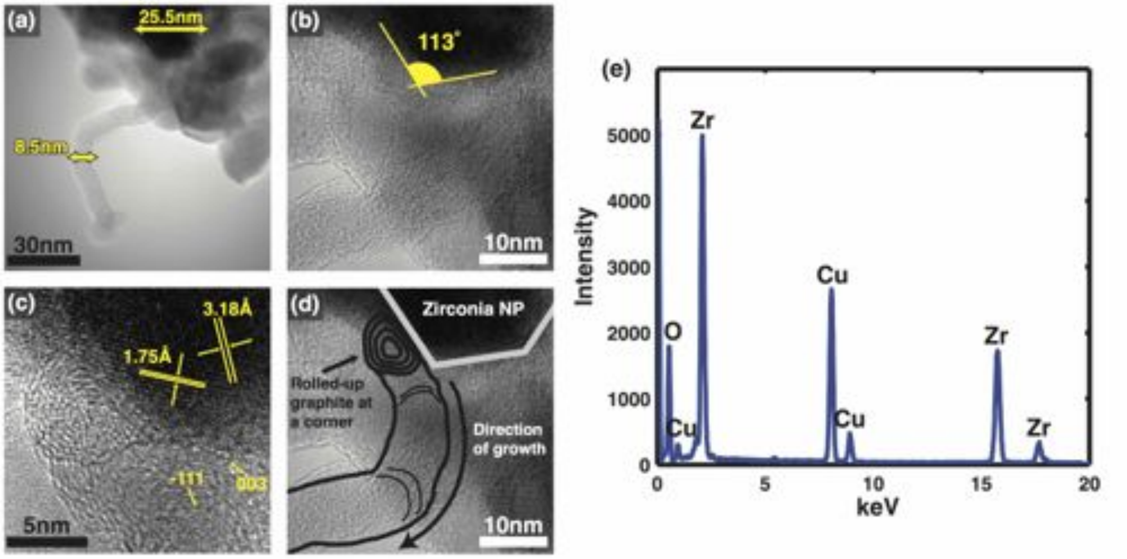

Figure 4.2: CNT grown from zirconia NPs.[92] (a) A CNT grown from a zirconia NP catalyst without any other NPs attached on its tip, indicating base-growth. Numbers indicate diameters of the zirconia NP catalyst and the CNT, 25.5 and 8.5 nm, respectively. (b) A magnified view of the CNT in (a). The CNT is grown from a corner of the zirconia NP. The number indicates the angle of the corner in degree. (c) A rolled-up graphitic appendage found at the CNT-zirconia NP interface. The lattice distance and the FFT pattern taken from the NP validate it to be monoclinic zirconia. (d) Schematic illustration of the Type 1 growth morphology imposed on (b). Information obtained from (c) is reflected on (b). (e) EDX taken from the area centering the root of CNT in (a). The diameter of the electron beam is about 80 nm.

NP surface but rather is localized as a separate substructure near the NP corner. The rest of the surface is observed to be covered by few-layer defective carbon domains or remains bare. This localized rolled-up graphitic appendage is consistently found in Type 1 growth as seen in Figures 4.2 to 4.4. According to the images of the entire CNT lengths, we conclude that these structures emanate from zirconia NPs *via* a base-growth mechanism (see Figures 4.2a and 4.3a). Point-localized EDX spectra taken from the area centered on the root of the attached CNT in Figure 4.2a is shown in Figure 4.2e. Lattice fringe analysis of zirconia NPs associated with Type 1 growth (see for example Figure 4.2c) was used to verify NP composition (note that the Cu peak observed in the EDX spectrum arises from the grid background). No MNPs are seen in the vicinity of the CNT-on-zirconia structures. It is concluded that MNPs are not responsible for the growth of such CNTs. Type 1 growth is only observed at high-angle corners (>110°) of monoclinic zirconia NPs as determined by HRTEM and FFT pattern analysis. Table 4.1 summarizes the calculated angles between reflections in order to determine whether the NP attached to the CNT or CNF can be assigned to any phase of zirconia. Measured angles are within 5% of error from calculated angles. In order to exclude other compounds and phases, a full list of lattice distance and corresponding Miller indices is provided in Appendix. Aggregated zirconia particles larger

Table 4.1: List of the FFT spot orientation used to determine the phase of each NP catalyst.[92]

| Possible indices | Measured angles between reflections | Calculated angles | Assigned phases | Figure number |
|---|---|---|---|---|
| {-111}/{003} | 117.9° | 120.2° | Monoclinic | Figure 4.2c |
| {-111}/{220} | 92.8° | 92.7° | Monoclinic | Figure 4.3c |
| {-111}/{-203} | 37.6 ° | 39.4° | Monoclinic | Figure 4.4b |
| {011}/{101} | 68.9° | 70.9° | Tetragonal | Figure 4.5c |
| {011}/{101} | 69.9° | 70.9° | Tetragonal | Figure 4.6b |

than 50 nm × 50 nm × 100 nm with flat surfaces are also observed, however neither CNTs nor CNFs are seen extending from the middle of such surfaces. This geometric preference toward NP corner is consistent with the model of CNT growth from non-MNPs previously proposed by Homma et al. as shown in Figure 2.5,[75] although the morphology observed is not exactly consistent with the representation of graphite lifting off a corner. Figures 4.3 and 4.4 are further examples of Type 1 growth. Rolled-up graphitic appendages at the interface between nanostructures and zirconia NP are again observed, along with either few-layer defective carbon domains or bare surfaces surrounding the NP. Typical CNTs found exhibiting Type 1 growth were 100 to 200 nm in length. The interface between the rolled-up appendages and the zirconia NP to which they are attached (Figures 4.2c, 4.3c, and 4.4b) appears to follow the planar surface of the NP, suggesting that these structures originate on the NP as opposed to attaching post-formation. All Type 1 growth observed are base-growth. The second morphology of CNSs attached to the zirconia NPs observed does not include a rolled-up appendage and is instead characterized by CNFs with approximately the same diameter as the zirconia catalyst NP. This morphology referred as Type 2 growth is represented in Figure 4.5. Both the diameters of the grown CNS and the active NP catalyst are smaller than Type 1 growth. CNF is observed extending from isolated particles while continuous conformal turbostratic carbon layers are observed following the contour surfaces of aggregates of multiple zirconia particles (Figure 4.5a). Those turbostratic carbon layers are thinner than the graphitic cage seen around MNP catalysts. In this type of growth, multiple individual CNFs extending from different zirconia NPs may merge into larger structures. Figure 4.6 shows an example of how multiple zirconia-attached CNFs may fuse into a larger-diameter CNS. As is the case with Type 1 growth, all Type 2 growth observed are base-growth.

### 4.3.3 Growth from Metals: Type M Growth

On the region of the TEM grids where MNPs were placed through controlled contact with a stainless steel instrument, CNTs attached to MNPs (Cr and Fe) formed on zirconia NP aggregates are observed. A graphitic cage is observed with these growths from oxide-

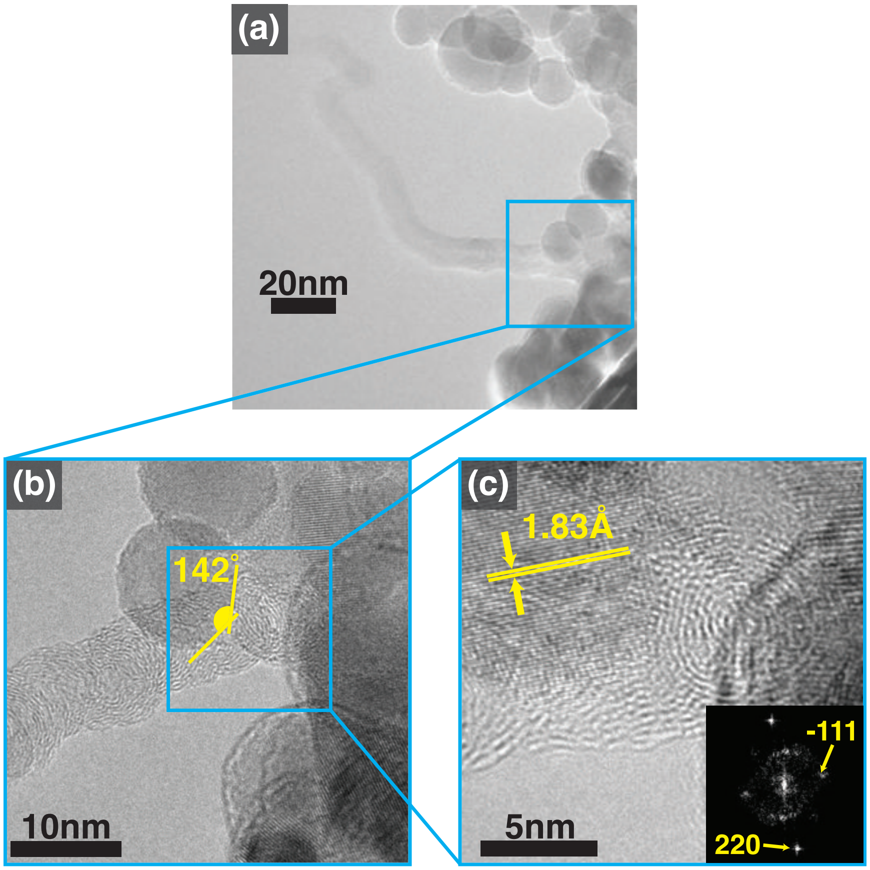

Figure 4.3: Another example of Type 1 growth of CNTs on the corner of zirconia NPs with larger diameter than the CNT itself.[92] (a) A base growth morphology of a CNT extending from a zirconia NP catalyst. (b) A rolled-up graphite appendage at the interface showing hollow interior and walls of the CNT. (c) Higher resolution and FFT pattern taken from the NP validating that the NP is monoclinic zirconia.

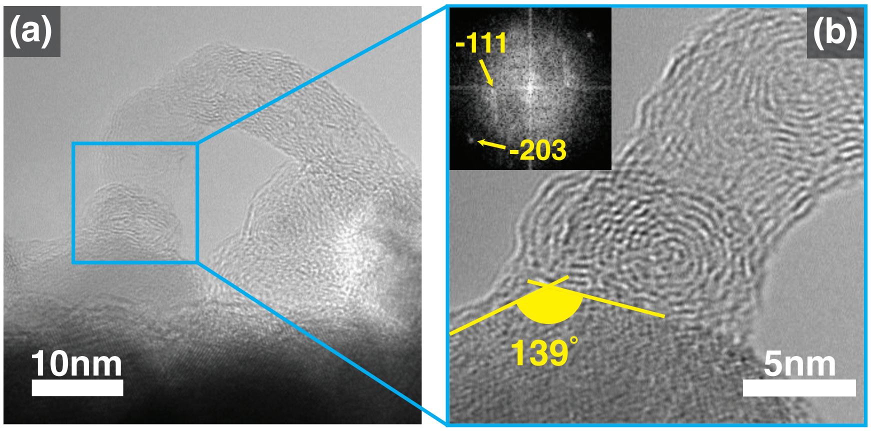

Figure 4.4: Third example of Type 1 growth of CNT.[92] (a) A zirconia NP catalyst growing a CNT and covered by a thin graphitic layer. (b) Higher resolution at the contact between the NP and the CNT. The FFT pattern taken from the NP validates the NP is monoclinic zirconia.

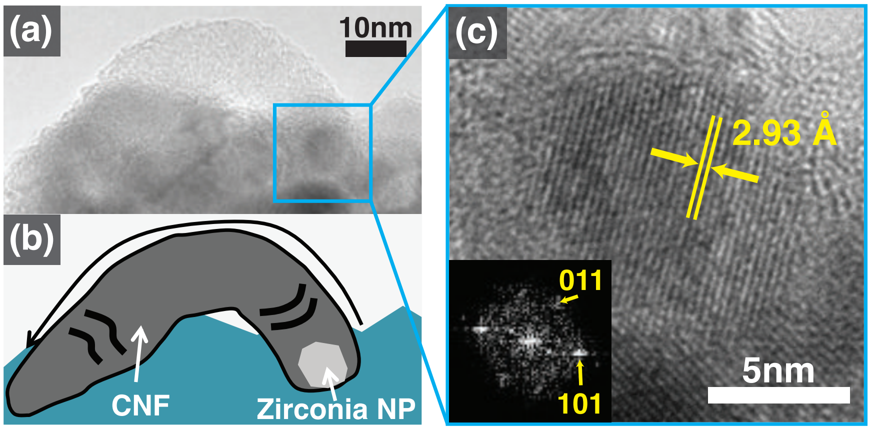

Figure 4.5: Type 2 growth from zirconia NP.[92] (a) A CNF growing from a zirconia NP with a comparable diameter. (b) Schematic illustration of (a). A black arrow indicates the direction of growth. (c) A high magnification view of the catalytic zirconia NP. The NP is buried in the zirconia NP aggregates. Faceted shape is observed. FFT pattern validates the NP is tetragonal zirconia.

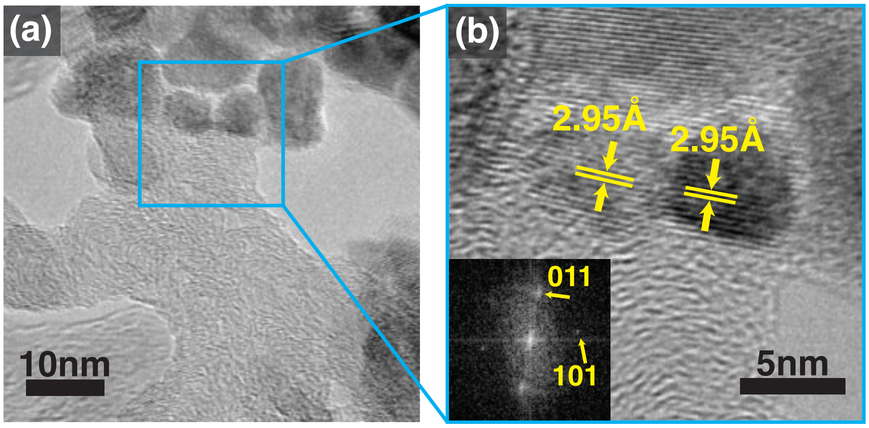

Figure 4.6: Examples of merging Type 2 CNFs synthesized by multiple zirconia NP catalysts.[92] (a) CNFs grown from two adjacent zirconia NPs and fused together. (b) A high magnification view of the zirconia NPs growing CNFs. FFT pattern is taken from the right zirconia NP and shows that the NP is tetragonal zirconia.

supported MNPs which encapsulates the MNP catalyst, and a CNT with approximately the same diameter as the MNP extends from the encapsulated NP. Here these growths are categorized into Type M growth, where M stands for metal. Figures 4.7a and 4.7b show a CNT grown from a Cr NP, and Figure 4.7c shows a CNT grown from an Fe NP. A graphitic cage is observed surrounding those MNPs. Additionally, MNP catalysts are occasionally seen protruding into the hollow length of the attached CNT as seen in Figure 4.7c, which was not seen with Type 1 nor Type 2 growth at all. Fe and Cr NPs are consistently found with a graphitic cage that is thicker than the thin carbon layers found covering zirconia NP catalysts. These morphologies indicate that with the conditions employed in this work the Type M growth is independent of zirconia on which the MNPs are placed, unlike the cases that both MNPs and metal oxide supports are involved.[93] We note that the TEM grids used in this work were comprised of Cu and that Cu NPs have also been reported to serve as catalysts for CVD growth of CNTs.[28] However, only on rare occasions were Cu NPs observed on the TEM grids and thus are generally believed to not have contributed to nanostructure growth either in terms of being a physical catalyst nor participating in terms of hydrocarbon transformation, the latter because of the SiN TEM grid growths being similar to the lacy carbon-coated Cu TEM grid growths. As discussed later, potential contribution from Cu was excluded by comparable growth on metal-free SiN TEM grids.

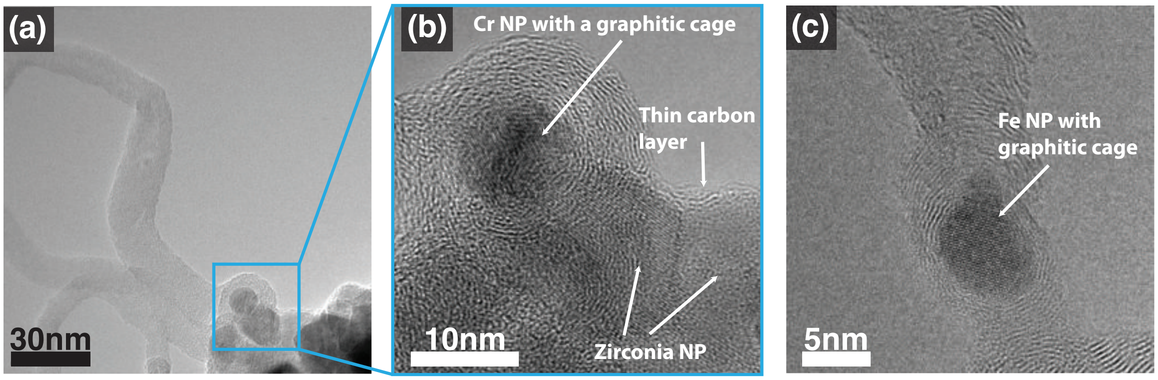

Figure 4.7: Type M growth observed in this work.[92] (a) A Cr NP adjacent to zirconia NPs. Only the Cr NP is growing a CNT. (b) A high magnification view of the Cr and zirconia NPs in (a). The graphitic cage around the Cr NP is much thicker than the carbon layer on zirconia NPs. Such carbon layers deposit only on the exposed surface of zirconia NPs, not on the interface of zirconia NPs aggregated together, indicating the layers are not formed by precipitation of carbon from zirconia NP saturated with carbon. (c) An Fe NP growing a CNT. Thick graphitic cage and projection of Fe NP into CNT hollow is observed.

## 4.4 Discussion

The parameters that affect CNSs grown from zirconia NPs are discussed. Type 1 growth, which is more frequently observed than Type 2 growth, is explained with surface-bound growth mechanisms. Such mechanisms are in agreement with the physical and chemical properties of zirconia. The stage that precedes the growth of CNTs in Type 1 growth is a rolled-up graphitic appendage, and its role in the surface-bound growth mechanisms is introduced.

### 4.4.1 Effect of NP Size and Shape

Table 4.2 summarizes the observations of the nanostructure morphologies found under HRTEM in this study, and and the features observed for MNP vs. zirconia NP catalysts studied in this work. A comparative schematic representation of Type 1, Type 2, and Type M growth are depicted in Figure 4.8. A graphitic multilayered cage is not observed for MONP (Type 1 and Type 2 growth), while it is always observed for MNPs (Type M growth). Instead, thin carbon layers on the exposed surfaces of zirconia NPs are occasionally observed. The interface between two or more zirconia NPs aggregated together does not have such layers (see Figure 4.7b). After annealing TEM grids drop-cast with catalyst precursors, before CVD, also exhibit NPs with similar thin graphitic layers, consistent with the previously reported propensity for zirconia NPs to graphitize amorphous carbon at elevated temperatures.[52] Therefore, we conclude that these thin graphitic layer domains are due to solid-state rearrangement of amorphous carbon either from lacy carbon or by decomposing carbon feedstock by zirconia NPs and not precipitation of carbon from over-saturated zirconia-carbon solid solutions (as is observed in some cases for MNP catalysts).

Table 4.2: Characterization of nanostructure growths observed in the present work

| | Zirconia Type 1 | Zirconia Type 2 | Metals Type M |
|---|---|---|---|
| Carbon around NP | Rolled-up graphite & thin graphitic layer | Thin graphitic layer | Graphitic cage |
| NP diameter ($D_{np}$) | 10 to 30 nm | 5 to 10 nm | 5 to 10 nm |
| Nanostructure diameter ($D_f$) | 5 to 10 nm | 5 to 10 nm | 5 to 10 nm |
| $D_{np}/D_f$ | 2 to 3 | 1 | 1 |
| Nanostructure-catalyst interface | Corner | Corner | All around |
| NP phase | Monoclinic | Tetragonal | - |
| nanostructure type | Turbostratic CNT | Turbostratic CNF | Turbostratic CNT |

Contact between CNSs and NP catalysts is another notable difference between Type M and oxide-based growth. In Type M growth, carbon atoms near MNP catalysts appear to be templated into a continuous graphitic cage surrounding the entire MNP catalyst. In Type 1 and Type 2 growth, on the other hand, zirconia NPs are attached to the elongated CNS only at the surface exposed to gas flow. As mentioned, when CNTs rather than CNFs result

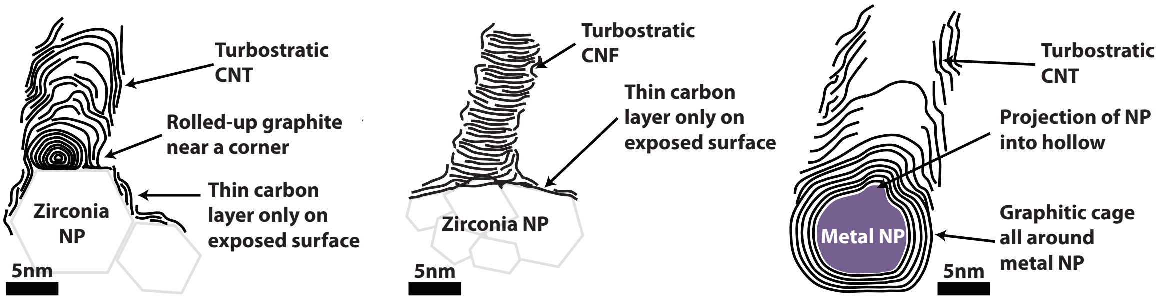

Figure 4.8: Schematic illustrations of Type 1 growth morphology for zirconia NPs (left), Type 2 growth morphology for zirconia NPs (middle), and Type M growth morphology for MNPs (right).[92]

from oxides (Type 1 growth), a rolled-up graphitic appendage near a corner of zirconia NPs is observed. Carbon nanoonions, a related CNS, are usually synthesized by pyrolysis without using MNP catalysts at high temperatures ranging from 900-1200°C,[94,95] and as low as 750°C using Co NP catalysts.[96] Energetic agitation of a catalyst is typically needed to form carbon nanoonions, indicating a high activation energy of the reaction. Catalyst-synthesized carbon nanoonions are also turbostratic and similar to the rolled-up graphitic appendages observed in this work. Therefore, we conclude that zirconia NPs are catalytically active at their surfaces within the vicinity of a zirconia NP corner.

These features are evidence that the growth process of CNSs from zirconia NP catalysts is surface-bound and different from the dissolution-based mechanism of growth seen with MNP catalysts.[97–99] This is consistent with the expected stability of zirconia NPs arising from the high melting point of zirconia (2715°C) and low diffusivity of carbon atoms at 750°C in zirconia ($1.23\times10^{-21}$ $m^2\cdot sec^{-1}$, $\sim$ 1 nm for 15 min),[100] compared to the diffusivity of carbon in $\alpha$ Fe ($10^{-10} m^2 \cdot sec^{-1}$, 11 orders of magnitude higher than in zirconia).[101] Additionally, no zirconia NP catalyst associated with carbon nanostructture growth contain phases assigned to zirconium carbide as determined by lattice fringe and FFT pattern analysis, which further supports that there has not been significant dissolution of carbon atoms into the zirconia NPs. These two differences in morphology as observed in this work also suggest why zirconia NPs have not been able to show growth yield as high as popular MNPs do, especially for hollow CNSs (CNTs) observed in Type 1 and Type M growth: it is conjectured here that a defective, spherical, graphitic template (*e.g.*, nanoonion or cage) may be necessary in order to direct amorphous carbon into curved graphite rather than flat graphite and to facilitate incorporation of carbon atoms into a growing hollow CNF or CNT. MNPs can serve as such a spherical object, since dissolution of carbon atoms into the MNP followed by precipitation of carbon forms the needed graphitic cage that follows the spherical shape of the NP. The free energy of the system decreases accordingly, enabling nucleation and growth of the CNT to occur spontaneously as carbon concentration in the MNPs reaches the solubility limit.[102,103] Zirconia NPs, on the other hand, seem to need a rolled-up appendage to serve as a graphitic template in order for CNT growth to occur. Indeed, as seen in the upper part of Figure 4.3a, we observe zirconia NPs that are partially covered by thin graphitic layers but without a rolled-up graphitic appendage and these NPs do not produce CNTs or CNFs. We conclude that formation of a rolled-up graphitic appendage, which appears to occur at corners of zirconia NPs, is a high-activation-energy process, translating into lower CNT growth yields when compared to CNT growth with MNPs.

### 4.4.2 Proposed Growth Mechanism Features

On the basis of the morphological differences observed in this work, we suggest a growth model of hollow nanofibrils grown from zirconia NP catalysts as follows (see Figure 4.9). First, adsorption of ethylene molecules occurs over the zirconia NP surface, as shown in Step 1 of Figure 4.9. The ethylene molecules may develop thin carbon layers not as thick as seen with Type M growth or may desorb before decomposition (*e.g.*, hydrogenation). A certain amount of the adsorbed ethylene molecules that diffuse over the surface and find chemisorption cites eventually decompose into carbon atoms or other fundamental structural unit (*e.g.*, methylene). Such sites are more often found near a corner which is richer in kinks. Then near the corner a dense carbon atom cluster is formed, which eventually transforms into a nascent rolled-up graphite. Step 2 of Figure 4.9 describes this process. Carbon atoms then accumulate, rolling into a rolled-up graphitic appendage by further surface diffusion and concurrent decomposition of feedstock molecules. At the beginning of the process, incorporating carbon atoms to extend rolled-up graphite would be the rate limiting step because of the high free energy associated with high curvature. At this point, diffusion and decomposition processes would supply a sufficient number of carbon atoms to develop a graphitic layers for the rolled-up graphitic appendage. As the rolled-up graphitic appendage grows, incorporation of carbon atoms accelerates because of the resulting lower curvature that in turn reduces the activation energy of incorporating additional carbon atoms. Increasingly more carbon atoms are then required to provide each subsequent layer of the growing rolled-up graphitic appendage, and diffusion and/or decomposition of feedstock molecules becomes the limiting step in growth of the structure. Each next layer becomes increasingly likely to have defects. Step 3 of Figure 4.9 depicts how this type of structure might appear. The outermost layer would consist of multiple graphitic patches, so eventually a portion of the layer lifts off[104] as spacing between layers in a carbon nanoonion increases[105] and thus interlayer binding force decreases. The appendage would not grow larger spherically, but rather a hollow carbon nanofirbil, namely a turbostratic CNT, would start to grow (Step 4 of Figure 4.9). Figure 4.10 shows an intermediate state consistent with the proposed model: a zirconia NP with a thin graphitic layer surrounding it. Near a high-angle corner of the zirconia NP (yellow arrow), a nascent carbon nanoonion is observed, which may represent a state between Steps 2 and 3 of Figure 4.9. CNSs from both Type 1 and 2 growth are composed of defect-rich (turbostratic) graphite. Even though smaller zirconia NPs (those that appear to facilitate Type 2 growth) do not grow hollow nanostructures (apparently due to their lack of associated rolled-up graphitic appendage), they are still active catalysts for both graphitization of amorphous carbon and growth of graphitic nanofibers. The size and edge angles of zirconia NPs, rather than phase, seems to be responsible for the propensity of a zirconia NP to form an appendage.

This suggests that dispersion and annealing of zirconia NP precursors on porous carbonaceous substrates could result in a higher population of prestructures for either Type 1 or Type 2 growth morphology. Steiner et al. demonstrated that zirconia NPs are effective catalysts for solid-state graphitization of amorphous carbon.[52] They observed that pyrolysis of zirconyl-doped resorcinol-form-aldehyde-type polymer aerogels produces zirconia NPs encapsulated in cage-like fullerenic nanostructures.[52] The caged zirconia NPs exhibit

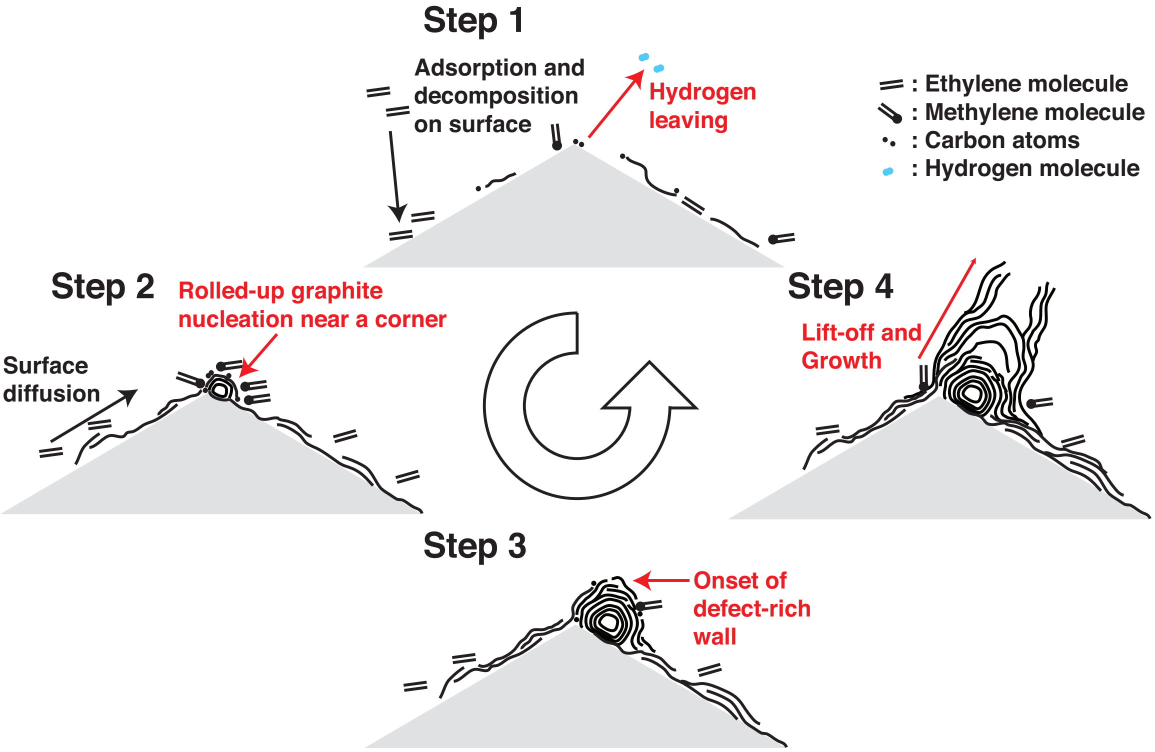

Figure 4.9: Description of the proposed Type 1 growth model.[92]

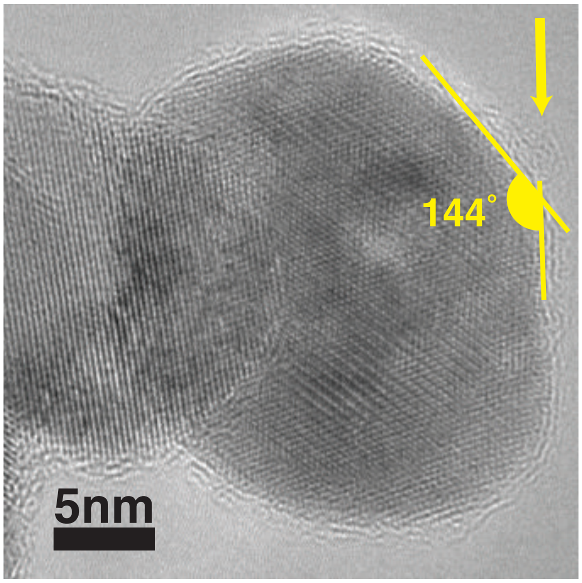

Figure 4.10: An intermediate state for Type 1 growth (see step 2 and 3 in Figure 4.9).[92] The yellow arrow indicates nucleation of rolled-up graphite near a high angle corner (144°).

similar diameters to zirconia NPs that result in Type 2 growth in the current study (Figures 4.5 and 4.6). In this case three reactions occur concurrently: (1) carbothermal reduction of polymer-bound zirconyl ions to zirconia NPs; (2) pyrolysis of RF polymer into amorphous carbon; and (3) solid-state catalytic conversion of the resulting amorphous carbon into graphitic nanostructures by zirconia NPs. In our experiments the zirconia NPs synthesized on lacy carbon were mostly larger in size and did not initially develop fullerene-like cages. Contextualizing the observations of Steiner III et al. through our model, pretreatment of zirconia NPs with solid and highly porous carbon would result in well dispersed, appropriately sized zirconia NPs surrounded by graphitic carbon matrix that would be active toward CNT growth, and thus serve as a means for enhancing the activity of zirconia toward CNT growth.

### 4.4.3 Proof of Concept: Carbon Gel Substrate CVD Implementation

To test the aforementioned hypothesis, we evaluate the effect of pyrolyzing two types of zirconia NP catalysts (monodisperse 4 nm diameter monoclinic zirconia NPs prepared by our collaborators according to the method of Joo et al.[78] and polydisperse zirconia NPs from solutions of zirconium oxychloride in isopropanol prepared according to the method of Steiner et al).[52] On carbonizable substrates with high surface area and porosity $\Pi$, namely RF polymer aerogels ($\Pi \leq 95\%$) and xerogels ($\Pi \sim 10\%$)), zircoina NP precursor solutions are drop-cast and then pyrolyzed. CVD growth is performed on those pyrolyzed substrates containing zirconia NP catalysts. Both types of substrates are of defect-rich carbonaceous material[106,107] so can potentially grow CNSs by themselves.[108] However, drop-casting zirconia precursor solution was expected to substantially increase the number of active sited towards CNS growth present in the materials. Following CVD, very sporadic CNT growth bundles may be found on the surfaces of both types of the substrates without zirconia (Figures 4.11a,b). Aerogels and xerogels with zirconia NPs, however, exhibit substantial nanostructure growth (Figures 4.11c-f) on the regions of the substrates where precursor solutions were applied. Carbon aerogel and xerogel substrates drop-cast with either source of zirconia yielded elongated CNS growth spanning ranges of the surface, especially edges of the substrates; such CNS growth that is not observed on the surface of the control samples, which only present individual bundles at best (Figures 4.11a,b).

A clear dependence of CNS diameter and length on the zirconia source is observed with aerogel substrates: substrates drop-cast with zirconium oxychloride resulted in finer, longer nanostructures, whereas substrates drop-cast with pre-fabricated monodisperse 4 nm diameter zirconia NPs resulted in thicker, shorter nanostructures sprouting over the areas of the substrate. It is believed that the two different zirconia sources distinguishably affect the diameter and length of the CNSs that form, as substrates containing the monodisperse prefabricated NPs would be expected to undergo a greater degree of zirconia NP coarsening than those drop-cast with solution-phase monomeric precursor, resulting in larger zirconia particle size and thus larger diameter of grown CNSs. On carbon xerogel substrates, zirconia NPs derived from zirconia oxychloride octahydrate showed greatly enhanced growth yield compared to control samples. The growth comprises a polydisperse variety of elongated CNSs, both thin and thick as well as long and short. Dispersion of prefabricated zirconia NPs on xerogels showed a large number of short-length bundles and even higher on carbon aerogel substrates. We submit that the high porosity and surface area of the aerogel substrate facilitates finer dispersion and therefore more efficient progression of the reactions required for solid-state graphitization of the aerogel's amorphous carbon framework into graphitic carbon. The higher yields observed when using the zirconium oxychloride solution, which contains molecularly dispersed zirconyl ions as well as fine diameter NPs, suggests that smaller particles afford longer lengths and higher yields of CNS than larger or agglomerated particles with carbon gel substrates.

In summary, we have found that pyrolytic pre-treatment of zirconia NPs with solid-state amorphous carbon is a viable method for activating such particles for CVD growth of CNTs and CNFs, result of solid-state catalytic graphitization of surrounding amorphous carbon. TEM imaging revealed these fibrils to be a mixture of turbostratic CNTs and CNFs, *i.e.*, a mixture of Type 1 and Type 2 growth from zirconia NPs. We note that TEM samples of those CNSs grown on these 3D substrates largely showed fibrils without zirconia NPs attached, that is, the fibrils were separated from the catalysts from which they grew. This supports the observation that the zirconia NPs in these substrates are surrounded by solid-state graphitic carbon, which anchors them into the substrate more firmly than the fibrils are attached to the NPs. We also note that the crystallinity of these CNTs is relatively

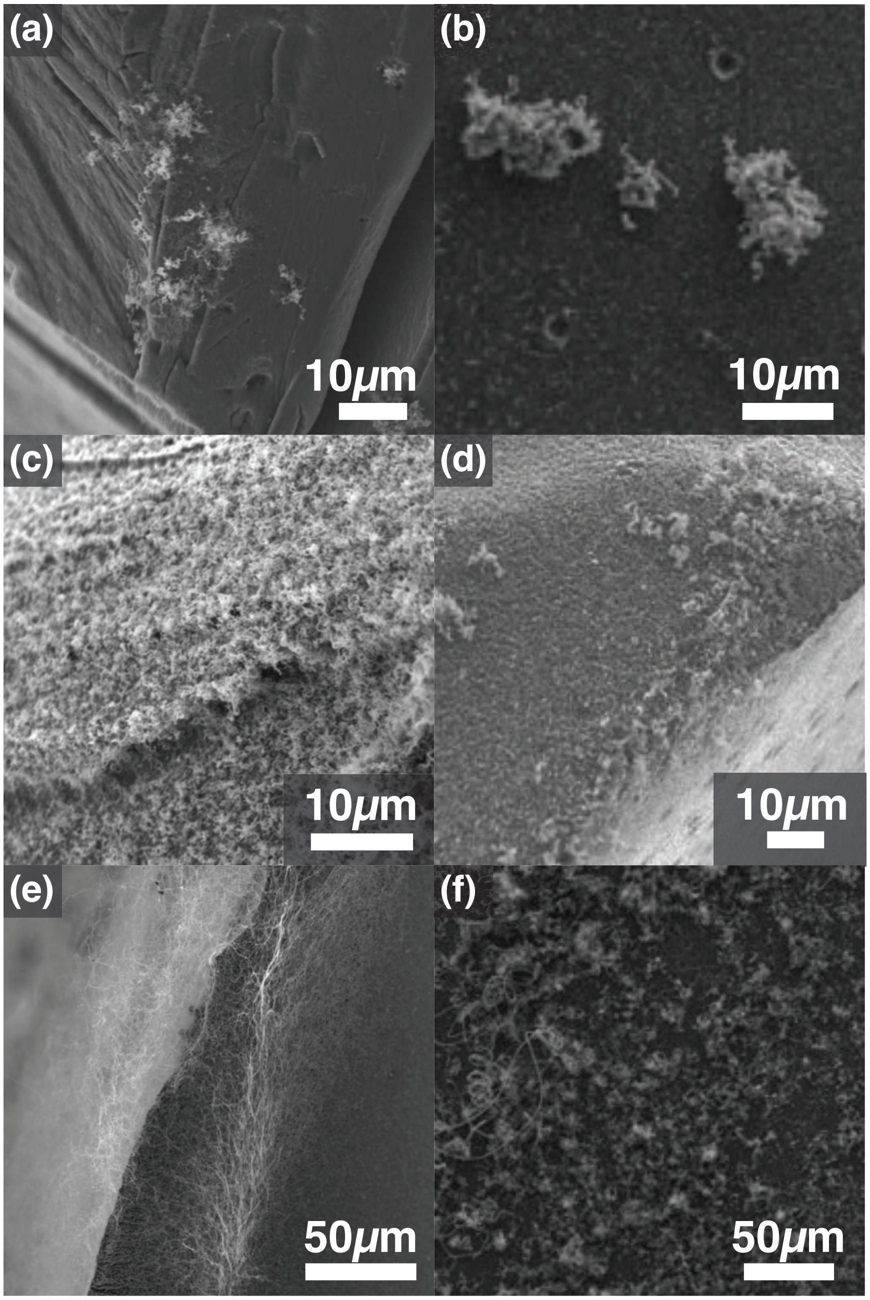

Figure 4.11: Representative growth morphologies obtained with carbon aerogel and xerogel substrates.[92] (a) Carbon aerogel without catalyst solution. (b) Carbon xerogel without catalyst solution. (c) Carbon aerogel with prefabricated zirconia NP solution. (d) Carbon xerogel with prefabricated zirconia NP solution. (e) Carbon aerogel with zirconia oxychloride octahydrate solution. (f) Carbon xerogel with zirconia oxychloride octahydrate solution.

lower than those previously reported with zirconia NPs,[52] indicative of changes in CVD parameters used (*e.g.*, gas pressure and carbon feedstock species) that should affect CNS growth by zirconia NP catalysts.

### 4.4.4 SiN Grid Direct Growth: Ruling out Metal Adatoms

To provide further evidence that metal adatoms do not play a role in the growth observations, metal-free SiN TEM grids and pyrolytic carbon-coated SiN TEM grids were tested in the same way as described for Cu TEM grid. In Figure 4.12, CNT growth from zirconia NPs is observed on a SiN grid. Although the interface structure is not always clearly seen through the SiN membrane, we observe a rolled-up graphitic appendage at a corner of the NP as Type 1. No metals are seen *via* EDX. CNT growth from zirconia on pyrolytic carbon-

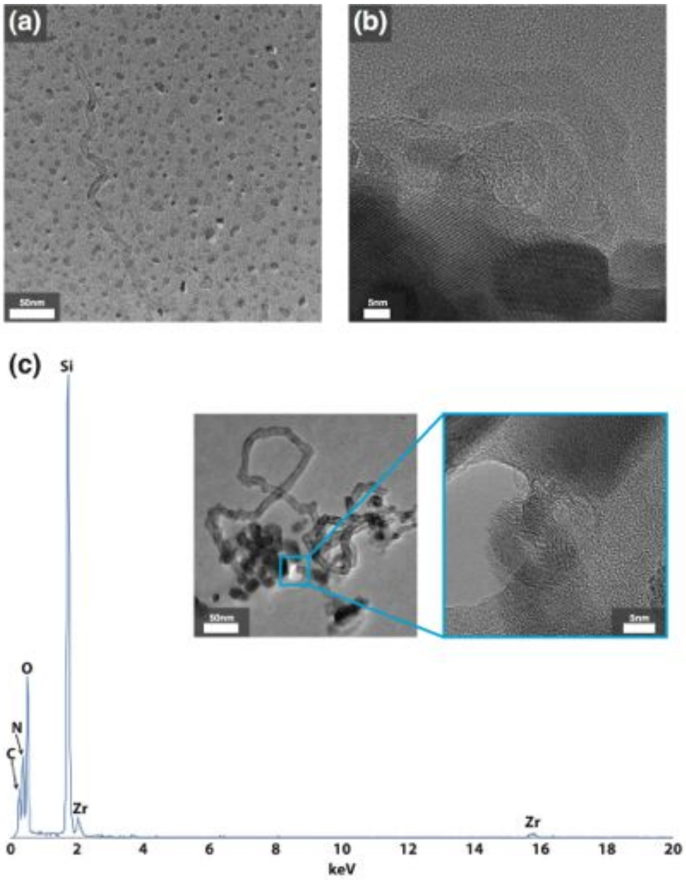

Figure 4.12: CNT growths observed on a SiN grid after CVD.[92] (a) A low magnification image. (b) A magnified image. It is routinely observed that the interface between the CNT and the zirconia NP is not visible. (c) Zirconia NPs growing multiple CNTs. EDX does not show any Fe, Cr, Cu, and other metals. At the interface we see a rolled-up graphitic appendage as we see with Type1 growth.

coated SiN grids is shown in Figures 4.13 and 4.14. In Figure 4.14 the rolled-up appendage characteristic to Type 1 growth was also found. In addition, we see clearly that an isolated zirconia NP grows a CNT as in Figure 4.15. These studies on SiN TEM grids indicate that neither the spatially separated control MNPs nor the Cu from the Cu TEM grids determine CNS growth. Recently, morphologies of CNSs similar to those investigated in this work have been reported in SOFCs comprised of YSZ.[58,109]

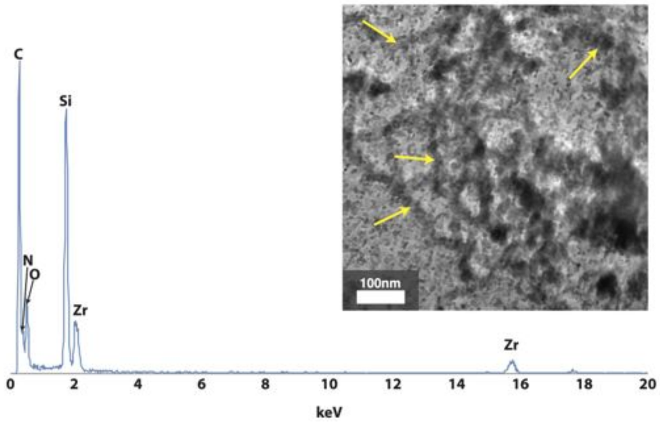

Figure 4.13: CNTs and CNFs growing from zirconia NP catalysts on pyrolytic carbon-coated SiN grid.[92] EDX does not show Fe, Cr, Cu, or other metals. Elongated objects pointed by yellow arrows are CNTs or CNFs.

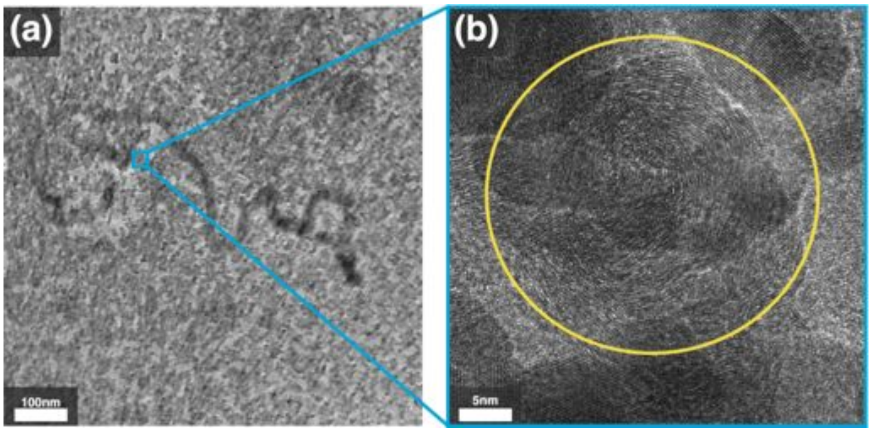

Figure 4.14: Type1 growth on pyrolytic carbon-coated SiN grid.[92] (a)A low magnification image. (b) A magnified image of the rolled-up graphitic appendage. The appendage circled in yellow shows lattice fringes of graphite and is attached to a zirconia NP in the bottom of (b).

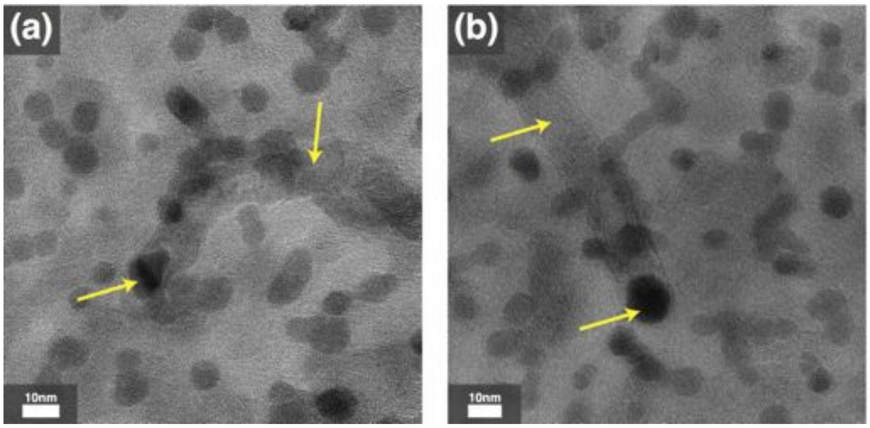

Figure 4.15: Examples of spatially separated zirconia NP catalysts growing CNTs.[92] The NPs and CNTs are annotated by yellow arrows and are seen through a 15 nm-thick SiN membrane.

## 4.5 Conclusions

Distinct differences in the morphologies of CNSs resulting from CVD growth employing zirconia NP catalysts and MNP catalysts are observed. Lattice-fringe resolved HRTEM and FFT pattern analysis unambiguously show that zirconia NPs, varying in shape and phase, grow both hollow and nonhollow fibrous CNSs without interactions with metals including Cu from lacy carbon-coated Cu TEM grids. We observe two nanostructure growth morphologies associated with zirconia NP catalysts: growth of CNTs with a rolled-up graphitic appendage on a high-angle corner of the NP, of smaller diameter than the parent NP (termed Type 1 growth), and growth of CNFs approximately the same in diameter as the NPs (termed Type 2 growth). In both cases, observed growth is always base-growth, and no substantial graphitic cage encapsulating the oxide NP catalyst is observed, whereas a well-developed multi-layer graphitic cage is almost always observed with MNP catalysts (termed Type M growth). On the basis of these observations, a growth model for zirconia NP catalysts is proposed. It is explained that the lower growth yield from zirconia NPs compared to MNPs by the high activation energy required to form a rolled-up graphitic appendage at zirconia NP corners. A practical method for achieving high-yield CVD growth of CNTs and CNFs with zirconia NPs is demonstrated, which exploits the mechanistic insights of the growth model proposed in this chapter.

Although we observed local improvements in the growth yield, high levels of homogeneity were not yet achieved in CNTs and CNFs produced *via* zirconia NP catalysts, which motivates additional work on CNS growth *via* MONP catalysts. In the following chapter, titania NP catalysts are extensively investigated to offer insight on approaches that could be utilized to enhance their growth yield, and model the physics governing their growth of CNSs.

# Chapter 5

# Quantitative Analysis of Growth with Titania NP Catalysts

This chapter articulates the study of titania NP-mediated growth of CNTs and CNFs *via* CVD. HRTEM was used to demonstrate that titania NPs can be effective catalysts for CNS growth.[54] The growth yield from titania NPs is found to be higher than zirconia NPs on conventional substrates under similar conditions, and is found to be better suited for studies focusing on the growth parameters. Although previous works focusing on CNS production *via* MONP catalysts only provided qualitative descriptions of the growth process, this chapter quantitatively characterizes and models the catalytic activity of titania NPs. Although the model proposed here contains a number of first order approximations, the resulting model predictions are in good agreement with the experimental observations in this work.

## 5.1 Introduction

As suggested by the previous literature, titania NPs are well-studied metal oxide species that can be used as a catalyst for CNT growth. The first two studies addressing this topic were able to show densely grown, horizontally aligned CNTs on silicon wafer substrates from titania NPs *via* CVD by SEM (it is expected that those wafers had a native oxide layer because no special notes are available in references).[48,53] These works, however, did not meet all the credibility criteria proposed in Chapter 2 since neiter *ex-situ* HRTEM nor *in-situ* characterization was provided, and the discussions do not provide sufficient proof for the proposed growth mechanisms to qualify them as more than just pure speculation. Later, Zhang et al. reported HRTEM characterization of titania NPs showing CNT growth in lattice-resolved magnification.[54] Although the growth was sparser than the previous two reports, Zhang et al. provided more insight on the growth mechanisms that govern titania NPs, inferring that the titania NPs were reduced from $TiO_2$ to $TiO_{1.04}$ (on average) during the CVD process. Very recently (and while the work herein was underway), Kang et al. demonstrated that closely packed, horizontally aligned single-wall CNTs grown *via* titania NP catalysts are well suited for application in electronics.[110] It was semiconducting SWNTs were preferentially fabricated, and that the selectivity was due to oxygen defects that reduced the formation energy for semiconducting SWNTs over metallic SWNTs. However, although this work did not provide data-sets with HRTEM or *in-situ* techniques to further support the impressive growth morphology, it is worthwhile to mention that titania may now be one of the closest to practical applications among MONP catalysts for CNT growth *via* CVD.

Therefore, in this thesis, titania is selected as a model MONP system for a parametric study focusing on improving the growth yield using standard substrates. While the number of species reported as active non-metallic catalysts is increasing, and some are corroborated with multiple publications, the combinations of CVD parameters that governs the growth yield was not studied in detail previously. For example, silica NP catalysts are in general tested with methane,[48,50,111,112] and titania NPs are studied with ethanol,[53,54,110] while sometimes groups utilize either feedstock with either silica or titania.[48,81] This is a striking difference from research on MNP catalysts, which has reported a variety of combinations of catalysts and carbon feedstock.[28,31,34,113] This series of studies on metallic NP catalysts has shown a broad range of results which has enabled researchers evaluate the key parameters for reproducible high-yield production of CNTs, and identify the growth mechanisms.[66,114,115] Therefore, similar studies on MONP catalysts are required to increase understanding towards more facile and controllable growth of CNSs from MONPs.

Here, we show titania NP-mediated CVD syntheses of graphitic nanostructures using methane, ethylene and acetylene as carbon feedstocks. Ethylene and acetylene are converted into few microns-long CNSs, and the growth yield is enhanced by the combination of several parameters including the nature of the carbon feedstock, the CVD temperature, time, and the chemistry of the substrate. In this work the highest growth yield is obtained using acetylene at 850°C for 30 minutes with NP catalyst with diameter $\sim$ 10 nm made by drop-casting titanium oxysulfate hydrate solution on a 13 nm sputtered alumina thin film. The resulting CNSs are found to be turbostratic CNTs and CNFs, ranging from hundreds of nanometers to a few $\mu$m in length. The catalytic activity of titania NPs are estimated to be lower than Fe catalysts by an order of magnitude, based on the approximate number of carbon atoms contained in CNSs synthesized *via* both types of catalysts. These results are contextualized by quantitative estimations for lift-off of CNS growth, where graphitic layers form over a MONP corner and lift off due to strain energy build-up, thereby initiating a step-by-step mechanism for the formation of turbostratic CNSs. The model is supported by HRTEM characterization of growth morphologies, and also explains why methane could only form graphitic layers, not CNSs. The results presented in this chapter will guide exploration of controllable metal-free synthesis of graphitic nanostructures, and may find applications for electrochemical systems where turbostratic structures can outperform crystalline carbon materials[116] and in other applications where MNP residue is disadvantageous.[40]

## 5.2 Experimental

Titania NP precursor solutions are prepared in a similar way to zirconia NP precursor solutions (as discussed in Chapter 4). The two different tube furnace setups used in this work are described, and the different CVD parameters for the five recipes attempted in this work are presented in detail as well as the characterization methods. Phase determination for the active catalysts found under TEM is implemented in the same way as in Chapter 4 for zirconia NP catalysts.

### 5.2.1 Sample Preparation

Titania MONP precursor solution was prepared with IPA (VWR, CAS No 67-63-0, >99.5%) and titanium (IV) oxysulfate hydrate procured from Sigma-Aldrich ($TiOSO_4 \cdot xH_2O$ CAS 13825-74-6). 0.16 g of the titanium oxysulfate hydrate was dissolved in 15.72 g (20 mL) of IPA to make saturated solutions. After ultrasonicating for 3 min and leaving the solution to settle for a day, the sediment and saturated supernatant were separated. The supernatant was used as catalyst precursor throughout the variety of experiments in this work.

Two types of substrates were prepared: silicon wafer with thermally grown 200 nm thick silica layer (called silica substrate in this chapter), and with 13 nm of alumina further on top of the silica layer (called alumina substrate in this chapter). A stoichiometric alumina target (99.995%) was sputtered on top of the silica substrate by a radio frequency magnetron sputtering machine (CCR) using argon gas (99.9995%) at $2.5\times10^{-4}$ mbar to prepare the alumina substrate. The prepared supernatant catalyst solution was drop-cast on these substrates. After the IPA evaporates completely, the samples were pyrolyzed under a flow of 200 sccm of argon at 800°C for 3 to 4 hours.

### 5.2.2 CVD Process

Recipes (see Table 5.1) with each carbon feedstock species are based on our previous experience growing CNTs using MNPs and zirconia NPs,[52,55,117,118] in the Wardle group at MIT and the Hofmann group at University of Cambridge. Recipes A (acetylene) and M (methane) use a 2 in diameter tube furnace with outer diameter $\phi = 51$ mm and length $L = 400$ mm, whereas recipe E (ethylene) uses a 1 in tube furnace with the outer diameter $\phi = 25$ mm and length $L = 360$ mm. For recipe A, the temperature was ramped to the set point at a rate of 20°C/min under 1000 sccm argon flow, followed by an additional 5 min at 4000 sccm argon flow. A flow of 500 sccm hydrogen and 200 sccm argon was then introduced for 3 min. For recipe M the temperature was ramped to the set point at a rate of 20°C/min under a flow of 1000 sccm argon, then adding 700 sccm of hydrogen for 10 min. For recipe E, after 2 min of flushing tube with 750 sccm of argon, the temperature is ramped to the set point at 75 °C/min under a flow of 100 sccm argon and 400 sccm hydrogen. All CVD processes were done under atmospheric pressure. Prepared samples were imaged by SEM (Zeiss Sigma-VP and Zeiss Ultra 55) and HRTEM (JEOL 2010F).

The two different substrates presented different catalyst morphologies due to different wetting behavior with IPA-based precursor solution. On alumina substrates, the titania NP catalysts were distributed more homogeneously than on silica substrate and CNS growth followed. Two different reaction temperatures, 750°C and 850°C, were chosen to compare the effect on growth in the typically employed range of temperatures for high growth yield using MNPs without excessive gas-phase pyrolytic soot formation. All CVD recipes were implemented with a control sample, a substrate that had no catalyst precursor on it in order to identify any inherent contamination, especially metals, that could grow CNSs. Recipes A-1, A-2, A-3 and M were also performed with a baseline MNP growth sample comprised of alumina-sputtered silicon with Fe NP catalysts. In this work none of the control samples showed any growth, and baseline samples always grew CNTs for all of the listed recipes, as expected. We exclude that the MONP-grown CNSs were grown from random metallic contamination using a combination of HRTEM and point-localized EDX. This way we confirmed that the CNFs and CNTs are indeed grown from titania particles and not from even trace amounts of metal contamination.

### 5.2.3 Characterization

Representative samples were investigated by Raman spectroscopy with a 532 nm laser throughout this work (Horiba Jobin Yvon MR800). HRTEM images and FFT patterns were used to determine species and phase with crystallographic information of titanium dioxide phases from literature.[119] To determine the phase of the NP and rule out Fe contamination, a table of lattice distances and corresponding Miller indices is included in Appendix A for $\alpha$ and $\gamma$ Fe,[84,85] iron carbide ($Fe_3C$),[120] titanium metal ($\alpha$, $\beta$, and $\omega$),[121] titanium oxide (anatase, rutile, and brookite),[122] and titanium carbide (for approximately $0.2 \leq x \leq 1$ of $TiC_x$).[123] Aluminum titanate occurs at 300°C higher than the growth temperature so it was excluded.[124] Alumina is also included in the table, especially the $\alpha$ phase,[125] a thermodynamically favored phase, and the $\gamma$ phase,[126] which is likely to ap-

Table 5.1: Summary of CVD recipes implemented in this work

| Recipe | feedstock | Temperature (°C) | Time (min) | Gas (sccm) | Substrate |
|---|---|---|---|---|---|
| A-1 | Acetylene | 750 | 30 | $Ar : C_2H_2 : H_2$<br>$= 200 : 10 : 500$ | Silica |
| A-2 | Acetylene | 750 | 30 | $Ar : C_2H_2 : H_2$<br>$= 200 : 10 : 500$ | Alumina |
| A-3 | Acetylene | 850 | 30 | $Ar : C_2H_2 : H_2$<br>$= 200 : 10 : 500$ | Alumina |
| E | Ethylene | 750 | 15 | $Ar : C_2H_4 : H_2$<br>$= 100 : 100 : 400$ | Silica |
| M | Methane | 900 | 15 | $CH_4 : H_2$<br>$= 500 : 100$ | Alumina |

pear in nanocrystalline alumina in sizes as small as the MONP catalysts we consider in this work.[127] The same 'C' script is used as in Chapter 4 to determine phases of catalytically active NPs.

## 5.3 Results

Different growth morphologies of CNTs and CNFs are observed by SEM for the five recipes. Recipe A-3, which uses acetylene, alumina substrate, and 850°C, provided the best result in terms of homogeneity of CNS growth, and is further characterized by HRTEM and Raman spectroscopy. The results with recipe A-3 lead to the quantitative analysis in the following sections.

### 5.3.1 Acetylene as Carbon Feedstock

Using these conditions, CNSs were first synthesized with acetylene (A-1, A-2, and A-3). Recipe A-1 shows $\sim 1-3$ $\mu$m long CNSs, with some occasionally grown longer than 5 $\mu$m as shown in Figure 5.1a. In recipe A-1 with a silica substrate we observe circular residue from catalyst precursor solvent evaporation, causing inhomogeneous catalyst deposition and resulting in the growth of CNSs exclusively within these regions. Recipe A-2 improves

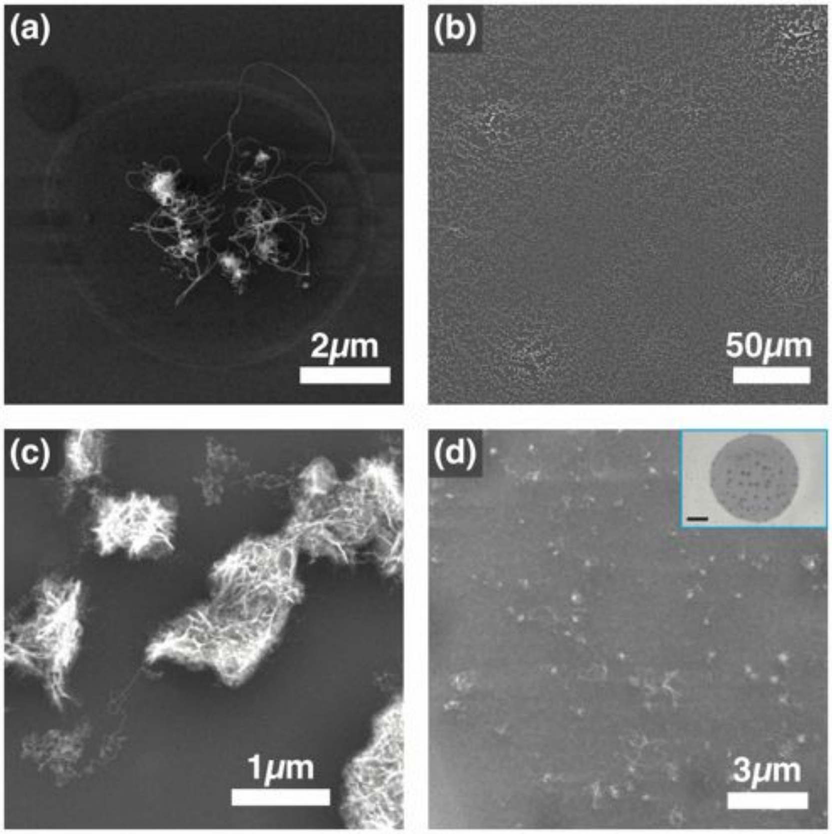

Figure 5.1: CNSs investigated by SEM from different recipes: (a) Representative growth morphology from recipe A-1. CNSs of a variety of lengths and diameters are observed in crowds. (b) Representative growth morphology from recipe A-3 at low magnification. Titania NPs are distributed evenly on the alumina substrate and CNSs are found homogeneously on the substrate. (c) A high magnification view of (b) focusing on several agglomerates of titania NP catalysts. Micron-long fibrils extend from the agglomerates. (d) Representative growth morphology for recipe E. The inset is the low magnification view showing the receded precursor residue spot with a scale bar 20 $\mu$m that is similar to the circular residue in (a).

the homogeneity of catalyst distribution by using an alumina substrate, attributed to more favorable solvent wetting. By raising the reaction temperature to 850°C from recipe A-2, recipe A-3 yields homogeneous and relatively high growth yield of nanofibrils (Figure 5.1b and 5.1c) with $\sim 1-3$ $\mu$m long.

### 5.3.2 Recipe A-3:Highest Yield for Titania MONP Catalyst

We investigated homogeneous CNS growth (recipe A-3) in more detail using HRTEM. Crowds of shorter turbostratic CNTs and CNFs, few 10s to some 100s of nm in length, are observed as shown in Figures 5.2 and 5.3, respectively. Their diameters are ~ 12 nm by HRTEM images, about the same as the diameters of titania NP catalysts observed in this work (~ 10 nm). The HRTEM images suggest that CNTs and CNFs are synthesized *via* a base-growth mechanism and attached to only the corners of the titania oxide NPs, without forming extensive graphitic structures on the catalyst surface such as a graphitic cage encapsulating a MNP catalyst.[128,129] This morphology is similar to the surface-bound mechanism observed with unreduced zirconia NPs as discussed in Chapter 4.[92] Combined with the stability of titania against thermochemical reduction,[130] it is likely that the titania NPs were not reduced to titanium metal during CVD. A substructure is observed especially clearly within those turbostratic CNTs where bundles of graphitic sheets are

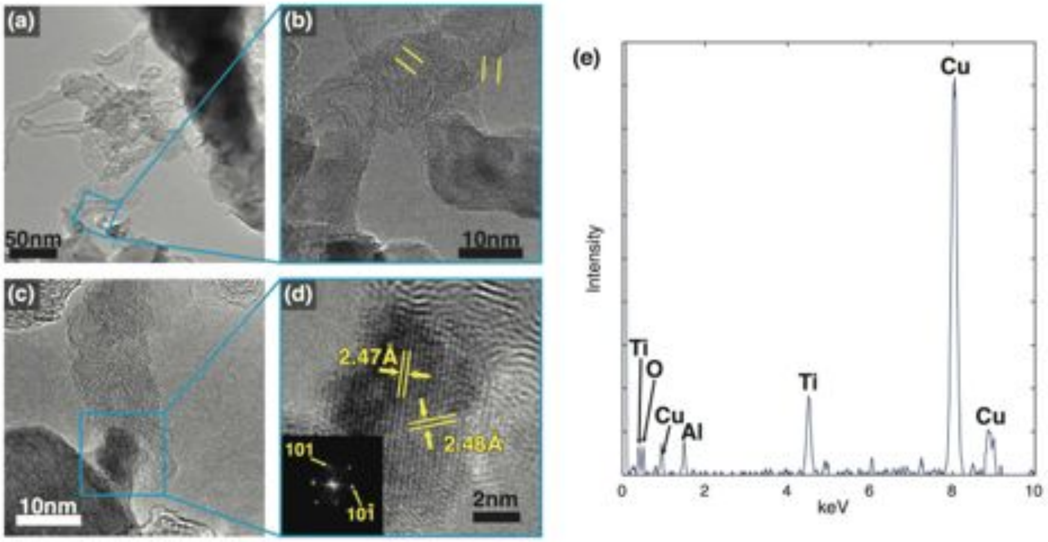

Figure 5.2: Representative turbostratic CNTs from recipe A-3 growth: (a) CNTs and CNFs grown from titania catalyst. Only base growth is observed, i.e, no NPs at the tips of the CNFs and CNTs. (b) Higher magnification of (a) showing the interface between a CNT and a titania NP catalyst. Few-layer stacks of graphitic sheets are found to form turbostratic CNTs, indicated by parallel yellow lines. (c) Interface between a CNT and a titania NP catalyst. (d) The catalyst NP in (c) at lattice-fringe resolved magnification. The NP catalyst is determined to be a rutile phase titania by FFT patterns and lattice fringes. (e) EDX pattern taken from (b). Cu peaks are from the TEM grid.

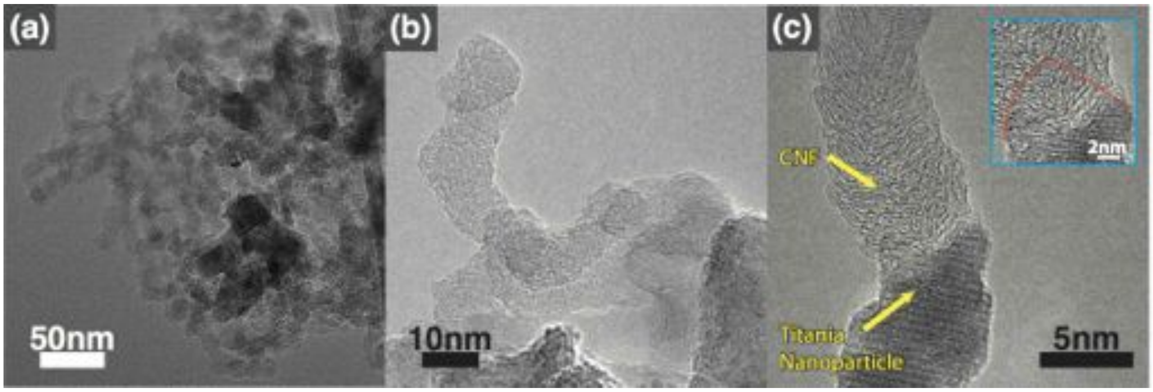

Figure 5.3: Representative turbostratic CNFs from recipe A-3: (a) A dense crowd of CNFs. (b) A representative CNF grown *via* base growth. (c) A high magnification view of the interface between CNF and a titania NP. The CNF is attached only to the NP corner, and the rest of the NP is devoid of carbon deposition. The inset is a close-up to present how the CNF grows from a NP corner. The corner is behind the root of CNT, and the red curve delineates the corners as seen in TEM contrast.

formed that contain edge defects, as indicated in Figure 5.2b and 5.2c by yellow lines. These observed structural and edge defects are reported to provide electrochemical activities absent in crystalline CNTs such as for sodium ion batteries,[131,132] fuel cells,[133] and dye-sensitized solar cells (DSSCs).[134] The structure of the titania precursor-derived NP catalyst is confirmed to be rutile $TiO_2$ by lattice-resolved HRTEM images and FFT indexing as in Figure 5.2d. The chemical composition of the titania is also corroborated by the point-localized EDX measurements in Fig 5.2e. These HRTEM observations are consistent with the Raman spectrum shown in Figure 5.4. Three Raman spectra taken at three different stages of recipe A-3 (as drop-cast, pyrolyzed, and after CVD) show that the titania NP catalyst converts acetylene into defect-rich graphitic CNSs including turbostratic CNTs, indicated by the D/G ratio (>1).[135] The spectra contain the characteristic Raman peaks of graphitic carbon: D peak (1339 $cm^{-1}$), G peak (1590 $cm^{-1}$), 2D peak (2669 $cm^{-1}$), D+D' peak (2930 $cm^{-1}$), and 2D' peak (3200 $cm^{-1}$).[136]

### 5.3.3 Ethylene and Methane as Carbon Feedstock

Ethylene and methane were also tested, and their results are compared with those of acetylene. Ethylene is converted into CNSs by titania NP catalysts with recipe E. The growth

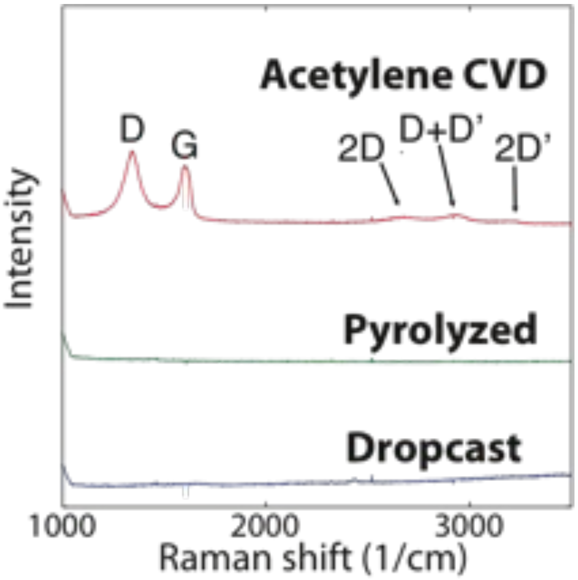

Figure 5.4: Raman spectra of recipe A-3 titania samples after drop-casting, pyrolysis at 800°C, and CVD at 850°C.

morphology shown in Figure 5.1d is similar to the results of recipe A-1 growth (Figure 5.2a), suggesting the presence of similar growth mechanisms. For the sake of imaging the catalyst-CNS interface from this relatively inhomogeneous growth by recipe E, CVD on SiN TEM grid in the same way as presented in Chapter 4 is implemented. We found a similar growth morphologies from recipe A-3, a CNT extending from a corner of a rutile titania NP on which no extensive graphitic deposition was made (Figure 5.5). The CNT resembles those often described as bamboo-like CNTs,[137] showing few-layer stacks of graphitic sheets with a larger interval than those found in growth with recipe A-3 (Figure 5.3b). Methane was the only feedstock without growth of CNTs and CNFs. The reaction temperature of recipe M was set to 900°C, as methane is more difficult to convert catalytically into CNTs than ethylene and acetylene, even for MNPs such as Fe.[55] As in Figure 5.6a, no fibrils are synthesized with recipe M. However, graphitic layers are synthesized on exposed surfaces of aggregated titania NPs as observed by TEM and Raman spectroscopy (Figure 5.6b and 5.6c). This result implies that titania can decompose all of the tested hydrocarbons into graphitic structures, similar to Fe NP catalysts. Still, the mechanisms and rates of decomposition seem comparable only between acetylene and ethylene, but not methane. Acetylene, which exhibits the highest yield, is used as the carbon feedstock for

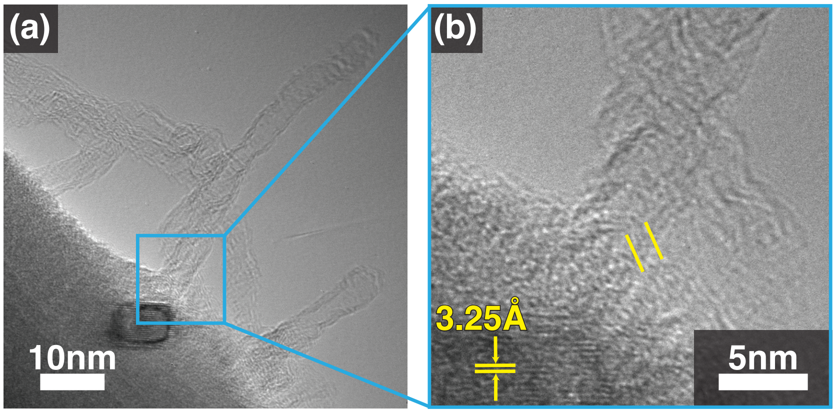

Figure 5.5: Recipe E replicated on SiN TEM grid. (a) A CNT extending from a titania NP catalyst located on the rim of the SiN membrane. (b) A higher magnification of (a) focusing on the catalytst-CNT interface. A stack of few layer graphitic sheets is annotated by parallel yellow lines.

the basis of further discussion about growth mechanisms *via* titania NP catalysts.

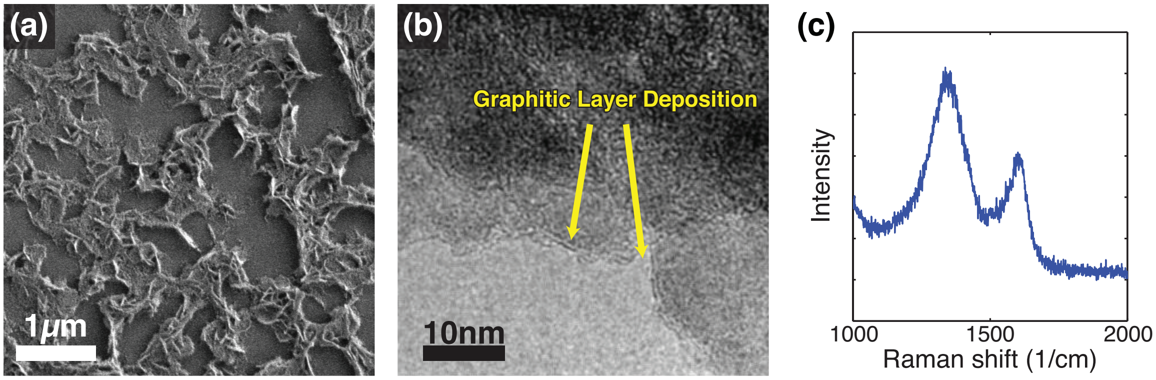

Figure 5.6: Recipe M samples investigated by SEM, HRTEM, and Raman spectroscopy. (a) SEM image with no growth of nanostructures observed. (b) HRTEM image of titania NP catalysts. A thin graphitic layer covers the catalyst surface continuously. (c) Raman spectrum of (a). Defect-rich graphite is indicated by the high D/G ratio.

## 5.4 Discussion

Growth yield with recipe A-3 was sufficient to enable the quantitative analysis of the catalytic activity of titania NP relative to the baseline Fe NPs. The approximate number of carbon atoms present in the representative CNS for recipe A-3 and the Fe baseline growth is compared to the number of acetylene molecules decomposed and incorporated into the

CNS per second. We also propose a model for the lift-off process, the beginning of growth of CNTs and CNFs from the graphitic layers formed over a corner of catalyst NPs. The calculation suggests that the strain energy stored in the bent portion of graphitic layers over a corner may have a significant contribution to the lift-off process.

### 5.4.1 Evaluation on the Relative Catalytic Activity of Titania NPs

Kinetics of CNT and CNF growth on titania with acetylene as carbon feedstock as implemented in recipe A-3 is discussed in this section. Based on the SEM and HRTEM investigations, the number of carbon atoms are estimated for the observed turbostratic CNTs and CNFs by assuming that those CNSs are crystalline CNFs, and also for the CNTs grown as baseline with Fe NP catalysts. Reliable representative values for length, diameter, and the number of walls are determined from SEM and TEM micrographs.

The number of carbon atoms in CNSs were estimated as follows. The volume per a carbon atom in graphite is $\mathrm{v_0} = \mathrm{a_0} \times \mathrm{d_{002}} = 2.72 \times 3.34$ Å$^3$, where $\mathrm{a_0}$ is the area occupied by a carbon atom in graphene, and $d_{002}$ is the inter-layer distance of graphene layers in graphite. We modeled the CNF as a Bernal-stacking graphitic pillar so that the number of carbon atoms in a CNF, $N_{CNF}$, is given as:

$$N_{CNF} = \frac{V}{v_0} = \frac{\pi r^2 l}{v_0} \tag{5.1}$$

Here $r$ is the radius and $l$ is the length of the CNF, both in Å. For CNTs, we estimate the number of atoms wall by wall, as the graphitic structure is distorted to form tubes. Given an area of $i$th wall of a multi-wall CNT as $\mathrm{A}_i$, the number of carbon atoms in the CNT, $N_{CNT}$, is:

$$N_{CNT} = \sum_{i=1}^{M} \frac{A_i}{a_0} = \sum_{i=1}^{M} \frac{2\pi l(r - d_{0002}(i-1))}{a_0} \tag{5.2}$$

where $M$ is the number of walls in the CNT, and the other values are the same as used to acquire $\mathrm{N}_{CNF}$. Table 5.2 summarizes the result of these estimations. For titania NP catalysts, SEM and TEM micrographs like Figures 5.1c, 5.2a and 5.3a are used to estimate the approximate range of length. Diameters are sampled from ten CNTs or CNFs and averaged. Figure 5.7 shows examples of SEM and TEM micrographs that are used for sampling Fe NP-mediated baseline growth. The average outer diameter was acquired from sampling ten CNTs in TEM micrographs. The number of walls observed was in the range of 3 to 4. The assembly rate, the number of acetylene molecules converted into CNSs by a catalyst per second, is obtained by dividing the calculated number of carbon atoms by the reaction time (1800 sec) and then halving it, considering that a single acetylene molecule contains two carbon atoms. As we observed by using SEM and TEM, recipe A-3 grows $\mu$m-long CNTs and CNFs and dense crowds of shorter CNTs and CNFs that are 10s- to 100s-nm long. In the case of $\mu$m-long CNTs and/or CNFs, the consumption rate of acetylene on titania NP catalysts may be comparable to Fe NPs. However, those are rather rare cases, and titania NP catalysts more often grow shorter CNTs and CNFs where the catalytic activities of titania and Fe NP catalysts differ by $2100/180 \approx 12$, scaled by the assembly rate. An order of magnitude difference in assembly rate can be attributed to the different kinetics occurring on the surface of MNPs vs. MONP. Chemisorption of acetylene molecule on the Fe NP surface likely involves $\pi$ back donation, which directly attacks carbon-carbon bonding by donating an electron from the $d\pi$ orbital of Fe to the anti-bonding $\pi^*$ orbital of acetylene.[138] On the titania NP surface, electrons in metal cations are attracted to oxygen anions. Therefore, in addition to $\pi$ donation that provides an electron from the $\pi$ orbital of acetylene to $d\sigma$ orbital of Fe, acetylene also can chemisorb on oxygen anions *via* hydrogen atoms.[139] This latter mechanism does not directly attack carbon-carbon bonding and hence slows down the dissociation. Moreover, chemisorption cites on the Fe NP surface can be vacated since carbon atoms diffuse into the NP body, while those cites on the titania NP surface will not become available again until the carbon atoms are graphitized and lifted-off. As a result, turnover frequency for titania NP catalysts is lower than Fe NP catalysts. This analysis does not evaluate yield as that would involve homogeneity of growth, a topic that is covered in Ch.9 where a relative comparison is made between MNPs and MONPs studied in this work. Different etching rate of carbon by hydrogen between titania and Fe catalysts also contributed to an order of magnitude difference in catalytic activity of titania and Fe NP.[140,141]

Table 5.2: Carbon atom assembly rates for observed CNSs (CNFs and CNTs) grown with recipe A-3.

| Catalyst | Nanostructure | OD (nm) | Length ($\mu$m) | Number of carbon atoms ($\times 10^6$) | Assembly rate ($10^3 \times$ sec$^{-1}$) |
|---|---|---|---|---|---|
| Titania | CNF | 12 | $0.1 - 1.0$ | $0.64 - 6.4$ | $0.18 - 1.8$ |
| Fe | 3-wall MWNT | 6.9 | 5.0 | 5.8 | 1.6 |
| Fe | 4-wall MWNT | 6.9 | 5.0 | 7.5 | 2.1 |

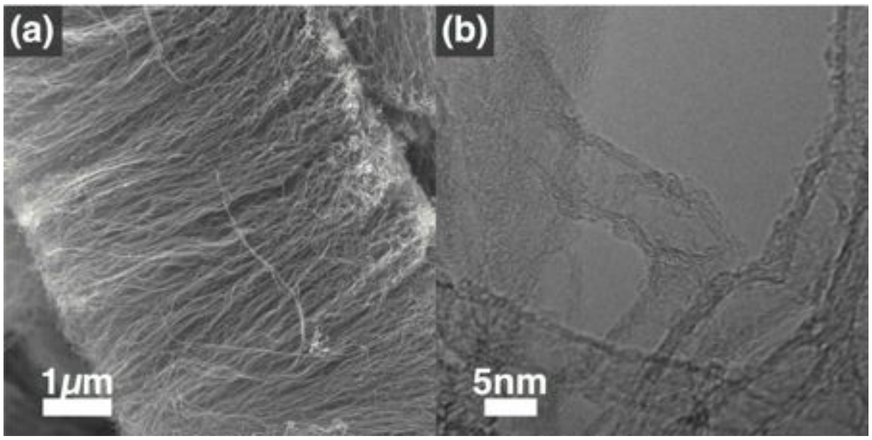

Figure 5.7: Examples of (a) SEM and (b) TEM micrographs of CNTs from Fe baseline growth used to acquire the outer diameter, the length, and the number of walls.

### 5.4.2 Quantitative Model of Lift-off

Next, we propose a lift-off mechanism of layered graphitic structures formed on MONP catalysts based on simple multi-layer graphene structural energetics at the MONP corner. The MONP corner anchors hydrocarbon molecules more strongly than the flat surface because of higher surface defect density, especially after high temperature treatment with hydrogen before CVD. Therefore, at the MONP corner, adsorbed hydrocarbon molecules with double or triple carbon-carbon bonding (*i.e.* ethylene and acetylene) are decomposed into carbon atoms and eventually graphitized, while on other surface they tend to detach by hydrogenation,[142,143] leaving the surface without carbon deposition (see Figures 5.2b, 5.2c, 5.3c, and 5.5). Suppose a multilayer graphene is grown over a 2D corner of a titania nanopartcle catalyst where two facets meet at the angle $\alpha$ (see Figure 5.8). The multilayer

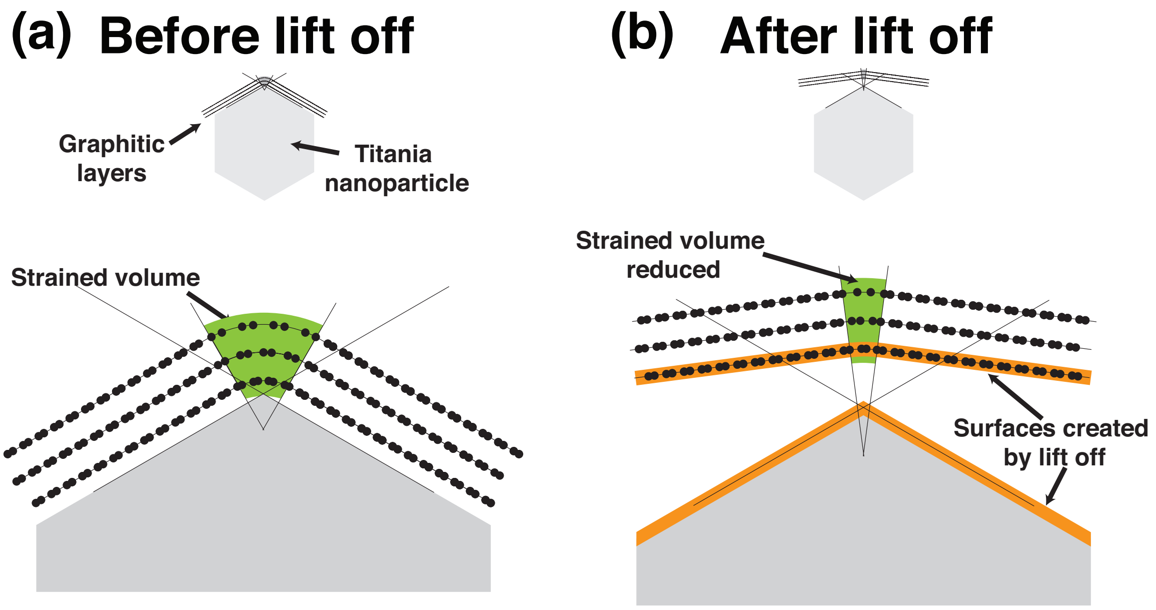

Figure 5.8: Schematic illustrations showing graphitic layer lift-off based on the plate model for the multilayer graphene (n=3). (a) Before lift-off. The shadowed areas over the bent portion of the multilayer graphene indicated by green shading is the volume where strain energy is stored. (b) After lift-off. Bending strain is relaxed and new surfaces are created as indicated by orange arrows. The z-axis is perpendicular to the figures.

graphene is bent at a radius of curvature $R$, storing bending strain energy that increases with the number of graphitic layers. As the multilayer graphene grows thicker, it will eventually lift off in order to relax this strain energy. Here we adopt a formulation by Zhang et al. regarding the relationship between bending strain energy $E$, the number of graphitic layers $n$, the angle of the MONP catalyst corner $\alpha$, and the second derivative of the bending energy density as bending stiffness $\kappa_{(n)}$.[144] Zhang et al. deals with multilayer graphene by assuming perfect bonding between layers as in the classic treatment of a solid (or layered) plate in bending following the Kirchhoff hypothesis for bending,[145] and our ‘plate model’ adopts their method. Due to the potential for inter-layer compliance (*i.e.*, imperfect layer bonding), the limiting case of non-interacting layers is considered as well and denoted as the ‘individual layer model’. For the plate and individual layer models, the total strain energy as function of $n$ and $\alpha$, $E_{plate(n,\alpha)}$ and $E_{indiv(n,\alpha)}$, were calculated. The layers in the multilayer graphene interact with each other *via* van der Waals interactions and therefore the behavior is bounded by these two cases. The bent multilayer graphene formed during catalysis is formed over the catalyst corner, and the distance $d$ between the titania NP catalyst surface and the multilayer graphene is estimated from HRTEM pictures of such interfaces and the effective thickness of the multilayer graphene $t_{eff(n)}$ given by Zhang et al.[144] Details of how the bending strain energy for the plate model $E_{plate(n,\alpha)}$ and the individual layer model $E_{indiv(n,\alpha)}$ were calculated are as follows. Figures 5.9a and 5.9b shows how $R$, $d$, $\alpha$, and $\beta$ were defined for the lift-off model. $\alpha+\beta=180°$ and $R$ is a function of the number of layers $n$ in the multilayer graphene and the angle of the catalyst NP corner $\alpha$, so we denote $R = R_{(n,\alpha)}$. In Figure 5.10, Figure 5.9a is magnified and relabeled with each vertex. Here:

$$R_{(n,\alpha)} = EF = EC + CF = EC + \frac{t_{eff(n)}}{2} \tag{5.3}$$

To calculate EC, see the $\triangle$ ACE. Since DC = $d$, we have:

$$AE = ECcos(\beta) = (ED + d)cos(\beta) \tag{5.4}$$

As the geometry has reflective symmetry across BE, we also have AE = ED. Therefore:

$$ED = (ED + d)cos(\beta) \Leftrightarrow ED = \frac{dcos(\beta)}{1 - cos(\beta)} \tag{5.5}$$

Since EC = ED + DC, we obtain:

$$R_{(n,\alpha)} = \frac{dcos(\beta)}{1 - cos(\beta)} + d + \frac{t_{eff(n)}}{2} = \frac{d}{1 - cos(\beta)} + \frac{t_{eff(n)}}{2} = R_0 + \frac{t_{eff(n)}}{2} \tag{5.6}$$

Then $d$ and thereby $R_0$ are calculated as follows. First, from HRTEM pictures, we measure the distance between the ‘edge of the contrast of the catalyst surface’ and the ‘center of the contrast of the graphitic layer attached on the surface’, which is approximately 3.5 Å (Figure 5.6b). Then for different number of graphitic layers, d is obtained as function of n in Å as follows:

$$d = d_{(n)} = 3.5 - 0.5(t_{eff(n)} - 3.4(n-1)) \tag{5.7}$$

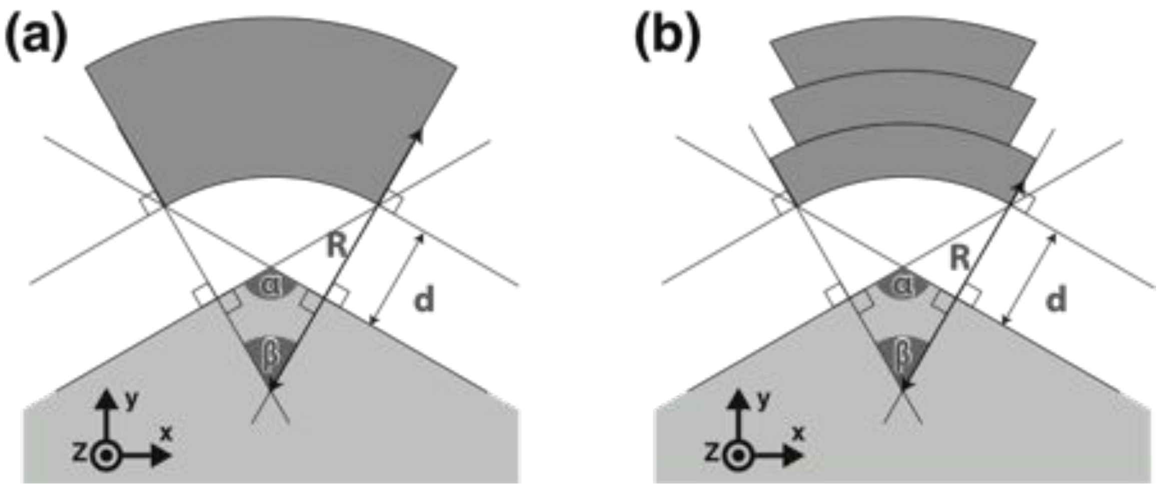

Figure 5.9: Schematic illustrations showing the two models adopted. (a) The plate model. The bending radius of curvature $R$ is defined as the length between the middle of the plate thickness and the center of the curvature circle. (b) The individual layer model. Each layer with its own bending radius $R$ stores strain energy that is disconnected from the other layers, *i.e.*, no interaction of layers.

From this $d_{(n)}$, $R_0$ is calculated.

We take the second derivative of the bending energy density as $\kappa_{(n)}$. The number of carbon atoms in the volume that stores strain energy $N$ was calculated by dividing the volume of the bent multilayer graphene that stores strain energy $V$ by $v_0$. The bending strain energy for the plate model $E_{plate(n,\alpha)}$ is given as below, with $E_b$ as the strain energy stored per carbon atom in a graphene layer, $L$ as the length of the titania NP corner along z axis in Figure 5.9 in nm for which the diameter of the NP is used, and $t$ in Å as the nominal thickness of multilayer graphene before bending defined as $t = n \times 3.34$:

$$E_{plate(n,\alpha)} = E_b \times N = \frac{\kappa_{(n)}}{2R_{(n,\alpha)}^2} \frac{LR_0(\pi - \alpha)t}{v_0} \tag{5.8}$$

For the individual layer model, the bending strain energy $E_{indiv(n,\alpha)}$ is given as the bending strain energy stored in a single layer graphene multiplied by the number of layers:

$$E_{indiv(n,\alpha)} = E_{plate(1,\alpha)} \times n \tag{5.9}$$

When lift-off occurs with the interfacial area between the titania NP catalyst and the multilayer graphene $A$, the bending strain energy is at least as high as the sum of surface energy

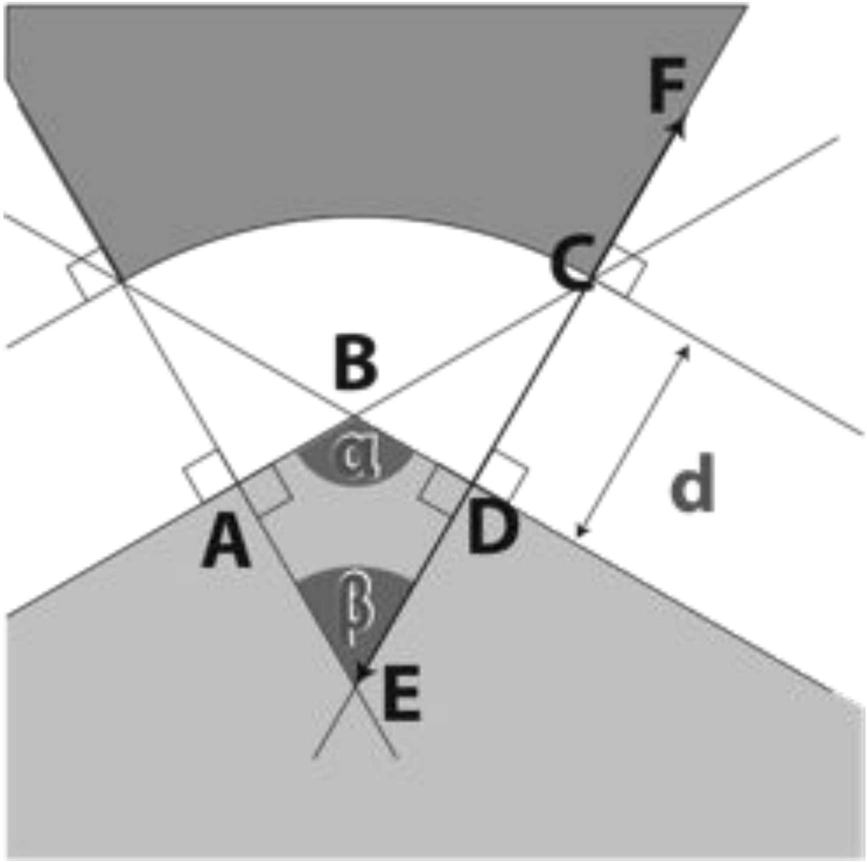

Figure 5.10: Figure 5.9 magnified and relabeled for geometric calculation.

associated with creating a free surface of area for both the graphitic layer and the titania NP. In terms of thermodynamics we can formulate the condition for lift off as follows[146]:

$$E_{(n,\alpha)} + \gamma_1 A \geq E_{(n,\beta)} + (\gamma_2 + \gamma_3)A \tag{5.10}$$

where $\gamma_1$ is the interfacial energy between the multilayer graphene and the titania NP catalyst, $E_{res}$ is the residual strain energy in the reduced strained volume of multilayer graphene after lift-off (Figure 5.8b), $\gamma_2$ is the surface energy of the multilayer graphene, and $\gamma_3$ is the surface energy of the titania NP catalyst. By introducing the adhesion energy of mutilayer graphene on the titania NP catalyst $\Gamma$:

$$E_{(n,\alpha)} \geq E_{(n,\beta)} + \Gamma A \tag{5.11}$$

The adhesion energy of graphene varies with the number of layers and the substrate that graphene is grown upon,[147–149] here titania. Although the adhesion energy between graphene and metal oxides has not been previously reported, the value can be estimated by assuming that graphene on silica will give a closer interfacial energy estimate in our situation than graphene on metals. The interaction between graphene and the substrates is assumed to be by van der Waals interaction alone,[150] and therefore depends on the surface electron density of the material. Therefore, in this work we adopt the adhesion energy experimentally measured by He et al. on silica. They reported that the adhesion energy of graphene on silica decreases rapidly as the number of layers increases: 0.47 J/m$^2$ for a single layer graphene, 0.35 J/m$^2$ for a bilayer graphene, and $\sim$ 0.3 J/m$^2$ for a triple-layer or thicker graphene,[149] which is comparable to the values measured by Koenig et al.[148] In our case, the interfacial area between the graphitic layer and the corner of the MONP is approximately 100 nm$^2$, given $\sim$ 10 nm of the diameter of the MONP catalysts. Therefore the threshold energy for $E_{plate(n,\alpha)}$ and $E_{indiv(n,\alpha)}$to lift off is 293 eV for a single layer graphene, 218 eV for a bilayer graphene, and $\sim$ 187 eV for a triple-layer or thicker graphene, considering that the strain energy in the graphitic layer is fully released ($E_{res}$ = 0).

$E_{plate(n,\alpha)}$ and $E_{indiv(n,\alpha)}$ as a function of the number of graphitic layers $n$ for selected angle of the MONP catalyst corners $\alpha$ are plotted in Figures 5.11a and 5.11b, respectively. Figure 5.11a shows that $E_{plate(n,\alpha)}$ rapidly increases, especially for $\alpha$ steeper than 130°. For such $\alpha$, if beyond two layers, the plate model predicts that the strain energy can become higher than the threshold energies with $E_{res}$ = 0 as indicated by red stars in Figure 5.11. For a three-layer or thicker graphene, even $\alpha$ larger than 150° can become an active site for lift-off. The individual layer model naturally yields significantly lower strain energy than the plate model as plotted in Figure 5.11b. Indeed, the shear modulus $C_{44}$ of turbostratic graphite is about one tenth that of pristine graphite[151,152] so that inter-layer compliance is not practically negligible. On the other hand, the strain energy could concentrate over a corner of a polyhedron where three or more facets meet, which would induce higher strain energy than the 2D estimation used here. HRTEM images show bundles of 5 $\sim$ 6 graphitic layers within turbostratic CNTs which might have resulted from contribution of thermal energy $k$T ($k$ is Boltzmann constant and T is temperature) in addition to strain energy and/or

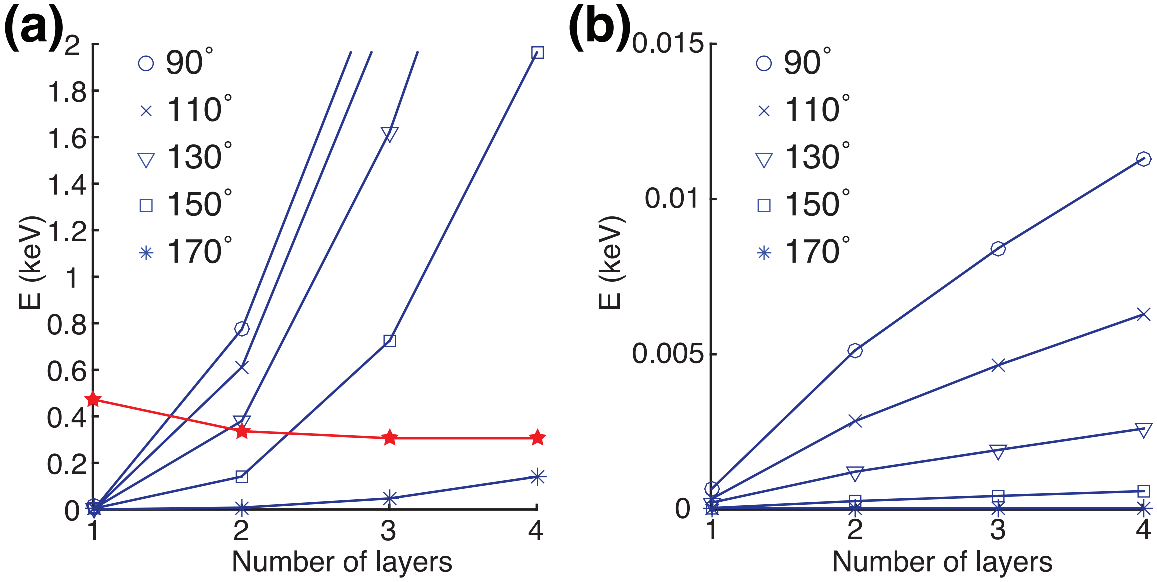

Figure 5.11: Total elastic energy as a function of the number of layers at selected angle of the titania NP catalyst corners $\alpha$ calculated with the proposed model. (a) Results from the plate model. Approximate threshold energies of lift-off for each number of graphitic layers are indicated by the red stars. (b) Results from the individual layer model. Calculations of energies are for an estimated interfacial area between the graphitic layer and the corner of the titania NP catalysts of approximately 100 nm$^2$, following from observed diameters of the titania NP catalysts of $\sim$ 10 nm

$E_{res}$ which was not equal to 0 (Figures 5.2b and 5.2c). Turbostratic CNFs consist of continuously stuck grpahitic layers instead of such bundles, indicating thinner graphitic layers almost fully released strain energy (Figure 5.3b). According to these observations, strain energy stored in the bent graphitic layer forming over a MONP catalyst corner can be a driving forth of lift-off. As a summary, Figure 5.12 schematically illustrates how repetitive lift-off of graphitic layers bent over a NP corner in a two-dimensional mode leads to the turbostratic CNSs observed from titania NPs. Depending on the interval between lift-off and the subsequent lift-off, the resulting CNS can be turbostratic CNFs or turbostratic CNTs that could resemble bamboo-like CNTs. It is worthwhile to note that the lack of CNT and CNF growth from recipe M that employs methane is also explained by the model presented. Due to the molecular structure that does not have a double or triple bond, methane is not removed by hydrogenation.[142,143] Therefore, decomposition of methane molecules is less concentrated at a MONP corner, resulting in a thin and continuous graphitic layer over an aggregate of MONPs as shown in Figure 5.6b. According to the model presented, a thin graphitic layer with large interfacial area tends not to lift off and thus does not convert to nanofibrils.

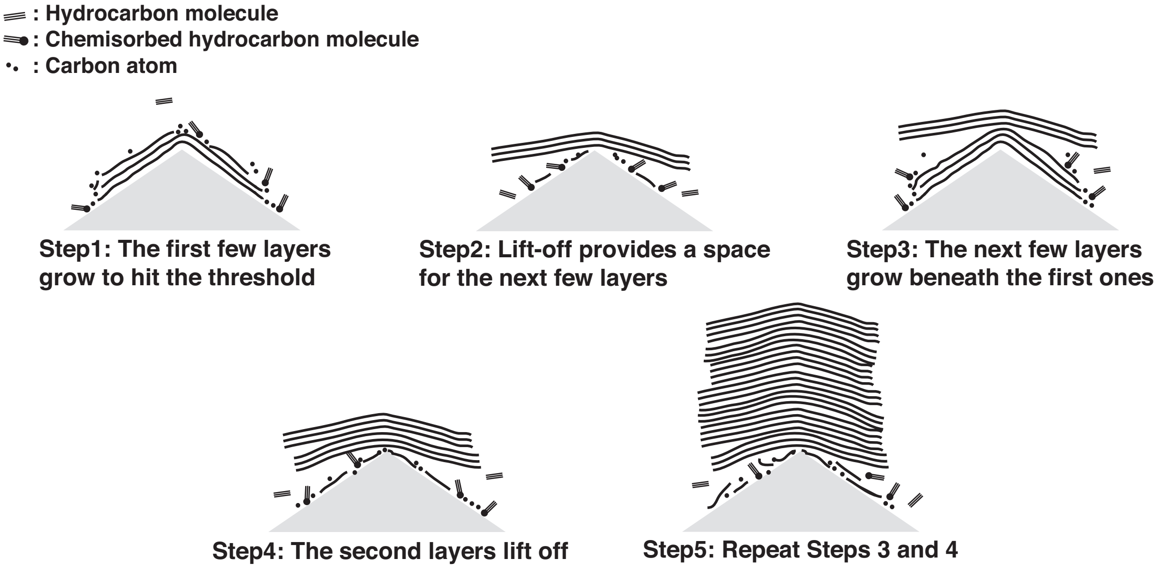

Figure 5.12: Illustration of growth model based on the repetitive lift-off of strained multilayer graphene stack. In this morphology, lift-off of the multilayer graphene stack is occurring at high frequency, and the resulting CNS is a turbostratic CNF.

## 5.5 Conclusions

Using ethylene and acetylene as carbon feedstock and titania NPs as catalysts, we have synthesized turbostratic CNTs and CNFs in a metal-free CVD process. The highest growth yield and homogeneity is obtained by employing acetylene, an alumina substrate, and a CVD reaction at 850°C. The chemical kinetic analysis of the number of acetylene molecules converted into CNSs on a titania NP catalyst corner per unit time estimated about an order of magnitude lower catalytic activity for titania compared with Fe. This is attributed to the difference between the two growth mechanisms, namely solvation-precipitation vs. surface-bound mechanisms, as well as the difference between the chemical properties of titania and Fe NP surface. We also provide a lift-off model for graphitic layers formed over a titania NP corner, where the angle of the catalyst corner plays a significant role. The prediction given by the model agrees with the substructure observed in the synthesized CNTs and CNFs using acetylene or ethylene, and the model also explains the morphology of the carbon deposition obtained by using methane which lacks both CNTs and CNFs. This model explains a key differentiating feature of turbostratic CNT and CNF growth from MONPs, where the NPs remain oxidized solid-state catalysts with low miscibility with carbon during the CVD synthesis of CNSs. Since the turbostratic CNTs and CNFs are attractive building blocks for applications such as electrochemical devices, metal-free CVD process investigated in this chapter will be particularly beneficial.

So far the previously reported MONP catalysts, zirconia and titania, are investigated to delve into growth mechanisms of CNSs that govern resulting growth yield. In the next chapter, MONPs of species that has not been investigated or well corroborated to be catalysts for CNS growth are tested and characterized as potential new MONP catalysts.

# Chapter 6

# Chemical Stability and Catalytic Activity of Other MONPs

Exploring CVD growth of CNSs with a diversity of metal oxide species, in addition to those discussed in the previous chapters, is one approach to acquiring insights into CVD growth of CNSs from MONPs by providing data about how CNS yield and morphology may vary with catalyst composition. In this chapter, CVD growth of CNSs employing chromia, vanadia, ceria, lithia, and alumina NPs is presented and discussed. The aim of this investigation, in addition to identifying additional MONPs that can serve as active catalysts, is to build a systematic understanding of the relationship between physicochemical properties of catalyst NPs and CNT growth behaviors resulting from CVD processing. *In-situ* characterization techniques such as *in-situ* TEM and XPS are powerful techniques for determining if metal oxides stay oxidized or are reduced to the underlying metal and/or form a carbide phase during the CVD process. Access to those techniques, however, is often not available due to the prohibitive cost and/or unavailability of large shared facilities, such as a synchrotrons. In this chapter, attempts to detect the phase of active catalysts with *ex-situ* techniques are discussed. Furthermore, since numerous non-metallic species have already been identified as catalysts, the full scope of materials that can serve as catalysts remains an open question. The results presented here provide a new perspective into the study of MONP catalysts, and may be relevant to researchers working in the fields of inorganic chemistry, as well catalysis in general.

## 6.1 Introduction: Promising MONP Catalyst Candidates

The elements for which one or more of their oxides were previously shown in the literature to act as effective as catalysts for CVD growth of CNTs and/or graphitic nanostructures are annotated in the periodic table shown in Figure 6.1. The oxides of elements labeled with a white circle have already reported in literature that they meet the credibility criteria outlined in chapter 2 based on literature data (Mg,[59,60] Si,[48–51] Zr,[52,92] Ta[55]). The oxides of elements labeled with a white triangle have not been reported to meet these criteria, but adequate data is currently available in the literature to illustrate their potential (Al,[47,48] Ti,[48,53,54] Ga,[59] Y,[58] Hf,[61] Er,[48]). For example, although alumina was reported to be a growth catalyst with TEM images with EDX, no lattice fringes and corresponding FFT or diffraction patterns are provided.[47] Elements labeled with a white star are those whose oxides were investigated for the first time in this work. The elements also labeled with a black circle are whose oxides are firmly corroborated in this work, and labeled with a black triangle are whose oxides are adequately corroborated in this work.

Chromia and vanadia were selected primarily to investigate the transition in the growth morphologies with MONP along the resistivity against reduction. There are two types of reductions that may occur during CVD for these oxides. First, chromia and vanadia may be reduced to chromium and vanadium metals directly. Literature discussing CNT growth may report that Fe oxide[153–155] and Ni oxide[156] NPs were found in the resulting samples and/or served as catalysts for CVD growth of CNTs. However, those metal oxides are known to be reduced before and during growth reaction, and it was more likely metallic phases that grew the CNTs.[157–159] Both hydrogen flow and deposited carbon can serve as reducing agents in these systems,[160] especially at temperatures normally employed by CVD process (500-1000°C). On the other hand, titania, for example, is difficult to reduce by hydrogen or carbothermally to titanium metal under these same conditions, located approximately 400 kj·mol$^{-1}$ below the oxidation of Fe, Ni and Co according to the Ellingham diagram.[161] Chromia and vanadia are expected to be moderately resistant against reduction to their metallic states under the range of partial pressure of oxygen (very small) and temperature normally employed by CVD, including atmospheric CVD conditions used

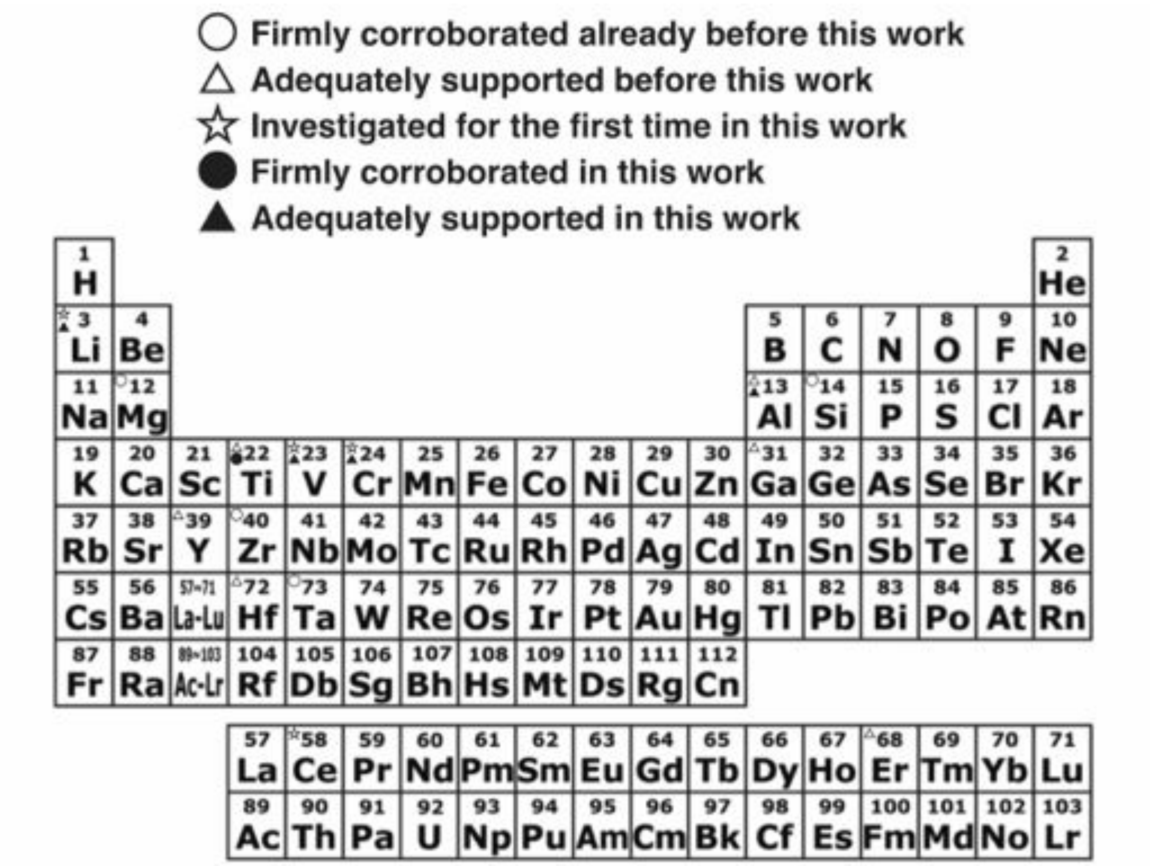

Figure 6.1: List of elements for which one or more of their oxides have been reported to serve as catalysts for synthesizing graphitic nanostructures by CVD, and which have been investigated in this thesiss.

herein. Therefore, it is hypothesized that if chromia and vanadia can catalyze CVD growth of CNTs, the morphology of the resulting CNTs would be a mixture of Type M growth and Type 1 growth as discussed in Chapter 4, which represent solvation-precipitation and surface-bound growth mechanisms, respectively.[92] The second type of reduction is carburization, or formation of carbide phases. Deposited carbon does not only deplete MONPs of their oxygen resulting in carbon dioxide and carbon monoxide as in smelting of metals, but also may result in carbide phases of the corresponding metallic species[160]. As a result, oxide species that are not thermally reduced by hydrogen at CVD growth temperatures may still be deoxygenated. For example, there is continuing debate in the literature whether or not silica NPs reduce to silicon carbide during CVD growth of CNTs.[65] According to the molar Gibbs free energy that are available[162] for the temperature range of interest (300-1100K), chromia (III) ($Cr_2O_3$) is almost always the most stable phase among the chromium-containing system. Chromium carbide ($Cr_{23}C_6$) is the most stable only for temperatures higher than 1000K. For the vanadium-containing system, vanadia (IV) ($VO_2$) is the most stable phase for the entire temperature range of interest, possessing molar Gibbs free energy 1300-1400 kj$\cdot$mol$^{-1}$ lower than vanadium carbide phases. On the other hand, according to the Cr-C and V-C phase diagrams,[163,164] chromium and vanadium both may form carbide phases that could be stabilized at room temperature once formed at CVD temperature. These carbide phases can then be leveraged to determine if chromia and vanadia have carburized during CVD, provided an *ex-situ* HRTEM dataset that meets the credibility criteria set forth in Chapter 2. The results with chromia and vanadia can provide information to help understand mechanisms of CNS growth with MONP catalysts.

Ceria, lithia, and alumina were evaluated to relate different metal valence states to the activity of metal oxides as catalysts. As mentioned, in chemistry and chemical engineering, MONPs are often used as heterogeneous catalysis for multiple reactions, especially those that alter structures of organic molecules such as dehydrogenation,[165] combustion,[166] epoxidation,[167] and ketonization.[168] In this scope, metal oxides can be categorized into solid-state acids and solid-state bases, depending on their tendency to give or take electrons or protons. For example, zirconia has $Zr^{4+}$ cations with exposed *d* orbitals of which all are fully vacant. Exposed on the surface of a NP, these $Zr^{4+}$ cations can accept electrons easily making zirconia serve as a Lewis acid. As a result different metal oxides may show different activity toward adsorption of hydrocarbon feedstock, subsequent decomposition into carbon atoms, and resulting CNS formation due to the oxidation state of the metal in the oxide. The outermost unoccupied orbitals for the transition metals in their ground state are *d* orbitals. This includes titanium, zirconium, iron, and chromium. The lanthanoids, the group to which cerium belongs, have f orbitals as their outermost unoccupied orbitals. Main group elements like aluminum have *p* orbitals for their outermost unoccupied orbitals, and alkali metals such as lithium have *s* orbitals as their outermost unoccupied orbital. These catalyst properties do not necessarily disappear at temperatures normally employed by CVD process. Therefore, the surface electronic structure affected by those orbitals is hypothesized to be a parameter that influences CNT growth mechanisms from MONP catalysts by CVD.

## 6.2 Experimental

Precursor solutions for the examined MONPs are synthesized similarly to zirconia and titania NPs in Chapters 4 and 5. CVD on standard silica substrates and TEM grids, both lacy carbon-coated Cu and SiN, are employed. The same procedure as the zirconia work in chapter 4 and recipe E of chapter 5 are followed here, except some cautions with vanadia precursor in order to form a thermally stable phase of oxide. Phase assignment is paid critical in this investigation since chromia and vanadia may have multiple oxide and carbide phases occurring simultaneously, in conjunction with their metal phases.

### 6.2.1 Precursor Solutions

Precursor solutions for each metal oxide species were prepared as follows: IPA (VWR CAS No 67-63-0, >99.5%) was used as solvent for all the precursor solutions prepared in this chaper. For chromia, chromium (VI) oxychloride ($CrO_2Cl_2$, Sigma-Aldrich, product number 200042, $\geq$99.99%) was mixed with IPA at the concentration of 0.001 mol per 20 mL. After a day, the color of solution changed from red to green, since the $Cr^{6+}$ reduces to $Cr^{3+}$ while IPA is oxidized to acetone. The precursor solution for chromia was prepared by diluting this green solution with IPA in a 10:1 ratio. For vanadia, vanadium (IV) oxysulfate hydrate ($VOSO_4{\cdot}xH_2O$, Sigma-Aldrich, product number 204862, $\geq$99.99%) was mixed with IPA at a concentration of 0.001 mol per 20 mL, considering x = 4 for $VOSO_4{\cdot}xH_2O$. A small amount of $VOSO_4{\cdot}xH_2O$ was insoluble, so only liquid phase was taken to drop-cast. For ceria, sol-gel-synthesized ceria NPs supplied by Prof. Taewang Hyeon's group at Seoul National University were used.[78] The ceria NPs were dispersed in IPA at a concentration of 14.25 mg per 20 mL, the same concentration as sol-gel-synthesized zirconia used in Chapter 4. The ceria NPs are less easily dispersed than the sol-gel-synthesized zirconia NPs in IPA and precipitate after an hour. Therefore, 3-5 minutes of ultrasonication was used to prepare these precursor solutions for drop-casting. For lithia, lithium nitrate ($LiNO_3$, Sigma-Aldrich, product number 229741, $\geq$99.99%) was mixed with IPA at a concentration of 0.001 mol per 20 mL. Lastly for alumina, aluminum nitrate nonahydrate ($Al(NO_3)_3 \cdot 9H_2O$, Sigma-Aldrich, product number 229415, 99.997%) was dissolved in IPA at a concentration of 0.001 mol per 20 mL. $Al(NO_3)_3 \cdot 9H_2O$ does not dissolve completely and precipitates just as $TiOSO_4 \cdot xH_2O$ does so its supernatant separated from precipitation after a day was used as the precursor solution for drop-casting.

### 6.2.2 Pyrolysis and CVD

The dimensions of tubes and the furnace used in this chapter is the same as that used in Chapter 4, *i.e.* zirconia NP work. For CVD growth on silica substrate (thermally-grown 200-nm silica on silicon wafer), one drop of prepared precursor solutions was drop-cast from a Pasteur pipette and completely dried in air before pyrolysis. The drop-cast samples were loaded into a quartz tube and pyrolyzed for 3 hours. Precursor solutions of chromia, ceria, lithia, and alumina were pyrolyzed at 800°C under a flow of 200 sccm of argon, and then cooled down to room temperautre before CVD process. Chromia can take on multiple oxidation states, but the resulting sample was always colored green indicating formation of $Cr_2O_3$. The precursor solution of vanadia was pyrolyzed at 500°C under a flow of 100 sccm of hydrogen mixed with 100 sccm of argon, and then cooled down before CVD process as well. The resulting sample was slightly colored blue, indicating formation of $VO_2$, which is thermally stable at temperatures employed for CVD growth of CNTs and CNFs. Although a well-known metal oxide catalyst, $V_2O_5$ was avoided as its melting point is lower than 700°C so that it would be expected to evaporate at the CVD temperatures employed.[169] CVD conditions and experimental setup were the same as those employed for the zirconia work discussed in Chapter 4 and for recipe E in Chapter 5, using ethylene gas as the carbon feedstock. For direct growth *via* CVD on TEM grids, first, precursor solutions were drop-cast onto a lacy carbon-coated Cu TEM grid or a SiN TEM grid and completely dried in air. The samples were set on a large piece of silica substrate and pyrolyzed under a flow of 200 sccm of argon for an hour, followed by the same CVD process used for growth on silica substrates. For these growth on TEM grids, pyrolysis is followed by CVD right after, instead of once cooled down to the room temperature. Between these processes, quartz tubes were baked out before use at 750°C in air for half to an hour based on need, and therefore not necessarily before every pyrolysis or CVD. For example, if the tube was stored in air longer than a day, it was baked out before processing in order to burn away any spurious deposits of organic contamination and to desorb residual water.

### 6.2.3 Characterization

SEM (JEOL 6010, ZEISS Ultra55) and HRTEM (JEOL 2010F and ZEISS Libra 80-200) with EDX were used to characterize samples. FFT patterns from TEM images were analyzed by ImageJ, and phases of active NP catalysts were analyzed to rule out metallic contamination in the same way as described in Chapters 4 and 5. The full list of crystallographic data used in this work is available in Appendix. A. Raman spectroscopy (Horiba Joain Yvon) was used to investigate the magnitude of graphitization of products grown from different metal oxides for select samples. For samples after CVD on silica substrate, *ex-situ* XPS (Thermo Scientific K-Alpha) was used to study the chemical states of metal cations.

### 6.2.4 Phase Assignment

Based on FFT patterns taken from HRTEM images, NPs were assigned for corresponding phases in the same way as described in Chapters 4 and 5. Chromia and vanadia are noted to have a metal phase, multiple carbide phases, and multiple oxide phases. Only well-studied phases were considered for this work. For chromia precursors, phases that were considered were chromium metal,[86] chromia (III) ($Cr_2O_3$),[170] chromia (IV) ($CrO_2$),[171] $Cr_3C_2$,[172] $Cr_7C_3$,[173] and $Cr_{23}C_6$.[174] Chromia (VI) ($CrO_3$) was excluded as the color change mentioned above indicated that $Cr^{6+}$ mostly disappeared, or hydrogen flow and carbon deposition during CVD had reduced $Cr^{6+}$. Chromia (II) (CrO) was also not considered since it decomposes at 300°C. For vanadia, phases that were considered were vanadium metal,[175] vanadia (III) ($V_2O_3$),[176] vanadia (IV) ($VO_2$),[177] VC, and $V_2C$.[178] Magnéli series, a series of vanadia given by the formula $V_nO_{2n-1}$ for $n \geq 2$,[179] are considered only with its stoichiometric extrema that can represent the compoment of the series, namely $VO_2$ at n = ∞ and $V_2O_3$ at n = 2. Since vanadia (IV) is a well-known thermochromic material that undergoes a metal-insulator transformation at 70°C, and since the high-temperature phase can appear at room temperature due to nanoscale effects similar to how tetragonal zirconia was observed in Chapter 4, these two phases were both considered for $VO_2$. $V_2O_3$ exhibits three phases, but only a corundum phase was considered since the pressure was always atmospheric and the temperatures were only as low as room temperature.[176] VC and $V_2C$ are disordered phases and can be substroichiometric, and known to be stable at temperatures higher than 1000°C.[178] These two carbide phases experience a disorder-order phase transformation as temperature decreases and result in a variety of ordered crystalline structures at room temperature, depending on the substroichiometry.[178,180,181] All the ordered vanadium carbide phases, two generated from the disordered VC ($V_8C_7$ and $V_6C_5$), and four from the disordered $V_2C$ ($\varepsilon$-$Fe_2N$ type, $\zeta$-$Fe_2N$ type, $\zeta'$-$Fe_2N$ type, and $\xi$-$Nb_2N$ type), are included in the investigation, with another carbide phase $\zeta$-$V_4C_3$ which neither belongs to the VC nor $V_2C$ families.[164,182] The phase analysis for oxide and carbide phases here is more involved than those applied to zirconia and titania in previous chapters, simply because chromia and vanadia can be more subject to reduction. For ceria, lithia, and alumina, the most common phases were considered: ceria ($CeO_2$),[183] lithia ($Li_2O$),[184] and $\alpha$ and $\gamma$ alumina.[126,185]

## 6.3 Results

All the MONP precursors synthesized in this section were tested with CVD on standard silica substrates. Chromia, vanadia, and alumina grew CNSs, and were therefore further characterized by CVD on a SiN TEM grid for HRTEM imaging. Ceria did not lead to the formation of CNSs under SEM, and showed very little synthesized CNSs except for a small amount of amorphous carbon deposition. Lithia seemed to react with either silica or SiN so that it was only further investigated *via* CVD on a lacy carbon-coated CuTEM grid.

### 6.3.1 CVD on Silica Substrates

Results of growth from chromia and vanadia NPs on silica substrates are summarized by SEM images shown in Figure 6.2 and HRTEM images shown in Figure 6.3, respectively. Chromia and vanadia showed sparse growth of CNSs. These growth morphologies are similar to those of titania NPs on silica substrates (Recipes A-1 and E in Chapter 4), especially for vanadia. The characteristic circular residue where growth from titania NPs are exclusively observed (See Figure 5.1a and the inset of Figure 5.1d) do not appear with chromia and vanadia NPs on silica substrates. Figures 6.2a and 6.2b show growth from chromia NPs. Chromia also appears as hexagonal platelets. Growth from chromia is sparse, and every growth spot has only few CNSs. Those growths are few hundred nm- to a micron-

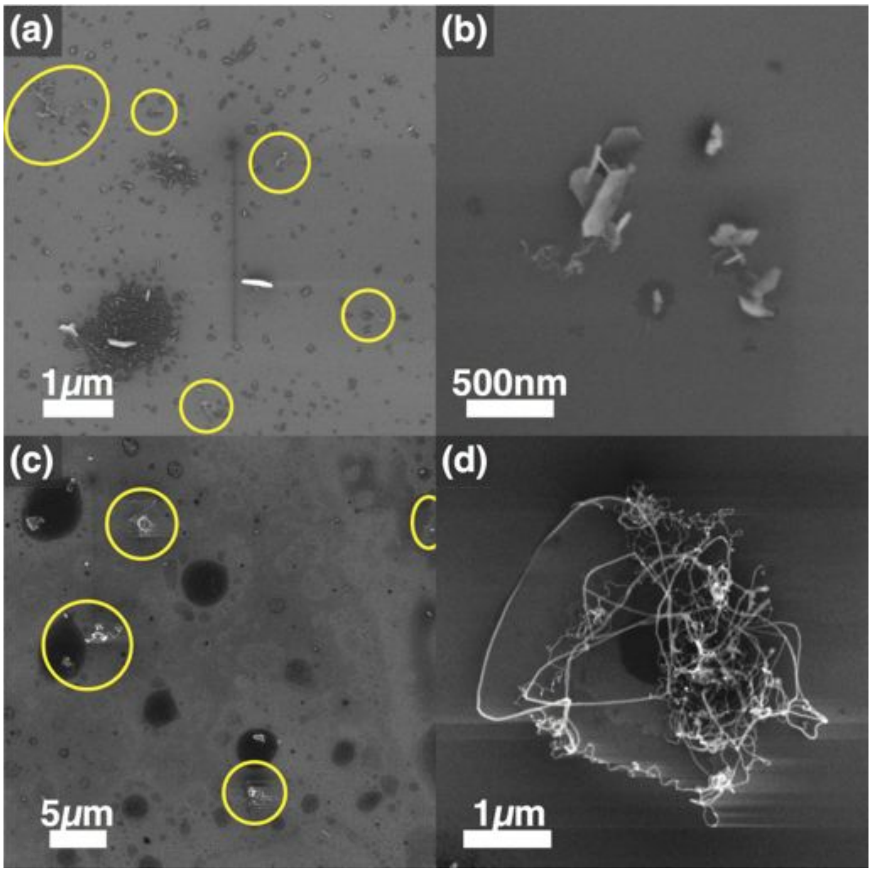

Figure 6.2: Growth morphologies from chromia and vanadia NPs formed on silica substrates. (a) Growth with chromia highlighted by yellow circles. (b) A higher magnification view of a growth spot with chromia in the form of hexagonal platelets. (c) Growth with vanadia highlighted by yellow circles. (b) A higher magnification view of a growth spot with vanadia.

long. Figures 6.2c and 6.2d are growth from vanadia NPs. Compared to the growth from chromia, the growth from vanadia has denser bundles of CNSs. In addition, those nanofibrils are longer than those grown with chromia, sometimes exceeding 10 $\mu$m. After CVD, chromia and vanadia NPs with synthesized CNSs on silica substrates were scraped off the substrates and transferred onto TEM grids to investigate by HRTEM. Figures 6.3a and 6.3b show post-CVD chromia and vanadia NPs. For both cases, 10-50 nm diameter NPs were found. Such NPs are covered with thin defective graphitic layers. It appears to be characteristic of chromia and vanadia for these layers to come off the NP surface as indicated by yellow arrows in Figure 6.3, indicating poor adhesion of the layers formed over the NPs. Phases of NPs were investigated from lattice fringes and FFT patterns. The NPs in Figure 6.3a showed a lattice distance of 2.41 Å and $\sim$ 3.55 Å as annotated. 2.41 Å can be assigned to several phases of chromia and chromium carbide, but not chromium metal. 3.55 Å also is too large for chromium metal and rather belongs to chromia or chromium carbide. The NPs in Figure 6.3b were analyzed in the same way. Lattice distances larger than the lattice parameter of the vanadium metal unit cell (>3.02 Å) were observed, which can be assigned to vanadia and is too large for carbide phases.

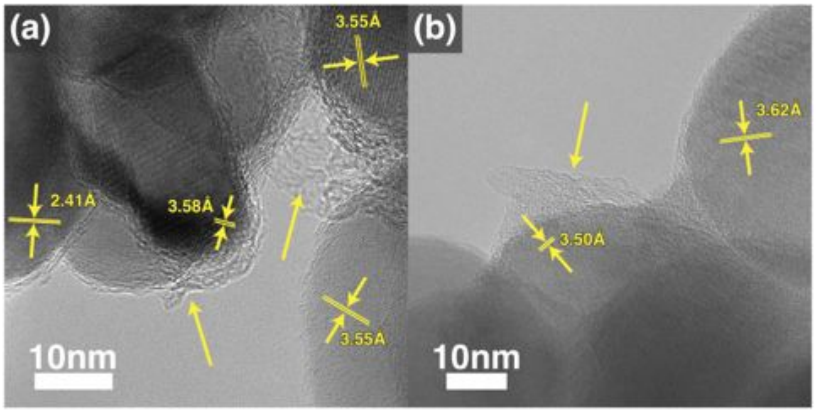

Figure 6.3: Chromia and vanadia NPs after CVD on silica substrate imaged by HRTEM. (a) Chromia precursor sample. NPs coated by graphitic layers showing large lattice distances that indicates the NP is not metallic. Yellow arrows indicate the graphitic layers coming off the NP surface which might lead to growth of CNTs and CNFs. (b) Vanadia precursor sample. Lattice distances indicate these NPs coated by graphitic layers are also not metallic. Graphitic layers come off the surface of the NPs, as observed with the chromia NPs (a).

Figure 6.4 shows XPS data taken from chromia and vanadia after CVD. XPS provides critical information for understanding growth mechanisms, especially from chromia and vanadia for which a variety of interactions with carbon are expected. Acquired peaks corresponding to Cr $2p_{3/2}$ and V $2p_{3/2}$ indicate that major valence states for these metal cations are $Cr^{3+}$ ($Cr_2O_3$),[186] and some vanadia phases that are not conclusive.[187] Peaks that correspond to zero valence states, which would appear at 574.2 eV for Cr and 512.4 eV for V as indicated by the dashed blue lines in Figure 6.4, were not observed,[186,188] revealing that neither metal or carbide were formed on silica substrate at the detectable resolution by XPS. Since the diameter of the probing X-ray was 400 nm, it is still possible that the surface layers of the chromia or vanadia NPs might have turned to a metal and/or a carbide phase. However, combined with lattice fringe analysis in Figure 6.3, it seems that chromia and vanadia was the composition of the majority of the NPs after CVD on silica, as optically observed before CVD. Both ceria and lithia NPs were not observed to grow CNTs nor CNFs. Figure 6.5 summarizes results obtained from ceria NPs. Ceria was found aggregated on silica substrate without any growth (Figure 6.5a). HRTEM reveals that, interestingly, ceria NPs contained very little carbon deposition, with only a few amorphous carbon occasionally observed (Figures 6.5b and 6.5c, annotated by yellow arrows). Even steps and kinks on the ceria NP surface, which would be preferential adsorption sites and hence likely covered by deposited carbon, often remain bare as observed in Figures 6.5b and 6.5d. To

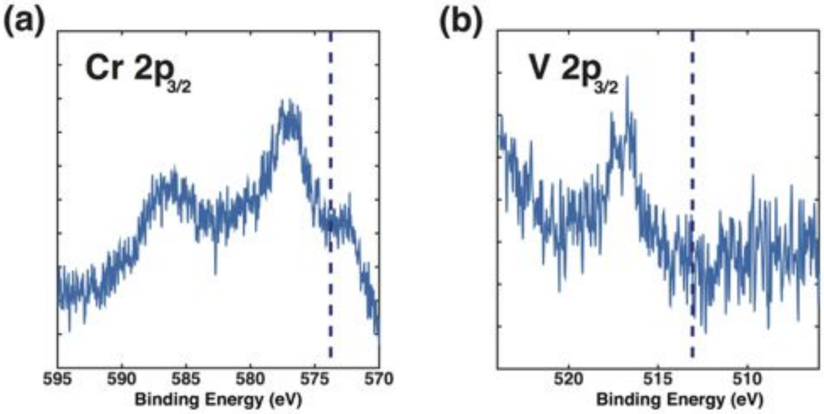

Figure 6.4: XPS from chromia and vanadia samples after CVD on silica. (a) A relatively broad peak around 577 eV corresponds to $Cr^{3+}$ ($Cr_2O_3$). (b) A peak around 515 $\sim$ 519 eV corresponds to some vanadia phase. For both NP types, the zero valence peak associated with metallic and carbide phases are not found (the position annotated by blue dashed lines).

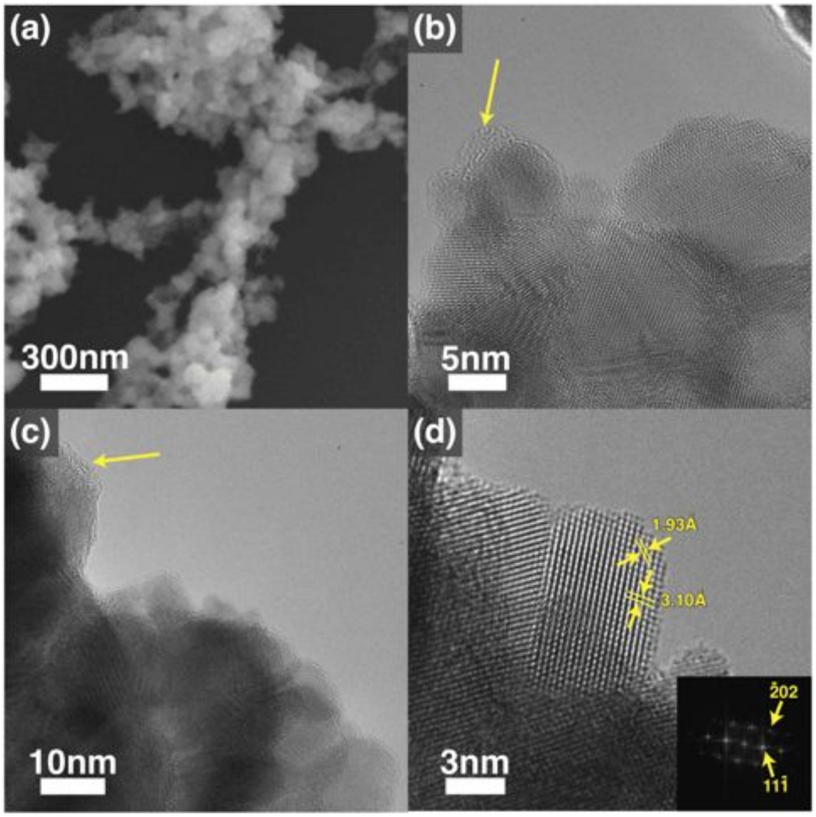

Figure 6.5: Ceria NPs after CVD on silica substrate. (a) SEM image showing aggregate of ceria NPs. (b) HRTEM image of mostly bare ceria NPs with a small amount of amorphous carbon deposition. The particle in the right hand side has a surface with several steps yet remains free of any carbon deposition. (c) The same as (b) but different area. (d) The ceria NP at the right center of (c) at higher magnification. The surfaces are left without deposition, and surface defects are clearly observed at atomistic resolution. The Inset shows the FFT pattern of ceria NP.

assess the result obtained with ceria, Raman spectra were taken from chromia and ceria and compared. These spectra in the range of 1000$\sim$2000 cm$^{-1}$ were decomposed into 5 components according to Ferrari et.al.,[189]: sp3 component (1200cm$^{-1}$), D peak (1340cm$^{-1}$), A peak corresponding to amorphous carbon (1510cm$^{-1}$), G peak (1590cm$^{-1}$), and D' peak (1620cm$^{-1}$). Raman shifts for each separated peak are approximate, based on other literature.[190,191] Figure 6.6 shows the results that indicate very low graphitization with ceria that is consistent with SEM and HRTEM images and analysis. Figure 6.7 summarizes results obtained from lithia. Observed by SEM, it is not certain if lithia NPs formed. The lithia precursor on silica substrate after CVD showed snowflake-like crystallites that are $\sim$

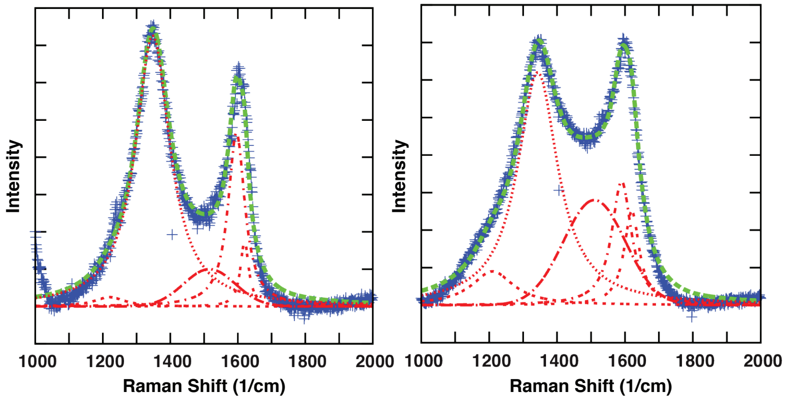

Figure 6.6: Raman spectrum comparison for CNSs grown from chromia (left) and ceria (right). The data taken from chromia (left) show only a minor contribution from amorphous carbon (Gaussian-shaped peak around $\sim$ 1505 cm$^{-1}$) and distinct G/D , compared to the data from ceria (right).

5 micron long. These crystallites adhered to the silica substrate so that they were not able to be transferred to a TEM grid for HRTEM observation. Finally, Figure 6.8 summarizes results obtained from alumina. On silica substrate, alumina showed the most impressive growth of nanofibrils with morphology similar to growth from titania. It seems that a thin alumina film was formed and cracked to leave NPs that grew those CNSs (Figure 6.8a). Split alumina was also observed around growth as a chunk (Figure 6.8b). Under SEM, NPs with $\sim$ 20 nm in diameter were found in the vicinity of growth (Figure 6.8d). As emphasized so far, the SEM images cannot solely substantiate growth from the MONPs. However, from CVD on silica substrates, chromia, vanadia, and alumina are observed to grow CNSs.

### 6.3.2 Direct Growth on TEM Grid

For the sake of efficiently collecting datasets that meet the credibility criteria, CVD was performed with TEM grids as substrate. As developed explained in Chapter 4, this technique is especially useful with sparse growth where the chance of transferring and imaging the interface between CNSs and NPs would be slim. Particularly intriguing results are acquired from chromia on SiN TEM grids. Figure 6.9a shows multiple NPs that are in

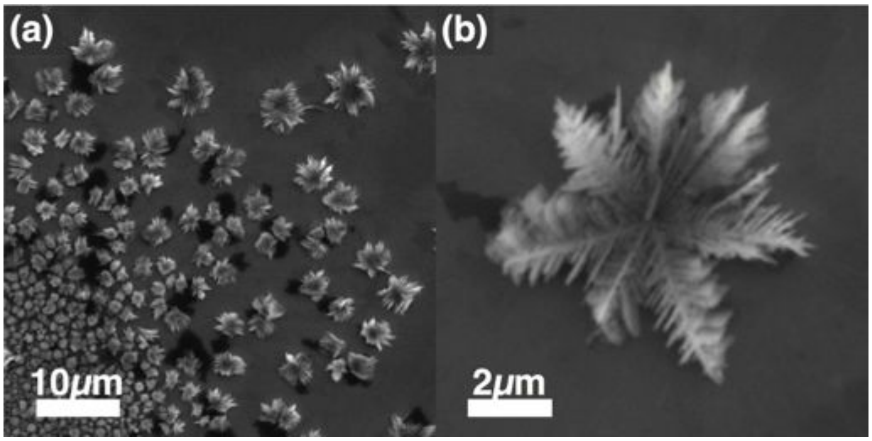

Figure 6.7: Lithia precursor on silica substrate after CVD as two magnifications. Snowflake like objects are formed.

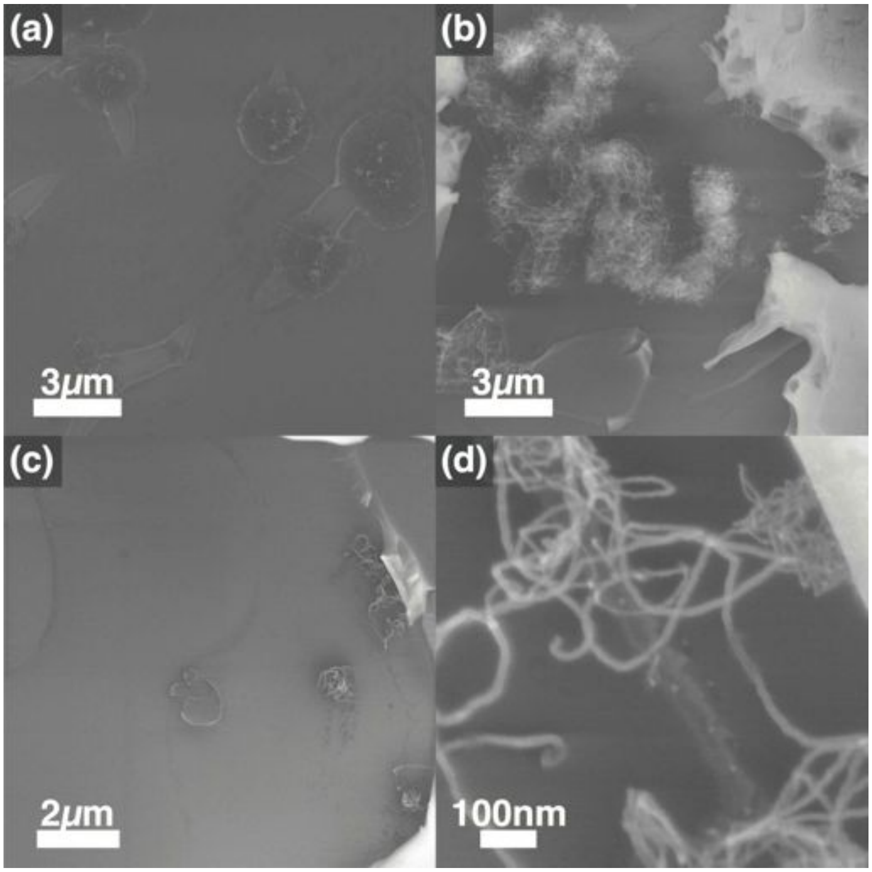

Figure 6.8: Alumina precursor on silica substrate after CVD imaged by SEM. (a) Bundles of CNTs and CNFs observed within the crack through the deposited alumina thin film. (b) A larger bundle of CNTs and CNFs. (c) Other bundles of CNTs and/or CNFs. (d) High magnification image of the root of bundles in (c). NPs with diameter ∼10nm are observed.

graphitic cages and/or have grown CNTs. Localized EDX taken from the area containing growth in Figure 6.9a is shown in Figure 6.9b, indicating no major contamination by metallic catalyst species, although a small amount of chlorine and potassium is noted. Aggregates of those NPs are magnified and appeared in Figures 6.9c and 6.9d for the right most growth in 6.9a, and Figures 6.9e and 6.9f for the middle growth in 6.9a. In contrast to the previously discussed growth from zirconia and titania NPs, the growth morphologies are more similar to those from MNP catalysts, Type M growth introduced in Chapter 4. The degree of graphitization is very high compared to turbostratic CNTs and CNFs grown with zirconia and titania NP catalysts. It should be noted, however, that 5-10 walls of the grown CNT were fractured as annotated by orange arrows in Figures 6.9b (also seen in the leftmost growth in Figure 6.9a). Such fractures are often associated with amorphous carbon. Interesting morphologies are seen in Figure 6.10, a further magnified Figure 6.9e. Divided into two pieces across the pink annotated line, the FFT pattern changes within the single NP. According to the FFT pattern, the right half of the NP is most likely be assigned to $Cr_2O_3$, but $Cr_7C_3$ and $Cr_23C_6$ are still also considered. $CrO_2$, $Cr_3C_2$, and chromium metal are excluded. Furhter selection could be helped by referring to X-ray diffraction (XRD), since the intensity of X-ray scattering and electron scattering by atoms only differ as a monotonic function of sin($\frac{\theta}{\lambda}$, where $\theta$ is the half-angle of scattering and $\lambda$ is the de Blogrie wavelength of electrons.[192] By comparing the XRD patterns of $Cr_2O_3$, $Cr_7C_3$, and $Cr_23C_6$[193,194] with the angles between diffractions calculated by the 'C' script, $Cr_2O_3$ is most likely. Diffraction spots shared with both half of the NP (annotated by white circles in the insets of Figure 6.10.) then indicate that the left half is also $Cr_2O_3$. There are, still, not enough information to definitively determine the crystallographic orientation of one side to the other in this $Cr_2O_3$ NP. Figure 6.11 provides another aspect of growth from chromia NPs. In addition to the CNS fracture with amorphous carbon (annotated by orange arrows in Figures 6.11a and 6.11b), here the graphitic layers are perpendicular to the NP surface as annotated by green arrows. This morphology was totally absent from zirconia and titania NP catalysts, and validates that chromia interacts with carbon atoms differently during CVD, again suggesting more similarity to MNP catalysts. Ctalyst-CNT interfaces by *in-situ* HRTEM investigation that this chromia-graphite interface resembles

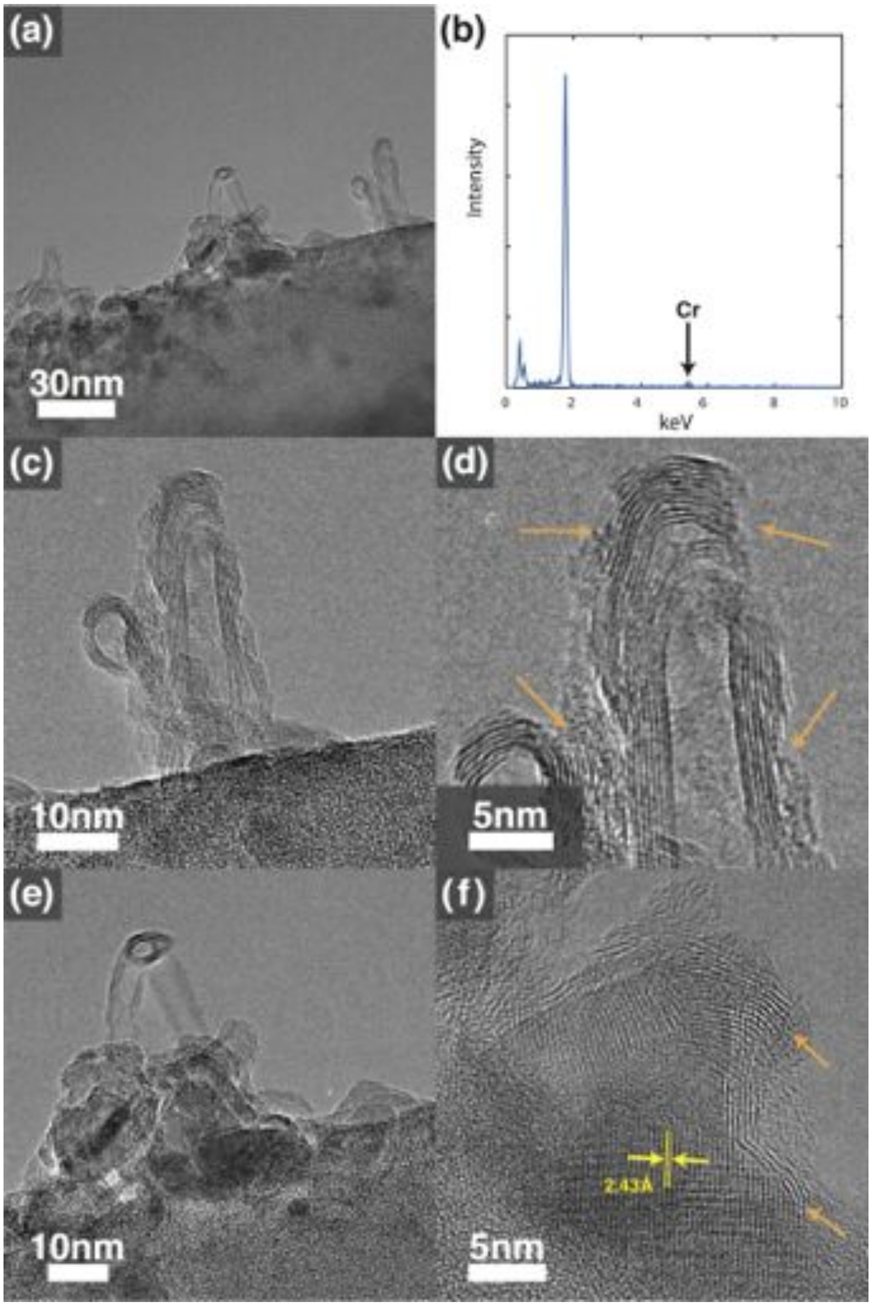

Figure 6.9: HRTEM images of growth morphologies from chromia on SiN TEM grid. (a) Overview. (b) Localized EDX taken from (a). (c) Growth in right hand side of (a). (d) High magnification of (c). (e) Growth at the middle of (a). (f) High magnification of (e).

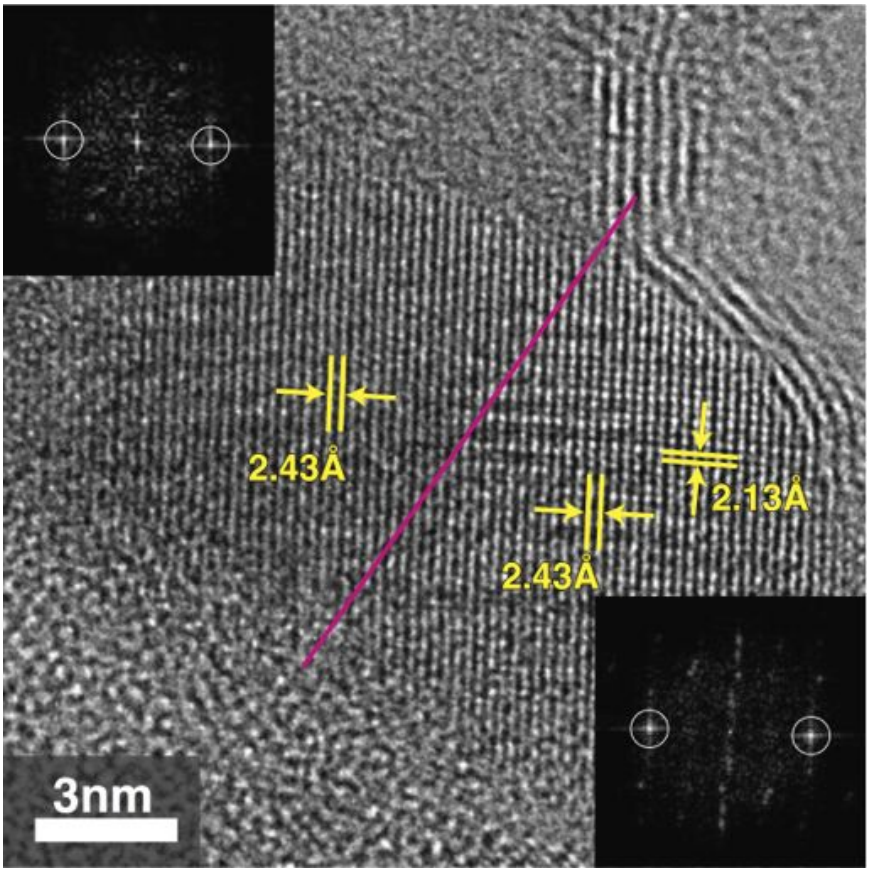

Figure 6.10: High magnification HRTEM image of Figure 6.9 (f) for chromia precursor growth on a SiN TEM grid. Insets are FFT patterns taken from the right and left parts of the NP divided by the pink line that starts from the cleavage of NP-graphitic layer interface. The diffraction spots annotated by white circles correspond to a 2.43Å lattice fringe that exists on both sides of the NP. Other diffraction spots that are not annotated are distinguished from one side to the other, showing structural variation within a single NP across the pink line.

has been reported by Yoshida et.al.,[68] showing an iron carbide NP growing a CNT. The FFT pattern is taken from the area including the blue square; however, as shown in the inset of Figure 6.11a, the NP structure is rich in twinning, so that clear diffraction spots were not exhibited (Figure 6.11d). Figure 6.11b is another example of an aggregate, again showing fractures in graphitic layers with amorphous carbon highlighted by orange arrows, and a twinned NP, magnified in Figure 6.11c. Figure 6.11e is the FFT pattern taken from Figure 6.11c, which is similar to Figure 6.11d. All the observed growth is base-growth. Figure 6.12 summarizes the growth morphology of graphitic nanostructures from vanadia NPs on a SiN TEM grid. There are both morphological similarities and dissimilarities between the results obtained with chromia precursor and vanadia precursor. Graphitic layers formed around NPs are oftentimes partially detached from the NP surface, occasionally in a tubular structure (Figures 6.12a and 6.12b). The number of graphitic layers was found to be generally less than 5, and so thinner than those synthesized with chromia. Fractures in the graphitic layers were not observed with vanadia NPs. FFT patterns were taken from NPs as shown in insets (Figures 6.12a, 6.12b. and 6.12c). Since there are thirteen phases including those with a large and complicated unit cell, phase determination was more difficult than any other species investigated in this thesis. Based on the lattice distances and the angle formed by those corresponding directions, the phase in Figure 6.12a can be assigned to three kinds of carbide phases: $V_6C_5$, $\zeta$-$V_4C_3$, or $\xi$-$Nb_2N$ type $V_2C$. The phase in Figure 6.12b in the same way can be assigned to the room temperature phase of $VO_2$ and $\zeta$-$Fe_2N$ type $V_2C$, in addition to the three carbide phases that Figure 6.12a can be assigned. Unlike chromia, no twinning was observed. Graphitic layers were occasionally attached to vanadia NP surfaces, but not necessarily on the basal plane (0001), as annotated by green arrows (Figures 6.12c and 6.12d). This morphology is rather similar to the graphitic layer perpendicularly extending from chromia precursor-derived NP surfaces. Figure 6.12e presents localized EDX taken from the area centering Figure 6.12a, showing no obvious metallic contamination or contribution. Ceria did not show any growth on SiN TEM grid, as expected. Lithia did not show any growth on SiN TEM grid. Considering that lithia might have reacted with silicon-derived solids to form lithium silicide/silicate (this is conjecture, since HRTEM was difficult), CVD on a lacy carbon-coated copper grid was conducted for

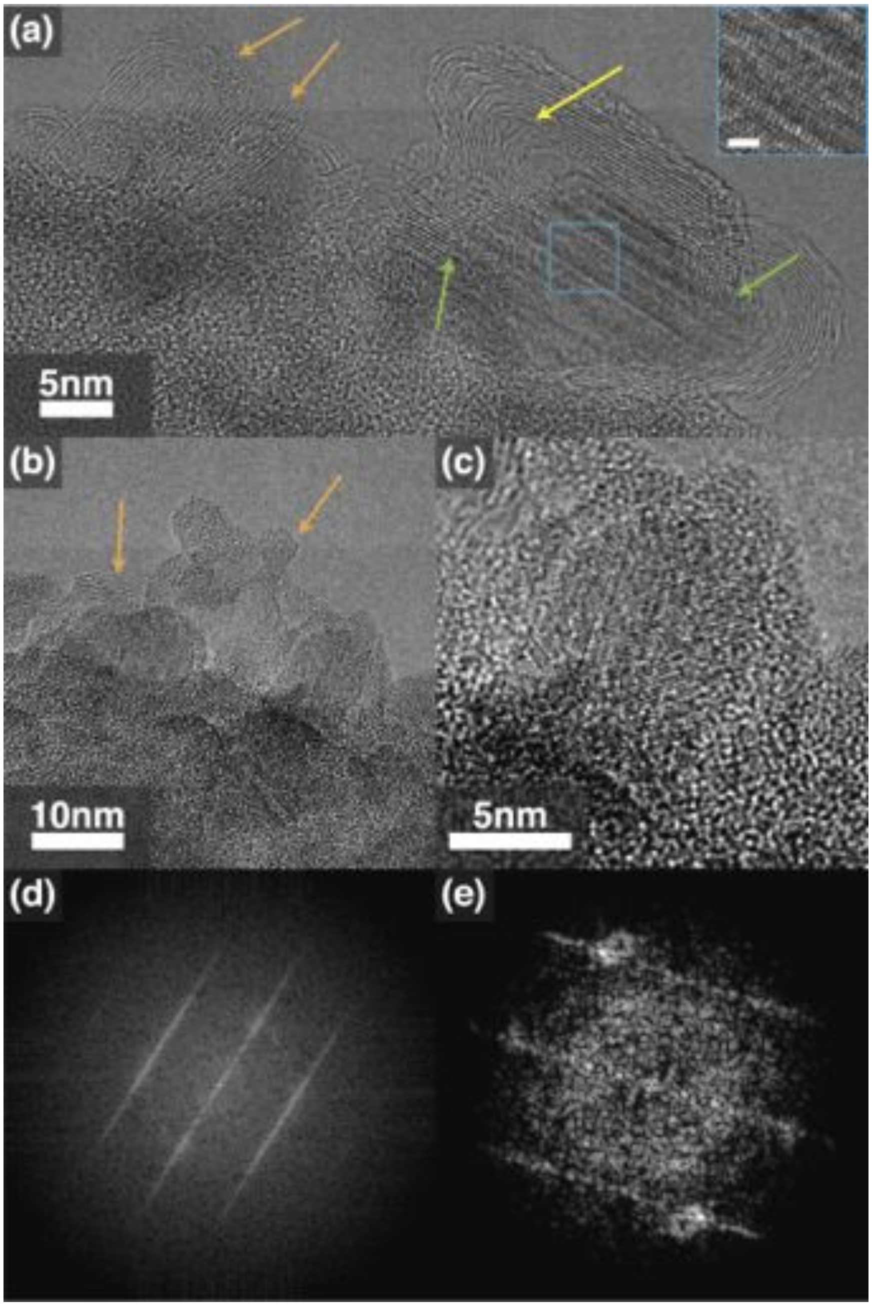

Figure 6.11: Another example of NPs observed on SiN TEM grid after CVD with chromia precursor. (a) NPs that seeded growth of CNTs. Tubular nanostructures that grew with fractures in their walls (orange arrows) and that started to grow from the NP in the right hand side of the image (yellow arrow). Green arrows show graphitic layers perpendicular to the NP surface. The center of the NP in the blue square is magnified in the inset, showing repetitive twinning. (b) Other NPs growing fractured tubular structures and with twinning. (c) The right NP in (b) at higher magnification. The twinned chromia NP is surrounded by amorphous carbon. (d) FFT pattern taken from the twinned NP in (a). (e) FFT pattern taken from the twinned NPs in (c).

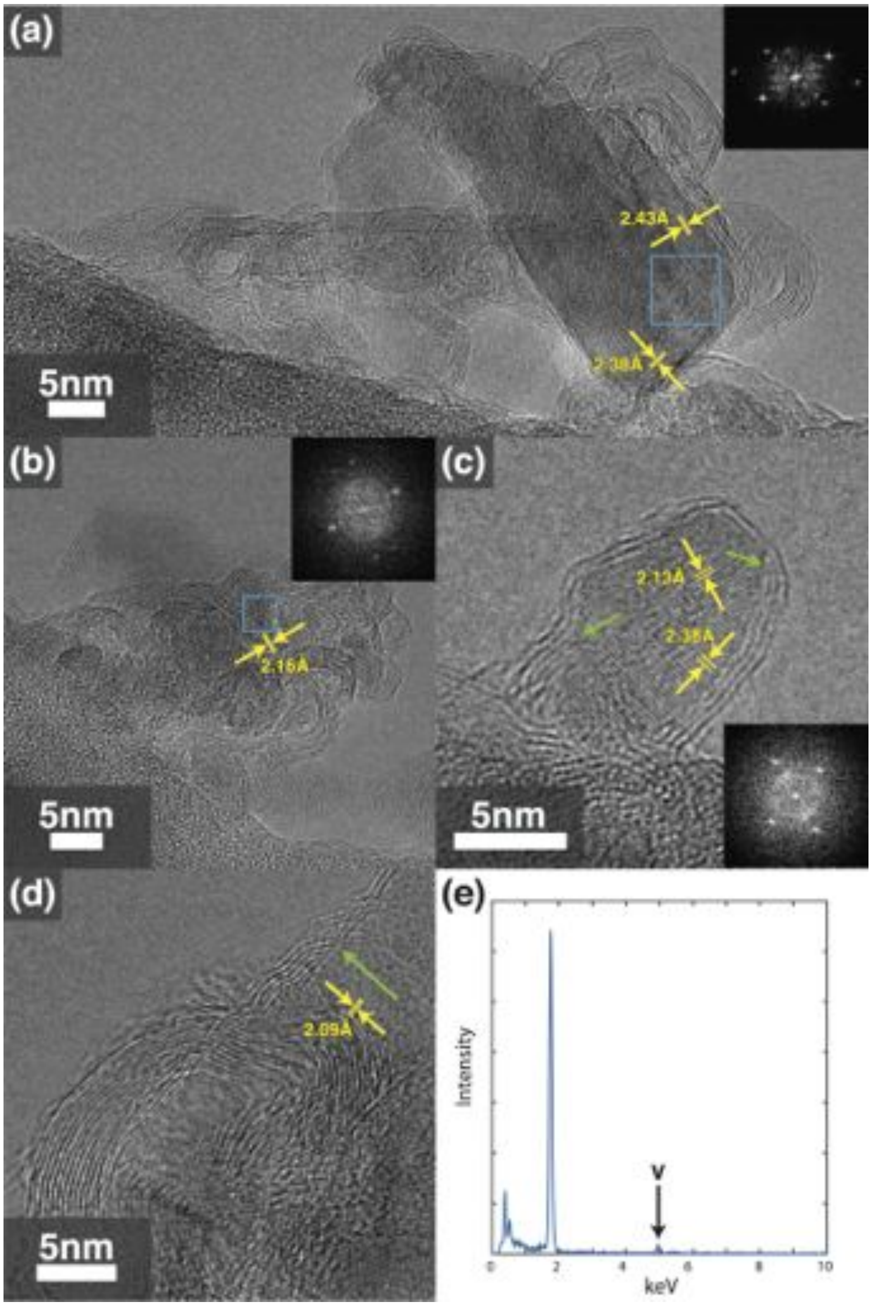

Figure 6.12: Growth morphology observed on SiN TEM grid after CVD with vanadia precursor. (a) A NP aggregate with CNTs grown. The inset is the FFT pattern taken from the blue square area. (b) Another example of NP aggregate where CNTs could be found growing. The inset is the FFT pattern taken from the blue square area. (c) A $VO_2$ NP with graphitic layers around. Graphitic layers extend from the surface as annotated by green arrows. (d) Another example of graphitic layers extending from the surface rather than attaching parallel to the basal plane. (e) Localized EDX taken from the area centering (a).

lithia. As shown in Figure 6.13, individual lithia NPs were found with graphitic layers. These layers appear to detach from of the NPs, especially from corners within their vicinity as annotated in Figures 6.13a and 6.13b. These images also support the model presented in Chapter 5 that a bent graphitic layer over the corner of metal-oxide NP catalyst eventually lifts off to reduce strain energy. FFT patterns are sssigned to $Li_2O$ as expected. For lithia, carbonate phases could appear. Their low melting point suggests that NPs of those phases would evaporate at 750°C, although their formation only on the NP surface cannot be ruled out. Figure 6.14 summarizes the results of growth with alumina NPs. Contrary to the relatively high growth observed on silica substrate, alumina on a SiN TEM grid did not show appreciable amount of nanofibril growth but often only with thin graphitic layers all around the NPs, sometimes as thin as a single layer. An $\alpha$ alumina NP in Figure 6.14b suggests an extension of graphitic nanosrtucture from the graphitic layers around the NPs, and we observe graphitic layers detached from the right side of the NP. Still it is difficult to determine if the extended nanostructure is a CNT or a CNF. Different substrate effects on growth kinetics between silica and SiN were not investigated in this work.

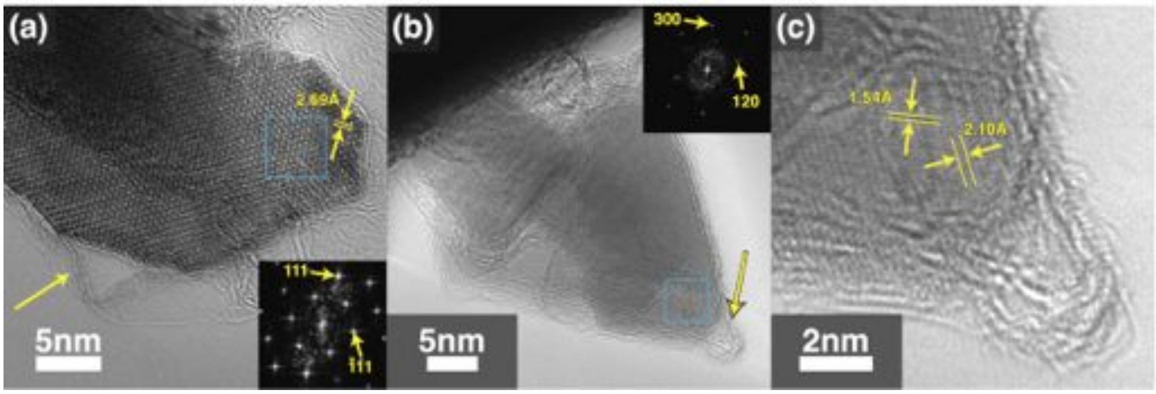

Figure 6.13: Lithia NPs with graphitic layers. (a) Graphitic layers detached from the lithia NP surface near a corner. A FFT pattern taken from the blue square is shown in the inset. (b) Another example of a graphitic layer detaching from the lithia NP surface but from a sharper corner. (c) A higher magnification image of the corner of the NP in (b).

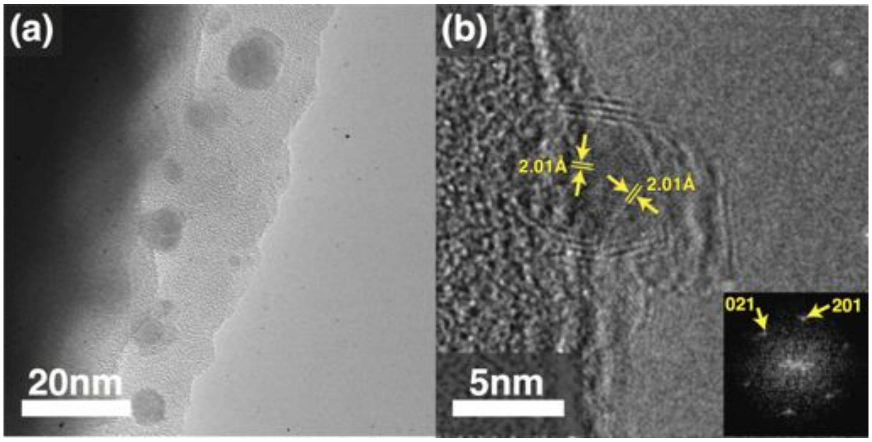

Figure 6.14: Alumina NPs on SiN TEM grid after CVD. (a) Individually dispersed alumina NPs without growth. (b) An alumina NP with single-layer graphene around it. The FFT pattern taken from the NP is assigend to be $\alpha$ alumina.

## 6.4 Discussion

Chromia and vanadia precursors successfully formed active catalytic NPs either on silica substrates and/or SiN TEM grids. It is optically observed that the chromia precursor was converted to $Cr_2O_3$, and vanadia precursor likely to $VO_2$ after pyrolysis. According to XPS, these MONPs were not carbothermally reduced during CVD, since the Cr-C and V-C phase diagrams indicate carbide phases would not be stable in the temperature regime relevant to this study. For vanadia, the XPS spectrum was not definitive on the valence state of vanadium cations in the oxide phase. XPS is consistent with characterization by HRTEM for chromia NP catalysts. However, for vanadia NP catalysts, HRTEM characterization indicates that the NPs might form carbide phases. Since an interesting CNS growth was observed for vanadia NPs, additional work is needed to explore carbide formation in vanadia NPs during CVD, as well as more precise XPS analysis.

While neither chromia nor vanadia precursors were found in their metallic phase post-CVD, it is true that some (likely the surface) of the NPs may be reduced to their metallic phase during CVD, and were transformed to their oxide or carbide phases when characterized by XPS or HRTEM after growth and exposure to ambient conditions. There are chromia and vanadia precursor-derived NPs growing CNS that appear similar to the Type M growth discussed in Chapter 4, which are encapsulated in a graphitic cage of thickness comparable to the diameter of the NPs (See and compare Figure 4.7 to Figure 6.9c and the left side of Figure 6.12b). These encapsulated NPs were only $\sim$ 5 nm in diameter, and this small dimension suggests that the resistivity of chromia and vanadia NPs against reduction depends on the size of NPs, with a threshold size of $\sim$ 10 nm in diameter, as observed by HRTEM.

Growth from chromia exhibits morphologies that were not observed with MONPs previously, which prevent the conclusions that $Cr_2O_3$ NPs are MONPs that grow CNTs. First of all, it is very energetically unfavorable to build an interface where the prismatic plane of graphite as thick as 10 graphene layers attaches to another surface (see Figure 6.11a). Considering that the higher surface energy of the prismatic plane of graphite is two orders of magnitude higher than that of the basal plane,[195] the only feasible process that could form such an interface would be precipitation of carbon from a NP saturated with carbon, as was the case of Fe NP catalysts.[36] It is assumed that, even so, the interface as shown in Figure 6.11a would still be so unstable that it could detach over the course of CNS growth. Then the terminated prismatic plain of the graphitic nanostructure can potentially be covered by something else, such as amorphous carbon. This might be the mechanism for the formation of ruptures in CNT walls 5-10 graphene layers thick, which is associated with amorphous carbon. Twinning of NP catalysts (Figure 6.11), or reconfiguration of NP crystal structure during CVD (Figure 6.10), also indicates that the growth mechanisms from chromia NPs are not surface-bound as concluded with zirconia and titania, but rather involves diffusion of carbon atoms inside the NP, which is potentially similar to the saturation-precipitation process for Type M growth defined in Chapter 4. Compared to the growth morphologies with vanadia NPs which are more similar with growth mechanisms that are bound on surface, the indication of growth mechanisms with chromia using the volume of NPs is consistent with the hypothesized trend from titania, through vanadia and chromia, to Fe. It is worth recalling that the growth from chromium metal as investigated in Chapter 4 has totally different morphologies, which is the same as popular metallic NP catalysts, wherein the chromium metal was encapsulated in a thick graphitic cage. Notably, there were not ruptures of well-crystallized graphitic layers, indicating the interface involving the prismatic plane of graphite seen in Figure 6.11a would not have formed if the chromia NP was reduced to the underlying metal. Therefore, the morphologies of growth from chromia NPs likely resulted from a saturation-precipitation process even when the NP was crystalline metal oxide, which offers a new insight for CNT growth mediated by MONP catalysts, and presents a transition from a MONP with surface-bound growth (titania) to a MNP with characteristics of saturation-precipitation growth.

While more elaborate study is needed with phase assignment, vanadia NPs have also shown catalytic activity toward CNT growth and graphitization. Similar to what was observed with chromia NPs, the degree of graphitization with vanadia NPs is generally higher than for zirconia and titania which grow turbostratic CNSs. Since vanadia NP catalysts do not show evidence of a saturation-precipitation process, surface-bound mechanisms for CNT growth are suggested, even though carbothermal reduction for carbide phases may occur at the same time. Unlike zirconia and titania NPs, vanadia NPs, either individually separated on a substrate or in aggregates, tend to have continuous graphitic layers. For example, it was not the case with vanadia NPs that only a corner was attached to graphitic nanostructures (See Figure 5.3c, for example). Amorphous carbon was not deposited with vanadia NPs. In general, vanadia NPs need further study to be firmly corroborated as MONP catalysts with the catalytically active phase of oxide. An interface was formed between the non-basal plane of the graphitic structure and the NP surface (Figures 6.12c and 6.12d). Compared to a similar result previously reported with magnesia where the graphitic layers grow parallel,[60] graphitic layers on vanadia seen in Figures 6.12c and 6.12d appear as if they had intentionally bent to attach to the NP surface by the non-basal plane of graphite, indicating that such an interface, counterintuitively, may be energetically stable.

Ceria, the only species that did not even result in deposited graphitic layers, suggests that it may not be true that any type of MONP can grow CNTs, or even can be active toward graphitization. Although the shape and distribution of ceria NPs could potentially be optimized to give CNS growth *via* CVD, the ceria NPs that were populated with surface defects but without much carbon deposition, as seen in Figure 6.4, strongly suggests that ceria is different from other MONPs. As introduced at the beginning of this chapter, the surface electronic state may account for this difference. One could argue that the results were due to the renowned functionality of ceria as oxygen supplier from lattices, as those oxygen could remove deposited carbon by forming cabron monoxide or dioxide.[196,197] The reaction temperature, however, here 750°, is actually lower by 100° than the reported temperature for the clear onset of solid state oxidation without introducing gaseous oxidants,[197] and therefore needs further corroboration. *in-situ* XPS will offer the best characterization for clarifying the chemical state of ceria during CVD. Lithia, with a vacant *s* orbital in its cations, and alumina, with a vacant *p* orbital in its cations, were also at least able to graphitize, suggesting that the shape of the outermost, vacant electron orbital of the cation may not be so significant, unlike the finding for ceria. Throughout the work in this chapter, it was common to observe graphitic layers that had detached partialy from MONPs corners. A strong example is given by observations of CVD with lithia on lacy-carbon coated Cu TEM grid that presents $2-3$ layers of graphene exfoliated from a corner of lithia NPs at an angle of 120-150°. Alumina NPs on a SiN grid, on the other hand, were often very spherical and surrounded by thin graphitic layers that seldom extend to be CNTs and CNFs. These observations are quite consistent with the lift-off model proposed for titania NP catalysts, and also with a key concept throughout this thesis that the shape (size and corner angles) of MONPs is of great importance. The exfoliated layers were not necessarily shaped into well-defined CNTs, turbostratic CNTs, or CNFs, but indicate that the instability caused by strain exerted on graphitic layers formed on MONPs plays a significant role in determining the final morphology of CNSs.

## 6.5 Conclusions

The results reported here illustrate that while chromia and vanadia can potentially serve as MONP catalysts to synthesize graphitic nanostructures including CNTs, firm evidence is still required especially in terms of the active phases. Their growth mechanisms seem different from those proposed with zirconia and titania NP catalysts, although mechanisms with chromia are closer in nature to those of MNPs like Fe, and those that govern growth with vanadia are more similar to zirconia and titania, where the growth mechanisms are surface-bound. According to the Ellingham diagram, we recognize the trend that resistivity to reduction leads to surface-bound growth mechanisms, and the border between stable MONP catalysts with surface-bound growth mechanisms and MNP catalysts lies around the group IV and V elements for the oxide of transition metals that belong to the fourth period of the Periodic Table. Ceria NPs provided an interesting case where even the deposition of carbon, a step before synthesizing graphitic nanostructures, may not necessarily occur. It could be due to the surface electronic structure related to cerium cations that prevent adsorption of ethylene, although more study on solid-state oxidation of deposited carbon on ceria is necessary. The hypothesis that the shape of MONPs affects CNT growth was supported with multiple metal oxide species investigated here, validating that the lift-off model is more generally applicable than titania NP catalysts. Investigation of multiple metal oxide species has brought about several important insights that deepen the understanding of growth mechanisms of CNSs grown with MONP catalysts, and has also resulted in several interesting research vectors including the effect of surface chemistry on growth mechanisms and a saturation-precipitation process that appears to occur in crystalline chromia NPs. An *ex-situ* method to assess the behavior of MONPs during CVD using data from thermodynamic databases was partially successful with chromia. It is expected that extending this research in these directions will lead to fruitful results that are not restricted to MONP catalysts, but also physical chemistry at the nanoscale in general.

Although the study of a wide variety of potential MONP catalysts has yielded valuable insight into their growth mechanisms as discussed through this chapter, the high yield and reproducible CNS growth necessary for the quantitative characterization of their growth mechanisms was not always attained. In the next chapter, a special form of titania nanowire is used to synthesize CNSs *via* CVD to help elucidate the underlying physics that govern the formation of graphitic nanostructures on one-dimensional metal oxide nanostructures.

# Chapter 7

# Graphitic Nanostructure Growth on Titania Nanowires

In this chapter, the insights acquired about MONP catalysts are applied to a different metal oxide nanostructure than NPs, *i.e.* nanowires. Growth of graphitic nanostructures on metal oxide nanowires provides a much needed perspective on the synthesis of graphitic nanostructures on one-dimensional metal oxide nanostructures. Although multiple studies report that graphene synthesis on flat substrates of non-metallic materials such as sapphire[62] and silica[63] tends to result in a film of polycrystalline graphene, nanowires exhibit an interesting geometry which has a NP-like curvature in one direction, and an extended flat surface perpendicular to the direction of the curvature. With titania nanowires as a model system, the evolution of graphitic nanostructures on such a unique growth geometry is studied at an atomic scale.

## 7.1 Introduction: Nanowire as Substrate

Metal oxide nanowires have been extensively investigated for their potential use in solar cells,[198,199] battery electrodes,[200] electronics,[201] and many other high value applications. While these applications might also hold potential for MONPs, nanowires outperform NPs in several aspects, especially with respect to transport properties. Highly porous aggregates of NPs are full of boundaries and interfaces that lead to interfacial phonon and electron scattering. For example, use of titania nanowires instead of titania NPs as a component for DSSC has been discussed in detail previously.[202,203] Furthermore, metal oxide nanowires can be obtained as NWAG, which is a freestanding, centimeter-large, spongy monolith comprised of entangled nanowires.[204] Such a material is easy to handle and mechanically robust, and is therefore preferred to NPs in many circumstances.

For its structure, metal oxide nanowires are an interesting non-metallic substrate to synthesize CNSs, especially graphitic nanostructures. Non-metallic flat substrates, especially dielectrics, are broadly studied for graphene synthesis *via* CVD for high-value applications.[62,63,205] Due to the two dimensional structure, however, high-resolution imaging is often limited to in-plane probing techniques, such as scanning tunneling microscope (STM)[206] that are not well-suited to image the graphene-substrate interface at an atomic scale. NPs have a large number of surface defects and high degree of local curvature. Therefore the mechanisms of graphitic nanostructure synthesis and their chemical and thermal stability would be distinctly different from graphitic nanostructures that formed on flat substrates. Nanowires exhibit flat surfaces with less population of surface defects than NPs, and TEM can be utilized to investigate the interface at an atomic scale without complicated preparation, which enables nanowires to act as model systems for the study of the growth mechanisms governing the synthesis of CNS, including graphene, on metal oxides.

From the deposition of amorphous carbon patches to their graphitization, the structural evolution of deposited carbon on the titania nanowire surface was quantified at an atomic scale using aberration-corrected (*i.e.*, Cs-corrected) TEM. By investigating titania NWAG after CVD for every 225 sec (up to 1575 sec), the graphitization is observed to terminate when the nanowire surface is covered by graphitic nanostructures at 1125 sec. Longer CVD only results in the deposition of an amorphous carbon layer at isolated locations on top of the graphitic nanostructure, providing no further changes in the morphology of previously synthesized graphitic nanostructure. From these observations, we conclude that the graphitization is facilitated by the titania nanowire surface that serves as a catalyst. We also show that amorphous carbon patches need a threshold diameter size to be graphitized. Furthermore, electronic conductivity of NWAG increases by 4 orders of magnitude after depositing graphitic nanostructures. Combined with Cs-corrected TEM investigation and Raman spectoscopy, the graphitic nanostructure covers the nanowire surface effectively continuously throughout the intricate three-dimensional morphology of the NWAG. These results provide intriguing mechanistic insights into the metal-free growth of graphitic nanostructures.

## 7.2 Experimental

NWAG samples are hydrothermally synthesized and cut into an appropriate size for the subsequent CVD process. Recipe E of chapter 5 is modified to yield the reproducible production of homogeneous graphitic nanostrucrures throughout the NWAG samples. A series of CVD processing steps is implemented for every 225 sec from 0 to 1575 sec to track the morphological evolution of the grown CNS. HRTEM and Raman spectroscopy are used for structural characterization, and a 4 point probe is used to measure the changes in bulk electrical conductivity after each CVD duration.

### 7.2.1 Titania NWAG Synthesis

Titania NWAG synthesis is based on the process recently reported by Jung et al.[204] Commercially available P25 (anatase titania NPs) is dissolved in 10 M potassium hydroxide solution so that P25 is at 7.5 mg $mL^{-1}$ of concentration. The mixture is stirred for 30 min and transferred to a Teflon vessel held in a stainless steel vessel. The sealed vessel is placed in a furnace and kept at 453 K for 16 to 24 hours. $K_2Ti_8O_17$ nanowire hydrogels are first synthesized by a simple hydrothermal reaction of titania NPs and potassium hydroxide solution. Then the obtained nanowire hydrogels are ion-exchanged into $H_2Ti_8O_17$ by acid treatment with 0.2 M nitric acid, and then washed with excess deionized water without stirring or filtering to keep the gel networks intact. Cut into various shapes, the hydrogels are subsequently placed into anhydrous ethanol overnight for solvent exchange. After that, the in-situ $H_2Ti_8O_17$ nanowire hydrogels are supercritically dried into aerogels to retain the original gel volume. In the last step, $H_2Ti_8O_17$ nanowire aerogels are transformed into anatase titania NWAG by heating at 600°C for 2 hr in air using fused quartz process tubes (25 mm OD × 22 mm ID × 76.2 cm length) placed inside a Lindberg/Blue M MiniMite

1-inch diameter electrical tube furnace. Process tubes used in this work are baked in air at 800°C for 1 hr to eliminate potential contamination if needed, as was the case of MONPs investigation in Chapter 6.

### 7.2.2 CVD on Titania NWAG

Argon, hydrogen, and ethylene (Airgas, UHP grade, 99.999%) are used for CVD. NWAG samples are first inserted into the process tube about 2 cm beyond the zone center toward the exhaust end of the tube. Then the same CVD process as used to prepare pyrolytic carbon-coated SiN TEM grids in chapter 4 is applied. The gas flow ratio, 100 sccm higher ethylene flow and 100 sccm lower hydrogen flow compared to recipe E of titania work, is adopted after several attempts with different gas flow ratios. In order to distinguish graphitic nanostructures catalytically synthesized on nanowires from those deposited as a result of gas phase pyrolysis, 750°C is chosen for the work in this chapter even though higher growth yield is achieved with 850°C using titania NP catalysts. A smaller set of 850C growths is performed to consider the effect of gas-phase pyrolysis of ethylene and contrast it with the 750C growths With this gas flow ratio and CVD temperature, graphitic layers are synthesized homogeneously and reproducibly on titania nanowires without causing gas phase pyrolysis. After each CVD duration (0, 225, 450, 675, 900, 1125, 1350, 1575 sec), the hydrogen and ethylene are turned off and the system is cooled to room temperature.

### 7.2.3 Characterization

For HRTEM imaging, Cs-corrected TEM (Zeiss Libra 80-200) is used to characterize the resulting morphology of carbon deposition and investigate the transformation mechanism of amorphous carbon into graphitic nanostructures. The standard HRTEM (JEOL 2010F used in previous chapters) is more likely to damage and collapse those CNSs formed on NWAG. Raman spectroscopy (Horiba Jobin Yvon HR 800) is used to quantitatively analyze the evolution of graphitization. Electrical conductivity is measured by a 4-point probe (Keithley SCS-4200). The depth of the electrode into the NWAG samples is 0.5 mm. NWAG samples are not compressed for the conductivity measurement.

## 7.3 Results and Discussion

Ethylene is used as a carbon feedstock throughout the NWAG study in this chapter. On the course of ramping up the temperature to 750°C under argon and hydrogen flow, the titania NWAG changes color from white to black before the introduction of the ethylene gas. The color gradually changes back from black to dark blue after exposed in air, not to perfectly white as NWAG initially is. It seems that the oxygen defects are created by the high temperature treatment with hydrogen, and that oxygen is then replenished to some extent from exposure to the air.[207] Excessive reduction could result in an irreversible dark color associated with a damaged lattice structure near the surface,[208] but the lattice structure is preserved here as discussed later. Therefore, the permanent change in NWAG color from white to black observed after CVD is attributed to the deposition of CNS. Not only on the surface of bulk piece of titania NWAG but also inside the NWAG turns black after CVD, which is indicative of that the gas flow infiltrated the bulk of the NWAG. Figure 7.1 compares the titania NWAG before it is loaded into the quarts tube and after CVD for 900 sec at 750°C.

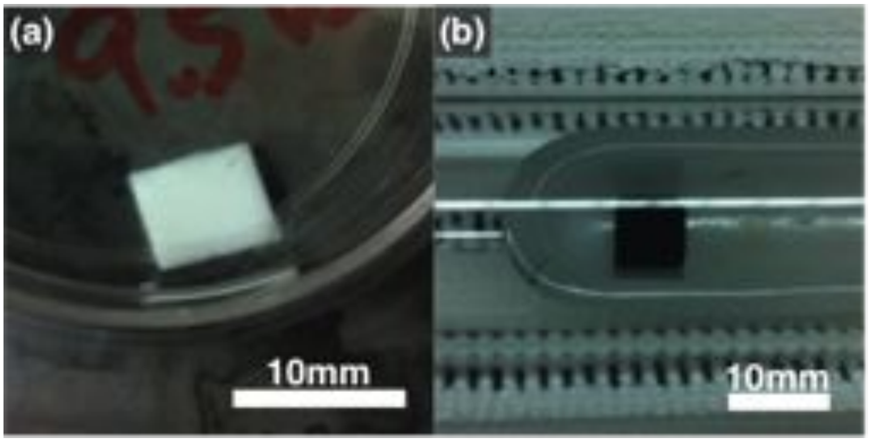

Figure 7.1: Pictures of titania NWAG sample before and after 750°C CVD (900 sec). (a) Before CVD in a container. (b) After CVD on a fused silica boat in a quartz tube. The color clearly changes from white to black.

Figure 7.2 shows representative microscopic morphologies of carbon deposition on titania nanowire surface imaged by Cs-corrected TEM, after a series of CVD for different lengths of time up to 1125 sec. In Figure 7.2a, 0 sec means that the temperature is elevated

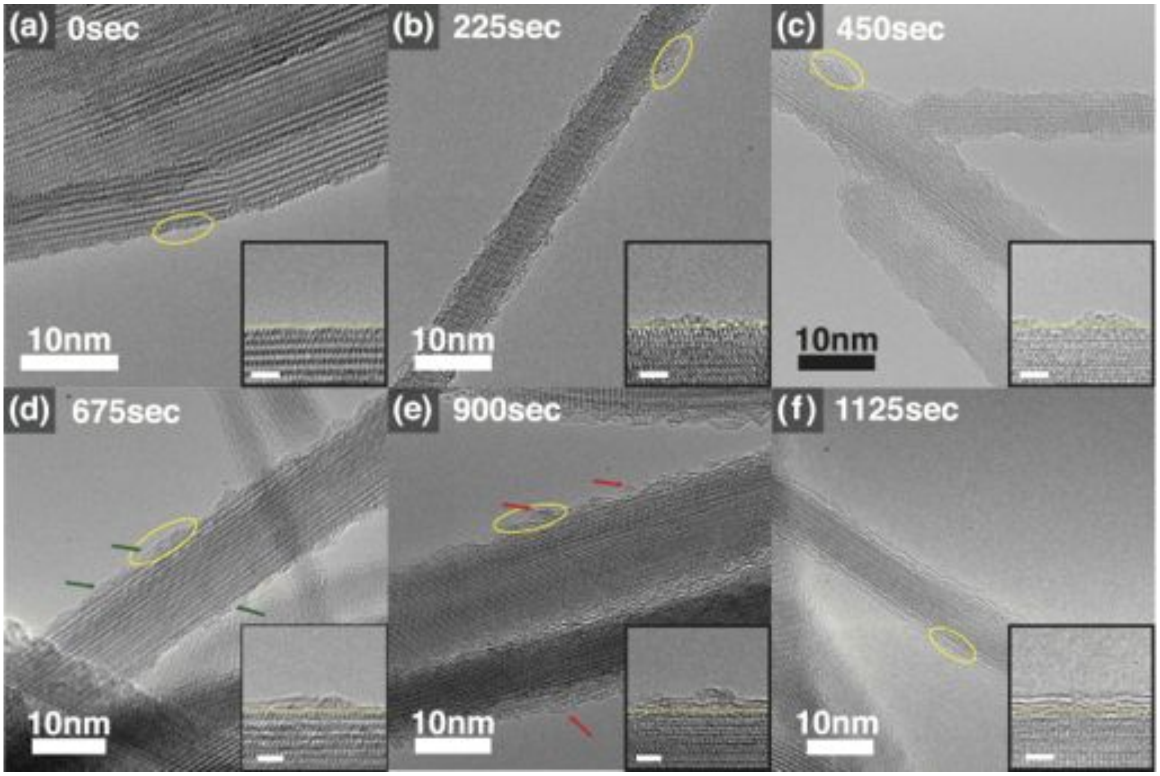

Figure 7.2: HRTEM pictures of NWAG after CVD for (a) 0 sec (b) 225 sec (c) 450 sec (d) 675 sec (e) 900 sec (f) 1125 sec. Insets magnify the area indicated by yellow ellipsoids, featuring a representative carbon deposition at each time step. Yellow lines in insets indicate the boundary between carbon deposition and the nanowire surface. Scale bars in insets are 2 nm.

to 750°C and cooled down right after that without introducing ethylene. We see that the bare nanowire before CVD shows some roughness but retains crystallinity near the surface. In Figure 7.2b after 225 sec of CVD, amorphous carbon patches are formed with lengths less than 5 nm along the wire length; due to the TEM imaging, no information is available about the patch evolution around the nanowire in the circumferential direction. Up to 675 sec, those patches grow more along the wire length than perpendicularly to the wire surface (Figures 7.2c and 7.2d). Graphitization starts to occur around 675 sec as indicated by green arrows in Figure 7.2d and accelerates after 900 sec (Figures 7.2d and 7.2e). The 900 sec CVD still leaves amorphous carbon residues seen as tiny clusters in Figure 7.2e, but by 1125 sec those are mostly incorporated into graphitic nanostructures (Figure 7.2f). Such graphitic nanostructures are $\sim 3-4$ graphene layers thick. 1350 sec or longer CVD does not grow the graphitic layer significantly beond the 1125 sec CVD (Figures

7.3a); instead, we occasionally see an amorphous carbon layer on top of the graphitic after CVD for 900 sec at 850°C, where we observe evidence of expected severe gas-phase pyrolysis of nanostructures previously synthesized, as shown in Figure 7.3b. This morphology is also seen after 1575 sec CVD. The amorphous carbon on top of the graphitic layers is clearly different from soot observed with titania NWAG ethylene. On the order of ∼ 7 nm-thick carbon soot is deposited coaxially on the titania nanowire surface after 900 sec of CVD (Figure 7.4). The soot shows traces of graphitic layers by HRTEM, and is hence not an amorphous structure, possibly because pyrolysis at 850°C converted ethylene into nanographene in gas phase. Therefore at 750°C, 100°C lower and without showing a soot deposition as seen in Figure 7.4, amorphous carbon patches are graphitized *via* titania nanowire surfaces as we will discuss. The graphitization is terminated once the graphitic nanostructures cover all the titania nanowire surfaces, supporting the catalytic activity of titania nanowires toward graphitization *via* CVD. According to this observation, it seems that the thickness of the amorphous carbon patch affects the number of layers resulting graphitic nanostructures will have.

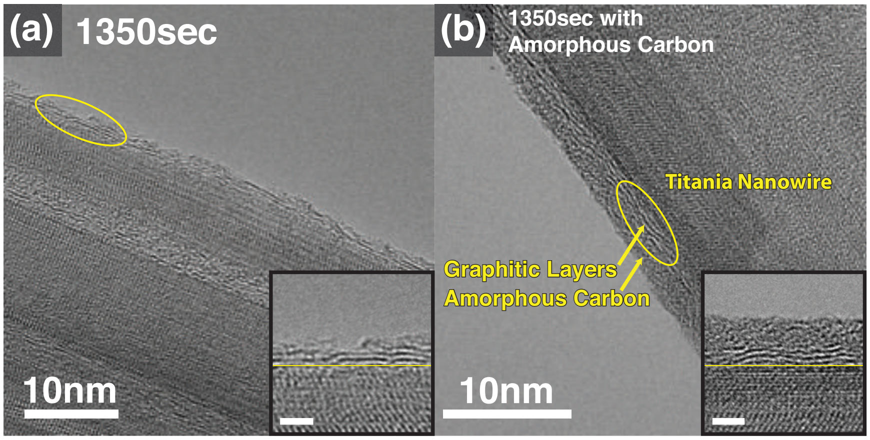

Figure 7.3: HRTEM pictures of NWAG after 750°C CVD for 1350 sec. (a) Area without amorphous carbon shows a ∼ 3 layer-thick graphitic structure similar to the sample after 1125 sec CVD, indicating no further graphitic layer. (b) On another area, amorphous carbon layer starts to deposit over graphitic layers.

In order to track the catalytic graphitization more quantitatively, Raman spectra are taken from all the samples with an excitation wavelength of 532 nm. The Raman spectra between 1000 to 1800 cm$^{-1}$ obtained from carbon materials are separated into 5 peaks as

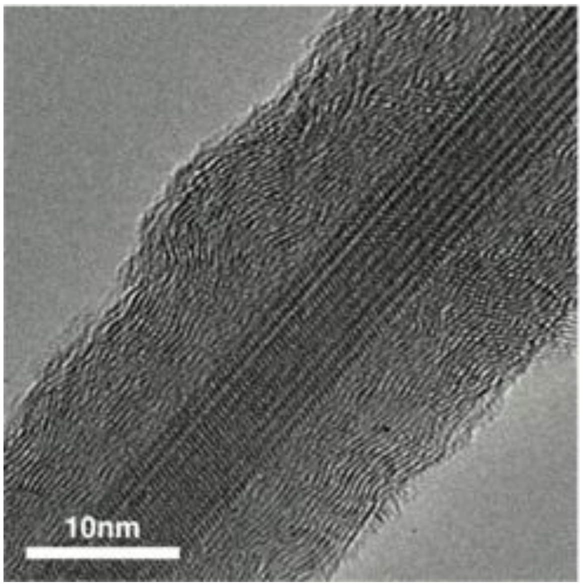

Figure 7.4: HRTEM micrograph of a titania nanowire deposited with pyrolytic graphite *via* gas phase pyrolysis of ethylene at 850°C. The thickness of deposited soot on the titania nanowire is comparable to the diameter of the nanowire itself, giving a distinctly different morphology from catalytically converted graphitic structures.

discussed in Chapter 6. Figure 7.5 shows representative Raman peak shapes after CVD for 225 to 1350 sec with each separated component. The D and G peaks are more clearly separated as the reaction time extends, indicating that the amount of amorphous carbon relative to graphitic carbon reduces. Peak area ratios are plotted in Figure 7.6(a) for D peak vs G peak (D/G) and G peak vs A peak (G/A). Samples after 225 and 450 sec CVD have peaks at the D and G peaks which could be attributed to different origins,[190] or occasional graphitization at intersections of titania nanowires as observed in Figure 7.2c. At 675 sec, the D/G ratio increases due to the initiation of graphitization, which forms tiny graphitic platelets that give rise to high D peak intensity.[189] Between 900 and 1125 sec, two significant changes are observed where the D/G ratio reduces and the G/A ratio increases about two-folds. Thereafter, both intensity ratios level off. As already shown in Figures 7.2e and 7.2f, most of the amorphous carbon residue is converted into graphitic nanostructure and the graphitic nanostructure stop growing (especially in the thickness direction) by 1125 sec. An increase in the G/A ratio is attributed to the graphitization of remaining amorphous carbon, and a decrease in the D/G ratio related to a change in the number of graphitic layer,[73] rather than improved crystallinity of graphitic nanostructure

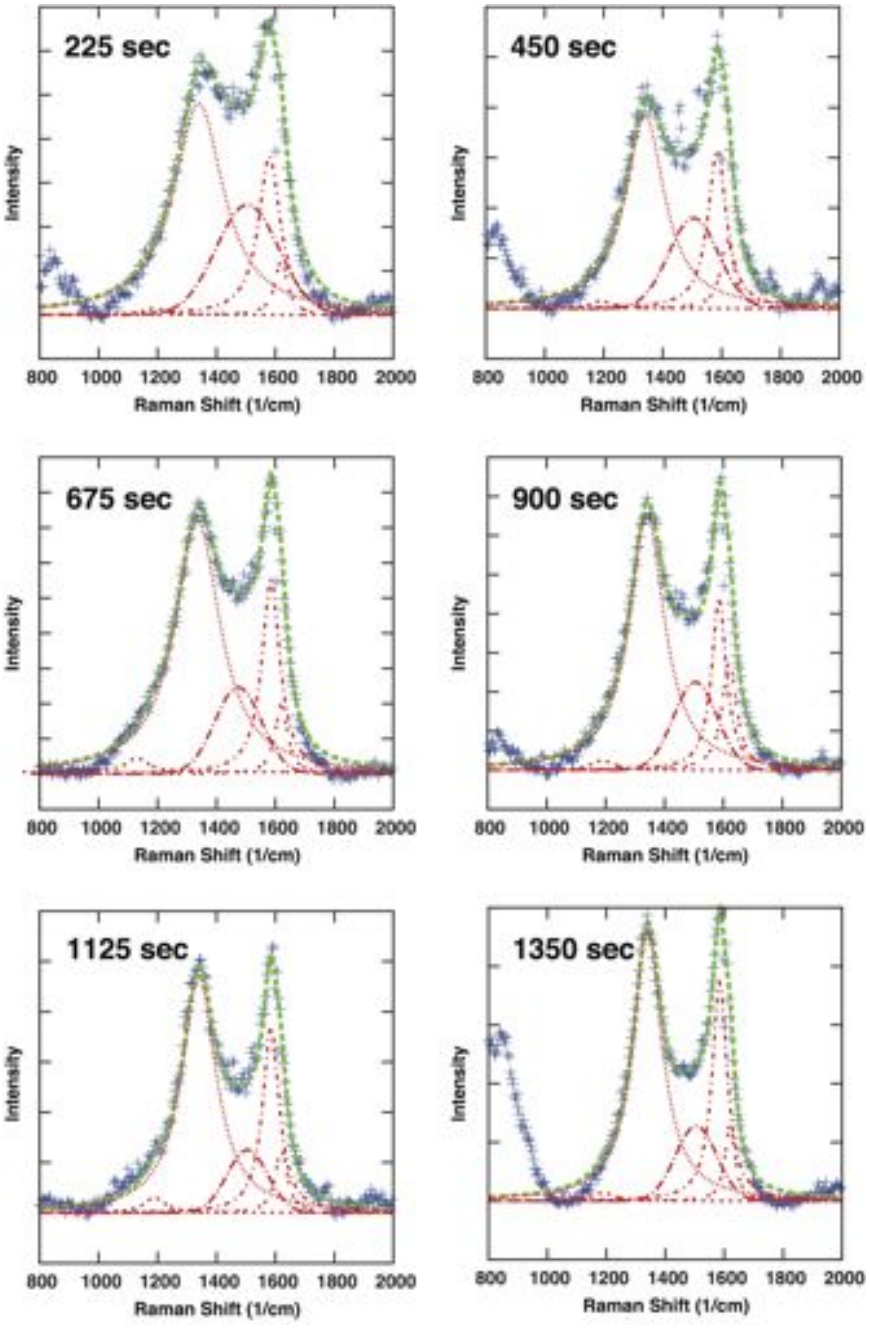

Figure 7.5: Raman spectra taken from the NWAG samples after CVD. Each spectrum raw data is shown in blue and is separated into 5 peaks from left to right in Raman shift. They correspond to the $sp^3$ component, D peak, amorphous carbon, G peak, and D' peak of graphitic carbon, and are shown by dashed red lines.

which will be discussed later.

CVD processing is also implemented to investigate the effect of thermal aging on amorphous carbon: 450 sec CVD is followed by another 450 or 900 sec thermal aging under argon flow. In Figure 7.6(b), these samples are compared with the sample just after 450 sec CVD, or 0 sec thermal aging. No clear evidence of improved graphitization with thermal aging is observed. As seen in Figure 7.2c, after 450 sec CVD, there are amorphous carbon patches separated from each other. Figure 7.6(b) indicates that those patches are not graphitized by aging. Considering the nm-scale dimensions of the amorphous carbon patches, it seems that the high surface energy of graphite[195] vs. amorphous carbon[209] prevented graphitization, although thermodynamically graphite is preferred to amorphous carbon in bulk.[210] Graphitization would occur after the amorphous carbon patches attain a certain threshold size. A single amorphous carbon patch may solely grow to reach the threshold size, or two or more patches may merge as each of them grows. The threshold size can be estimated by two methods: from the Raman spectrum or directly *via* HRTEM. From the Raman spectra in Figure 7.5, estimation of the mean graphite domain size **R** is given by a recently proposed formula.[211] This formula is more suitable than the one that

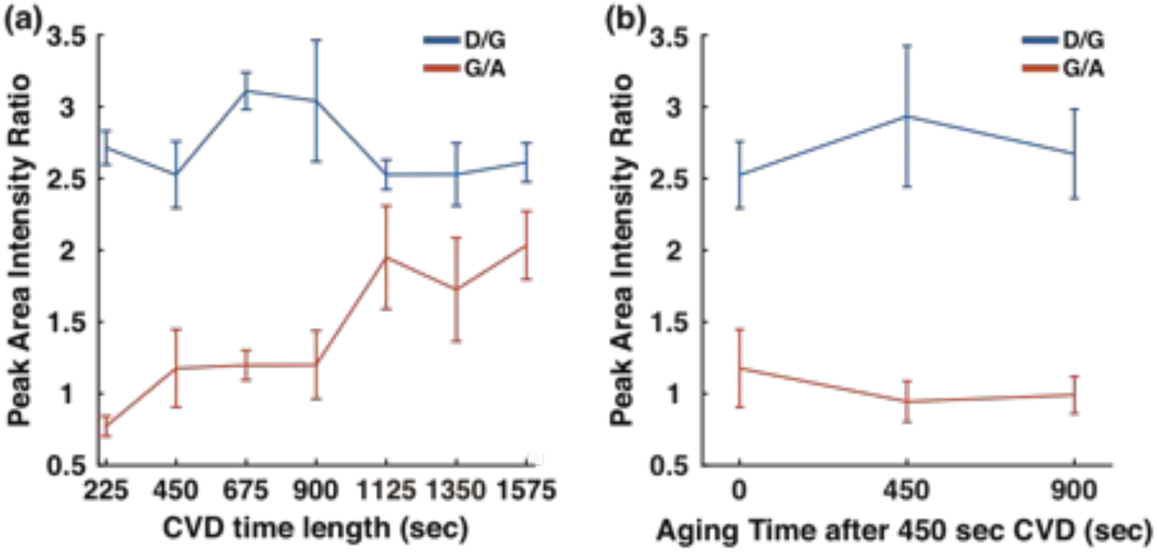

Figure 7.6: D/G and G/A peak area intensity ratios for the samples after CVD. The error bars in both (a) and (b) indicate standard deviation. (a) D/G and G/A ratios of samples after different CVD durations. (b) D/G and G/A ratios of samples after different thermal aging durations following 450 sec CVD.

was widely utilized.[212] According to the formula, **R** increases monotonically as CVD time extends until 900 sec and levels off thereafter as shown in Figure 7.7. By sampling 10 **R** using ImageJ from HRTEM micrographs of samples after each CVD duration, the same trend suggested by Raman is obtained, although The measured values are smaller than the estimation by $2-3$ nm. **R** at 675 sec CVD, where the graphitization occurs at an observable magnitude by HRTEM, is interpreted as the threshold size, and the value is around $5-7$ nm. **R** after 900 sec may suggest that the nanowire diameter hinders growth of domain size. Or, from the mechanisms of catalytic graphitization, it may also be the case that titania nanowires can catalyze graphitization but not growth of the resulting graphite domains to achieve higher crystallinity and larger domain size.

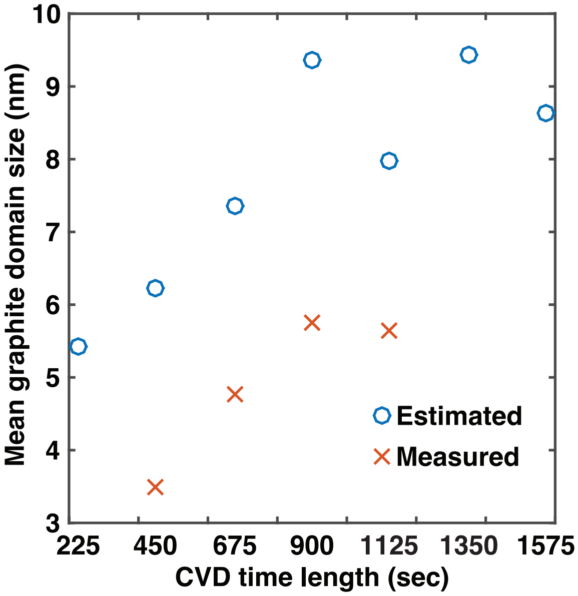

Figure 7.7: Estimated (utilizing equations from Maslova et. al.[211]) and measured (from HRTEM) mean diameters of graphite domain for each CVD time length.

Bulk electrical conductivity of titania NWAG after different time of CVD is plotted in Figure 7.8. A jump in electrical conductivity is observed after 675 sec which is greater than 4 orders of magnitude. Graphitization is initiated around 675 sec as discussed previously. Moreover, the graphitic layers are percolated through the surface of entangled titania nanowires. At this point the graphitic layers do not necessarily cover the entire surface of all the nanowires in NWAG, but a conductive path is built by the standard percolation mechanism[213]. Then, electrical conductivity is nearly leveled off at 900 sec after slight increase between 675 and 900 sec, corresponding to the completion of the conductive path associated with further graphitization. The electrical conductivity after 1125 sec CVD was 2.42 S/m, which rivals highly porous all-carbon foams.[214,215]

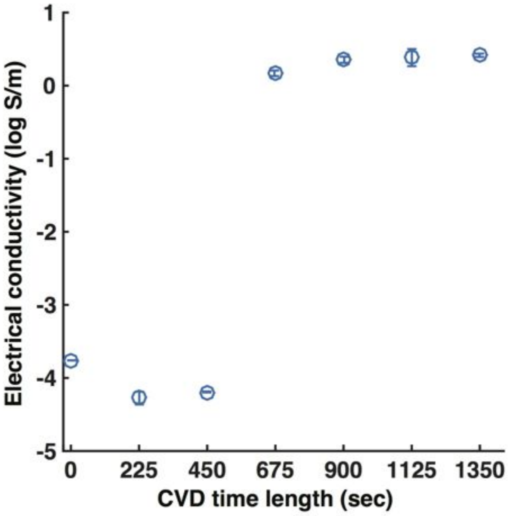

Figure 7.8: Electrical conductivity of titania NWAG after different time length of CVD durations.

By combining the HRTEM investigation, the D/G and the G/A peak ratio from Raman spectra, the estimation on the mean domain size **R**, and the bulk electrical conductivity, the mechanisms of graphitic nanostructure growth is summarized as follows: 1) amorphous carbon patches grow to attain the minimum size to be graphitized around 675 sec, causing a jump in the G/D ratio. Also the graphitic nanostructures start to percolate and establish a conductive path at this CVD duration.[213] Then, 2) Graphitization proceeds through 900 sec (electrical conductivity levels off), while leaving amorphous residue on its exterior as in Figure 7.2e. Next, 3) around 1125 sec, the number of graphitic layers increases to attain the maximum (the D/G ratio decreases and levels off thereafter), and amorphous residue is converted almost completely (the jump in the G/A ratio). Finally 4) for longer CVD than 1125 sec, amorphous carbon may occasionally deposit on top of those graphitic nanostructure as seen in Figures 7.3, ostensibly, because access to catalytically active titania nanowire surfaces are prohibited. Improved crystallinity could alternatively be the cause of the decreasing D/G ratio between 900 and 1125 sec. However, changes in crystallinity are assumed not to be as significant as the increase in the number of graphitic layers since **R** leveled off at 900 sec.

Our observations and analysis suggest that the titania nanowire surfaces serve as catalysts to facilitate graphitization which would only be realized at much higher temperatures without catalysts.[216] Among the published work regarding graphitization on metal oxides, a similar result is reported using magnesia by Rümmeli et al.[60] They also report that the number of graphitic layers did not change as a function of CVD duration. The graphitic nanostructures synthesized in this chapter are also thinner and more homogeneous in thickness than those by Rümmeli et al. The morphology of the synthesized graphitic nanostructure on the metal oxide can be affected by several factors. Our observation that amorphous carbon patches grow along the wire, rather than perpendicularly on the titania nanowire surface as observed in Figure 7.3, might be due to the rim of amorphous carbon patches on the titania nanowire surface serving as the preferred adsorption sites rather than the surface of amorphous carbon patches. The height of the initial amorphous carbon patch strongly correlates with the height of resulting graphitic nanostructures; *i.e.* the number of layers in the graphitic nanostrutures.

## 7.4 Conclusions

In this chapter, the CVD growth of a multilayer graphitic structure on titania NWAG is investigated. The catalytic conversion of amorphous carbon into a graphitic nanostructure is characterized by Cs-corrected TEM micrographs for different CVD durations. When the graphitic structure becomes $\sim 3 - 4$ layers thick at maximum, graphitization terminates, indicating that the titania nanowire surface facilitates graphitization. The conversion process of amorphous carbon patches into few layer nano-graphenes is quantitatively analyzed by Raman spectroscopy, indicating that there is a threshold diameter of $> 5$ nm for amorphous carbon patch to be graphitized on the 10 nm diameter titania NWAG surface. The graphitic layers form a continuous skin, or multi-layer concentric shell, around the nanowires and throughout the intricate three-dimensional structure of titania NWAG, improving the electronic conductivity from a standard value for titania to a value comparable to some graphitic carbon-based aerogels. These results could help inspire studies on the mechanisms of graphitic nanostructure formation on metal oxides with a variety of species and shapes. The unique carbon-metal oxide ”wire-in-shell” architecture can potentially be used as components of electrochemical devices, which can be fabricated in a facile process.

Up to this point, the CVD processes utilized here were on par with the state-of-the-art techniques that were designed specifically for MNP catalysts. However, these approaches overlook the unique photo-active properties of some metal oxide catalysts that could enhance their growth yield, and in the next chapter, photocatalysis of titania NPs and NWAG during CVD is explored as a potential next-generation technique for enhanced CNS synthesis.

# Chapter 8

# *In-situ* Photoexcitation CVD Furnace

In previous chapters, mechanisms and increased growth yield strategies of CNS growth mediated by a variety of MONPs and nanowires *via* CVD were explored. However, these studies did not explore the impact of a unique MONP property, their photo-activity, and how such a phenomenon could be utilized to facilitate enhanced CVD growth of CNTs *via* MONPs. Given the current state-of-the-art of MONP catalyzed CNT growth as context, this chapter details the challenges and progress made on the development of a feasible *in-situ* photo-excited MONP CVD approach for CNS synthesis. This chapter concludes with preliminary results of this novel MONP-based synthesis approach, and the outlook of such an approach and its importance for the production of next-generation CNS based materials is discussed.

## 8.1 Experimental Realization

So far the leading MONP-based CNS growth in terms of yield and homogeneity is the titania NP mediated growth explored in Chapter 5. To enhance the growth yield of MONP approaches to be on par with MNP based techniques, *i.e.* capable of synthesizing scalable CNT forests/arrays, the unique physical and/or chemical properties of the catalysts needs to be exploited. In terms of photocatalytic activity, titania NP catalysts have recently shown great potential for (non-CNS) activity at temperatures below $\sim 200^{\circ}$C, which makes them leading candidates for this study and low temperature photo-excited CVD in general.

A previous study by Steiner[12] was the first to propose photo-excitation of MONPs to enhance their catalytic activity in CVD. However, while this idea was interesting, there were several extant scientific and technical challenges that needed to be overcome before a facile photo-excited MONP CVD technique could become a reality. First, the design of the reactor had to be further refined. The initially proposed concept employed a newly-designed, full-quartz photoreactor furnace (FqPF) that operates as a cold-wall furnace. This was based on a design in which the entire FqPF would be placed inside a photoreactor that would omni-directionally emit ultraviolet (UV) light to excite the photocatalytic titania NPs on a substrate that is located on a bridge inside the FqPF (See Figure 8.1). However, in this setup, gas flow would not be laminar in nature and therefore the fluid-dynamic parameters would be different from the conventional CVD setup typically employed in already established techniques. Also, although the bandgap of the semiconductor decreases at high temperatures, previous reports indicate that the photocatalytic activity of those materials usually hit their maxima at around 200°C. Particularly for a system that oxidizes ethylene gas by flowing through a titania catalyst bed under UV irradiation, the maximum photocatalytic activity was achieved at around 180°C,[217] which is a much lower temperature than that employed by conventional CVD growth recipes including the ones studied in earlier chapters. Photocatalytic conversion of nitrogen monoxide to ammonia by titania showed maximum efficiency at 160°C.[218] It was also a concern that growth of CNSs could absorb much of the UV[219] so that light would eventually be blocked from exciting the MONP catalysts.

In this chapter, a relatively inexpensive and feasible technique is implemented to investigate this novel research vector, and preliminary results are discussed. While the first implementation of photoexcitation-coupled MONP catalytic CVD was achieved, a direct link between the photocatalytic activity of titania NP catalysts and the resulting CNT growth could not be inferred. However, although the initial performance goals of this first generation CVD approach were not met, there is hope that second- and third-generation photo-excited MONP based CVD techniques could build on the key findings and takeaways detailed here to achieve CNS growth yields that are comparable or outperform those of leading MNP based CVD processes.

## 8.2 Installation

The entire setup of the reactor used here is refined following a number of iterations, from the original FqPF, to the current setup that uses an accessory photoreactor furnace(APF) that is appended on one end of a conventional tube furnace setup. Accordingly, the UV source and the access to UV radiation for the sample are also altered to work with the revised setup.

### 8.2.1 Full-quartz Photoreactor Furnace (FqPF)

As the first attempt, the setup previously proposed by Steiner is completed, and the key components are shown in Figure 8.1. The FqPF is manufactured by G Finkenbeiner Inc. Scientific, MA, and is comprised of two pieces, a top and bottom part. Those dimensions are sized to fit into the UV photoreactor (Rayonet RPR 200). The top part has a gas inlet, a gas outlet, and a window that allows the infrared pyrometer (two-color pyrometer Newport IR2) to measure the temperature of the substrate where the catalysts reside on a substrate. The gas flow comes through the gas inlet, and the outlet facing the inlet is used as an emergency vent. The pyrometer is located above the window so that the temperature of the reaction can be measured in a non-contact way. The bottom part has a bridge to fix a heat pad and a gas outlet. The heat pad is inserted into the bridge, and heat generated from the pad is transferred to the sample sitting on the bridge inside the apparatus. Tubing to the gas inlets and outlet are made of stainless steel piping that is designed to fit in the Rayonet photoreactor. 253.7 nm of UV is irradiated from the bulbs.

The next step entails the completion of the electric circuit and testing of the heat pad to run at the temperatures of interest under gas flow. A $MoSi_2$ heat pad cartridge was inserted into the bridge. Silicon grease for vacuum apparatus was applied to fill in the gap between the two pieces of the FqPF. The simulated gas flow was only argon, but the flow rate was equal to the total flow rate of argon, hydrogen, and ethylene in a conventional CVD recipe (such as was for recipe E of titania NP catalyst work). 10 min after turning the heat pad on, the pyrometer measured around 850°C. Then, the apparatus was kept at temperature for $\sim 60$ min, which was $4\times$ as long as the duration of a standard CVD recipe. Meanwhile,

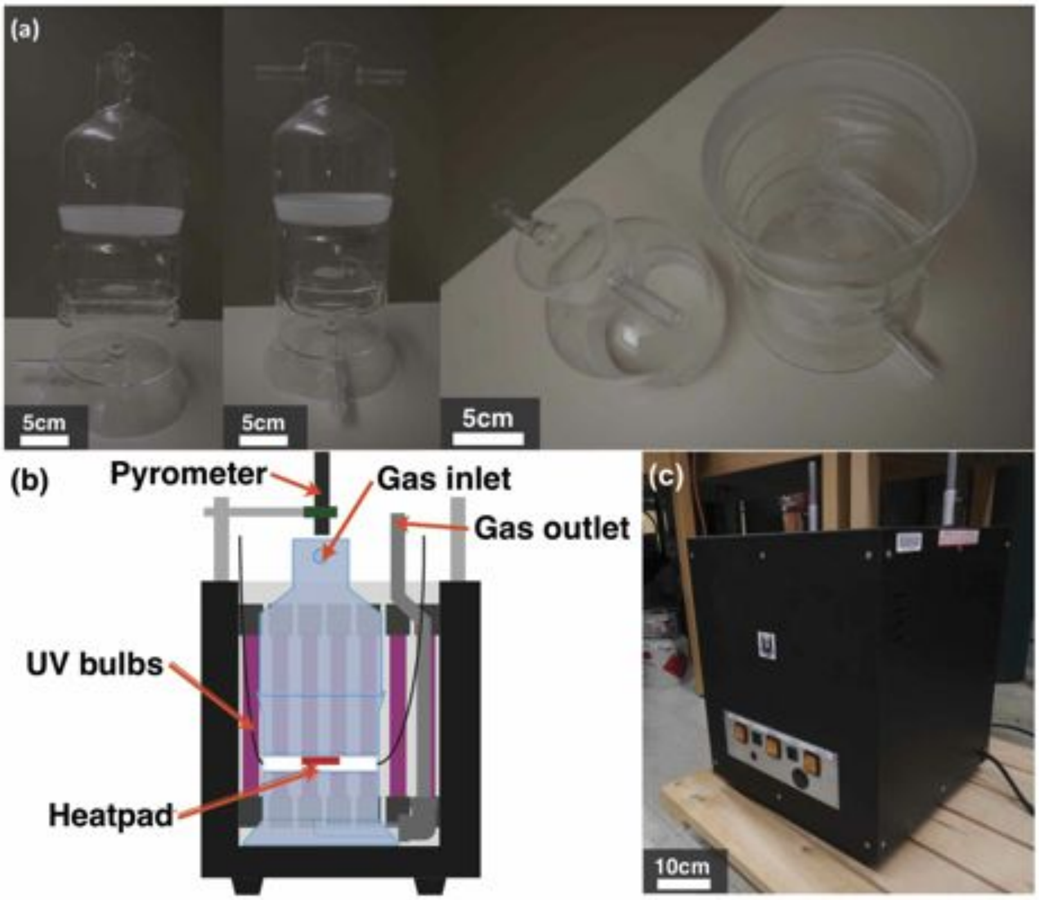

Figure 8.1: Pictures of the FqPF built to be a cold-wall CVD furnace. Scale bars are approximate. (a) The FqPF from different views. (b) A sketch of the FqPT apparatus set in the photoreactor. (c) Rayonet photoreactor tested with the apparatus.

maximum temperature readings were recorded, hitting around 880°C during the test run before leveling off. Since no incidents such as grease burning, top parts popping off, or gas flow leakage from the gap between two pieces were observed, safety was positively assessed for the next steps. With this set up, CVD growth was implemented with and without the photoreactor using ethylene as carbon feedstock (Figure 8.2). However, no apparent growth was observed with all the samples tested. The only observed change on samples was the blackening of the titania NWAG sample, which was discussed as due to the depletion of oxygen in Chapter 7 (Figure 8.2d). A shorter wavelength of UV was also tested (184.9 nm), but ethylene was found to decompose in gas phase and converted to spherical microparticles inside the apparatus ($\sim 1\ \mu$m in diameter, Figure 8.2e). After further testing, the pyrometer was found to experience significant errors in the estimated temperatures, where fluctuations of 10s of °C could be exhibited with a slight change in pyrometer position. It was also discovered that the $MoSi_2$ heatpad was not powerful enough to elevate the temperature of the reaction spot, even when fully powered without a temperature controller, only heating the reaction zone up to $\sim$ 400°C.

Other heaters were therefore tested (MHI Spiral Microheater, MC-MP-1900-350-IPL, MC-GAXP-30 and MC-GAXP-130). This time, a thermocouple placed between two metal plates was used instead of the pyrometer to directly measure the temperature above the bridge. The brittleness of MC-MP-1900-350-IPL prevented practical operation (after its first test run, it was mechanically broken upon attempted removal). For MC-GAXP-30 and MC-GAXP-130, the temperature-wattage relationships were measured using a variable power source and revealed that MC-GAXP-130 was the best choice. After sizing the legs, MC-GAXP-130 was mounted on a machined insulator cartridge to fit stably inside the bridge (Figure 8.3c). CVD growth was attempted with the MC-GAXP-130 for several times at around 750°C, with multiple samples, CVD recipes, and the photoreactor on and off. However, we were unable to observe growth of CNTs. Abandoning the FqPF concept, we chose another strategy as explained in the following subsection. Figure 8.3 was taken during those test-runs including the photoreactor in action.

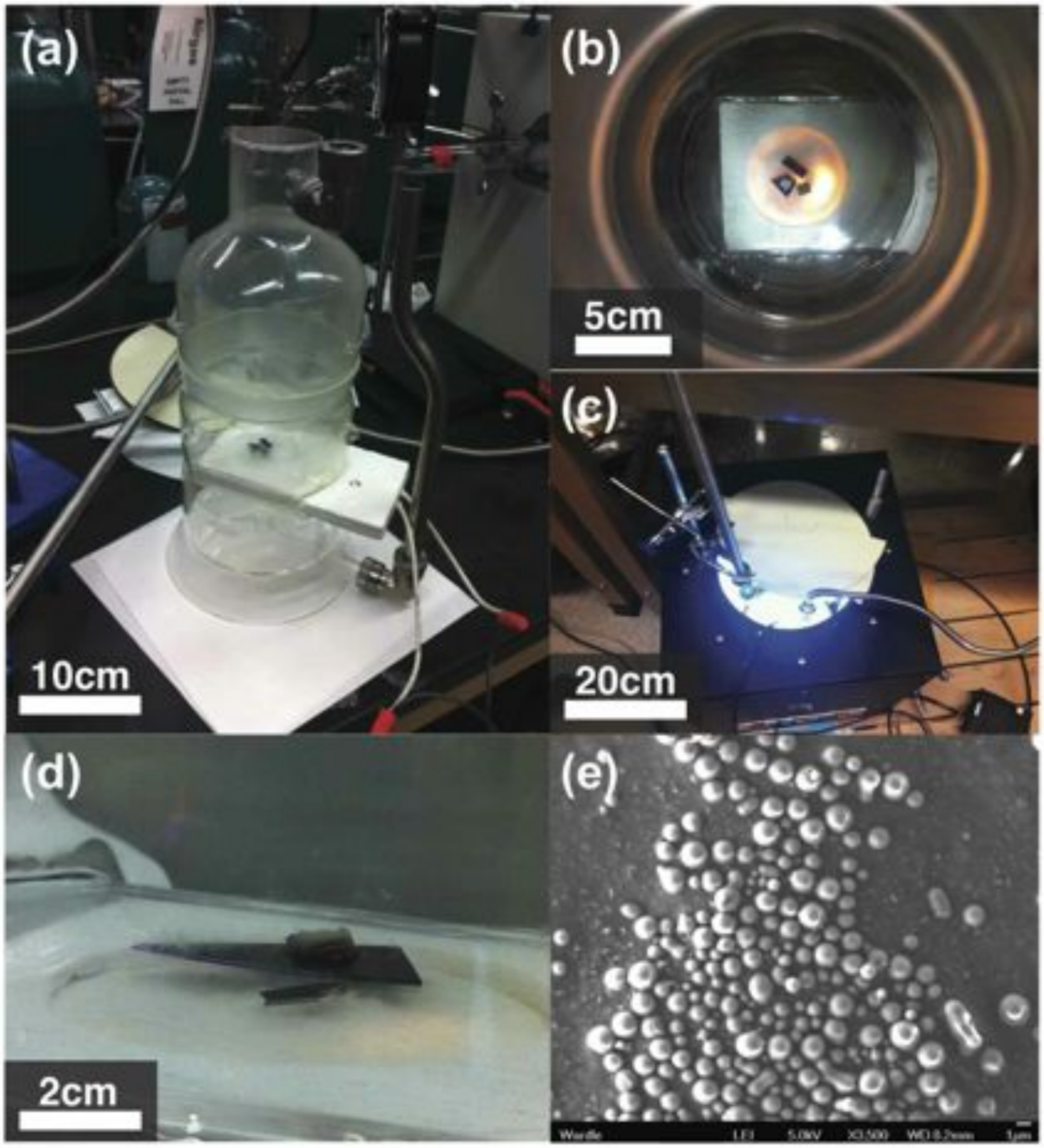

Figure 8.2: Testing scenes of the FqPF with the $MoSi_2$ heatpad. (a) An overview of the apparatus with samples and the heatpad loaded. (b) The reaction zone seen from the top during a test run without the photoreactor. (c) Testing with the photoreactor. (d) Titania NWAG sample placed on silica substrate. During the test run, the NWAG turned black gradually from its bottom to top. (e) SEM image of spherical microparticles derived from ethylene deposited inside the apparatus after testing in 184.7 nm UV.

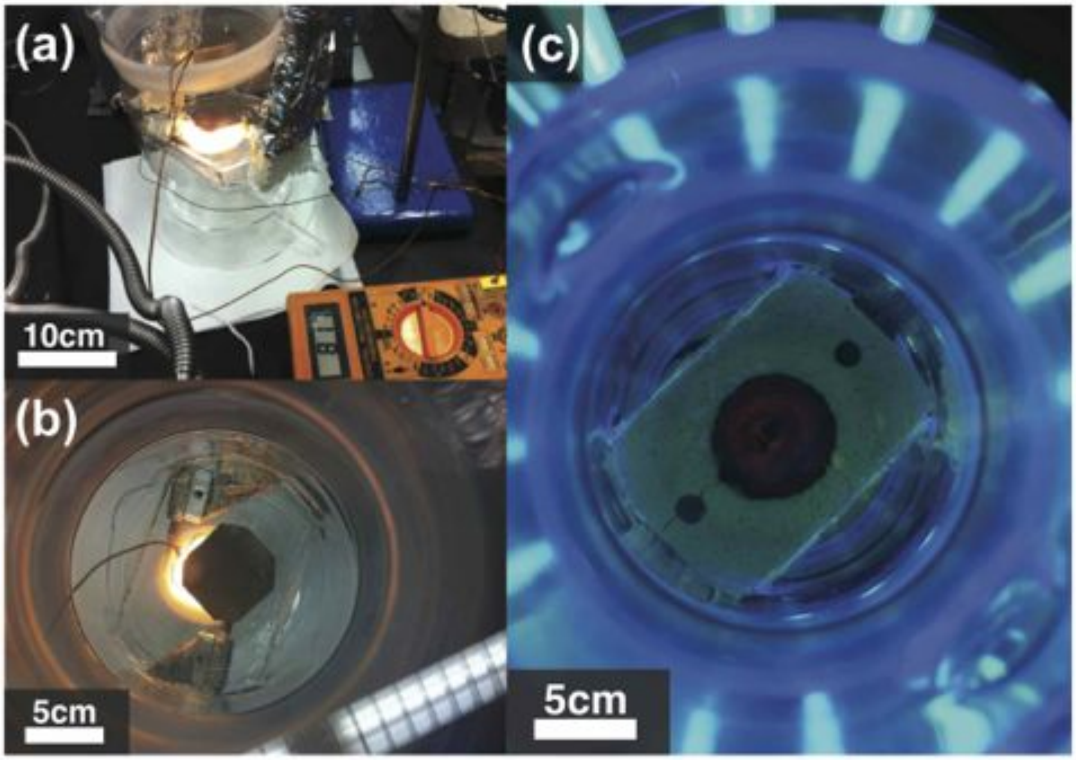

Figure 8.3: Testing scenes of the FqPF with MC-MP-1900-350-IPL and MC-GAXP-130. (a) An overview of testing setup. (b) MC-MP-1900-350-IPL microheater inserted inside the bridge. The thermocouple was located on the bridge to measure the temperature directly. (c) Photocatalysis-assisted CVD testing with MC-GAXP-130 microheater.

### 8.2.2 Accessory Photoreactor Furnace (APF)

To replace the FqPF, a smaller APF was built. The exhaust end of the quartz tube was extended from the conventional minimite tube furnace and enclosed in the APF. Therefore the geometry of the furnace was the same as a conventional hot-wall quartz tube furnace commonly used in CNT growth. This furnace can let light enter inside to photocatalytcally activate the catalysts on the substrate from the multiple UV sources that were tested. The details of the fundamental setup of the APF is shown in Figure 8.4. The body of the furnace was built with insulator blocks. The furnace was supported on an adjustable jack so that the extended exhaust end of the quartz tube ran through the furnace body. Inside the furnace, a MC-GAXP-130 microheater was situated to heat up the quartz tube from its bottom. The lid of the furnace was also made of the same insulating material as the furnace with a

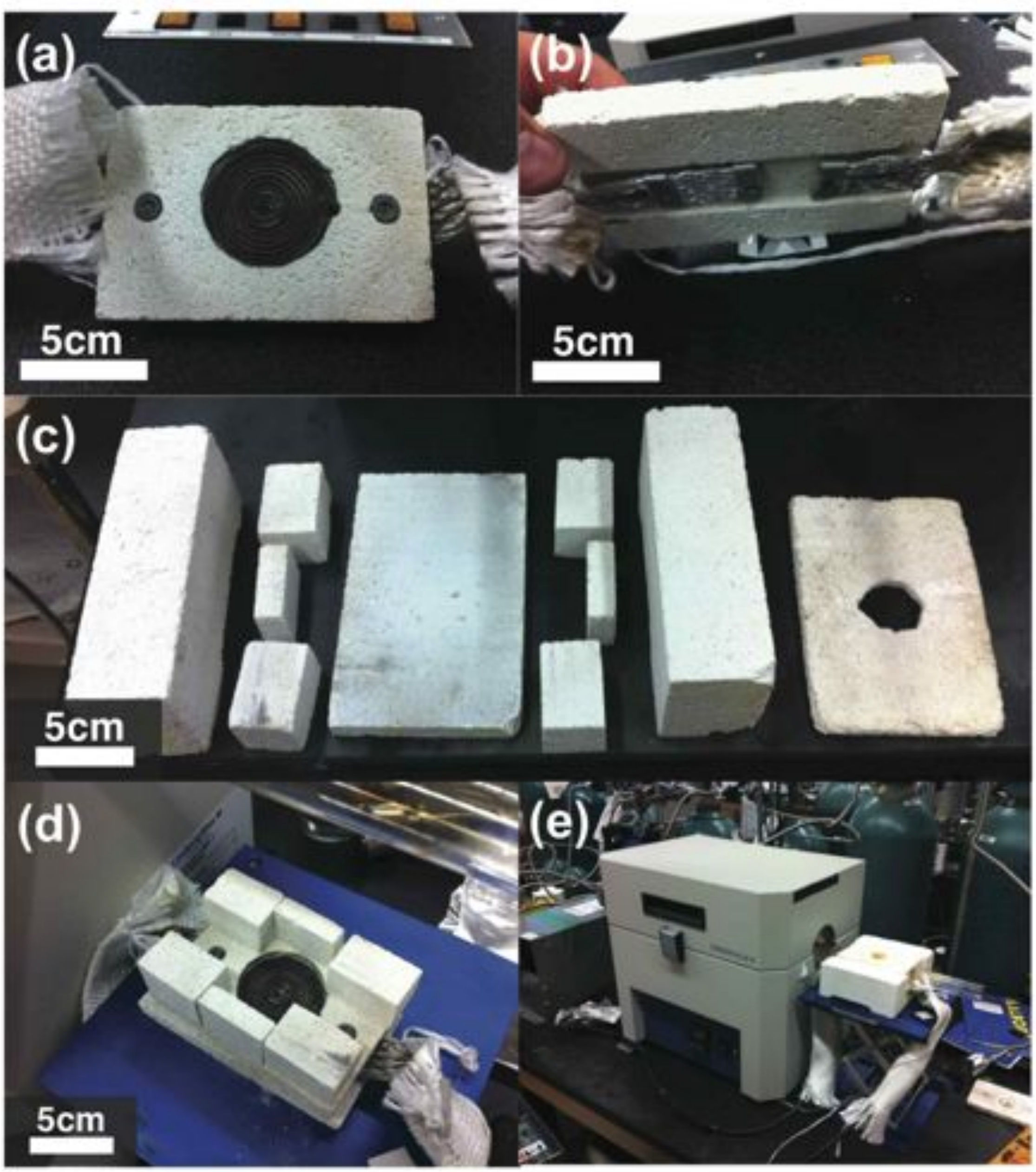

Figure 8.4: The detail of APF. (a) A MC-GAXP-130 microheater mounted on an insulator cartridge. Two braided metal wires shrouded with alumina fiber cloth connected to the AC transformer. (b) The rear view of (a). (c) The building blocks of the furnace body before assembly. The right most piece is the lid with a hole. (d) The assembled furnace supported on a jack. (e) Heating test with the APF.

window of $\sim$ 1” diameter to simultaneously insulate the heat and let the light shine onto the sample. The conventional tube furnace worked as a ‘preheater ’so that the carbon feedstock molecules were activated before arriving at the reaction zone of the accessary furnace. With this APF setup, CVD without UV irradiation was first implemented to confirm its functionality. Growth from standard Fe NP catalysts on alumina-sputtered silica substrate was observed as shown in Figure 8.5, using ethylene as a carbon feedstock, 750°C as the preheater temperature, and 750°C as the APF temperature (thermocouple reading outside the quartz tube). The growth was sparse and did not form a CNT forest as usually seen with Fe NP catalysts.

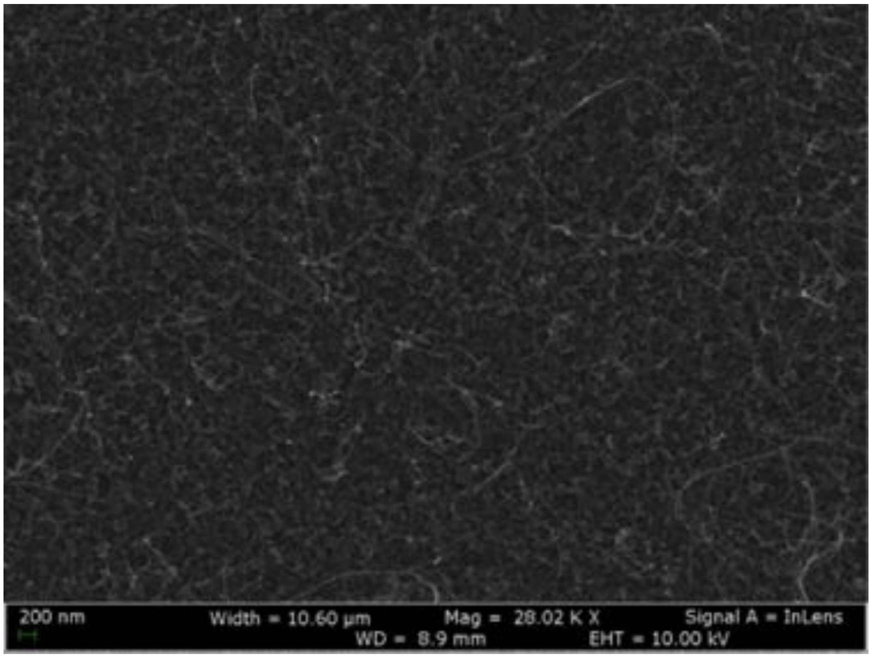

Figure 8.5: CNT growth from iron NPs on alumina-sputtered silica substrate using the APF without UV irradiation for functionality confirmation.

After confirming growth with the APF, growth with and without irradiation was compared. First, the Rayonet UV photoreactor was tested with this APF. The entire APF and the supporting jack was encased in the photoreactor that was tilted by 90°. Then a 365 nm UV handy light was used as the light source. However, both were unsuccessful to obtain results that were distinguishable between the cases of with and without irradiation. Figure 8.6 presents setup used for those tests.

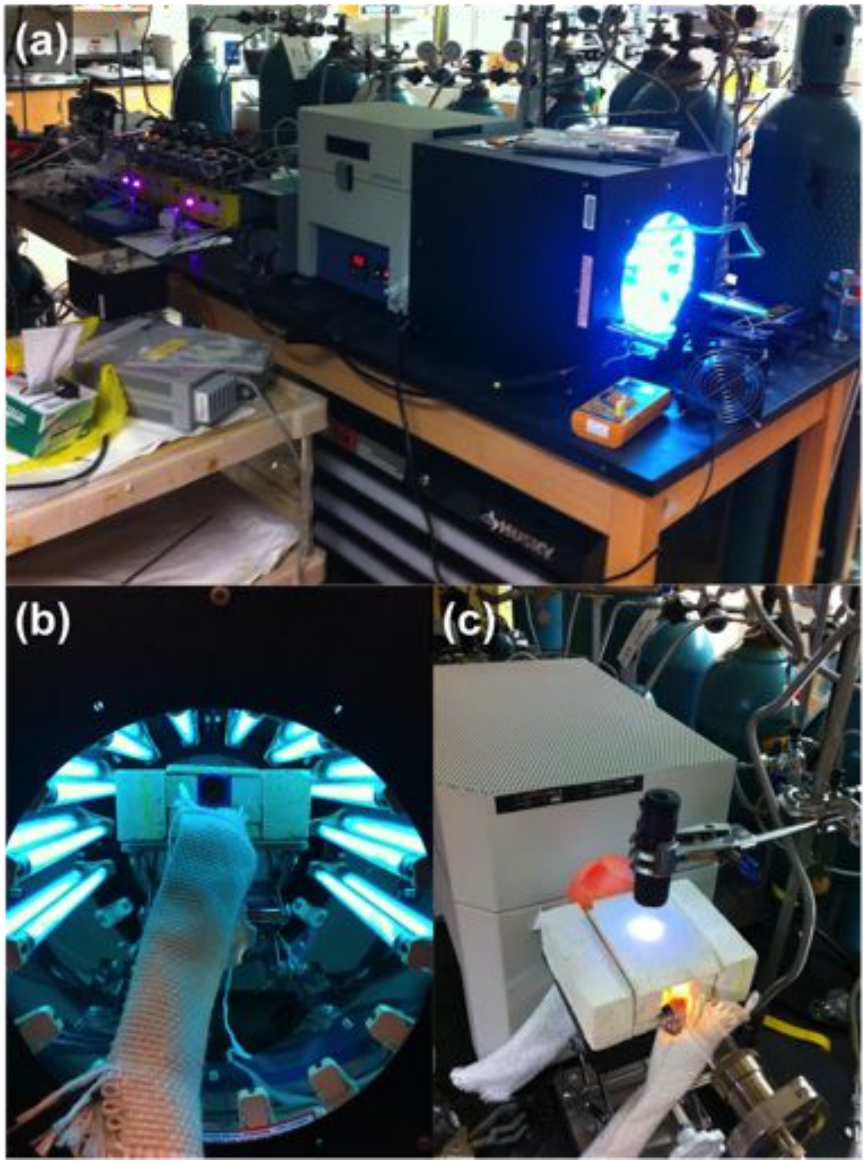

Figure 8.6: UV-assisted CVD testing. (a) With Rayonet UV photoreactor. The photoreactor was tilted 90° so that the entire APF was located inside. (b) Inside the photoreactor. Half of the UV bulbs were removed to create space for the jack on which the APF is supported. (c) UV handy-light shining on a sample during CVD.

## 8.3 Blu-ray Laser Photoreactor Furnace (BrLPF)

The final setup tested in this work was the use of a blu-ray laser diode as a light source. It was known from titania NWAG work shown in Figure 8.2d that oxygen in titania would start depleting at a temperature as low as 400°C to turn from white to black, indicating absorption under visible light range. Moreover, the intensity of the light source would be higher, and the thermal insulation improved with a smaller diameter of the hole on the lid. As mentioned in the previous section, previously temperature readings were from the outside the quartz furnace, which would be different from that inside. Further improvements on insulation were considered by making the lid insulator thicker, binding the building blocks of the furnace body using black cement, and adding insulation on both sides of the APF where the quartz tube passed through (See Figure 8.7). This configuration is referred to as ‘Blu-ray Laser Photoreactor Furnace (BrLPF)’ from here on.

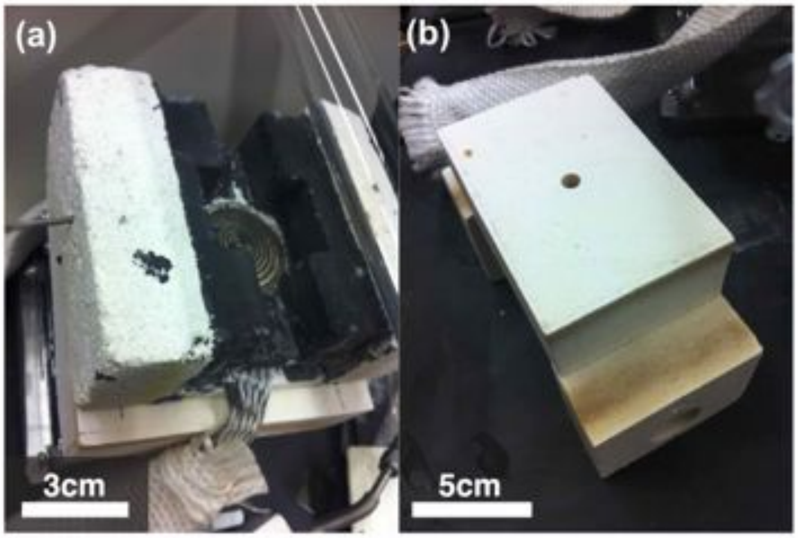

Figure 8.7: Improved insulation applied to the APF to form the BrLPF configuration. (a) Black cement binding the insulationblocks together. (b) The thicker lid insulator and additional insulators. The lid has a small hole $\sim$ 5 mm in diameter, and the additional insulators have an $\sim$ 25 mm hole for the quartz tube.

Electronics were also newly built to control the heater temperature and the blu-ray laser semi-automatically. A schematic illustration of the electronics is shown in Figure 8.8. The AC transformer and SCR controller (MHI ST9001) were the same as those used in the setup introduced earlier in this chapter.

### 8.3.1 Laser Unit

The laser unit was powered through an AC/DC adaptor (GX-0518). Of the two power inputs, 5V-2A output is used to drive the blu-ray laser diode (SONY SLD 3132VF), and

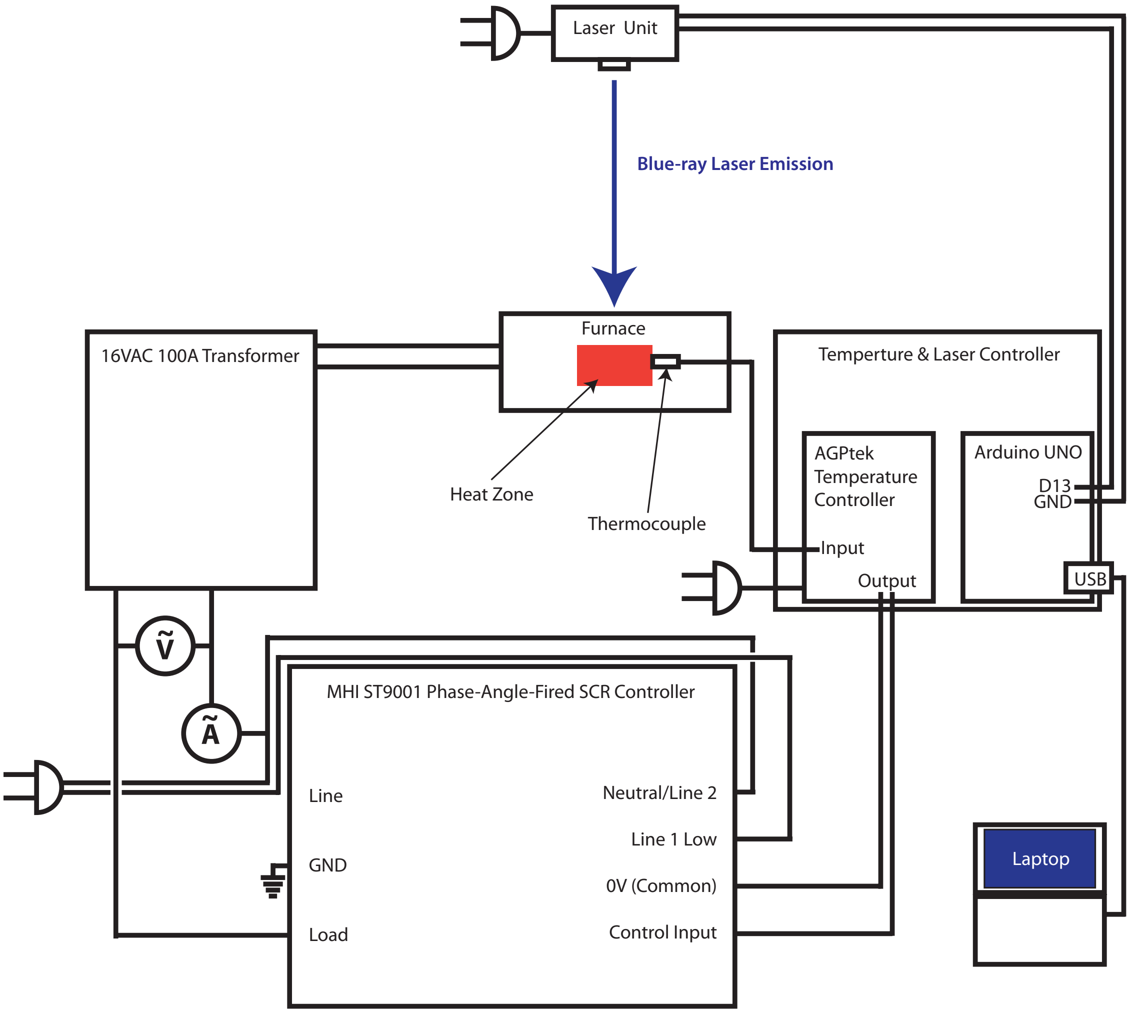

Figure 8.8: A schematic illustration of the electronics for controlling the BrLPF setup.

12V-2A output is used to turn on the mini-fan that prevents the laser diode from overheating by the heat generated by the laser diode itself. The diode emits 405 nm blu-ray laser. A driver circuit is built to safely power the laser diode, while the controlled amperage consumed by the laser diode is observed by a galvanometer. The collimator lens was fixed so that the laser makes a spot with a 2-mm diameter at a distance of 125-150 mm (5-6”) away from the substrate. See Figure 8.9 for more information.

### 8.3.2 Temperature and Laser Controller

A controller for the furnace temperature and the laser unit was also built in a single case (Figure 8.10). Inside the case is an AGPtek K-Type SNR PID Temperature Controller

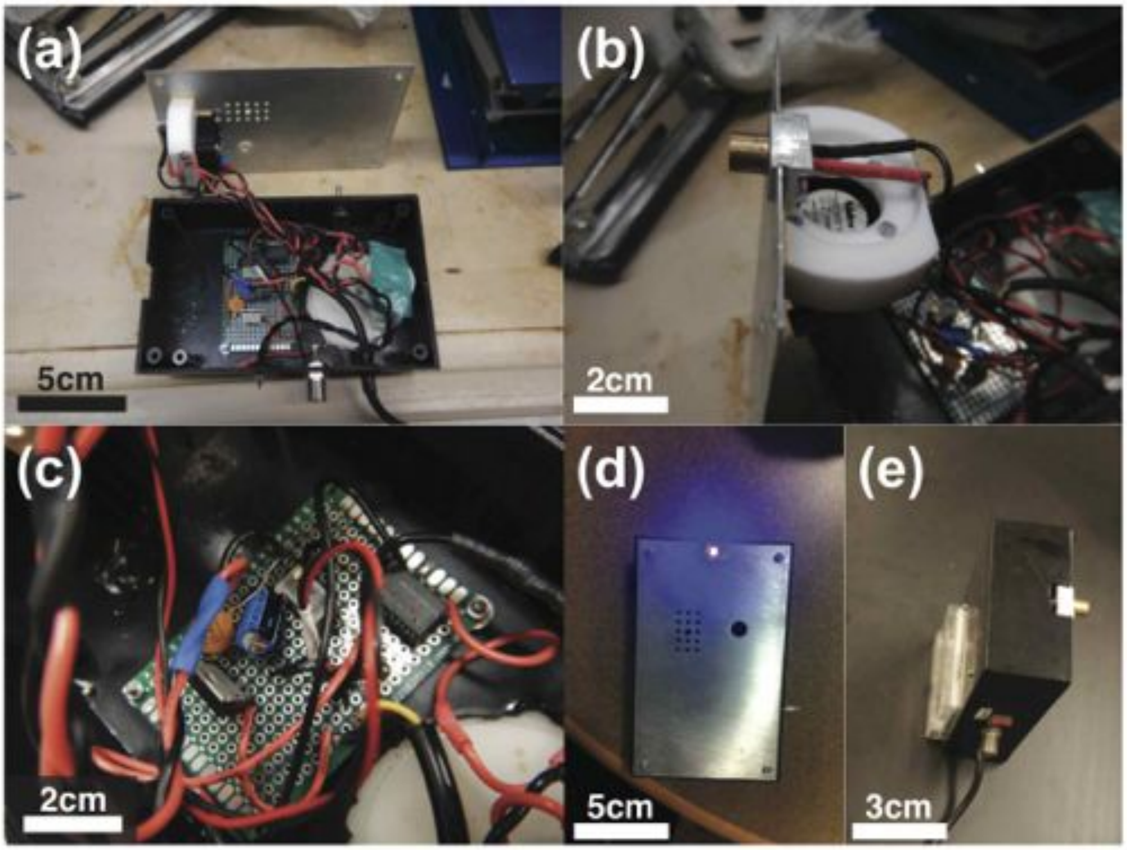

Figure 8.9: The laser unit for the BrLPF. (a) Overview of the unit interior. The blu-ray laser diode is mounted on the aluminum metal cover with a mini cooling fan directly behind it. The body of the case has a galvanometer and a driver circuit for the blu-ray laser diode. (b) Close up on the laser diode. The diode is in contact with the metal cover that also helps dissipate heat generated by the diode. The mini cooling fan is set upright to the cover *via* a Teflon pedestal. A collimator lens is encased in the brass column. (c) Close up of the circuit board. A driver circuit is embedded to prevent the laser diode from damage due to voltage surges and over powering. The relay switch (a black box on the right side of the picture) completes the circuit. (d) Laser emission. A toggle switch on the right wall of the unit turns laser emission on and off. (e) The galvanometer mounted on the back can show the current consumed by the laser diode. The red switch changes from emission mode to current observation mode.

and Arduino UNO. The temperature controller was powered directly from the wall plug, and the Arduino UNO was powered by USB cable connected to a laptop computer. A thermocouple sends signals that are amplified by an operational amplifier (AD595-AQ) to the temperature controller input so that the temperature controller in turn outputs voltage to command the SCR controller and control power sent to the microheater. This output

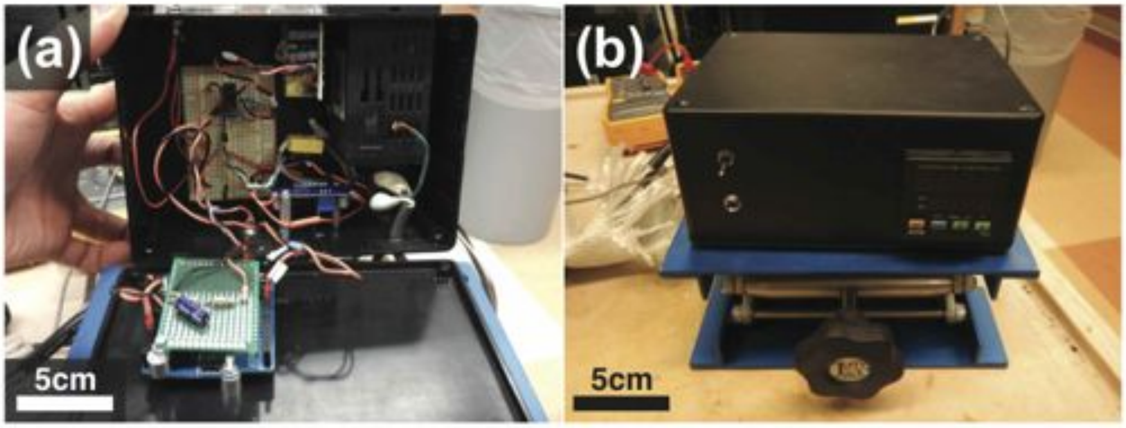

Figure 8.10: Temperature and laser controller. (a) Inside Overview. The operational amplifier is mounted on the breadboard. The Arduino UNO board is set on the base of the case. (b) Outside overview. The toggle switch turns the entire BrLPF setup on.

voltage from the temperature controller is also delivered to an Arduino UNO so that the Arduino UNO outputs voltage to turn on the circuit in the laser unit *via* a relay switch. The PID temperature controller was adjusted but the temperature oscillates around the set point ±10°C. Figure 8.11 shows the BrLPF setup. The toggle switch on the front of the temperature and laser controller turns on/off the entire system.

Figure 8.11: The BrLPF setup running CVD growth.

## 8.4 Preliminary Results

This BrLPF setup was used to compare the results of CVD with and without the blu-ray laser. Titania NP catalysts used in Chapter 5 and titania NWAG used in Chapter 6 were processed with a standard CVD recipe using ethylene as a carbon feedstock. The BrLPF is not controlled by the same software that our group uses to turn on/off the mass-flow controllers, so the temperatures in the preheater (the Minimite tube furnace in Figure 8.11) and the BrLPF do not ramp up at the same rate. Normally the preheater warms up faster, so that the automated process code sent from the software has to be paused until the BrLPF reaches the desired temperature. Once both furnaces arrive at the set point, the process code resumes to start the CVD reaction.

The results are shown in Figures 8.12 and 8.13. For CVD with titania NP catalysts on silica substrate, the preheater and the BrLPF were set to 750°C. First of all, the fact that growth occurred with titania NP catalysts on silica substrate, which would be more difficult than growing CNTs from standard Fe NP catalysts, is already a great improvement. This could be attributed to improved insulation. The growth morphology was identical to that of recipe E in Chapter 5, which is consistent because recipe E was the basis for the recipe used. The difference in turning on/off the blu-ray laser, however, was not clearly observed. For titania NWAG, the same recipe as the 450-sec CVD in Chapter 7 was tested. Both with and without blu-ray laser tests showed an improved graphitization for 450-sec CVD, presumably due to preheating. Titania nanowires in both samples exhibited up to three layers of graphene-like CNS. The results without blu-ray laser are similar to those observed for the 900-sec CVD in Chapter 7. The results with the blu-ray laser appear to be as graphitized as those of the 1125 sec CVD in Chapter 7, which indicates more graphitization than without blu-ray. These observed differences in degree of graphitization as a result of blu-ray laser irradiation, however, require more in-depth investigations and quantification.

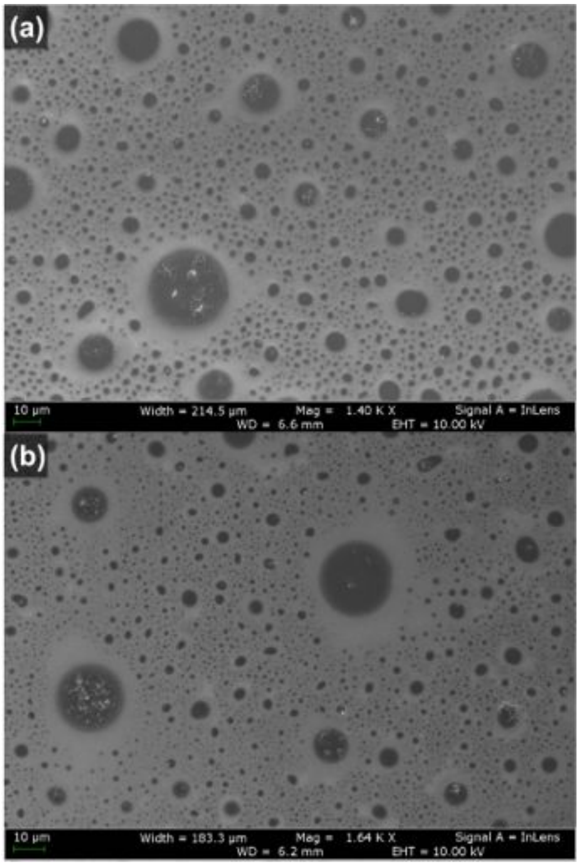

Figure 8.12: Growth obtained using the BrLPF with titania NP catalysts on silica substrate. Except for the furnace setup, the same recipe was used as the recipe E in Chapter 5. (a) Without blu-ray laser. (b) With blu-ray laser.

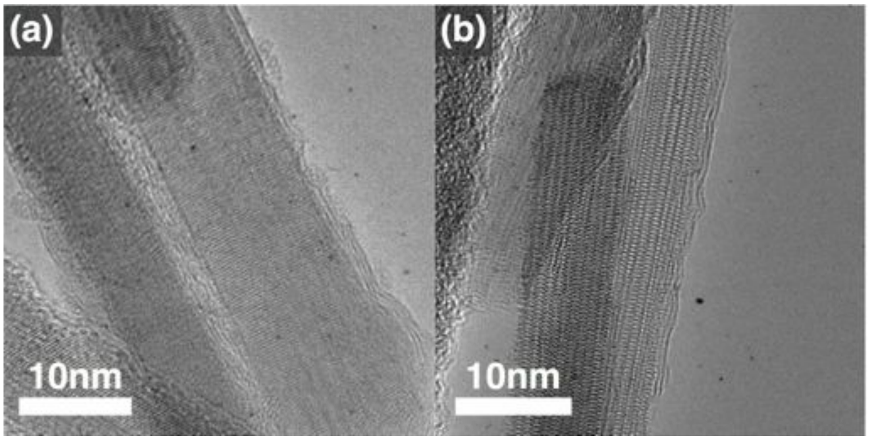

Figure 8.13: Graphitic layers synthesized on titania nanowires using the BrLPF. (a) Without blu-ray laser. In addition to the graphitic layers, amorphous carbon residue similar to that of the 900 sec 750°C CVD in Chapter 7 is observed. (b) With blu-ray laser. Well crystallized graphitic layers are observed.

## 8.5 Conclusions

The synergetic effect between photocatalytic excitation and CNT growth from MONP catalysts was investigated *via* a newly built BrLPF setup utilizing titania NPs and NWAG. Although the furnace was successfully built and tested, the effect of the photocatalytic activity of MONPs on their resulting CNT growth remains unclear for the model titania NPs system. Using the titania NWAG samples (from Chapter 7), the effect on graphitization was also studied. However, this effect is currently also inconclusive, and was observed to not be as significant as the effect of preheating. There is is additional parameter space regarding the BrLPF setup that could be further investigated: shorter wavelengths of laser, laser intensity, lower temperatures in the BrLPF etc. However, the preliminary results indicate that the photocatalytic activity of MONPs may not directly effect the growth of CNS, and that more in-depth future studies are required to evaluate this potential MONP growth yield enhancement mechanism for CNTs.

In the next chapter, the findings and contributions of this dissertation are outlined, and future work that could enable further enhancement of the CNT growth yield and facilitate more precise investigation and modeling of the CNT growth mechanisms of MONPs and nanowires is recommended.

# Chapter 9

# Conclusions and Recommendation for Future Work

This thesis has investigated the synthesis of CNS *via* CVD from metal oxide catalysts. This work culminated in the identification of growth mechanism features of CNSs using those metal oxide catalysts, quantification of the impact of CVD parameters and their effect on the CNS growth yield and heterogeneity, the development of relationships among properties of MONPs and the resulting CNS morphology, and application of this knowledge to unexplored systems: metal-oxide nanowires as substrates and synergistic effects of photocatalysis on CNS synthesis.

## 9.1 Conclusions

Significant advances were realized toward both objectives introduced in Chapter 3: growth yield and mechanisms investigations. The major contributions of this dissertation are summarized as follows:

- Both CNTs and CNFs were observed to grow by using zirconia NP catalysts, based on their shapes and sizes. The growth morphologies indicate that the mechanisms zirconia NPs employ are surface-bound, consistent with the significantly high melting point and low diffusivity of carbon. It was an unexpected finding that zirconia

NPs larger than 10 nm in diameter first synthesize fullerene-like appendages in the vicinity of a corner prior to CNT growth, which agrees with the previously published sketch of growth mechanisms with inert MONPs in terms of the significance of the corner of the NP catalysts. Considering the process of forming an appendage would take an extra step, and applying the knowledge that zirconia can graphitize the surrounding amorphous carbon, zirconia NPs were impregnated into highly-porous amorphous carbon substrates. This type of sample successfully demonstrated enhanced growth of CNTs and CNFs from these NP catalysts.

- Titania NPs have become a model system not only to explore the parametric space of CVD growth conditions, but also to provide a quantitative understanding to MONP catalyst research. Different carbon feedstock species, substrates, and temperatures investigated to enhance the growth yield from titania NPs. This parametric study arrived at a homogeneous and relatively dense growth of CNTs and CNFs using acetylene gas over an alumina substrate at 850°C.

- The results of this relatively dense growth from titania NPs were further investigated to evaluate the relative catalytic activity compared to Fe NPs. Although the process was somewhat simplified, being scaled by the number of acetylene molecules converted into carbon atoms, the catalytic activity of titania NPs was approximately an order of magnitude lower than that of Fe NPs. This figure is in agreement with the qualitative impressions empirically accumulated through this thesis.

- Another accomplishment with the study of the titania NP catalysts was to propose a lift-off model for graphitic layers formed over the titania NP catalysts. Characterization by HRTEM showed that the CNTs and CNFs were only in contact with titania NP catalysts on the NP corners and without additional carbon deposits. The strain energy exerted on synthesized graphitic layers bent over the corner was proposed as the causes of lift-off from titania NPs. Although the model also contains simplifications, the obtained results suggest that the strain energy could potentially be the cause of lift-off of the graphitic layer. This calculation does not only provide one of the earliest quantitative details on titania NP-mediated growth, but may also be leveraged to study growth with other MONPs.

- Multiple metal oxide species were investigated to characterize the influence of their different physical and chemical properties on growth morphologies. Chromia generated very unique morphologies of CNS that inspired additional research into the saturation-precipitation processes even at solid crystal states. Vanadia also yielded interesting CNS morphologies showing that the surface-bound process is able to build an interface between the non-basal plane of graphite and the NP surface. Since vanadia indicated that its mechanisms of CNS growth unlikely involve the bulk of the NPs, and rather surface-bound mechanisms are expected, we propose a trend of growth mechanisms in the order seen on the Periodic Table from titania (most stable against reduction and surface-bound mechanisms) to Fe (reduced to metal and saturation-precipitation mechanisms). This systematic understanding on growth mechanisms lead to a new high-level view of the active NP catalyst phases of other metal oxide NPs during CVD.

- Ceria did not form any graphitic layers and was only very occasionally decorated with amorphous carbon. This is a striking difference from other metal oxide species studied in this work and may suggest the significance of the surface electronic structure in the adsorption and decomposition of carbon feedstock.

- Several results acquired while studying multiple metal oxides support the lift-off model derived during the titania NP work. Lithia NPs, for example, were found with graphitic layers that detached from the surface near the corner of NPs. Alumina NPs on a silicon nitride grid, $\sim 5$ nm in diameter, tend to be individually caged in a very thin graphitic layer and seldom showed growth, which agrees with the model that thin graphitic layers with large NP catalyst contact areas would not lift-off.

- Using titania NWAG, the growth mechanisms of graphitic layers on metal oxides were investigated. By applying the knowledge acquired from the preceding work of this thesis, catalytic conversion of amorphous carbon into graphitic layers over the surface of titania nanowires was extensively characterized and analyzed. The acquired insights on the physics underlying catalytic graphitization can inspire the mechanisms of similar CNS growth over other metal oxide species in a variety of shapes. The improved electrical conductivity by the graphitic nanostructure network suggests applications in the field of electrochemistry.

- The last portion of this thesis, *in-situ* photo-excitation of titania NP catalysts and titania NWAG during CVD using a blu-ray laser, was finally implemented with a major redesign and construction of the entire furnace system. The custom-made furnace was proven to be effective for CNS synthesis. The laser excitation in the current approach was not found to yield quantifiable differences in the CNS growth yield and resulting morphology.

Relative catalytic activities between MONP catalysts investigated in this thesis are compared as follows. Since the CVD parameters were not always identical for all the species, the comparison is not always direct. The ranking is based on images taken by SEM and TEM interpreted by the author. Titania (E), chromia, vanadia, ceria, and alumina plotted in Figure 9.1 correspond to those metal oxides tested with the same CVD parameters as recipe E introduced in Chapter 5: ethylene carbon feedstock, 750°C, 15 min, 200 nm thick silica substrate on silicon wafer. Zirconia (Carbon) corresponds to the result obtained with carbon xerogel and aerogel as substrates, but otherwise exhibits the same parameters as zirconia (Silica). Titania (A-3) corresponds to the result obtained in Chapter 5 with recipe A-3: acetylene carbon feedstock, 850°C, 30 min, 13 nm thick alumina substrate sputtered on 200 nm thick silica substrate on silicon wafer. Growth from chromia, vanadia, ceria, and alumina in Figure 9.1 are not refined by the proposed CVD parameters. The X axis in Figure 9.1 is the growth yield scaled by orders of magnitude adopting the result of titania (E) as a standard (= 1), and the Y axis is homogeneity of the resulting growth ranked into four 'grades'. D corresponds to only sparse growth, C corresponds to nearly continuous localized growth, B corresponds to nearly continuous growth over a large area of the substrate surface, and A is continuous uniform growth throughout the substrate. Representative growth homogeneity of each grade is presented on the left in Figure 9.1. The CNT forests with Fe NP catalysts also exhibit growth yield of $\geq 10,000$. Ceria, without any growth, is

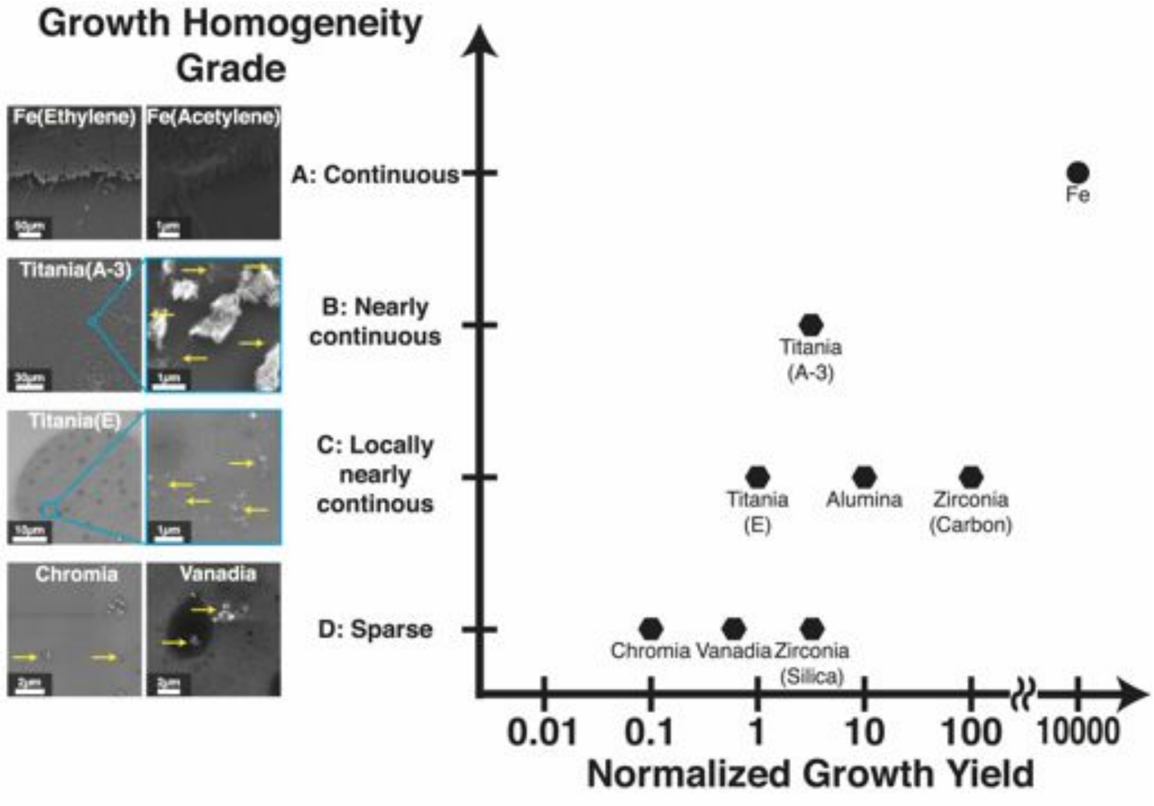

Figure 9.1: Summary of catalytic activity for the investigated MONP catalysts in terms of growth yield and homogeneity. Growth yield is scaled by orders of magnitude, visually from SEM and TEM imaging, with recipe E growth of titania NPs as the standard (1). Growth homogeneity is graded in four levels: D corresponds to only sparse growth, C corresponds to nearly continuous localized growth, B corresponds to nearly continuous growth over a large area of the substrate surface, and A is continuous uniform growth throughout the substrate. Insets for each growth homogeneity grade represent corresponding growth morphology by SEM images. For grade D, C, and B, CNTs and CNFs are pointed by yellow arrows.

not plotted.

The results related to CNS growth mechanisms investigation are more numerous than those resulting from the growth yield investigations, especially for CNT and CNF. However, the limitations of these studies as outlined in Chapter 3 still exist, and their resolution is desired through further work.

## 9.2 Recommendations for Future Work

Throughout this dissertation, model systems that have the potential to overcome the current limitations of the state-of-the-art metal-free CNS growth systems are explored, with special attention given to catalysts composed of zirconia and titania (either NP or NWAG). These systems are the leading chemistries for next-generation MONP catalysts because they promise further enhancement of growth yield, quantitative characterization of CNS growth, and *in-situ* characterizations of growth mechanisms. Findings from this thesis could also help identify, and systematically characterize, other metal oxide species that might have CNS catalytic activity that makes their use in CVD worth pursuing. To address the unanswered questions raised in this dissertation, the following future work is recommended:

- Controlled distribution of zirconia NP impregnation over regularly-shaped carbon aerogels and xerogels, which will help zirconia-mediated metal-free growth of CNTs become one step closer toward practical applications. Different combinations of CVD parameters should also be explored to test the surface-bound growth mechanisms. For example, increase in ethylene flow will accelerate carbon feeding to the corners of zirconia NPs so that rolled-up graphitic appendages may grow larger before the onset of wall defect, resulting in larger diameter of CNTs by Type 1 growth.

- Exploration of several MONP sample types with each attempted recipe with acetylene (A-1, A-2 and A-3) will be necessary to help quantify the improvement of growth yield,.

- A more statistically robust study on catalytic activity of titania NP catalysts, by sampling after different CVD durations to clarify incubation time for CNS growth, will further validate the estimates provided in this work.

- The adhesion energy used in the lift-off model between the titania and graphene surfaces is estimated to be of similar order of magnitude as the adhesion energy characteristic of graphene on silica. Titania NWAG investigated in Chapter 7 could provide an experimental route to estimate this value through exploration of graphitic nanostructure growth between bundled titania nanowires, which would require that the van der Waals interaction between titania nanowires are overcome during growth.

- Instead of drop-casting precursor solution that forms unpredictable shapes of titania NPs, shape-controlled, pre-engineered titania NPs are very interesting to substantiate the lift-off model, and are anticipated to provide further improved growth of CNTs and CNFs. Such a result will enable a statistical understanding on the rate constant of lift-off at a given (CVD) reaction temperature.

- Further electrochemical characterizations such as capacitance measurement are desired for practical applications of titania NWAG with CVD-grown graphitic nanostructure, especially in energy devices.

- Titania NWAG is also suggested model system to quantify the conversion rate of hydrocarbons into different types of carbon (amorphous and graphite) for its dramatically higher growth yield of CNS, mostly few-layer graphene films, when compared to MONP-catalyzed CNT and CNF growth investigated in this thesis. Future work should also include TG-DTA on samples after different CVD time to further quantify the catalytic graphitization mechanisms on the titania nanowire surface.

- For all the metal oxide species investigated in this work, either NPs or nanowires, environmental TEM (E-TEM) will be one of the most interesting next steps. The CVD condition that E-TEM employs, especially the low pressure of carbon feedstock, can be replicated by vacuum CVD. The best sample for initial testing is titania NWAG which shows the highest yield of CNS growth compared to any other MONPs growing CNTs and CNFs. Chromia, vanadia, and lithium oxide could also benefit from this technique to firmly corroborate the phases present on their surface (and in their bulk) during CVD, since multiple phases of oxide, carbide, and carbonate may form from the metal oxide species investigated in this work. Auger electron spectroscopy, especially *in-situ* if possible, will be a powerful tool to understand whether any non-oxide phases occur locally, *i.e.* only on the NP surface, such as the emergence of carbonate phases on lithium oxide NPs.

- Since firm corroboration of oxides of lanthanides may potentially extend the understanding on the relationship between surface electronic properties and catalytic activity, and thereby the resulting CNS morphology, future studies on these high molecular weight species is suggested.

- For the laser furnace, future studies should focus on refinement of the laser intensity and/or installation of a higher power UV laser.

This thesis work contributed to research on metal oxide catalysts for CNS synthesis *via* CVD from the perspective of fundamental science with the end goal of practical commercial application. It is the sincere hope of the author that the scientific contributions provided in the course of this dissertation will help contribute to the prosperity of human society in the future.

# Appendix A

# The Table of Lattice Distances and Corresponding Miller Indices

The complete list of lattice distances and corresponding Miller indices used for phase assignation in this thesis is shown. The lattice distance $d_{hkl}$ is calculated by inserting the lattice parameters from literature to the following formula.

For cubic crystal system: $d_{hkl} = \dfrac{1}{\sqrt{\dfrac{h^2+k^2+l^2}{a^2}}}$

For tetragonal crystal system: $d_{hkl} = \dfrac{1}{\sqrt{\dfrac{h^2+k^2}{a^2}+\dfrac{l^2}{c^2}}}$

For orthorhombic crystal system: $d_{hkl} = \dfrac{1}{\sqrt{\dfrac{h^2}{a^2}+\dfrac{k^2}{b^2}+\dfrac{l^2}{c^2}}}$

For hexagonal crystal system: $d_{hkl} = \dfrac{1}{\sqrt{\dfrac{4}{3}\dfrac{h^2+hk+k^2}{a^2}+\dfrac{l^2}{c^2}}}$

For monoclinic crystal system: $d_{hkl} = \dfrac{sin\beta}{\sqrt{\dfrac{h^2}{a^2}+\dfrac{k^2 sin^2\beta}{b^2}+\dfrac{l^2}{c^2}-\dfrac{2hlcos\beta}{ac}}}$

$4 \geq$ Å $d_{hkl} \geq 1.7$ Å are listed. Negative Miller indices are listed only for hexagonal and monoclinic crystal systems and when the resulting $d_{hkl}$ is not trivial.

Table A.1: Lattice distances and corresponding Miller indices used for phase assignment by FFT patterns.

Zirconium[79]
Crystal system: Hexagonal
a = 3.23 å, c = 5.14 å

| h | k | l | d (Å) |
|---|---|---|---|
| 0 | 1 | 0 | 2.80 |
| 1 | 0 | 0 | 2.80 |
| -1 | 0 | 0 | 2.80 |
| 0 | -1 | 0 | 2.80 |
| -1 | 1 | 0 | 2.80 |
| 1 | -1 | 0 | 2.80 |
| 0 | 0 | 2 | 2.57 |
| 0 | 1 | 1 | 2.46 |
| 1 | 0 | 1 | 2.46 |
| -1 | 0 | 1 | 2.46 |
| 0 | -1 | 1 | 2.46 |
| -1 | 1 | 1 | 2.46 |
| 1 | -1 | 1 | 2.46 |
| 0 | 1 | 2 | 1.89 |
| -1 | 0 | 2 | 1.89 |
| 0 | -1 | 2 | 1.89 |
| 1 | 0 | 2 | 1.89 |
| -1 | 1 | 2 | 1.89 |
| 1 | -1 | 2 | 1.89 |
| 0 | 0 | 3 | 1.71 |

Cubic zirconia[80]
Crystal system: Cubic
a = 5.17 å

| h | k | l | d (Å) |
|---|---|---|---|
| 0 | 1 | 1 | 3.65 |
| 1 | 1 | 0 | 3.65 |
| 1 | 0 | 1 | 3.65 |
| 1 | 1 | 1 | 2.98 |
| 0 | 0 | 2 | 2.59 |
| 0 | 2 | 0 | 2.59 |
| 2 | 0 | 0 | 2.59 |
| 2 | 1 | 0 | 2.31 |
| 1 | 2 | 0 | 2.31 |
| 0 | 1 | 2 | 2.31 |
| 0 | 2 | 1 | 2.31 |
| 2 | 0 | 1 | 2.31 |
| 1 | 0 | 2 | 2.31 |
| 1 | 1 | 2 | 2.11 |
| 1 | 2 | 1 | 2.11 |
| 2 | 1 | 1 | 2.11 |
| 0 | 2 | 2 | 1.83 |
| 2 | 2 | 0 | 1.83 |
| 2 | 0 | 2 | 1.83 |
| 0 | 0 | 3 | 1.72 |
| 0 | 3 | 0 | 1.72 |
| 3 | 0 | 0 | 1.72 |
| 1 | 2 | 2 | 1.72 |
| 2 | 1 | 2 | 1.72 |
| 2 | 2 | 1 | 1.72 |

Tetragonal zirconia[81]
Crystal system: tetragonal
a = 3.60 å, c = 5.17 å

| h | k | l | d (Å) |
|---|---|---|---|
| 0 | 1 | 0 | 3.60 |
| 1 | 0 | 0 | 3.60 |
| 0 | 1 | 1 | 2.96 |
| 1 | 0 | 1 | 2.96 |
| 0 | 0 | 2 | 2.59 |
| 1 | 1 | 0 | 2.55 |
| 1 | 1 | 1 | 2.29 |
| 0 | 1 | 2 | 2.10 |
| 1 | 0 | 2 | 2.10 |
| 1 | 1 | 2 | 1.82 |
| 0 | 2 | 0 | 1.80 |
| 2 | 0 | 0 | 1.80 |
| 0 | 0 | 3 | 1.72 |
| 0 | 2 | 1 | 1.70 |
| 2 | 0 | 1 | 1.70 |

Monoclinic zirconia[82]
Crystal system: Monoclinic
a = 5.14 å, b = 5.20 å, c = 5.32å
β = 99.1 deg

| h | k | l | d (Å) |
|---|---|---|---|

|  |  |  |  |
|---|---|---|---|
| -1 | 0 | 1 | 3.98 |
| 1 | 0 | -1 | 3.98 |
| 0 | 1 | 1 | 3.70 |
| 0 | 1 | -1 | 3.70 |
| 1 | 1 | 0 | 3.63 |
| -1 | 1 | 0 | 3.63 |
| 1 | 0 | 1 | 3.39 |
| -1 | 1 | 1 | 3.16 |
| 1 | 1 | -1 | 3.16 |
| 1 | 1 | 1 | 2.84 |
| 0 | 0 | 2 | 2.63 |
| 0 | 0 | -2 | 2.63 |
| 0 | 2 | 0 | 2.60 |
| 2 | 0 | 0 | 2.54 |
| -2 | 0 | 0 | 2.54 |
| -1 | 0 | 2 | 2.50 |
| 1 | 0 | -2 | 2.50 |
| -2 | 0 | 1 | 2.44 |
| 2 | 0 | -1 | 2.44 |
| 0 | 1 | 2 | 2.34 |
| 0 | 1 | -2 | 2.34 |
| 0 | 2 | 1 | 2.33 |
| 0 | 2 | -1 | 2.33 |
| 1 | 2 | 0 | 2.31 |
| -1 | 2 | 0 | 2.31 |
| 2 | 1 | 0 | 2.28 |
| -2 | 1 | 0 | 2.28 |
| -1 | 1 | 2 | 2.25 |
| 1 | 1 | -2 | 2.25 |
| -2 | 1 | 1 | 2.21 |
| 2 | 1 | -1 | 2.21 |
| 1 | 0 | 2 | 2.20 |
| -1 | 2 | 1 | 2.18 |
| 1 | 2 | -1 | 2.18 |
| 2 | 0 | 1 | 2.16 |
| 1 | 2 | 1 | 2.06 |
| 1 | 1 | 2 | 2.02 |
| 2 | 1 | 1 | 1.99 |
| -2 | 0 | 2 | 1.99 |
| 2 | 0 | -2 | 1.99 |
| -2 | 1 | 2 | 1.86 |
| 2 | 1 | -2 | 1.86 |
| 0 | 2 | 2 | 1.85 |
| 0 | 2 | -2 | 1.85 |
| 2 | 2 | 0 | 1.82 |
| -2 | 2 | 0 | 1.82 |
| -1 | 2 | 2 | 1.80 |
| 1 | 2 | -2 | 1.80 |
| -2 | 2 | 1 | 1.78 |
| 2 | 2 | -1 | 1.78 |
| 0 | 0 | 3 | 1.75 |
| 0 | 0 | -3 | 1.75 |
| -1 | 0 | 3 | 1.74 |
| 1 | 0 | -3 | 1.74 |
| 0 | 3 | 0 | 1.73 |

Zirconium carbide[83]
Crystal system: Cubic
a = 4.69-4.70 å

The lattice parameter for 0.66≤x≤1 of $ZrC_x$

|  |  |  |  |
|---|---|---|---|
| 1 | 0 | 1 | 3.33-3.32 |
| 0 | 1 | 1 | 3.33-3.32 |
| 1 | 1 | 0 | 3.33-3.32 |
| 1 | 1 | 1 | 2.71 |
| 0 | 2 | 0 | 2.35 |
| 0 | 0 | 2 | 2.35 |
| 2 | 0 | 0 | 2.35 |
| 2 | 0 | 1 | 2.10 |
| 1 | 0 | 2 | 2.10 |
| 1 | 2 | 0 | 2.10 |
| 0 | 2 | 1 | 2.10 |
| 2 | 1 | 0 | 2.10 |
| 0 | 1 | 2 | 2.10 |
| 1 | 1 | 2 | 1.92 |
| 2 | 1 | 1 | 1.92 |
| 1 | 2 | 1 | 1.92 |

Copper[87]
Crystal system: Cubic
a = 3.61 å

| h | k | l | d (Å) |
|---|---|---|---|

| | | | |
|---|---|---|---|
| 0 | 0 | 1 | 3.61 |
| 0 | 1 | 0 | 3.61 |
| 1 | 0 | 0 | 3.61 |
| 0 | 1 | 1 | 2.56 |
| 1 | 1 | 0 | 2.56 |
| 1 | 0 | 1 | 2.56 |
| 1 | 1 | 1 | 2.09 |
| 0 | 0 | 2 | 1.81 |
| 0 | 2 | 0 | 1.81 |
| 2 | 0 | 0 | 1.81 |

### Copper oxide (I)[88]

Crystal system: Cubic
a = 4.27 å

| h | k | l | d (Å) |
|---|---|---|---|
| 0 | 1 | 1 | 3.02 |
| 1 | 1 | 0 | 3.02 |
| 1 | 0 | 1 | 3.02 |
| 1 | 1 | 1 | 2.47 |
| 0 | 0 | 2 | 2.13 |
| 0 | 2 | 0 | 2.13 |
| 2 | 0 | 0 | 2.13 |
| 0 | 1 | 2 | 1.91 |
| 0 | 2 | 1 | 1.91 |
| 2 | 0 | 1 | 1.91 |
| 1 | 0 | 2 | 1.91 |
| 2 | 1 | 0 | 1.91 |
| 1 | 2 | 0 | 1.91 |
| 1 | 1 | 2 | 1.74 |
| 1 | 2 | 1 | 1.74 |
| 2 | 1 | 1 | 1.74 |

### Copper oxide (II)[89]

Crystal system: Monoclinic
a = 4.68 å, b = 3.42 å, c = 5.13 å
β = 99.54 deg

| h | k | l | d (Å) |
|---|---|---|---|
| -1 | 0 | 1 | 3.73 |
| 1 | 0 | -1 | 3.73 |
| 0 | 1 | 0 | 3.42 |
| 1 | 0 | 1 | 3.16 |
| 0 | 1 | 1 | 2.83 |
| 0 | 1 | -1 | 2.83 |
| 1 | 1 | 0 | 2.75 |
| -1 | 1 | 0 | 2.75 |
| 0 | 0 | 2 | 2.53 |
| 0 | 0 | -2 | 2.53 |
| -1 | 1 | 1 | 2.52 |
| 1 | 1 | -1 | 2.52 |
| -1 | 0 | 2 | 2.39 |
| 1 | 0 | -2 | 2.39 |
| 1 | 1 | 1 | 2.32 |
| 2 | 0 | 0 | 2.31 |
| -2 | 0 | 0 | 2.31 |
| -2 | 0 | 1 | 2.25 |
| 2 | 0 | -1 | 2.25 |
| 1 | 0 | 2 | 2.08 |
| 0 | 1 | 2 | 2.03 |
| 0 | 1 | -2 | 2.03 |
| 2 | 0 | 1 | 1.98 |
| -1 | 1 | 2 | 1.96 |
| 1 | 1 | -2 | 1.96 |
| 2 | 1 | 0 | 1.91 |
| -2 | 1 | 0 | 1.91 |
| -2 | 1 | 1 | 1.88 |
| 2 | 1 | -1 | 1.88 |
| -2 | 0 | 2 | 1.87 |
| 2 | 0 | -2 | 1.87 |
| 1 | 1 | 2 | 1.78 |
| 2 | 1 | 1 | 1.71 |
| 0 | 2 | 0 | 1.71 |

### α-Iron[84]

Crystal system: Cubic
a = 2.86 å

| h | k | l | d (Å) |
|---|---|---|---|
| 0 | 0 | 1 | 2.86 |
| 0 | 1 | 0 | 2.86 |
| 1 | 0 | 0 | 2.86 |
| 0 | 1 | 1 | 2.03 |
| 1 | 1 | 0 | 2.03 |
| 1 | 0 | 1 | 2.03 |

### γ-Iron[85]

Crystal system: Cubic
a = 2.79 å

The lattice parameter of this phase is not directly available around room temperature, but the value is acquired by extrapolation.

| h | k | l | d (Å) |
|---|---|---|---|
| 0 | 0 | 1 | 2.79 |
| 0 | 1 | 0 | 2.79 |
| 1 | 0 | 0 | 2.79 |
| 0 | 1 | 1 | 1.97 |
| 1 | 1 | 0 | 1.97 |
| 1 | 0 | 1 | 1.97 |

Iron carbide[120]
Crystal system: Orthorhombic
a = 5.09 å, b = 6.74 å, c = 4.53 å

| h | k | l | d (Å) |
|---|---|---|---|
| 0 | 1 | 1 | 3.76 |
| 1 | 0 | 1 | 3.38 |
| 0 | 2 | 0 | 3.37 |
| 1 | 1 | 1 | 3.02 |
| 1 | 2 | 0 | 2.81 |
| 0 | 2 | 1 | 2.70 |
| 2 | 0 | 0 | 2.55 |
| 1 | 2 | 1 | 2.39 |
| 2 | 1 | 0 | 2.38 |
| 0 | 0 | 2 | 2.27 |
| 0 | 3 | 0 | 2.25 |
| 2 | 0 | 1 | 2.22 |
| 0 | 1 | 2 | 2.15 |
| 2 | 1 | 1 | 2.11 |
| 1 | 0 | 2 | 2.07 |
| 1 | 3 | 0 | 2.05 |
| 2 | 2 | 0 | 2.03 |
| 0 | 3 | 1 | 2.01 |
| 1 | 1 | 2 | 1.98 |
| 0 | 2 | 2 | 1.88 |
| 1 | 3 | 1 | 1.87 |
| 2 | 2 | 1 | 1.85 |
| 1 | 2 | 2 | 1.76 |

α-Titanium[121]
Crystal system: Hexagonal
a = 2.957, c = 4.685

| | | | |
|---|---|---|---|
| 0 | 1 | 0 | 2.56 |
| 1 | 0 | 0 | 2.56 |
| -1 | 0 | 0 | 2.56 |
| -1 | 1 | 0 | 2.56 |
| 0 | -1 | 0 | 2.56 |
| 1 | -1 | 0 | 2.56 |
| 0 | 0 | 2 | 2.34 |
| 0 | 1 | 1 | 2.25 |
| 1 | 0 | 1 | 2.25 |
| -1 | 0 | 1 | 2.25 |
| -1 | 1 | 1 | 2.25 |
| 0 | -1 | 1 | 2.25 |
| 1 | -1 | 1 | 2.25 |
| 0 | 1 | 2 | 1.73 |
| 1 | 0 | 2 | 1.73 |
| -1 | 0 | 2 | 1.73 |
| -1 | 1 | 2 | 1.73 |
| 0 | -1 | 2 | 1.73 |
| 1 | -1 | 2 | 1.73 |

β-Titanium[121]
Crystal system: Cubic
a = 3.33

| h | k | l | d (Å) |
|---|---|---|---|
| 0 | 0 | 1 | 3.33 |
| 0 | 1 | 0 | 3.33 |
| 1 | 0 | 0 | 3.33 |
| 0 | 1 | 1 | 2.35 |
| 1 | 1 | 0 | 2.35 |
| 1 | 0 | 1 | 2.35 |
| 1 | 1 | 1 | 1.92 |

ω-Titanium[121]
Crystal system: Hexagonal
a = 4.60, c = 2.82

| h | k | l | d (Å) |
|---|---|---|---|
| 0 | 1 | 0 | 3.98 |
| 1 | 0 | 0 | 3.98 |

| | | | |
|---|---|---|---|
| -1 | 0 | 0 | 3.98 |
| -1 | 1 | 0 | 3.98 |
| 0 | -1 | 0 | 3.98 |
| 1 | -1 | 0 | 3.98 |
| 0 | 0 | 1 | 2.82 |
| 0 | 1 | 1 | 2.30 |
| 1 | 0 | 1 | 2.30 |
| -1 | 0 | 1 | 2.30 |
| -1 | 1 | 1 | 2.30 |
| 0 | -1 | 1 | 2.30 |
| 1 | -1 | 1 | 2.30 |
| 1 | 1 | 0 | 2.30 |
| -1 | 2 | 0 | 2.30 |
| -2 | 1 | 0 | 2.30 |
| 1 | -2 | 0 | 2.30 |
| 2 | -1 | 0 | 2.30 |
| 0 | 2 | 0 | 1.99 |
| 2 | 0 | 0 | 1.99 |
| -2 | 0 | 0 | 1.99 |
| -2 | 2 | 0 | 1.99 |
| 0 | -2 | 0 | 1.99 |
| 2 | -2 | 0 | 1.99 |
| 1 | 1 | 1 | 1.78 |
| -1 | 2 | 1 | 1.78 |
| -2 | 1 | 1 | 1.78 |
| 1 | -2 | 1 | 1.78 |
| 2 | -1 | 1 | 1.78 |

Anatase titania[122]
Crystal system: Tetragonal
a = 3.73 å, c = 9.37 å

| h | k | l | d (Å) |
|---|---|---|---|
| 0 | 1 | 0 | 3.73 |
| 1 | 0 | 0 | 3.73 |
| 0 | 1 | 1 | 3.47 |
| 1 | 0 | 1 | 3.47 |
| 0 | 0 | 3 | 3.12 |
| 0 | 1 | 2 | 2.92 |
| 1 | 0 | 2 | 2.92 |
| 1 | 1 | 0 | 2.64 |
| 1 | 1 | 1 | 2.54 |
| 0 | 1 | 3 | 2.40 |
| 1 | 0 | 3 | 2.40 |
| 0 | 0 | 4 | 2.34 |
| 1 | 1 | 2 | 2.30 |
| 1 | 1 | 3 | 2.02 |
| 0 | 1 | 4 | 1.98 |
| 1 | 0 | 4 | 1.98 |
| 0 | 0 | 5 | 1.87 |
| 0 | 2 | 0 | 1.87 |
| 2 | 0 | 0 | 1.87 |
| 0 | 2 | 1 | 1.83 |
| 2 | 0 | 1 | 1.83 |
| 0 | 2 | 2 | 1.73 |
| 2 | 0 | 2 | 1.73 |

Rutile titania[122]
Crystal system: Tetragonal
a = 4.58 å, c = 2.95 å

| h | k | l | d (Å) |
|---|---|---|---|
| 1 | 1 | 0 | 3.24 |
| 0 | 0 | 1 | 2.95 |
| 0 | 1 | 1 | 2.48 |
| 1 | 0 | 1 | 2.48 |
| 0 | 2 | 0 | 2.29 |
| 2 | 0 | 0 | 2.29 |
| 1 | 1 | 1 | 2.18 |
| 2 | 1 | 0 | 2.05 |
| 1 | 2 | 0 | 2.05 |
| 0 | 2 | 1 | 1.81 |
| 2 | 0 | 1 | 1.81 |

Brookite titania[122]
Crystal system: Orthorhombic
a = 5.44 å, b = 9.17 å, c = 5.14 å

| h | k | l | d (Å) |
|---|---|---|---|
| 1 | 0 | 1 | 3.73 |
| 1 | 2 | 0 | 3.50 |
| 1 | 1 | 1 | 3.46 |
| 0 | 2 | 1 | 3.42 |
| 0 | 3 | 0 | 3.05 |
| 1 | 2 | 1 | 2.89 |

| | | | |
|---|---|---|---|
| 2 | 0 | 0 | 2.72 |
| 1 | 3 | 0 | 2.66 |
| 0 | 3 | 1 | 2.63 |
| 2 | 1 | 0 | 2.61 |
| 0 | 0 | 2 | 2.57 |
| 0 | 1 | 2 | 2.47 |
| 2 | 0 | 1 | 2.40 |
| 1 | 3 | 1 | 2.36 |
| 2 | 2 | 0 | 2.34 |
| 2 | 1 | 1 | 2.32 |
| 1 | 0 | 2 | 2.32 |
| 0 | 4 | 0 | 2.29 |
| 1 | 1 | 2 | 2.25 |
| 0 | 2 | 2 | 2.24 |
| 2 | 2 | 1 | 2.13 |
| 1 | 4 | 0 | 2.11 |
| 0 | 4 | 1 | 2.09 |
| 1 | 2 | 2 | 2.07 |
| 2 | 3 | 0 | 2.03 |
| 0 | 3 | 2 | 1.97 |
| 1 | 4 | 1 | 1.95 |
| 2 | 3 | 1 | 1.89 |
| 2 | 0 | 2 | 1.87 |
| 1 | 3 | 2 | 1.85 |
| 0 | 5 | 0 | 1.83 |
| 2 | 1 | 2 | 1.83 |
| 3 | 0 | 0 | 1.81 |
| 3 | 1 | 0 | 1.78 |
| 2 | 4 | 0 | 1.75 |
| 1 | 5 | 0 | 1.74 |
| 2 | 2 | 2 | 1.73 |
| 0 | 5 | 1 | 1.73 |
| 0 | 0 | 3 | 1.71 |
| 0 | 4 | 2 | 1.71 |
| 3 | 0 | 1 | 1.71 |

Titanium carbide[123]
Crystal system: Cubic
a = 4.29-4.33 å
The lattice parameter for 0.2≤x≤1 of $TiC_x$

| h | k | l | d (Å) |
|---|---|---|---|
| 0 | 1 | 1 | 3.03-3.06 |
| 1 | 1 | 0 | 3.03-3.06 |
| 1 | 0 | 1 | 3.03-3.06 |
| 1 | 1 | 1 | 2.47-2.50 |
| 0 | 0 | 2 | 2.14-2.16 |
| 0 | 2 | 0 | 2.14-2.16 |
| 2 | 0 | 0 | 2.14-2.16 |
| 0 | 1 | 2 | 1.92-1.93 |
| 0 | 2 | 1 | 1.92-1.93 |
| 2 | 0 | 1 | 1.92-1.93 |
| 1 | 0 | 2 | 1.92-1.93 |
| 2 | 1 | 0 | 1.92-1.93 |
| 1 | 2 | 0 | 1.92-1.93 |
| 1 | 1 | 2 | 1.75-1.77 |
| 1 | 2 | 1 | 1.75-1.77 |
| 2 | 1 | 1 | 1.75-1.77 |

α-Alumina[125]
Crystal system: Hexagonal
a = 4.76 å, c = 12.99 å

| h | k | l | d (Å) |
|---|---|---|---|
| 0 | 1 | 1 | 3.93 |
| 1 | 0 | 1 | 3.93 |
| -1 | 0 | 1 | 3.93 |
| -1 | 1 | 1 | 3.93 |
| 0 | -1 | 1 | 3.93 |
| 1 | -1 | 1 | 3.93 |
| 0 | 1 | 2 | 3.48 |
| 1 | 0 | 2 | 3.48 |
| -1 | 0 | 2 | 3.48 |
| -1 | 1 | 2 | 3.48 |
| 0 | -1 | 2 | 3.48 |
| 1 | -1 | 2 | 3.48 |
| 0 | 0 | 4 | 3.25 |
| 0 | 1 | 3 | 2.99 |
| 1 | 0 | 3 | 2.99 |
| -1 | 0 | 3 | 2.99 |
| -1 | 1 | 3 | 2.99 |
| 0 | -1 | 3 | 2.99 |
| 1 | -1 | 3 | 2.99 |

| | | | |
|---|---|---|---|
| 0 | 0 | 5 | 2.60 |
| 0 | 1 | 4 | 2.55 |
| 1 | 0 | 4 | 2.55 |
| -1 | 0 | 4 | 2.55 |
| -1 | 1 | 4 | 2.55 |
| 0 | -1 | 4 | 2.55 |
| 1 | -1 | 4 | 2.55 |
| 1 | 1 | 0 | 2.38 |
| -2 | 1 | 0 | 2.38 |
| -1 | 2 | 0 | 2.38 |
| 2 | -1 | 0 | 2.38 |
| 1 | -2 | 0 | 2.38 |
| 1 | 1 | 1 | 2.34 |
| -1 | 2 | 1 | 2.34 |
| -2 | 1 | 1 | 2.34 |
| 1 | -2 | 1 | 2.34 |
| 2 | -1 | 1 | 2.34 |
| 1 | 1 | 2 | 2.23 |
| -1 | 2 | 2 | 2.23 |
| -2 | 1 | 2 | 2.23 |
| 1 | -2 | 2 | 2.23 |
| 2 | -1 | 2 | 2.23 |
| 0 | 1 | 5 | 2.20 |
| 1 | 0 | 5 | 2.20 |
| -1 | 0 | 5 | 2.20 |
| -1 | 1 | 5 | 2.20 |
| 0 | -1 | 5 | 2.20 |
| 1 | -1 | 5 | 2.20 |
| 0 | 0 | 6 | 2.16 |
| 1 | 1 | 3 | 2.09 |
| -1 | 2 | 3 | 2.09 |
| -2 | 1 | 3 | 2.09 |
| 1 | -2 | 3 | 2.09 |
| 2 | -1 | 3 | 2.09 |
| 0 | 2 | 0 | 2.06 |
| 2 | 0 | 0 | 2.06 |
| -2 | 0 | 0 | 2.06 |
| -2 | 2 | 0 | 2.06 |
| 0 | -2 | 0 | 2.06 |
| 2 | -2 | 0 | 2.06 |
| 0 | 2 | 1 | 2.03 |
| 2 | 0 | 1 | 2.03 |
| -2 | 0 | 1 | 2.03 |
| -2 | 2 | 1 | 2.03 |
| 0 | -2 | 1 | 2.03 |
| 2 | -2 | 1 | 2.03 |
| 0 | 2 | 2 | 1.96 |
| 2 | 0 | 2 | 1.96 |
| -2 | 0 | 2 | 1.96 |
| -2 | 2 | 2 | 1.96 |
| 0 | -2 | 2 | 1.96 |
| 2 | -2 | 2 | 1.96 |
| 1 | 1 | 4 | 1.92 |
| -1 | 2 | 4 | 1.92 |
| -2 | 1 | 4 | 1.92 |
| 1 | -2 | 4 | 1.92 |
| 2 | -1 | 4 | 1.92 |
| 0 | 1 | 6 | 1.92 |
| 1 | 0 | 6 | 1.92 |
| -1 | 0 | 6 | 1.92 |
| -1 | 1 | 6 | 1.92 |
| 0 | -1 | 6 | 1.92 |
| 1 | -1 | 6 | 1.92 |
| 0 | 2 | 3 | 1.86 |
| 2 | 0 | 3 | 1.86 |
| -2 | 0 | 3 | 1.86 |
| -2 | 2 | 3 | 1.86 |
| 0 | -2 | 3 | 1.86 |
| 2 | -2 | 3 | 1.86 |
| 0 | 0 | 7 | 1.85 |
| 1 | 1 | 5 | 1.75 |
| -1 | 2 | 5 | 1.75 |
| -2 | 1 | 5 | 1.75 |
| 1 | -2 | 5 | 1.75 |
| 2 | -1 | 5 | 1.75 |
| 0 | 2 | 4 | 1.74 |
| 2 | 0 | 4 | 1.74 |
| -2 | 0 | 4 | 1.74 |
| -2 | 2 | 4 | 1.74 |
| 0 | -2 | 4 | 1.74 |
| 2 | -2 | 4 | 1.74 |

γ-Alumina[126]
Crystal system: Cubic
a = 7.9 å

| h | k | l | d (Å) |
|---|---|---|---|
| 0 | 0 | 2 | 3.95 |
| 0 | 2 | 0 | 3.95 |
| 2 | 0 | 0 | 3.95 |
| 0 | 1 | 2 | 3.53 |
| 0 | 2 | 1 | 3.53 |
| 2 | 0 | 1 | 3.53 |
| 1 | 0 | 2 | 3.53 |
| 2 | 1 | 0 | 3.53 |
| 1 | 2 | 0 | 3.53 |
| 1 | 1 | 2 | 3.23 |
| 1 | 2 | 1 | 3.23 |
| 2 | 1 | 1 | 3.23 |
| 0 | 2 | 2 | 2.79 |
| 2 | 2 | 0 | 2.79 |
| 2 | 0 | 2 | 2.79 |
| 0 | 0 | 3 | 2.63 |
| 0 | 3 | 0 | 2.63 |
| 3 | 0 | 0 | 2.63 |
| 1 | 2 | 2 | 2.63 |
| 2 | 1 | 2 | 2.63 |
| 2 | 2 | 1 | 2.63 |
| 0 | 1 | 3 | 2.50 |
| 0 | 3 | 1 | 2.50 |
| 1 | 3 | 0 | 2.50 |
| 3 | 1 | 0 | 2.50 |
| 3 | 0 | 1 | 2.50 |
| 1 | 0 | 3 | 2.50 |
| 1 | 1 | 3 | 2.38 |
| 1 | 3 | 1 | 2.38 |
| 3 | 1 | 1 | 2.38 |
| 2 | 2 | 2 | 2.28 |
| 0 | 2 | 3 | 2.19 |
| 0 | 3 | 2 | 2.19 |
| 2 | 3 | 0 | 2.19 |
| 3 | 2 | 0 | 2.19 |
| 3 | 0 | 2 | 2.19 |
| 2 | 0 | 3 | 2.19 |
| 1 | 2 | 3 | 2.11 |
| 1 | 3 | 2 | 2.11 |
| 2 | 3 | 1 | 2.11 |
| 3 | 2 | 1 | 2.11 |
| 3 | 1 | 2 | 2.11 |
| 2 | 1 | 3 | 2.11 |
| 0 | 0 | 4 | 1.98 |
| 0 | 4 | 0 | 1.98 |
| 4 | 0 | 0 | 1.98 |
| 0 | 1 | 4 | 1.92 |
| 0 | 4 | 1 | 1.92 |
| 1 | 4 | 0 | 1.92 |
| 4 | 1 | 0 | 1.92 |
| 4 | 0 | 1 | 1.92 |
| 1 | 0 | 4 | 1.92 |
| 2 | 2 | 3 | 1.92 |
| 2 | 3 | 2 | 1.92 |
| 3 | 2 | 2 | 1.92 |
| 1 | 4 | 1 | 1.86 |
| 4 | 1 | 1 | 1.86 |
| 0 | 3 | 3 | 1.86 |
| 3 | 3 | 0 | 1.86 |
| 3 | 0 | 3 | 1.86 |
| 1 | 1 | 4 | 1.86 |
| 1 | 3 | 3 | 1.81 |
| 3 | 3 | 1 | 1.81 |
| 3 | 1 | 3 | 1.81 |
| 0 | 2 | 4 | 1.77 |
| 0 | 4 | 2 | 1.77 |
| 2 | 4 | 0 | 1.77 |
| 4 | 2 | 0 | 1.77 |
| 4 | 0 | 2 | 1.77 |
| 2 | 0 | 4 | 1.77 |
| 1 | 2 | 4 | 1.72 |
| 1 | 4 | 2 | 1.72 |
| 2 | 4 | 1 | 1.72 |
| 4 | 2 | 1 | 1.72 |
| 4 | 1 | 2 | 1.72 |
| 2 | 1 | 4 | 1.72 |

### Chromium[86]

Crystal system: Cubic
a = 2.89 å

| h | k | l | d (Å) |
|---|---|---|---|
| 0 | 0 | 1 | 2.89 |
| 0 | 1 | 0 | 2.89 |
| 1 | 0 | 0 | 2.89 |
| 0 | 1 | 1 | 2.04 |
| 1 | 1 | 0 | 2.04 |
| 1 | 0 | 1 | 2.04 |

### Chromia (III)[170]

Crystal system: Hexagonal
a = 4.96 å, c = 13.6 å

| h | k | l | d (Å) |
|---|---|---|---|
| 0 | 1 | 2 | 3.63 |
| 1 | 0 | 2 | 3.63 |
| -1 | 0 | 2 | 3.63 |
| 0 | -1 | 2 | 3.63 |
| -1 | 1 | 2 | 3.63 |
| 1 | -1 | 2 | 3.63 |
| 0 | 0 | 4 | 3.40 |
| 0 | 1 | 3 | 3.12 |
| 1 | 0 | 3 | 3.12 |
| -1 | 0 | 3 | 3.12 |
| 0 | -1 | 3 | 3.12 |
| -1 | 1 | 3 | 3.12 |
| 1 | -1 | 3 | 3.12 |
| 0 | 0 | 5 | 2.72 |
| 0 | 1 | 4 | 2.67 |
| 1 | 0 | 4 | 2.67 |
| -1 | 0 | 4 | 2.67 |
| 0 | -1 | 4 | 2.67 |
| -1 | 1 | 4 | 2.67 |
| 1 | -1 | 4 | 2.67 |
| 1 | 1 | 0 | 2.48 |
| -2 | 1 | 0 | 2.48 |
| -1 | 2 | 0 | 2.48 |
| 2 | -1 | 0 | 2.48 |
| 1 | -2 | 0 | 2.48 |
| 1 | 1 | 1 | 2.44 |
| -1 | 2 | 1 | 2.44 |
| 1 | -2 | 1 | 2.44 |
| -2 | 1 | 1 | 2.44 |
| 2 | -1 | 1 | 2.44 |
| 1 | 1 | 2 | 2.33 |
| -1 | 2 | 2 | 2.33 |
| -2 | 1 | 2 | 2.33 |
| 1 | -2 | 2 | 2.33 |
| 2 | -1 | 2 | 2.33 |
| 0 | 1 | 5 | 2.30 |
| 1 | 0 | 5 | 2.30 |
| -1 | 0 | 5 | 2.30 |
| 0 | -1 | 5 | 2.30 |
| -1 | 1 | 5 | 2.30 |
| 1 | -1 | 5 | 2.30 |
| 0 | 0 | 6 | 2.27 |
| 1 | 1 | 3 | 2.17 |
| -1 | 2 | 3 | 2.17 |
| -2 | 1 | 3 | 2.17 |
| 1 | -2 | 3 | 2.17 |
| 2 | -1 | 3 | 2.17 |
| 0 | 2 | 0 | 2.15 |
| 2 | 0 | 0 | 2.15 |
| -2 | 0 | 0 | 2.15 |
| 0 | -2 | 0 | 2.15 |
| -2 | 2 | 0 | 2.15 |
| 2 | -2 | 0 | 2.15 |
| 0 | 2 | 1 | 2.12 |
| 2 | 0 | 1 | 2.12 |
| -2 | 0 | 1 | 2.12 |
| 0 | -2 | 1 | 2.12 |
| -2 | 2 | 1 | 2.12 |
| 2 | -2 | 1 | 2.12 |
| 0 | 2 | 2 | 2.05 |
| 2 | 0 | 2 | 2.05 |
| -2 | 0 | 2 | 2.05 |
| 0 | -2 | 2 | 2.05 |
| -2 | 2 | 2 | 2.05 |
| 2 | -2 | 2 | 2.05 |
| 0 | 1 | 6 | 2.00 |
| 1 | 0 | 6 | 2.00 |

| | | | |
|---|---|---|---|
| -1 | 0 | 6 | 2.00 |
| 0 | -1 | 6 | 2.00 |
| -1 | 1 | 6 | 2.00 |
| 1 | -1 | 6 | 2.00 |
| 1 | 1 | 4 | 2.00 |
| -1 | 2 | 4 | 2.00 |
| -2 | 1 | 4 | 2.00 |
| 1 | -2 | 4 | 2.00 |
| 2 | -1 | 4 | 2.00 |
| 0 | 0 | 7 | 1.94 |
| 0 | 2 | 3 | 1.94 |
| 2 | 0 | 3 | 1.94 |
| -2 | 0 | 3 | 1.94 |
| 0 | -2 | 3 | 1.94 |
| -2 | 2 | 3 | 1.94 |
| 2 | -2 | 3 | 1.94 |
| 1 | 1 | 5 | 1.83 |
| -2 | 1 | 5 | 1.83 |
| 2 | -1 | 5 | 1.83 |
| -1 | 2 | 5 | 1.83 |
| 1 | -2 | 5 | 1.83 |
| 0 | 2 | 4 | 1.82 |
| 2 | 0 | 4 | 1.82 |
| -2 | 0 | 4 | 1.82 |
| 0 | -2 | 4 | 1.82 |
| -2 | 2 | 4 | 1.82 |
| 2 | -2 | 4 | 1.82 |
| 0 | 1 | 7 | 1.77 |
| 1 | 0 | 7 | 1.77 |
| -1 | 0 | 7 | 1.77 |
| 0 | -1 | 7 | 1.77 |

Chromia (IV)[171]
Crystal system: Tetragonal
a = 4.42 å, c = 2.92 å

| h | k | l | d (Å) |
|---|---|---|---|
| 1 | 1 | 0 | 3.13 |
| 0 | 0 | 1 | 2.92 |
| 0 | 1 | 1 | 2.44 |
| 1 | 0 | 1 | 2.44 |
| 0 | 2 | 0 | 2.21 |
| 2 | 0 | 0 | 2.21 |
| 1 | 1 | 1 | 2.13 |
| 2 | 1 | 0 | 1.98 |
| 1 | 2 | 0 | 1.98 |
| 0 | 2 | 1 | 1.76 |
| 2 | 0 | 1 | 1.76 |

Chromium carbide, $Cr_3C_2$[172]
Crystal system: Orthorhombic
a = 5.53 å, b =  2.29 å, c = 11.47 å

| h | k | l | d (Å) |
|---|---|---|---|
| 1 | 0 | 2 | 3.98 |
| 0 | 0 | 3 | 3.82 |
| 1 | 0 | 3 | 3.15 |
| 0 | 0 | 4 | 2.87 |
| 2 | 0 | 0 | 2.77 |
| 2 | 0 | 1 | 2.69 |
| 1 | 0 | 4 | 2.55 |
| 2 | 0 | 2 | 2.49 |
| 0 | 0 | 5 | 2.29 |
| 0 | 1 | 0 | 2.29 |
| 0 | 1 | 1 | 2.25 |
| 2 | 0 | 3 | 2.24 |
| 0 | 1 | 2 | 2.13 |
| 1 | 0 | 5 | 2.12 |
| 1 | 1 | 0 | 2.12 |
| 1 | 1 | 1 | 2.08 |
| 2 | 0 | 4 | 1.99 |
| 1 | 1 | 2 | 1.99 |
| 0 | 1 | 3 | 1.96 |
| 0 | 0 | 6 | 1.91 |
| 1 | 1 | 3 | 1.85 |
| 3 | 0 | 0 | 1.84 |
| 3 | 0 | 1 | 1.82 |
| 1 | 0 | 6 | 1.81 |
| 0 | 1 | 4 | 1.79 |
| 2 | 0 | 5 | 1.77 |
| 2 | 1 | 0 | 1.76 |
| 3 | 0 | 2 | 1.76 |
| 2 | 1 | 1 | 1.74 |
| 1 | 1 | 4 | 1.70 |

Chromium carbide, $Cr_7C_3$[173]
Crystal system: Hexagonal
a = 13.98 å, c = 4.523 å

| h | k | l | d (Å) |
|---|---|---|---|
| 1 | 1 | 1 | 3.80 |
| -1 | 2 | 1 | 3.80 |
| -2 | 1 | 1 | 3.80 |
| 1 | -2 | 1 | 3.80 |
| 2 | -1 | 1 | 3.80 |
| 0 | 2 | 1 | 3.62 |
| 2 | 0 | 1 | 3.62 |
| -2 | 0 | 1 | 3.62 |
| 0 | -2 | 1 | 3.62 |
| -2 | 2 | 1 | 3.62 |
| 2 | -2 | 1 | 3.62 |
| 2 | 2 | 0 | 3.50 |
| -4 | 2 | 0 | 3.50 |
| -2 | 4 | 0 | 3.50 |
| 4 | -2 | 0 | 3.50 |
| 2 | -4 | 0 | 3.50 |
| 3 | 1 | 0 | 3.36 |
| 1 | 3 | 0 | 3.36 |
| -4 | 1 | 0 | 3.36 |
| -1 | 4 | 0 | 3.36 |
| 4 | -1 | 0 | 3.36 |
| 1 | -4 | 0 | 3.36 |
| -4 | 3 | 0 | 3.36 |
| -3 | 4 | 0 | 3.36 |
| 4 | -3 | 0 | 3.36 |
| 3 | -4 | 0 | 3.36 |
| 1 | 2 | 1 | 3.22 |
| 2 | 1 | 1 | 3.22 |
| -1 | 3 | 1 | 3.22 |
| -3 | 1 | 1 | 3.22 |
| 1 | -3 | 1 | 3.22 |
| 3 | -1 | 1 | 3.22 |
| -3 | 2 | 1 | 3.22 |
| -2 | 3 | 1 | 3.22 |
| 3 | -2 | 1 | 3.22 |
| 2 | -3 | 1 | 3.22 |
| 0 | 4 | 0 | 3.03 |
| 4 | 0 | 0 | 3.03 |
| -4 | 0 | 0 | 3.03 |
| 0 | -4 | 0 | 3.03 |
| -4 | 4 | 0 | 3.03 |
| 4 | -4 | 0 | 3.03 |
| 0 | 3 | 1 | 3.01 |
| 3 | 0 | 1 | 3.01 |
| -3 | 0 | 1 | 3.01 |
| 0 | -3 | 1 | 3.01 |
| -3 | 3 | 1 | 3.01 |
| 3 | -3 | 1 | 3.01 |
| 3 | 2 | 0 | 2.78 |
| 2 | 3 | 0 | 2.78 |
| -5 | 2 | 0 | 2.78 |
| -2 | 5 | 0 | 2.78 |
| 5 | -2 | 0 | 2.78 |
| 2 | -5 | 0 | 2.78 |
| -5 | 3 | 0 | 2.78 |
| -3 | 5 | 0 | 2.78 |
| 5 | -3 | 0 | 2.78 |
| 3 | -5 | 0 | 2.78 |
| 2 | 2 | 1 | 2.77 |
| -4 | 2 | 1 | 2.77 |
| -2 | 4 | 1 | 2.77 |
| 4 | -2 | 1 | 2.77 |
| 2 | -4 | 1 | 2.77 |
| 1 | 3 | 1 | 2.70 |
| 3 | 1 | 1 | 2.70 |
| -1 | 4 | 1 | 2.70 |
| -4 | 1 | 1 | 2.70 |
| 1 | -4 | 1 | 2.70 |
| 4 | -1 | 1 | 2.70 |
| -4 | 3 | 1 | 2.70 |
| -3 | 4 | 1 | 2.70 |
| 4 | -3 | 1 | 2.70 |
| 3 | -4 | 1 | 2.70 |
| 4 | 1 | 0 | 2.64 |
| 1 | 4 | 0 | 2.64 |
| -5 | 1 | 0 | 2.64 |
| -1 | 5 | 0 | 2.64 |

| | | | |
|---|---|---|---|
| 5 | -1 | 0 | 2.64 |
| 1 | -5 | 0 | 2.64 |
| -5 | 4 | 0 | 2.64 |
| -4 | 5 | 0 | 2.64 |
| 5 | -4 | 0 | 2.64 |
| 4 | -5 | 0 | 2.64 |
| 0 | 4 | 1 | 2.52 |
| 4 | 0 | 1 | 2.52 |
| -4 | 0 | 1 | 2.52 |
| 0 | -4 | 1 | 2.52 |
| -4 | 4 | 1 | 2.52 |
| 4 | -4 | 1 | 2.52 |
| 0 | 5 | 0 | 2.42 |
| 5 | 0 | 0 | 2.42 |
| -5 | 0 | 0 | 2.42 |
| 0 | -5 | 0 | 2.42 |
| -5 | 5 | 0 | 2.42 |
| 5 | -5 | 0 | 2.42 |
| 3 | 2 | 1 | 2.37 |
| 2 | 3 | 1 | 2.37 |
| -5 | 2 | 1 | 2.37 |
| -2 | 5 | 1 | 2.37 |
| 5 | -2 | 1 | 2.37 |
| 2 | -5 | 1 | 2.37 |
| -5 | 3 | 1 | 2.37 |
| -3 | 5 | 1 | 2.37 |
| 5 | -3 | 1 | 2.37 |
| 3 | -5 | 1 | 2.37 |
| 3 | 3 | 0 | 2.33 |
| -6 | 3 | 0 | 2.33 |
| -3 | 6 | 0 | 2.33 |
| 6 | -3 | 0 | 2.33 |
| 3 | -6 | 0 | 2.33 |
| 4 | 2 | 0 | 2.29 |
| 2 | 4 | 0 | 2.29 |
| -6 | 2 | 0 | 2.29 |
| -2 | 6 | 0 | 2.29 |
| 6 | -2 | 0 | 2.29 |
| 2 | -6 | 0 | 2.29 |
| -6 | 4 | 0 | 2.29 |
| -4 | 6 | 0 | 2.29 |
| 6 | -4 | 0 | 2.29 |
| 4 | -6 | 0 | 2.29 |
| 1 | 4 | 1 | 2.28 |
| 4 | 1 | 1 | 2.28 |
| -1 | 5 | 1 | 2.28 |
| -5 | 1 | 1 | 2.28 |
| 1 | -5 | 1 | 2.28 |
| 5 | -1 | 1 | 2.28 |
| -5 | 4 | 1 | 2.28 |
| -4 | 5 | 1 | 2.28 |
| 5 | -4 | 1 | 2.28 |
| 4 | -5 | 1 | 2.28 |
| 0 | 0 | 2 | 2.26 |
| 0 | 1 | 2 | 2.22 |
| 1 | 0 | 2 | 2.22 |
| -1 | 0 | 2 | 2.22 |
| -1 | 1 | 2 | 2.22 |
| 0 | -1 | 2 | 2.22 |
| 1 | -1 | 2 | 2.22 |
| 5 | 1 | 0 | 2.17 |
| 1 | 5 | 0 | 2.17 |
| -6 | 1 | 0 | 2.17 |
| -1 | 6 | 0 | 2.17 |
| 6 | -1 | 0 | 2.17 |
| 1 | -6 | 0 | 2.17 |
| 1 | 1 | 2 | 2.15 |
| -1 | 2 | 2 | 2.15 |
| -2 | 1 | 2 | 2.15 |
| 1 | -2 | 2 | 2.15 |
| 2 | -1 | 2 | 2.15 |
| 0 | 5 | 1 | 2.13 |
| 5 | 0 | 1 | 2.13 |
| -5 | 0 | 1 | 2.13 |
| 0 | -5 | 1 | 2.13 |
| 0 | 2 | 2 | 2.12 |
| 2 | 0 | 2 | 2.12 |
| -2 | 0 | 2 | 2.12 |
| 0 | -2 | 2 | 2.12 |
| -2 | 2 | 2 | 2.12 |
| 2 | -2 | 2 | 2.12 |
| 3 | 3 | 1 | 2.07 |

| | | | |
|---|---|---|---|
| -6 | 3 | 1 | 2.07 |
| -3 | 6 | 1 | 2.07 |
| 6 | -3 | 1 | 2.07 |
| 3 | -6 | 1 | 2.07 |
| 4 | 2 | 1 | 2.04 |
| 2 | 4 | 1 | 2.04 |
| -6 | 2 | 1 | 2.04 |
| -2 | 6 | 1 | 2.04 |
| 6 | -2 | 1 | 2.04 |
| 2 | -6 | 1 | 2.04 |
| 1 | 2 | 2 | 2.03 |
| 2 | 1 | 2 | 2.03 |
| -1 | 3 | 2 | 2.03 |
| -3 | 1 | 2 | 2.03 |
| -2 | 3 | 2 | 2.03 |
| -3 | 2 | 2 | 2.03 |
| 1 | -3 | 2 | 2.03 |
| 3 | -1 | 2 | 2.03 |
| 2 | -3 | 2 | 2.03 |
| 3 | -2 | 2 | 2.03 |
| 0 | 6 | 0 | 2.02 |
| 6 | 0 | 0 | 2.02 |
| -6 | 0 | 0 | 2.02 |
| 0 | -6 | 0 | 2.02 |
| 4 | 3 | 0 | 1.99 |
| 3 | 4 | 0 | 1.99 |
| -7 | 3 | 0 | 1.99 |
| -3 | 7 | 0 | 1.99 |
| 7 | -3 | 0 | 1.99 |
| 3 | -7 | 0 | 1.99 |
| 0 | 3 | 2 | 1.97 |
| 3 | 0 | 2 | 1.97 |
| -3 | 0 | 2 | 1.97 |
| 0 | -3 | 2 | 1.97 |
| -3 | 3 | 2 | 1.97 |
| 3 | -3 | 2 | 1.97 |
| 1 | 5 | 1 | 1.96 |
| 5 | 1 | 1 | 1.96 |
| -1 | 6 | 1 | 1.96 |
| -6 | 1 | 1 | 1.96 |
| 1 | -6 | 1 | 1.96 |

| | | | |
|---|---|---|---|
| 6 | -1 | 1 | 1.96 |
| 5 | 2 | 0 | 1.94 |
| 2 | 5 | 0 | 1.94 |
| -7 | 2 | 0 | 1.94 |
| -2 | 7 | 0 | 1.94 |
| 7 | -2 | 0 | 1.94 |
| 2 | -7 | 0 | 1.94 |
| 2 | 2 | 2 | 1.90 |
| -2 | 4 | 2 | 1.90 |
| -4 | 2 | 2 | 1.90 |
| 2 | -4 | 2 | 1.90 |
| 4 | -2 | 2 | 1.90 |
| 1 | 3 | 2 | 1.88 |
| 3 | 1 | 2 | 1.88 |
| -1 | 4 | 2 | 1.88 |
| -4 | 1 | 2 | 1.88 |
| 1 | -4 | 2 | 1.88 |
| 4 | -1 | 2 | 1.88 |
| -4 | 3 | 2 | 1.88 |
| -3 | 4 | 2 | 1.88 |
| 4 | -3 | 2 | 1.88 |
| 3 | -4 | 2 | 1.88 |
| 6 | 1 | 0 | 1.85 |
| 1 | 6 | 0 | 1.85 |
| -7 | 1 | 0 | 1.85 |
| -1 | 7 | 0 | 1.85 |
| 7 | -1 | 0 | 1.85 |
| 1 | -7 | 0 | 1.85 |
| 0 | 6 | 1 | 1.84 |
| 6 | 0 | 1 | 1.84 |
| -6 | 0 | 1 | 1.84 |
| 0 | -6 | 1 | 1.84 |
| 4 | 3 | 1 | 1.82 |
| 3 | 4 | 1 | 1.82 |
| 0 | 4 | 2 | 1.81 |
| 4 | 0 | 2 | 1.81 |
| -4 | 0 | 2 | 1.81 |
| 0 | -4 | 2 | 1.81 |
| -4 | 4 | 2 | 1.81 |
| 4 | -4 | 2 | 1.81 |
| 5 | 2 | 1 | 1.78 |

| | | | |
|---|---|---|---|
| 2 | 5 | 1 | 1.78 |
| -7 | 2 | 1 | 1.78 |
| -2 | 7 | 1 | 1.78 |
| 7 | -2 | 1 | 1.78 |
| 2 | -7 | 1 | 1.78 |
| 2 | 3 | 2 | 1.75 |
| 3 | 2 | 2 | 1.75 |
| -2 | 5 | 2 | 1.75 |
| -5 | 2 | 2 | 1.75 |
| -3 | 5 | 2 | 1.75 |
| 2 | -5 | 2 | 1.75 |
| 5 | -2 | 2 | 1.75 |
| 3 | -5 | 2 | 1.75 |
| -5 | 3 | 2 | 1.75 |
| 5 | -3 | 2 | 1.75 |
| 4 | 4 | 0 | 1.75 |
| 5 | 3 | 0 | 1.73 |
| 3 | 5 | 0 | 1.73 |
| 0 | 7 | 0 | 1.73 |
| 7 | 0 | 0 | 1.73 |
| -7 | 0 | 0 | 1.73 |
| 0 | -7 | 0 | 1.73 |
| 1 | 4 | 2 | 1.72 |
| 4 | 1 | 2 | 1.72 |
| -1 | 5 | 2 | 1.72 |
| -5 | 1 | 2 | 1.72 |
| 1 | -5 | 2 | 1.72 |
| 5 | -1 | 2 | 1.72 |
| 1 | 6 | 1 | 1.71 |
| 6 | 1 | 1 | 1.71 |
| -1 | 7 | 1 | 1.71 |
| 1 | -7 | 1 | 1.71 |
| -7 | 1 | 1 | 1.71 |
| 7 | -1 | 1 | 1.71 |

Chromium carbide, $Cr_{23}C_6$[174]
Crystal system: Cubic
a = 10.65 å

| h | k | l | d (Å) |
|---|---|---|---|
| 2 | 0 | 2 | 3.77 |
| 0 | 2 | 2 | 3.77 |
| 2 | 2 | 0 | 3.77 |
| 2 | 1 | 2 | 3.55 |
| 1 | 2 | 2 | 3.55 |
| 2 | 2 | 1 | 3.55 |
| 0 | 0 | 3 | 3.55 |
| 0 | 3 | 0 | 3.55 |
| 3 | 0 | 0 | 3.55 |
| 3 | 0 | 1 | 3.37 |
| 1 | 0 | 3 | 3.37 |
| 0 | 1 | 3 | 3.37 |
| 0 | 3 | 1 | 3.37 |
| 1 | 3 | 0 | 3.37 |
| 3 | 1 | 0 | 3.37 |
| 1 | 1 | 3 | 3.21 |
| 3 | 1 | 1 | 3.21 |
| 1 | 3 | 1 | 3.21 |
| 2 | 2 | 2 | 3.07 |
| 3 | 0 | 2 | 2.95 |
| 2 | 0 | 3 | 2.95 |
| 0 | 2 | 3 | 2.95 |
| 0 | 3 | 2 | 2.95 |
| 2 | 3 | 0 | 2.95 |
| 3 | 2 | 0 | 2.95 |
| 3 | 1 | 2 | 2.85 |
| 2 | 1 | 3 | 2.85 |
| 1 | 2 | 3 | 2.85 |
| 3 | 2 | 1 | 2.85 |
| 1 | 3 | 2 | 2.85 |
| 2 | 3 | 1 | 2.85 |
| 0 | 0 | 4 | 2.66 |
| 0 | 4 | 0 | 2.66 |
| 4 | 0 | 0 | 2.66 |
| 2 | 2 | 3 | 2.58 |
| 3 | 2 | 2 | 2.58 |
| 4 | 0 | 1 | 2.58 |
| 1 | 0 | 4 | 2.58 |
| 2 | 3 | 2 | 2.58 |
| 0 | 1 | 4 | 2.58 |
| 0 | 4 | 1 | 2.58 |
| 1 | 4 | 0 | 2.58 |
| 4 | 1 | 0 | 2.58 |

| | | | |
|---|---|---|---|
| 3 | 0 | 3 | 2.51 |
| 4 | 1 | 1 | 2.51 |
| 1 | 1 | 4 | 2.51 |
| 1 | 4 | 1 | 2.51 |
| 0 | 3 | 3 | 2.51 |
| 3 | 3 | 0 | 2.51 |
| 3 | 1 | 3 | 2.44 |
| 1 | 3 | 3 | 2.44 |
| 3 | 3 | 1 | 2.44 |
| 4 | 0 | 2 | 2.38 |
| 2 | 0 | 4 | 2.38 |
| 0 | 2 | 4 | 2.38 |
| 0 | 4 | 2 | 2.38 |
| 2 | 4 | 0 | 2.38 |
| 4 | 2 | 0 | 2.38 |
| 4 | 1 | 2 | 2.32 |
| 2 | 1 | 4 | 2.32 |
| 4 | 2 | 1 | 2.32 |
| 1 | 2 | 4 | 2.32 |
| 1 | 4 | 2 | 2.32 |
| 2 | 4 | 1 | 2.32 |
| 3 | 2 | 3 | 2.27 |
| 2 | 3 | 3 | 2.27 |
| 3 | 3 | 2 | 2.27 |
| 4 | 2 | 2 | 2.17 |
| 2 | 2 | 4 | 2.17 |
| 2 | 4 | 2 | 2.17 |
| 4 | 0 | 3 | 2.13 |
| 3 | 0 | 4 | 2.13 |
| 0 | 0 | 5 | 2.13 |
| 0 | 5 | 0 | 2.13 |
| 5 | 0 | 0 | 2.13 |
| 0 | 3 | 4 | 2.13 |
| 0 | 4 | 3 | 2.13 |
| 3 | 4 | 0 | 2.13 |
| 4 | 3 | 0 | 2.13 |
| 4 | 1 | 3 | 2.09 |
| 3 | 1 | 4 | 2.09 |
| 5 | 0 | 1 | 2.09 |
| 1 | 0 | 5 | 2.09 |
| 1 | 3 | 4 | 2.09 |

| | | | |
|---|---|---|---|
| 4 | 3 | 1 | 2.09 |
| 1 | 4 | 3 | 2.09 |
| 3 | 4 | 1 | 2.09 |
| 0 | 1 | 5 | 2.09 |
| 0 | 5 | 1 | 2.09 |
| 1 | 5 | 0 | 2.09 |
| 5 | 1 | 0 | 2.09 |
| 3 | 3 | 3 | 2.05 |
| 1 | 1 | 5 | 2.05 |
| 5 | 1 | 1 | 2.05 |
| 1 | 5 | 1 | 2.05 |
| 4 | 2 | 3 | 1.98 |
| 3 | 2 | 4 | 1.98 |
| 5 | 0 | 2 | 1.98 |
| 2 | 0 | 5 | 1.98 |
| 2 | 3 | 4 | 1.98 |
| 4 | 3 | 2 | 1.98 |
| 2 | 4 | 3 | 1.98 |
| 3 | 4 | 2 | 1.98 |
| 0 | 2 | 5 | 1.98 |
| 0 | 5 | 2 | 1.98 |
| 2 | 5 | 0 | 1.98 |
| 5 | 2 | 0 | 1.98 |
| 5 | 1 | 2 | 1.94 |
| 2 | 1 | 5 | 1.94 |
| 1 | 2 | 5 | 1.94 |
| 5 | 2 | 1 | 1.94 |
| 1 | 5 | 2 | 1.94 |
| 2 | 5 | 1 | 1.94 |
| 4 | 0 | 4 | 1.88 |
| 0 | 4 | 4 | 1.88 |
| 4 | 4 | 0 | 1.88 |
| 4 | 1 | 4 | 1.85 |
| 2 | 2 | 5 | 1.85 |
| 5 | 2 | 2 | 1.85 |
| 1 | 4 | 4 | 1.85 |
| 4 | 4 | 1 | 1.85 |
| 2 | 5 | 2 | 1.85 |
| 5 | 0 | 3 | 1.83 |
| 3 | 0 | 5 | 1.83 |
| 3 | 3 | 4 | 1.83 |

| | | | |
|---|---|---|---|
| 4 | 3 | 3 | 1.83 |
| 3 | 4 | 3 | 1.83 |
| 0 | 3 | 5 | 1.83 |
| 0 | 5 | 3 | 1.83 |
| 3 | 5 | 0 | 1.83 |
| 5 | 3 | 0 | 1.83 |
| 5 | 1 | 3 | 1.80 |
| 3 | 1 | 5 | 1.80 |
| 1 | 3 | 5 | 1.80 |
| 5 | 3 | 1 | 1.80 |
| 1 | 5 | 3 | 1.80 |
| 3 | 5 | 1 | 1.80 |
| 4 | 2 | 4 | 1.78 |
| 2 | 4 | 4 | 1.78 |
| 4 | 4 | 2 | 1.78 |
| 0 | 0 | 6 | 1.78 |
| 0 | 6 | 0 | 1.78 |
| 6 | 0 | 0 | 1.78 |
| 6 | 0 | 1 | 1.75 |
| 1 | 0 | 6 | 1.75 |
| 0 | 1 | 6 | 1.75 |
| 0 | 6 | 1 | 1.75 |
| 1 | 6 | 0 | 1.75 |
| 6 | 1 | 0 | 1.75 |
| 5 | 2 | 3 | 1.73 |
| 3 | 2 | 5 | 1.73 |
| 2 | 3 | 5 | 1.73 |
| 5 | 3 | 2 | 1.73 |
| 1 | 1 | 6 | 1.73 |
| 6 | 1 | 1 | 1.73 |
| 2 | 5 | 3 | 1.73 |
| 3 | 5 | 2 | 1.73 |
| 1 | 6 | 1 | 1.73 |

Vanadium[175]
Crystal system: Cubic
a = 3.03 å

| h | k | l | d (Å) |
|---|---|---|---|
| 0 | 1 | 0 | 3.03 |
| 0 | 0 | 1 | 3.03 |
| 1 | 0 | 0 | 3.03 |
| 1 | 0 | 1 | 2.14 |
| 0 | 1 | 1 | 2.14 |
| 1 | 1 | 0 | 2.14 |
| 1 | 1 | 1 | 1.75 |

Vanadia (III)[176]
Crystal system: Hexagonal
a = 4.95 å, c = 14.00 å

| h | k | l | d (Å) |
|---|---|---|---|
| 0 | 1 | 2 | 3.66 |
| 1 | 0 | 2 | 3.66 |
| -1 | 0 | 2 | 3.66 |
| 0 | -1 | 2 | 3.66 |
| -1 | 1 | 2 | 3.66 |
| 1 | -1 | 2 | 3.66 |
| 0 | 0 | 4 | 3.50 |
| 0 | 1 | 3 | 3.16 |
| 1 | 0 | 3 | 3.16 |
| -1 | 0 | 3 | 3.16 |
| 0 | -1 | 3 | 3.16 |
| -1 | 1 | 3 | 3.16 |
| 1 | -1 | 3 | 3.16 |
| 0 | 0 | 5 | 2.80 |
| 0 | 1 | 4 | 2.71 |
| 1 | 0 | 4 | 2.71 |
| -1 | 0 | 4 | 2.71 |
| 0 | -1 | 4 | 2.71 |
| -1 | 1 | 4 | 2.71 |
| 1 | -1 | 4 | 2.71 |
| 1 | 1 | 0 | 2.48 |
| -2 | 1 | 0 | 2.48 |
| -1 | 2 | 0 | 2.48 |
| 2 | -1 | 0 | 2.48 |
| 1 | -2 | 0 | 2.48 |
| 1 | 1 | 1 | 2.44 |
| -1 | 2 | 1 | 2.44 |
| -2 | 1 | 1 | 2.44 |
| 1 | -2 | 1 | 2.44 |
| 2 | -1 | 1 | 2.44 |
| 0 | 1 | 5 | 2.34 |
| 1 | 0 | 5 | 2.34 |

| | | | |
|---|---|---|---|
| -1 | 0 | 5 | 2.34 |
| 0 | -1 | 5 | 2.34 |
| -1 | 1 | 5 | 2.34 |
| 1 | -1 | 5 | 2.34 |
| 0 | 0 | 6 | 2.33 |
| 1 | 1 | 2 | 2.33 |
| -1 | 2 | 2 | 2.33 |
| -2 | 1 | 2 | 2.33 |
| 1 | -2 | 2 | 2.33 |
| 2 | -1 | 2 | 2.33 |
| 1 | 1 | 3 | 2.19 |
| -1 | 2 | 3 | 2.19 |
| -2 | 1 | 3 | 2.19 |
| 1 | -2 | 3 | 2.19 |
| 2 | -1 | 3 | 2.19 |
| 0 | 2 | 0 | 2.14 |
| 2 | 0 | 0 | 2.14 |
| -2 | 0 | 0 | 2.14 |
| 0 | -2 | 0 | 2.14 |
| -2 | 2 | 0 | 2.14 |
| 2 | -2 | 0 | 2.14 |
| 0 | 2 | 1 | 2.12 |
| 2 | 0 | 1 | 2.12 |
| -2 | 0 | 1 | 2.12 |
| 0 | -2 | 1 | 2.12 |
| -2 | 2 | 1 | 2.12 |
| 2 | -2 | 1 | 2.12 |
| 0 | 1 | 6 | 2.05 |
| 1 | 0 | 6 | 2.05 |
| -1 | 0 | 6 | 2.05 |
| 0 | -1 | 6 | 2.05 |
| -1 | 1 | 6 | 2.05 |
| 1 | -1 | 6 | 2.05 |
| 0 | 2 | 2 | 2.05 |
| 2 | 0 | 2 | 2.05 |
| -2 | 0 | 2 | 2.05 |
| 0 | -2 | 2 | 2.05 |
| -2 | 2 | 2 | 2.05 |
| 2 | -2 | 2 | 2.05 |
| 1 | 1 | 4 | 2.02 |
| -1 | 2 | 4 | 2.02 |
| -2 | 1 | 4 | 2.02 |
| 1 | -2 | 4 | 2.02 |
| 2 | -1 | 4 | 2.02 |
| 0 | 0 | 7 | 2.00 |
| 0 | 2 | 3 | 1.95 |
| 2 | 0 | 3 | 1.95 |
| -2 | 0 | 3 | 1.95 |
| 0 | -2 | 3 | 1.95 |
| -2 | 2 | 3 | 1.95 |
| 2 | -2 | 3 | 1.95 |
| 1 | 1 | 5 | 1.85 |
| -1 | 2 | 5 | 1.85 |
| 1 | -2 | 5 | 1.85 |
| -2 | 1 | 5 | 1.85 |
| 2 | -1 | 5 | 1.85 |
| 0 | 2 | 4 | 1.83 |
| 2 | 0 | 4 | 1.83 |
| -2 | 0 | 4 | 1.83 |
| 0 | -2 | 4 | 1.83 |
| -2 | 2 | 4 | 1.83 |
| 2 | -2 | 4 | 1.83 |
| 0 | 1 | 7 | 1.81 |
| 1 | 0 | 7 | 1.81 |
| -1 | 0 | 7 | 1.81 |
| 0 | -1 | 7 | 1.81 |
| -1 | 1 | 7 | 1.81 |
| 1 | -1 | 7 | 1.81 |
| 0 | 0 | 8 | 1.75 |
| 0 | 2 | 5 | 1.70 |
| 2 | 0 | 5 | 1.70 |
| -2 | 0 | 5 | 1.70 |
| 0 | -2 | 5 | 1.70 |
| -2 | 2 | 5 | 1.70 |
| 2 | -2 | 5 | 1.70 |

Metallic vanadia (IV) [177]
Crystal system: Tetragonal
a = 4.55 å, c = 2.85 å

| h | k | l | d (Å) |
|---|---|---|---|
| 1 | 1 | 0 | 3.22 |
| 0 | 0 | 1 | 2.85 |

| | | | |
|---|---|---|---|
| 0 | 1 | 1 | 2.42 |
| 1 | 0 | 1 | 2.42 |
| 0 | 2 | 0 | 2.28 |
| 2 | 0 | 0 | 2.28 |
| 1 | 1 | 1 | 2.13 |
| 2 | 1 | 0 | 2.04 |
| 1 | 2 | 0 | 2.04 |
| 0 | 2 | 1 | 1.78 |
| 2 | 0 | 1 | 1.78 |

Insulator vanadia (IV) [177]
Crystal system: Monoclinic
a = 5.74 å, b = 4.52å, c = 5.38 å
β = 122.61 deg

| h | k | l | d (Å) |
|---|---|---|---|
| -1 | 1 | 1 | 3.31 |
| 1 | 1 | -1 | 3.31 |
| 1 | 1 | 0 | 3.30 |
| -1 | 1 | 0 | 3.30 |
| 0 | 1 | 1 | 3.20 |
| 0 | 1 | -1 | 3.20 |
| -2 | 0 | 1 | 2.87 |
| 2 | 0 | -1 | 2.87 |
| -1 | 0 | 2 | 2.68 |
| 1 | 0 | -2 | 2.68 |
| 1 | 0 | 1 | 2.67 |
| -2 | 0 | 2 | 2.43 |
| 2 | 0 | -2 | 2.43 |
| -2 | 1 | 1 | 2.42 |
| 2 | 1 | -1 | 2.42 |
| 2 | 0 | 0 | 2.42 |
| -2 | 0 | 0 | 2.42 |
| -1 | 1 | 2 | 2.30 |
| 1 | 1 | -2 | 2.30 |
| 1 | 1 | 1 | 2.30 |
| 0 | 0 | 2 | 2.26 |
| 0 | 0 | -2 | 2.26 |
| 0 | 2 | 0 | 2.26 |
| -2 | 1 | 2 | 2.14 |
| 2 | 1 | -2 | 2.14 |
| 2 | 1 | 0 | 2.13 |
| -2 | 1 | 0 | 2.13 |
| -1 | 2 | 1 | 2.05 |
| 1 | 2 | -1 | 2.05 |
| 1 | 2 | 0 | 2.05 |
| -1 | 2 | 0 | 2.05 |
| 0 | 1 | 2 | 2.02 |
| 0 | 1 | -2 | 2.02 |
| 0 | 2 | 1 | 2.02 |
| 0 | 2 | -1 | 2.02 |
| -3 | 0 | 2 | 1.88 |
| 3 | 0 | -2 | 1.88 |
| -3 | 0 | 1 | 1.87 |
| 3 | 0 | -1 | 1.87 |
| -2 | 0 | 3 | 1.78 |
| 2 | 0 | -3 | 1.78 |
| -2 | 2 | 1 | 1.78 |
| 2 | 2 | -1 | 1.78 |
| 2 | 0 | 1 | 1.77 |
| -3 | 1 | 2 | 1.73 |
| 3 | 1 | -2 | 1.73 |
| -1 | 0 | 3 | 1.73 |
| 1 | 0 | -3 | 1.73 |
| -3 | 1 | 1 | 1.73 |
| 3 | 1 | -1 | 1.73 |
| -1 | 2 | 2 | 1.73 |
| 1 | 2 | -2 | 1.73 |
| 1 | 0 | 2 | 1.72 |
| 1 | 2 | 1 | 1.72 |

Vanadium carbide, disordered (VC) [178]
Crystal system: Cubic
a = 4.14-4.34 å

The lattice parameter for the lower to upper substoichiometric range of $VC_x$

| h | k | l | d (Å) |
|---|---|---|---|
| 0 | 1 | 1 | 2.93-3.07 |
| 1 | 1 | 0 | 2.93-3.07 |
| 1 | 0 | 1 | 2.93-3.07 |
| 1 | 1 | 1 | 2.39-2.51 |
| 0 | 0 | 2 | 2.07-2.17 |
| 0 | 2 | 0 | 2.07-2.17 |

| | | | |
|---|---|---|---|
| 2 | 0 | 0 | 2.07-2.17 |
| 0 | 1 | 2 | 1.85-1.94 |
| 0 | 2 | 1 | 1.85-1.94 |
| 2 | 0 | 1 | 1.85-1.94 |
| 1 | 0 | 2 | 1.85-1.94 |
| 2 | 1 | 0 | 1.85-1.94 |
| 1 | 2 | 0 | 1.85-1.94 |
| 1 | 1 | 2 | 1.69-1.77 |
| 1 | 2 | 1 | 1.69-1.77 |
| 2 | 1 | 1 | 1.69-1.77 |

Vanadium carbide ($V_8C_7$) [180]
Crystal system: Cubic
a = 8.334 å

| h | k | l | d (Å) |
|---|---|---|---|
| 1 | 0 | 2 | 3.73 |
| 0 | 1 | 2 | 3.73 |
| 2 | 0 | 1 | 3.73 |
| 2 | 1 | 0 | 3.73 |
| 0 | 2 | 1 | 3.73 |
| 1 | 2 | 0 | 3.73 |
| 1 | 1 | 2 | 3.40 |
| 2 | 1 | 1 | 3.40 |
| 1 | 2 | 1 | 3.40 |
| 2 | 0 | 2 | 2.95 |
| 0 | 2 | 2 | 2.95 |
| 2 | 2 | 0 | 2.95 |
| 0 | 0 | 3 | 2.78 |
| 0 | 3 | 0 | 2.78 |
| 3 | 0 | 0 | 2.78 |
| 2 | 1 | 2 | 2.78 |
| 1 | 2 | 2 | 2.78 |
| 2 | 2 | 1 | 2.78 |
| 1 | 0 | 3 | 2.64 |
| 0 | 1 | 3 | 2.64 |
| 0 | 3 | 1 | 2.64 |
| 1 | 3 | 0 | 2.64 |
| 3 | 1 | 0 | 2.64 |
| 3 | 0 | 1 | 2.64 |
| 1 | 1 | 3 | 2.51 |
| 1 | 3 | 1 | 2.51 |
| 3 | 1 | 1 | 2.51 |
| 2 | 2 | 2 | 2.41 |
| 2 | 0 | 3 | 2.31 |
| 0 | 2 | 3 | 2.31 |
| 0 | 3 | 2 | 2.31 |
| 2 | 3 | 0 | 2.31 |
| 3 | 2 | 0 | 2.31 |
| 3 | 0 | 2 | 2.31 |
| 2 | 1 | 3 | 2.23 |
| 1 | 2 | 3 | 2.23 |
| 1 | 3 | 2 | 2.23 |
| 2 | 3 | 1 | 2.23 |
| 3 | 2 | 1 | 2.23 |
| 3 | 1 | 2 | 2.23 |
| 0 | 0 | 4 | 2.08 |
| 0 | 4 | 0 | 2.08 |
| 4 | 0 | 0 | 2.08 |
| 1 | 0 | 4 | 2.02 |
| 0 | 1 | 4 | 2.02 |
| 2 | 2 | 3 | 2.02 |
| 2 | 3 | 2 | 2.02 |
| 0 | 4 | 1 | 2.02 |
| 1 | 4 | 0 | 2.02 |
| 3 | 2 | 2 | 2.02 |
| 4 | 1 | 0 | 2.02 |
| 4 | 0 | 1 | 2.02 |
| 1 | 1 | 4 | 1.96 |
| 0 | 3 | 3 | 1.96 |
| 1 | 4 | 1 | 1.96 |
| 3 | 3 | 0 | 1.96 |
| 3 | 0 | 3 | 1.96 |
| 4 | 1 | 1 | 1.96 |
| 1 | 3 | 3 | 1.91 |
| 3 | 3 | 1 | 1.91 |
| 3 | 1 | 3 | 1.91 |
| 0 | 2 | 4 | 1.86 |
| 0 | 4 | 2 | 1.86 |
| 2 | 4 | 0 | 1.86 |
| 2 | 0 | 4 | 1.86 |
| 4 | 2 | 0 | 1.86 |
| 4 | 0 | 2 | 1.86 |

| | | | |
|---|---|---|---|
| 1 | 2 | 4 | 1.82 |
| 1 | 4 | 2 | 1.82 |
| 2 | 4 | 1 | 1.82 |
| 2 | 1 | 4 | 1.82 |
| 4 | 2 | 1 | 1.82 |
| 4 | 1 | 2 | 1.82 |
| 2 | 3 | 3 | 1.78 |
| 3 | 3 | 2 | 1.78 |
| 3 | 2 | 3 | 1.78 |
| 2 | 4 | 2 | 1.70 |
| 2 | 2 | 4 | 1.70 |
| 4 | 2 | 2 | 1.70 |

Vanadium carbide ($V_6C_5$) [180]
Crystal system: Hexagonal/Trigonal
a = 5.09 å, c = 14.40 å

| h | k | l | d (Å) |
|---|---|---|---|
| 1 | 0 | 2 | 3.76 |
| 0 | 1 | 2 | 3.76 |
| -1 | 0 | 2 | 3.76 |
| -1 | 1 | 2 | 3.76 |
| 0 | -1 | 2 | 3.76 |
| 1 | -1 | 2 | 3.76 |
| 0 | 0 | 4 | 3.60 |
| 1 | 0 | 3 | 3.25 |
| 0 | 1 | 3 | 3.25 |
| -1 | 0 | 3 | 3.25 |
| -1 | 1 | 3 | 3.25 |
| 0 | -1 | 3 | 3.25 |
| 1 | -1 | 3 | 3.25 |
| 0 | 0 | 5 | 2.88 |
| 1 | 0 | 4 | 2.79 |
| 0 | 1 | 4 | 2.79 |
| -1 | 0 | 4 | 2.79 |
| -1 | 1 | 4 | 2.79 |
| 0 | -1 | 4 | 2.79 |
| 1 | -1 | 4 | 2.79 |
| 1 | 1 | 0 | 2.55 |
| -2 | 1 | 0 | 2.55 |
| -1 | 2 | 0 | 2.55 |
| 2 | -1 | 0 | 2.55 |
| 1 | -2 | 0 | 2.55 |
| 1 | 1 | 1 | 2.51 |
| -2 | 1 | 1 | 2.51 |
| -1 | 2 | 1 | 2.51 |
| 2 | -1 | 1 | 2.51 |
| 1 | -2 | 1 | 2.51 |
| 1 | 0 | 5 | 2.41 |
| 0 | 1 | 5 | 2.41 |
| -1 | 0 | 5 | 2.41 |
| -1 | 1 | 5 | 2.41 |
| 0 | -1 | 5 | 2.41 |
| 1 | -1 | 5 | 2.41 |
| 0 | 0 | 6 | 2.40 |
| 1 | 1 | 2 | 2.40 |
| -2 | 1 | 2 | 2.40 |
| -1 | 2 | 2 | 2.40 |
| 2 | -1 | 2 | 2.40 |
| 1 | -2 | 2 | 2.40 |
| 1 | 1 | 3 | 2.25 |
| -2 | 1 | 3 | 2.25 |
| -1 | 2 | 3 | 2.25 |
| 2 | -1 | 3 | 2.25 |
| 1 | -2 | 3 | 2.25 |
| 2 | 0 | 0 | 2.20 |
| 0 | 2 | 0 | 2.20 |
| -2 | 0 | 0 | 2.20 |
| -2 | 2 | 0 | 2.20 |
| 0 | -2 | 0 | 2.20 |
| 2 | -2 | 0 | 2.20 |
| 2 | 0 | 1 | 2.18 |
| 0 | 2 | 1 | 2.18 |
| -2 | 0 | 1 | 2.18 |
| -2 | 2 | 1 | 2.18 |
| 0 | -2 | 1 | 2.18 |
| 2 | -2 | 1 | 2.18 |
| 0 | 1 | 6 | 2.11 |
| 1 | 0 | 6 | 2.11 |
| -1 | 0 | 6 | 2.11 |
| -1 | 1 | 6 | 2.11 |
| 0 | -1 | 6 | 2.11 |
| 1 | -1 | 6 | 2.11 |

| | | | |
|---|---|---|---|
| 2 | 0 | 2 | 2.11 |
| 0 | 2 | 2 | 2.11 |
| -2 | 0 | 2 | 2.11 |
| -2 | 2 | 2 | 2.11 |
| 0 | -2 | 2 | 2.11 |
| 2 | -2 | 2 | 2.11 |
| 1 | 1 | 4 | 2.08 |
| -1 | 2 | 4 | 2.08 |
| -2 | 1 | 4 | 2.08 |
| 1 | -2 | 4 | 2.08 |
| 2 | -1 | 4 | 2.08 |
| 0 | 0 | 7 | 2.06 |
| 2 | 0 | 3 | 2.00 |
| 0 | 2 | 3 | 2.00 |
| -2 | 0 | 3 | 2.00 |
| -2 | 2 | 3 | 2.00 |
| 0 | -2 | 3 | 2.00 |
| 2 | -2 | 3 | 2.00 |
| 1 | 1 | 5 | 1.91 |
| -1 | 2 | 5 | 1.91 |
| -2 | 1 | 5 | 1.91 |
| 1 | -2 | 5 | 1.91 |
| 2 | -1 | 5 | 1.91 |
| 0 | 2 | 4 | 1.88 |
| 2 | 0 | 4 | 1.88 |
| -2 | 0 | 4 | 1.88 |
| -2 | 2 | 4 | 1.88 |
| 0 | -2 | 4 | 1.88 |
| 2 | -2 | 4 | 1.88 |
| 0 | 1 | 7 | 1.86 |
| 1 | 0 | 7 | 1.86 |
| -1 | 0 | 7 | 1.86 |
| -1 | 1 | 7 | 1.86 |
| 0 | -1 | 7 | 1.86 |
| 1 | -1 | 7 | 1.86 |
| 0 | 0 | 8 | 1.80 |
| 0 | 2 | 5 | 1.75 |
| 2 | 0 | 5 | 1.75 |
| -2 | 0 | 5 | 1.75 |
| -2 | 2 | 5 | 1.75 |
| 0 | -2 | 5 | 1.75 |
| 2 | -2 | 5 | 1.75 |
| 1 | 1 | 6 | 1.75 |
| -1 | 2 | 6 | 1.75 |
| -2 | 1 | 6 | 1.75 |
| 1 | -2 | 6 | 1.75 |
| 2 | -1 | 6 | 1.75 |

Vanadium carbide (ζ-$V_4C_3$) [180]
Crystal system: Hexagonal/Trigonal
a = 2.92 å, c = 29.83 å

| h | k | l | d (Å) |
|---|---|---|---|
| 0 | 0 | 8 | 3.73 |
| 0 | 0 | 9 | 3.31 |
| 0 | 0 | 10 | 2.98 |
| 1 | 0 | 0 | 2.53 |
| 0 | 1 | 0 | 2.53 |
| -1 | 0 | 0 | 2.53 |
| -1 | 1 | 0 | 2.53 |
| 0 | -1 | 0 | 2.53 |
| 1 | -1 | 0 | 2.53 |
| 1 | 0 | 1 | 2.52 |
| 0 | 1 | 1 | 2.52 |
| -1 | 0 | 1 | 2.52 |
| -1 | 1 | 1 | 2.52 |
| 0 | -1 | 1 | 2.52 |
| 1 | -1 | 1 | 2.52 |
| 1 | 0 | 2 | 2.49 |
| 0 | 1 | 2 | 2.49 |
| -1 | 0 | 2 | 2.49 |
| -1 | 1 | 2 | 2.49 |
| 0 | -1 | 2 | 2.49 |
| 1 | -1 | 2 | 2.49 |
| 1 | 0 | 3 | 2.45 |
| 0 | 1 | 3 | 2.45 |
| -1 | 0 | 3 | 2.45 |
| -1 | 1 | 3 | 2.45 |
| 0 | -1 | 3 | 2.45 |
| 1 | -1 | 3 | 2.45 |
| 1 | 0 | 4 | 2.39 |
| 0 | 1 | 4 | 2.39 |
| -1 | 0 | 4 | 2.39 |

| | | | |
|---|---|---|---|
| -1 | 1 | 4 | 2.39 |
| 0 | -1 | 4 | 2.39 |
| 1 | -1 | 4 | 2.39 |
| 1 | 0 | 5 | 2.33 |
| 0 | 1 | 5 | 2.33 |
| -1 | 0 | 5 | 2.33 |
| -1 | 1 | 5 | 2.33 |
| 0 | -1 | 5 | 2.33 |
| 1 | -1 | 5 | 2.33 |
| 0 | 1 | 6 | 2.25 |
| 1 | 0 | 6 | 2.25 |
| -1 | 0 | 6 | 2.25 |
| -1 | 1 | 6 | 2.25 |
| 0 | -1 | 6 | 2.25 |
| 1 | -1 | 6 | 2.25 |
| 0 | 1 | 7 | 2.17 |
| 1 | 0 | 7 | 2.17 |
| -1 | 0 | 7 | 2.17 |
| -1 | 1 | 7 | 2.17 |
| 0 | -1 | 7 | 2.17 |
| 1 | -1 | 7 | 2.17 |
| 0 | 1 | 8 | 2.09 |
| 1 | 0 | 8 | 2.09 |
| -1 | 0 | 8 | 2.09 |
| 0 | -1 | 8 | 2.09 |
| 0 | 1 | 9 | 2.01 |
| 1 | 0 | 9 | 2.01 |
| -1 | 0 | 9 | 2.01 |
| 0 | -1 | 9 | 2.01 |

Vanadium carbide, disordered ($V_2C$) [180]
Crystal system: Hexagonal
a = 2.88 å, c = 4.57 å

| h | k | l | d (Å) |
|---|---|---|---|
| 0 | 1 | 0 | 2.50 |
| 1 | 0 | 0 | 2.50 |
| -1 | 0 | 0 | 2.50 |
| 0 | -1 | 0 | 2.50 |
| -1 | 1 | 0 | 2.50 |
| 1 | -1 | 0 | 2.50 |
| 0 | 0 | 2 | 2.29 |
| 0 | 1 | 1 | 2.19 |
| 1 | 0 | 1 | 2.19 |
| -1 | 0 | 1 | 2.19 |
| 0 | -1 | 1 | 2.19 |
| -1 | 1 | 1 | 2.19 |
| 1 | -1 | 1 | 2.19 |

Vanadium carbide, ε-$Fe_2N$ ($V_2C$) [180]
Crystal system: Hexagonal
a = 5.00 å, c = 4.55 å

| h | k | l | d (Å) |
|---|---|---|---|
| 0 | 1 | 1 | 3.14 |
| 1 | 0 | 1 | 3.14 |
| -1 | 0 | 1 | 3.14 |
| -1 | 1 | 1 | 3.14 |
| 0 | -1 | 1 | 3.14 |
| 1 | -1 | 1 | 3.14 |
| 1 | 1 | 0 | 2.50 |
| -2 | 1 | 0 | 2.50 |
| -1 | 2 | 0 | 2.50 |
| 2 | -1 | 0 | 2.50 |
| 1 | -2 | 0 | 2.50 |
| 0 | 0 | 2 | 2.28 |
| 1 | 1 | 1 | 2.19 |
| -1 | 2 | 1 | 2.19 |
| -2 | 1 | 1 | 2.19 |
| 1 | -2 | 1 | 2.19 |
| 2 | -1 | 1 | 2.19 |
| 0 | 2 | 0 | 2.17 |
| 2 | 0 | 0 | 2.17 |
| -2 | 0 | 0 | 2.17 |
| -2 | 2 | 0 | 2.17 |
| 0 | -2 | 0 | 2.17 |
| 2 | -2 | 0 | 2.17 |
| 0 | 1 | 2 | 2.01 |
| 1 | 0 | 2 | 2.01 |
| -1 | 0 | 2 | 2.01 |
| -1 | 1 | 2 | 2.01 |
| 0 | -1 | 2 | 2.01 |
| 1 | -1 | 2 | 2.01 |
| 0 | 2 | 1 | 1.96 |

|  |  |  |  |
|---|---|---|---|
| 2 | 0 | 1 | 1.96 |
| -2 | 0 | 1 | 1.96 |
| -2 | 2 | 1 | 1.96 |
| 0 | -2 | 1 | 1.96 |
| 2 | -2 | 1 | 1.96 |

### Vanadium carbide, ζ-Fe$_2$N (V$_2$C) [180]

Crystal system: Orthorhombic

a = 4.57 å, b = 5.74 å, c = 5.03 å

| h | k | l | d (Å) |
|---|---|---|---|
| 0 | 1 | 1 | 3.78 |
| 1 | 1 | 0 | 3.58 |
| 1 | 0 | 1 | 3.38 |
| 1 | 1 | 1 | 2.91 |
| 0 | 2 | 0 | 2.87 |
| 0 | 0 | 2 | 2.52 |
| 0 | 2 | 1 | 2.49 |
| 1 | 2 | 0 | 2.43 |
| 0 | 1 | 2 | 2.30 |
| 2 | 0 | 0 | 2.29 |
| 1 | 0 | 2 | 2.20 |
| 1 | 2 | 1 | 2.19 |
| 2 | 1 | 0 | 2.12 |
| 2 | 0 | 1 | 2.08 |
| 1 | 1 | 2 | 2.06 |
| 2 | 1 | 1 | 1.96 |
| 0 | 3 | 0 | 1.91 |
| 0 | 2 | 2 | 1.89 |
| 0 | 3 | 1 | 1.79 |
| 2 | 2 | 0 | 1.79 |
| 1 | 3 | 0 | 1.76 |
| 1 | 2 | 2 | 1.75 |

### Vanadium carbide, ζ'-Fe$_2$N (V$_2$C) [180]

Crystal system: Orthorhombic

a = 4.55 å, b = 11.49 å, c = 10.06 å

| h | k | l | d (Å) |
|---|---|---|---|
| 1 | 1 | 1 | 3.90 |
| 0 | 3 | 0 | 3.83 |
| 0 | 2 | 2 | 3.78 |
| 0 | 3 | 1 | 3.58 |
| 1 | 2 | 0 | 3.57 |
| 1 | 0 | 2 | 3.37 |
| 1 | 2 | 1 | 3.36 |
| 0 | 0 | 3 | 3.35 |
| 1 | 1 | 2 | 3.24 |
| 0 | 1 | 3 | 3.22 |
| 0 | 3 | 2 | 3.05 |
| 1 | 3 | 0 | 2.93 |
| 1 | 2 | 2 | 2.91 |
| 0 | 2 | 3 | 2.90 |
| 0 | 4 | 0 | 2.87 |
| 1 | 3 | 1 | 2.81 |
| 0 | 4 | 1 | 2.76 |
| 1 | 0 | 3 | 2.70 |
| 1 | 1 | 3 | 2.63 |
| 1 | 3 | 2 | 2.53 |
| 0 | 3 | 3 | 2.52 |
| 0 | 0 | 4 | 2.52 |
| 0 | 4 | 2 | 2.49 |
| 0 | 1 | 4 | 2.46 |
| 1 | 2 | 3 | 2.44 |
| 1 | 4 | 0 | 2.43 |
| 1 | 4 | 1 | 2.36 |
| 0 | 2 | 4 | 2.30 |
| 0 | 5 | 0 | 2.30 |
| 2 | 0 | 0 | 2.28 |
| 0 | 5 | 1 | 2.24 |
| 2 | 1 | 0 | 2.23 |
| 2 | 0 | 1 | 2.22 |
| 1 | 3 | 3 | 2.21 |
| 1 | 0 | 4 | 2.20 |
| 1 | 4 | 2 | 2.19 |
| 0 | 4 | 3 | 2.18 |
| 2 | 1 | 1 | 2.18 |
| 1 | 1 | 4 | 2.16 |
| 2 | 2 | 0 | 2.12 |
| 0 | 3 | 4 | 2.10 |
| 0 | 5 | 2 | 2.09 |
| 2 | 0 | 2 | 2.07 |
| 2 | 2 | 1 | 2.07 |
| 1 | 2 | 4 | 2.06 |
| 1 | 5 | 0 | 2.05 |

| | | | |
|---|---|---|---|
| 2 | 1 | 2 | 2.04 |
| 0 | 0 | 5 | 2.01 |
| 1 | 5 | 1 | 2.01 |
| 0 | 1 | 5 | 1.98 |
| 1 | 4 | 3 | 1.97 |
| 2 | 3 | 0 | 1.96 |
| 2 | 2 | 2 | 1.95 |
| 2 | 3 | 1 | 1.92 |
| 0 | 6 | 0 | 1.92 |
| 1 | 3 | 4 | 1.91 |
| 1 | 5 | 2 | 1.90 |
| 0 | 2 | 5 | 1.90 |
| 0 | 5 | 3 | 1.90 |
| 0 | 4 | 4 | 1.89 |
| 2 | 0 | 3 | 1.88 |
| 0 | 6 | 1 | 1.88 |
| 2 | 1 | 3 | 1.86 |
| 1 | 0 | 5 | 1.84 |
| 2 | 3 | 2 | 1.82 |
| 1 | 1 | 5 | 1.82 |
| 0 | 6 | 2 | 1.79 |
| 2 | 2 | 3 | 1.79 |
| 2 | 4 | 0 | 1.78 |
| 0 | 3 | 5 | 1.78 |
| 1 | 6 | 0 | 1.77 |
| 2 | 4 | 1 | 1.76 |
| 1 | 2 | 5 | 1.75 |
| 1 | 5 | 3 | 1.75 |
| 1 | 4 | 4 | 1.75 |
| 1 | 6 | 1 | 1.74 |

Vanadium carbide, ξ-Nb$_2$N (V$_2$C)[180]
Crystal system: Orthorhombic
a = 4.97 å, b = 3.09 å, c = 10.92 å

| | | | |
|---|---|---|---|
| 1 | 0 | 2 | 3.68 |
| 0 | 0 | 3 | 3.64 |
| 0 | 1 | 0 | 3.09 |
| 0 | 1 | 1 | 2.97 |
| 1 | 0 | 3 | 2.94 |
| 0 | 0 | 4 | 2.73 |
| 0 | 1 | 2 | 2.69 |
| 1 | 1 | 0 | 2.62 |
| 1 | 1 | 1 | 2.55 |
| 2 | 0 | 0 | 2.49 |
| 2 | 0 | 1 | 2.42 |
| 1 | 0 | 4 | 2.39 |
| 1 | 1 | 2 | 2.37 |
| 0 | 1 | 3 | 2.36 |
| 2 | 0 | 2 | 2.26 |
| 0 | 0 | 5 | 2.18 |
| 1 | 1 | 3 | 2.13 |
| 2 | 0 | 3 | 2.05 |
| 0 | 1 | 4 | 2.05 |
| 1 | 0 | 5 | 2.00 |
| 2 | 1 | 0 | 1.94 |
| 2 | 1 | 1 | 1.91 |
| 1 | 1 | 4 | 1.89 |
| 2 | 0 | 4 | 1.84 |
| 2 | 1 | 2 | 1.83 |
| 0 | 0 | 6 | 1.82 |
| 0 | 1 | 5 | 1.78 |
| 2 | 1 | 3 | 1.71 |

Ceria[185]
Crystal system: Cubic
a = 5.41 å

| h | k | l | d (Å) |
|---|---|---|---|
| 1 | 0 | 1 | 3.83 |
| 0 | 1 | 1 | 3.83 |
| 1 | 1 | 0 | 3.83 |
| 1 | 1 | 1 | 3.12 |
| 0 | 2 | 0 | 2.71 |
| 0 | 0 | 2 | 2.71 |
| 2 | 0 | 0 | 2.71 |
| 2 | 0 | 1 | 2.42 |
| 1 | 0 | 2 | 2.42 |
| 0 | 2 | 1 | 2.42 |
| 1 | 2 | 0 | 2.42 |
| 0 | 1 | 2 | 2.42 |
| 2 | 1 | 0 | 2.42 |
| 1 | 1 | 2 | 2.21 |
| 2 | 1 | 1 | 2.21 |
| 1 | 2 | 1 | 2.21 |

| | | | |
|---|---|---|---|
| 2 | 0 | 2 | 1.91 |
| 0 | 2 | 2 | 1.91 |
| 2 | 2 | 0 | 1.91 |
| 0 | 3 | 0 | 1.80 |
| 0 | 0 | 3 | 1.80 |
| 3 | 0 | 0 | 1.80 |
| 3 | 0 | 1 | 1.71 |
| 1 | 0 | 3 | 1.71 |
| 0 | 3 | 1 | 1.71 |
| 1 | 3 | 0 | 1.71 |
| 0 | 1 | 3 | 1.71 |
| 3 | 1 | 0 | 1.71 |

Lithia ($Li_2O$) [184]
Crystal system: Cubic
a = 4.61 å

| h | k | l | d (Å) |
|---|---|---|---|
| 1 | 0 | 1 | 3.26 |
| 0 | 1 | 1 | 3.26 |
| 1 | 1 | 0 | 3.26 |
| 1 | 1 | 1 | 2.66 |
| 0 | 2 | 0 | 2.31 |
| 0 | 0 | 2 | 2.31 |
| 2 | 0 | 0 | 2.31 |
| 2 | 0 | 1 | 2.06 |
| 1 | 0 | 2 | 2.06 |
| 0 | 2 | 1 | 2.06 |
| 1 | 2 | 0 | 2.06 |
| 0 | 1 | 2 | 2.06 |
| 2 | 1 | 0 | 2.06 |
| 1 | 1 | 2 | 1.88 |
| 2 | 1 | 1 | 1.88 |
| 1 | 2 | 1 | 1.88 |

# References

[1] M. F. L. De Volder, S. H. Tawfick, R. H. Baughman, A. J. Hart, *Science* **339**, 535 (2013).

[2] A. Zurutuza, C. Marinelli, *Nature Nanotechnology* **9**, 730 (2014).

[3] S. Iijima, *Nature* **354**, 56 (1991).

[4] Y. Ando, X. Zhao, T. Sugai, M. Kumar, *Materials Today* **7**, 22 (2004).

[5] G. D. Nessim, *Nanoscale* **2**, 1306 (2010).

[6] P. Nikolaev, *et al.*, *Chemical Physics Letters* **313**, 91 (1999).

[7] I. W. Chiang, *et al.*, *The Journal of Physical Chemistry B* **105**, 8297 (2001).

[8] B. Kitiyanan, W. Alvarez, J. Harwell, D. Resasco, *Chemical Physics Letters* **317**, 497 (2000).

[9] K. S. Novoselov, *et al.*, *Science* **306**, 666 (2004).

[10] Y. Zhang, L. Zhang, C. Zhou, *Accounts of Chemical Research* **46**, 2329 (2013).

[11] D. M. Guldi, V. Sgobba, *Chemical Communications* **47**, 606 (2010).

[12] S. A. Steiner, Carbon nanotube growth on challenging substrates : applications for carbon-fiber composites, Phd thesis, Massachusetts Institute of Technology (2011).

[13] N. Halonen, *et al.*, *physica status solidi b* **248**, 2500 (2011).

[14] A. Magrez, *et al.*, *ACS Nano* **4**, 3702 (2010).

[15] M. Jung, *et al.*, *Diamond and Related Materials* **10**, 1235 (2001). 11th European Conference on Diamond, Diamond-like Materials, Carbon Nanotubes, Nitrides and Silicon Carbide.

[16] D. N. Futaba, *et al.*, *Phys. Rev. Lett.* **95**, 056104 (2005).

[17] S. Hofmann, P. Braeuninger-Weimer, R. S. Weatherup, *The Journal of Physical Chemistry Letters* **6**, 2714 (2015).

[18] W. Wang, *et al.*, *Nano Energy* **2**, 294 (2013).

[19] S. Bhaviripudi, X. Jia, M. S. Dresselhaus, J. Kong, *Nano Letters* **10**, 4128 (2010).

[20] F. H. Monteiro, *et al.*, *The Journal of Physical Chemistry C* **116**, 3281 (2012).

[21] S. Chen, *et al.*, *Advanced Materials* **25**, 2062 (2013).

[22] Y. Li, *et al.*, *Nano Letters* **4**, 317 (2004).

[23] M. R. Maschmann, *et al.*, *Carbon* **44**, 10 (2006).

[24] A. Oberlin, M. Endo, T. Koyama, *Journal of Crystal Growth* **32**, 335 (1976).

[25] K. Hernadi, A. Fonseca, J. B. Nagy, D. Bernaerts, A. A. Lucas, *Carbon* **34**, 1249 (1996).

[26] E. F. Kukovitsky, S. G. L'vov, N. A. Sainov, V. A. Shustov, L. A. Chernozatonskii, *Chemical Physics Letters* **355**, 497 (2002).

[27] Y. Homma, *et al.*, *The Journal of Physical Chemistry B* **107**, 12161 (2003).

[28] D. Takagi, Y. Homma, H. Hibino, S. Suzuki, Y. Kobayashi, *Nano Letters* **6**, 2642 (2006).

[29] O. Jost, *et al.*, *Applied Physics Letters* **75**, 2217 (1999).

[30] Y. Li, *et al.*, *Chemistry of Materials* **13**, 1008 (2001).

[31] J. Kong, A. M. Cassell, H. Dai, *Chemical Physics Letters* **292**, 567 (1998).

[32] M. J. Bronikowski, *Carbon* **44**, 2822 (2006).

[33] V. Kayastha, Y. K. Yap, S. Dimovski, Y. Gogotsi, *Applied Physics Letters* **85**, 3265 (2004).

[34] S. Maruyama, R. Kojima, Y. Miyauchi, S. Chiashi, M. Kohno, *Chemical Physics Letters* **360**, 229 (2002).

[35] S. C. Lyu, *et al.*, *Chemistry of Materials* **15**, 3951 (2003).

[36] Q. Yu, *et al.*, *Applied Physics Letters* **93**, 113103 (2008).

[37] X. Li, *et al.*, *Science* **324**, 1312 (2009).

[38] C. T. Wirth, C. Zhang, G. Zhong, S. Hofmann, J. Robertson, *ACS Nano* **3**, 3560 (2009).

[39] A. Rinzler, *et al.*, *Applied Physics A: Materials Science & Processing* **67**, 29 (1998).

[40] L. Wang, A. Ambrosi, M. Pumera, *Angewandte Chemie International Edition* **52**, 13818 (2013).

[41] E. L. K. Chng, H. L. Poh, Z. Sofer, M. Pumera, *Physical Chemistry Chemical Physics* **15**, 5615 (2013).

[42] C. Ge, *et al.*, *NPG Asia Materials* **4**, e32 (2012).

[43] J. W. Suk, *et al.*, *ACS Nano* **5**, 6916 (2011).

[44] D. L. Mafra, T. Ming, J. Kong, *Nanoscale* **7**, 14807 (2015).

[45] S. Boncel, K. K. K. Koziol, *Applied Surface Science* **301**, 488 (2014).

[46] D. Takagi, H. Hibino, S. Suzuki, Y. Kobayashi, Y. Homma, *Nano Letters* **7**, 2272 (2007).

[47] H. Liu, *et al.*, *Appl. Phys. Express* **1**, 014001 (2008).

[48] S. Huang, Q. Cai, J. Chen, Y. Qian, L. Zhang, *Journal of the American Chemical Society* **131**, 2094 (2009).

[49] B. Liu, *et al.*, *Acs Nano* **3**, 3421 (2009).

[50] T. Liu, *et al.*, *Carbon* **56**, 167 (2013).

[51] Y. Chen, J. Zhang, *Carbon* **49**, 3316 (2011).

[52] S. A. Steiner, *et al.*, *Journal of the American Chemical Society* **131**, 12144 (2009).

[53] Q. Cai, Y. Hu, Y. Liu, S. Huang, *Applied Surface Science* **258**, 8019 (2012).

[54] L. Zhang, *et al.*, *Carbon* **55**, 253 (2013).

[55] B. C. Bayer, *et al.*, *RSC Advances* **3**, 4086 (2013).

[56] D. Takagi, Y. Kobayashi, Y. Homma, *Journal of the American Chemical Society* **131**, 6922 (2009).

[57] X. Xu, C. Yang, Z. Yang, K. Yang, S. Huang, *Carbon* **80**, 490 (2014).

[58] M. Kogler, *et al.*, *Chemistry of Materials* **26**, 1690 (2014).

[59] M. H. Rümmeli, *et al.*, *Chemistry of Materials* **19**, 4105 (2007).

[60] M. H. Rümmeli, *et al.*, *ACS Nano* **4**, 4206 (2010).

[61] P. R. Kidambi, *et al.*, *physica status solidi RRL* **5**, 341 (2011).

[62] K. Saito, T. Ogino, *J. Phys. Chem. C* **118**, 5523 (2014).

[63] H. Medina, *et al.*, *Adv. Funct. Mater.* **22**, 2123 (2012).

[64] N. R. Franklin, Y. Li, R. J. Chen, A. Javey, H. Dai, *Applied Physics Letters* **79**, 4571 (2001).

[65] A. Bachmatiuk, *et al.*, *ACS Nano* **3**, 4098 (2009).

[66] S. Hofmann, *et al.*, *Nano Letters* **7**, 602 (2007).

[67] S. Helveg, *et al.*, *Nature* **427**, 426 (2004).

[68] H. Yoshida, S. Takeda, T. Uchiyama, H. Kohno, Y. Homma, *Nano Letters* **8**, 2082 (2008).

[69] M. Lin, *et al.*, *Nano Letters* **7**, 2234 (2007).

[70] D. M. Tang, *et al.*, *ACS Nano* **8**, 292 (2014).

[71] S. Hofmann, G. Csnyi, A. C. Ferrari, M. C. Payne, J. Robertson, *Physical Review Letters* **95**, 036101 (2005).

[72] J. Robertson, *Journal of Materials Chemistry* **22**, 19858 (2012).

[73] A. Reina, *et al.*, *Nano Letters* **9**, 30 (2009).

[74] P. R. Kidambi, *et al.*, *Nano Letters* **13**, 4769 (2013).

[75] Y. Homma, H. Liu, D. Takagi, Y. Kobayashi, *Nano Research* **2**, 793 (2009).

[76] S. Saadi, *et al.*, *The Journal of Physical Chemistry C* **114**, 11221 (2010).

[77] S. A. Steiner, R. Li, B. L. Wardle, *ACS Applied Materials & Interfaces* **5**, 4892 (2013).

[78] J. Joo, *et al.*, *Journal of the American Chemical Society* **125**, 6553 (2003).

[79] J. Goldak, L. T. Lloyd, C. S. Barrett, *Physical Review* **144**, 478 (1966).

[80] R. Srinivasan, R. J. De Angelis, G. Ice, B. H. Davis, *Journal of Materials Research* **6**, 1287 (1991).

[81] L. Chen, *et al.*, *The Journal of Physical Chemistry C* **115**, 9370 (2011).

[82] M. Winterer, R. Delaplane, R. McGreevy, *Journal of Applied Crystallography* **35**, 434 (2002).

[83] R. V. Sara, *Journal of the American Ceramic Society* **48**, 243 (1965).

[84] P. Pietrokowsky, *Journal of Applied Physics* **37**, 4560 (1966).

[85] Z. S. Basinski, W. Hume-Rothery, A. L. Sutton, *Proceedings of the Royal Society of London A: Mathematical, Physical and Engineering Sciences* **229**, 459 (1955).

[86] M. E. Straumanis, C. C. Weng, *Acta Crystallographica* **8**, 367 (1955).

[87] M. E. Straumanis, L. S. Yu, *Acta Crystallographica Section A* **25**, 676 (1969).

[88] T. D. Golden, *et al.*, *Chemistry of Materials* **8**, 2499 (1996).

[89] J. B. Forsyth, S. Hull, *Journal of Physics: Condensed Matter* **3**, 5257 (1991).

[90] S. Mulik, C. Sotiriou-Leventis, N. Leventis, *Chemistry of Materials* **19**, 6138 (2007).

[91] R. Pekala, C. Alviso, *Novel Forms of Carbon*, C. L. Renschler, J. J. Pouch, D. M. Cox, eds. (Materials Research Soc, 1992), vol. 270.

[92] A. Kudo, *et al.*, *J. Am. Chem. Soc.* **136**, 17808 (2014).

[93] M. H. Rümmeli, *et al.*, *Journal of the American Chemical Society* **129**, 15772 (2007).

[94] Y. Z. Jin, *et al.*, *Carbon* **43**, 1944 (2005).

[95] P. Serp, *et al.*, *Carbon* **4**, 621 (2001).

[96] Z.-X. Xu, J.-D. Lin, V. A. L. Roy, Y. Ou, D.-W. Liao, *Materials Science and Engineering: B* **123**, 102 (2005).

[97] C. Klinke, J.-M. Bonard, K. Kern, *Physical Review B* **71**, 035403 (2005).

[98] M. Chhowalla, *et al.*, *Journal of Applied Physics* **90**, 5308 (2001).

[99] M. Diarra, A. Zappelli, H. Amara, F. Ducastelle, C. Bichara, *Physical Review Letters* **109**, 185501 (2012).

[100] V. B. Vykhodets, *et al.*, *JETP Letters* **93**, 5 (2011).

[101] C. A. Wert, *Phys. Rev.* **79**, 601 (1950).

[102] C. P. Deck, K. Vecchio, *Carbon* **44**, 267 (2006).

[103] F. Ding, A. Rosn, K. Bolton, *The Journal of Chemical Physics* **121**, 2775 (2004).

[104] D. Schebarchov, S. C. Hendy, E. Ertekin, J. C. Grossman, *Physical Review Letters* **107**, 185503 (2011).

[105] Y. Gan, F. Banhart, *Advanced Materials* **20**, 4751 (2008).

[106] G. A. M. Reynolds, A. W. P. Fung, Z. H. Wang, M. S. Dresselhaus, R. W. Pekala, *Journal of Non-Crystalline Solids* **188**, 27 (1995).

[107] C. Alegre, *et al.*, *Catalysts* **2**, 466 (2012).

[108] J. H. Lin, *et al.*, *Chemistry of Materials* **23**, 1637 (2011).

[109] Y. Tao, S. D. Ebbesen, W. Zhang, M. B. Mogensen, *ChemCatChem* **6**, 1220 (2014).

[110] L. Kang, *et al.*, *Nano Lett.* **15**, 403 (2015).

[111] B. Liu, *et al.*, *Journal of the American Chemical Society* **131**, 2082 (2009).

[112] B. Liu, *et al.*, *Journal of the American Chemical Society* **131**, 2082 (2009).

[113] K. Mukhopadhyay, *et al.*, *Chemical Physics Letters* **303**, 117 (1999).

[114] S. Esconjauregui, C. M. Whelan, K. Maex, *Carbon* **47**, 659 (2009).

[115] F. Ding, *et al.*, *Nano Letters* **8**, 463 (2008).

[116] X. Mao, *et al.*, *Chemistry of Materials* **27**, 4574 (2015).

[117] B. C. Bayer, *et al.*, *The Journal of Physical Chemistry C* **115**, 4359 (2011).

[118] R. Cartwright, *et al.*, *Carbon* **81**, 639 (2015).

[119] M. Lazzeri, A. Vittadini, A. Selloni, *Physical Review B* **63**, 155409 (2001).

[120] W. C. Chiou Jr., E. A. Carter, *Surface Science* **530**, 88 (2003).

[121] M. Jafari, M. Vaezzadeh, S. Noroozizadeh, *Metallurgical and Materials Transactions A* **41**, 3287 (2010).

[122] U. Diebold, *Surface Science Reports* **48**, 53 (2003).

[123] M. Guemmaz, G. Moraitis, A. Mosser, M. A. Khan, J. C. Parlebas, *Journal of Electron Spectroscopy and Related Phenomena* **83**, 173 (1997).

[124] S. Hoffmann, S. T. Norberg, M. Yoshimura, *Journal of Electroceramics* **16**, 327 (2006).

[125] J. F. Shackelford, R. H. Doremus, *Ceramic and Glass Materials* (Springer US, 2008).

[126] I. Levin, D. Brandon, *Journal of the American Ceramic Society* **81**, 1995 (1998).

[127] J. M. McHale, A. Auroux, A. J. Perrotta, A. Navrotsky, *Science* **277**, 788 (1997).

[128] B. C. Bayer, *et al.*, *Applied Physics Letters* **105**, 143111 (2014).

[129] C. T. Wirth, *et al.*, *Chemistry of Materials* **24**, 4633 (2012).

[130] G. Z. Chen, D. J. Fray, T. W. Farthing, *Nature* **407**, 361 (2000).

[131] M. M. Doeff, Y. Ma, S. J. Visco, L. C. D. Jonghe, *Journal of The Electrochemical Society* **140**, L169 (1993).

[132] S.-W. Kim, D.-H. Seo, X. Ma, G. Ceder, K. Kang, *Advanced Energy Materials* **2**, 710 (2012).

[133] K. Waki, *et al.*, *Energy Environ. Sci.* **7**, 1950 (2014).

[134] L. Kavan, J. H. Yum, M. Grtzel, *ACS Nano* **5**, 165 (2011).

[135] B. Rebollo-Plata, *et al.*, *Materials Characterization* **58**, 809 (2007).

[136] A. C. Ferrari, D. M. Basko, *Nature Nanotechnology* **8**, 235 (2013).

[137] M. Lin, *et al.*, *Nano Letters* **7**, 2234 (2007). PMID: 17604403.

[138] D. Borgmann, H. Behner, M. Pirner, G. Wedler, *Langmuir* **2**, 261 (1986).

[139] A. V. Ivanov, A. E. Koklin, E. B. Uvarova, L. M. Kustov, *Phys. Chem. Chem. Phys.* **5**, 4718 (2003).

[140] I. Vlassiouk, *et al.*, *ACS Nano* **5**, 6069 (2011).

[141] E. Vietzke, *et al.*, *Journal of Nuclear Materials* **145–147**, 443 (1987).

[142] H. P. Koh, R. Hughes, *Journal of Catalysis* **33**, 7 (1974).

[143] A. C. Gluhoi, J. W. Bakker, B. E. Nieuwenhuys, *Catalysis Today* **154**, 13 (2010).

[144] D.-B. Zhang, E. Akatyeva, T. Dumitrică, *Phys. Rev. Lett.* **106**, 255503 (2011).

[145] S. Timoshenko, S. Woinowsky-Krieger, *Theory of Plates and Shells* (McGraw-Hill, 1959).

[146] H. B. Callen, *Thermodynamics and an Introduction to Thermostatistics* (John Wiley & Sons, 1985).

[147] T. Yoon, *et al.*, *Nano Letters* **12**, 1448 (2012).

[148] S. P. Koenig, N. G. Boddeti, M. L. Dunn, J. S. Bunch, *Nature Nanotechnology* **6**, 543 (2011).

[149] Y. He, W. F. Chen, W. B. Yu, G. Ouyang, G. W. Yang, *Scientific Reports* **3** (2013).

[150] Z. H. Aitken, R. Huang, *Journal of Applied Physics* **107**, 123531 (2010).

[151] O. L. Blakslee, D. G. Proctor, E. J. Seldin, G. B. Spence, T. Weng, *Journal of Applied Physics* **41**, 3373 (1970).

[152] A. Bosak, M. Krisch, M. Mohr, J. Maultzsch, C. Thomsen, *Phys. Rev. B* **75**, 153408 (2007).

[153] P. R. Poulsen, *et al.*, *AIP Conference Proceedings* **544**, 504 (2000).

[154] X. Liu, *et al.*, *The Journal of Physical Chemistry B* **110**, 20102 (2006).

[155] K. J. MacKenzie, O. M. Dunens, A. T. Harris, *Carbon* **59**, 344 (2013).

[156] Q. Zhou, F. Gu, C. Li, *Journal of Alloys and Compounds* **474**, 358 (2009).

[157] S. P. Chai, S. H. S. Zein, A. R. Mohamed, *Applied Catalysis A: General* **326**, 173 (2007).

[158] F. Dillon, M. Copley, A. A. Koos, P. Bishop, N. Grobert, *RSC Adv.* **3**, 20040 (2013).

[159] W. Qian, T. Liu, F. Wei, Z. Wang, Y. Li, *Applied Catalysis A: General* **258**, 121 (2004).

[160] B. M. Eick, J. P. Youngblood, *Journal of Materials Science* **44**, 1159 (2009).

[161] H. Ellingham, *Journal of the Society of Chemical Industry* **63**, 125 (1944).

[162] I. Barin, *Thermochemical Data of Pure Substances, Third Edition* (VCH Verlagsgesellschaft mbH., 1995).

[163] M. Venkatraman, J. P. Neumann, *Bulletin of Alloy Phase Diagrams* **11**, 152 (1990).

[164] V. N. Lipatnikov, A. I. Gusev, P. Ettmayer, W. Lengauer, *Journal of Physics: Condensed Matter* **11**, 163 (1999).

[165] J. Gascn, C. Tllez, J. Herguido, M. Menndez, *Applied Catalysis A: General* **248**, 105 (2003).

[166] C.-H. Wang, S.-S. Lin, *Journal of Environmental Science and Health, Part A* **39**, 1631 (2004).

[167] S. El-Korso, *et al.*, *Journal of Molecular Catalysis A: Chemical* **394**, 89 (2014).

[168] M. Gliński, J. Kijeński, *Reaction Kinetics and Catalysis Letters* **69**, 123 (2000).

[169] A. Y. Borisevich, P. K. Davies, *Journal of the American Ceramic Society* **87**, 1047 (2004).

[170] S. Greenwald, *Nature* **177**, 286 (1956).

[171] G. P. Singh, S. Ram, J. Eckert, H.-J. Fecht, *Journal of Physics: Conference Series* **144**, 012110 (2009).

[172] Rundqvis.S, G. Runnsjo, *Acta Chemica Scandinavica* **23**, 1191 (1969).

[173] J. Xie, N. Chen, J. Shen, L. Teng, S. Seetharaman, *Acta Materialia* **53**, 2727 (2005).

[174] A. Bowman, G. Arnold, E. Storms, N. Nereson, *Acta Crystallographica Section B-Structural Crystallography and Crystal Chemistry* **28**, 3102 (1972).

[175] B. Vasyutin, G. Kartmazo, Y. Smirnov, V. Finkel, *Physics of Metals and Metallography* **21**, 134 (1966).

[176] Y. Guo, S. J. Clark, J. Robertson, *The Journal of Chemical Physics* **140**, 054702 (2014).

[177] V. Eyert, *Annalen der Physik* **11**, 650 (2002).

[178] A. Aouni, P. Weisbecker, T. H. Loi, E. Bauer-Grosse, *Thin Solid Films* **469-470**, 315 (2004).

[179] J. Allred, R. Cava, *Journal of Solid State Chemistry* **198**, 10 (2013).

[180] M. Kikuchi, S. Nagakura, S. Oketani, *Tetsu-to-Hagane* **57**, 1009 (1971).

[181] J. D. Venables, D. Kahn, R. G. Lye, *Philosophical Magazine* **18**, 177 (1968).

[182] K. Yvon, E. Parthé, *Acta Crystallographica Section B* **26**, 149 (1970).

[183] G. Linker, *et al.*, *Thin Solid Films* **471**, 320 (2005).

[184] S. Hull, T. W. D. Farley, W. Hayes, M. T. Hutchings, *Journal of Nuclear Materials* **160**, 125 (1988).

[185] W. E. Lee, K. P. D. Lagerlof, *Journal of Electron Microscopy Technique* **2**, 247 (1985).

[186] C. Xu, M. Hassel, H. Kuhlenbeck, H.-J. Freund, *Surface Science* **258**, 23 (1991).

[187] J. Mendialdua, R. Casanova, Y. Barbaux, *Journal of Electron Spectroscopy and Related Phenomena* **71**, 249 (1995).

[188] G. A. Sawatzky, D. Post, *Phys. Rev. B* **20**, 1546 (1979).

[189] A. C. Ferrari, J. Robertson, *Physical Review B* **61**, 14095 (2000).

[190] J. Schwan, S. Ulrich, V. Batori, H. Ehrhardt, S. R. P. Silva, *Journal of Applied Physics* **80**, 440 (1996).

[191] Y. Ohgi, *et al.*, *ECS Transactions* **41**, 1225 (2011).

[192] N. F. Mott, *Proceedings of the Royal Society of London A: Mathematical, Physical and Engineering Sciences* **127**, 658 (1930).

[193] K. Hirota, K. Mitani, M. Yoshinaka, O. Yamaguchi, *Materials Science and Engineering: A* **399**, 154 (2005).

[194] K. Jiao, *et al.*, *Chem. Commun.* pp. 5618–5620 (2005).

[195] H. Zaidi, F. Robert, D. Paulmier, *Thin Solid Films* **264**, 46 (1995).

[196] Z. Liu, *et al.*, *The Journal of Physical Chemistry C* **119**, 18248 (2015).

[197] K. Z. Li, H. Wang, Y. G. Wei, D. X. Yan, *The Journal of Physical Chemistry C* **113**, 15288 (2009).

[198] X. Feng, *et al.*, *Nano Letters* **8**, 3781 (2008).

[199] A. L. Briseno, *et al.*, *Nano Letters* **10**, 334 (2010).

[200] P. Meduri, C. Pendyala, V. Kumar, G. U. Sumanasekera, M. K. Sunkara, *Nano Letters* **9**, 612 (2009).

[201] D. Chen, Z. Liu, B. Liang, X. Wang, G. Shen, *Nanoscale* **4**, 3001 (2012).

[202] M. Law, L. E. Greene, J. C. Johnson, R. Saykally, P. Yang, *Nat Mater* **4**, 455 (2005).

[203] B. Liu, E. S. Aydil, *Journal of the American Chemical Society* **131**, 3985 (2009).

[204] S. M. Jung, H. Y. Jung, W. Fang, M. S. Dresselhaus, J. Kong, *Nano Letters* **14**, 1810 (2014).

[205] S. Tang, *et al.*, *Nat Commun* **6**, (2015).

[206] T. Niu, M. Zhou, J. Zhang, Y. Feng, W. Chen, *Journal of the American Chemical Society* **135**, 8409 (2013).

[207] E. Carter, A. F. Carley, D. M. Murphy, *The Journal of Physical Chemistry C* **111**, 10630 (2007).

[208] X. Chen, L. Liu, P. Y. Yu, S. S. Mao, *Science* **331**, 746 (2011).

[209] J. S. Chen, *et al.*, *Journal of Applied Physics* **89**, 7814 (2001).

[210] R. C. Powles, N. A. Marks, D. W. M. Lau, D. G. McCulloch, D. R. McKenzie, *Carbon* **63**, 416 (2013).

[211] O. A. Maslova, M. R. Ammar, G. Guimbretire, J.-N. Rouzaud, P. Simon, *Physical Review B* **86**, 134205 (2012).

[212] D. Knight, W. White, *Journal of Materials Research* **4**, 385 (1989).

[213] W. Bauhofer, J. Z. Kovacs, *Composites Science and Technology* **69**, 1486 (2009). CNT-NET 07 Special Issue with regular papers.

[214] Z. Yu, *et al.*, *Nano Energy* **11**, 611 (2015).

[215] L. Wang, A. Ambrosi, M. Pumera, *Angewandte Chemie International Edition* **52**, 13818 (2013).

[216] R. E. Franklin, *Proceedings of the Royal Society of London A: Mathematical, Physical and Engineering Sciences* **209**, 196 (1951).

[217] T. A. Westrich, K. A. Dahlberg, M. Kaviany, J. W. Schwank, *The Journal of Physical Chemistry C* **115**, 16537 (2011).

[218] A. Yamamoto, Y. Mizuno, K. Teramura, T. Shishido, T. Tanaka, *Catalysis Science & Technology* **3**, 1771 (2013).

[219] K. Mizuno, *et al.*, *Proceedings of the National Academy of Sciences* **106**, 6044 (2009).